UNIVERSITY OF CALIFORNIA

Los Angeles

Probing and Controlling Interactions and Assemblies at the Nanoscale

A dissertation submitted in partial satisfaction of the

requirements for the degree Doctor of Philosophy

in Chemistry

by

Alexandra Marie Mendoza

2018

ABSTRACT OF THE DISSERTATION

Probing and Controlling Interactions and Assemblies at the Nanoscale

by

Alexandra Marie Mendoza

Doctor of Philosophy in Chemistry

University of California, Los Angeles, 2018

Professor Paul S. Weiss, Chair

Understanding how to tune molecular assemblies and the properties of surfaces of different materials at the meso- and nanoscales can lead to unique and controllable interactions at interfaces for a variety of applications. I used dipolar forces to control the adsorption and alignment of liquid crystals (LCs), which are highly sensitive to surface interactions. This work utilized carboranethiol and -dithiol isomers, which possess the same geometry and lattice when self-assembled on Au{111}, but differ in the magnitude and direction of their dipole moments. Hence, self-assembled monolayers (SAMs) of carboranethiol isomers enabled us to deconvolve dipole interactions from other factors that influence LC alignment. We fabricated LC devices using carboranethiol SAMs on transparent gold surfaces, prepared by oblique evaporation, and measured the LC orientation and anchoring energy on surfaces treated with each isomer. These results suggested that the dipole moment direction strongly influences the LC alignment and anchoring energy.

In the second part of my dissertation, I used bioinspired omniphobic surface coating for rapid cell deformation devices to enable high-throughput intracellular cargo delivery. Currently, devices clog within minutes, rendering them inefficient for sustainable cell processing. We have developed a method for coating commercial poly(tetrafluoroethylene) syringe and poly(ethylene terephthalate) filters with slippery liquid-infused porous surfaces (SLIPS). We see that without this coating, essentially no cells are recovered from the device, due to clogging. However, with the SLIPS coating, we are able to recover 25-50% of cells. Additionally, we have successfully delivered a green fluorescent protein plasmid and a CD19 chimeric antigen receptors to Jurkat cells, a model T lymphocyte cell line, while maintaining high cell viability. These devices made from economical commercial materials will enable new opportunities in the development of gene and cellular therapies for a wide variety of disease treatments, which are currently limited due to toxicity, low throughput, and off-target effects.

This dissertation of Alexandra Marie Mendoza is approved.

Andrea M. Kasko

Xiangfeng Duan

Jeffrey I. Zink

Paul S. Weiss, Committee Chair

University of California, Los Angeles

2018

For my parents,

who gave me the tools and foundation for success.

Table of Contents

CHAPTER II

Surface Dipole Control of Liquid Crystals

CHAPTER IV

Delivery of a CD19 Expressing Chimeric Antigen Receptor *via* Rapid Cell Deformation

CHAPTER V

Conclusions and Future Prospects

List of Abbreviations and Symbols

Acronyms and Symbols

1O2	*o*-1,2-carboranedithiol
5CB	4-cyano-4′-pentylbiphenyl
9O12	*o*-9,12-carboranedithiol
α	molecular polarizability tensors
AAVV	adeno-associated viral vector
AC	time-varying
ADA	adenosine deaminase
AFM	atomic force microscopy
Ag	silver
Au	gold
$\overrightarrow{\mathbf{Au}}$	gold evaporation direction
C11	1-undecanethiol
C12	1-dodecanethiol
C18	1-octadecanethiol
CAR	chimeric antigen receptor
CCP	cell penetrating peptides
CRISPR	clustered regularly interspaced short palindromic repeats
δ	delta
Δε	dielectric anisotropies
Δn	liquid crystal birefringence

d	wedge thickness
DAPI	4',6-diamidino-2-phenylindole
DC	constant, time independent
ddPCR	digital droplet polymerase chain reaction
DI	deionized
DNA	deoxyribonucleic acid
EGFP-EGFR	enhanced green fluorescent protein-epidermal growth factor receptor
γ	gamma
Γ	optical retardation
GFP	green fluorescent protein
GMP	good manufacturing practice
FBS	fetal bovine serum
FDA	Food and Drug Administration
H_2O_2	hydrogen peroxide
H_2SO_4	sulfuric acid
hcp	hexagonal close-packed
HSC	hematopoietic stem cell
HSCT	hematopoietic stem cell transplant
I	current
J WT	Jurkat wild type
K_{22}	twist elastic constant
λ	wavelength
LC	liquid crystal

μ	permanent molecular dipole moment
μCP	microcontact printing
μDP	microdisplacement printing
m	fringe order integer
M1	*m*-1-carboranethiol
M9	*m*-9-carboranethiol
MBBA	*N*-(4-methoxybenzylidene)-4-butylaniline
mRNA	messenger ribonucleic acid
n	sample size
NaOH	sodium hydroxide
$\boldsymbol{\eta_d}$	equilibrium director orientations
NILV	non-integrating lentiviral vector
$\boldsymbol{\eta_0}$	easy alignment axis
O1	*o*-1-carboranethiol
O9	*o*-9-carboranethiol
φ	angle at which the director deviates from the easy axes
Ψ	angular twist
$\boldsymbol{p}_{\parallel}$	parallel dipole moment orientation
$\boldsymbol{p}_{\perp}$	perpendicular dipole moment orientation
P	pressure
PBS	phosphate-buffered saline
PDMS	poly(dimethylsiloxane)
PET	poly(ethylene terephthalate)

PTFE	poly(tetrafluoroethylene)
RNA	ribonucleic acid
RPMI	Roswell Park Memorial Institute
σ	uncertainty
SAM	self-assembled monolayer
SCD	sickle cell disease
SCID	severe combined immunodeficiency
SEM	scanning electron microscopy
SLIPS	slippery liquid-infused porous surfaces
STM	scanning tunneling microscope
T	temperature
T cells	T lymphocytes
TALEN	transcription activator-like effector nucleases
TCR	T-cell receptors
$\mathbf{T_{NI}}$	transition temperature
$\boldsymbol{W_{az}}$	azimuthal anchoring energy
ZFN	zinc fingers nucleases

Units

Å	Ångström
bp	base pair
C	Celsius
cm	centimeter

D	Debye
eV	electron volt
h	hour
kb	kilobase
kHz	kilohertz
µJ	microjoule
µL	microliter
µm	micrometer
m	meter
mg	milligram
min	minute
mL	milliliter
mm	millimeter
mM	millimolar
MΩ·cm	milliohm-centimeter
ms	millisecond
nm	nanometer
s	second
V	volt

Acknowledgments

I want to first thank my parents, Cynthia and Richard Mendoza, who have always supported and encouraged me to pursue a career in science. Thank you for teaching me what hard work is, giving me everything I needed to be successful, and always believing in me. I want to also thank my brother, Michael Mendoza, for being my partner in crime and for believing in me. To my Rivero family, thank you for your unwavering support and love. I am so lucky to have such a supportive and loving family.

I am grateful for the mentorship of my advisor, Professor Paul S. Weiss. Thank you for showing me how to be a scientist, how to tackle new and exciting problems, and instilling in me to never be scared to jump into new fields. I value how you have taught me to think of our science with big picture goals always in mind and your invaluable advice on presenting and writing. These lessons and skills have shaped me into the scientist I am today, and will stay with me as I move on from graduate school. I am also thankful to my committee members, Professors Jeffrey I. Zink, Xiangfeng Duan, and Andrea M. Kasko, for their support and guidance during the course of my dissertation work.

I am extremely thankful to the Weiss group members, who shared their knowledge, expertise, and friendship with me. I would like to thank Dr. Jeffrey J. Schwartz for your mentorship and for being an excellent teacher and friend. I would also like to thank Natcha Wattanatorn, you have been a great friend and labmate. I appreciate that we have been able to work so closely and always be there to teach and learn from one another. Additionally, I would like to thank Dr. Steve J. Jonas for branching our group into the exciting field of gene and cellular delivery and for the help and expertise you have offered me during my last few years of graduate school. Moreover, I want to thank Dr. Nako Nakatsuka, you have been a

true friend since the first day of graduate school. Graduate school would not have been the same without you – we had so many adventures together and you have been a great friend throughout it all. I am so proud of you and am lucky to have such a strong, smart, and generous friend and colleague. I am beyond thrilled for your next step as a postdoctoral scholar in Switzerland at the Swiss Federal Institute of Technology in Zurich and I cannot wait to see where this next chapter takes you. I would also like to thank Dr. John M. Abendroth for your scientific help, support, and friendship during graduate school. As well, I would like to thank Kevin M. Cheung for being a great friend and labmate. I would like to thank the rest of the Weiss group for their support and I wish them luck in all their future endeavors.

For the later part of my dissertation work, I am grateful to our collaborators, Professor Satiro N. De Oliveria and Dr. Tzu (Iris) T. Chiou. The expertise your group shared with me truly excelled my exciting gene delivery work. Iris, you taught a chemist cell biology, not an easy task. I am so thankful for your patience and hard work; learning from you evolved my biology knowledge and appreciation for it.

I would like to thank all of the funding organizations that have supported me and my research during my graduate school tenure. I would like to thank the UCLA Graduate Division for the Eugene V. Cota Robles Fellowship and the National Science Foundation for the Graduate Research Fellowship (DGE-1144087). Additionally, the first part of my dissertation work was supported by the U.S. Department of Energy (DE-SC-0005025) and the Keck Foundation. The later part of my Ph.D. work was generously supported by the Alex's Lemonade Stand Foundation for Childhood Cancer Research, the Hyundai Hope on Wheels Foundation, the St. Baldrick's Foundation, and the Tower Cancer Research Foundation. I

would like to thank Adaptive Surface Technologies, Inc., Professor Joanna Aizenberg, and Dr. Philseok Kim for their insight into the design of SLIPS materials throughout our collaboration.

As well, I would like to thank my OCDS (Organization for Cultural Diversity in Science) family. You were such an important aspect of my graduate school experience. I made so many friends along the way and will have a lifelong connection and network. I would like to thank my predecessors, Dr. Crystal Valdez and Professor Steven Lopez for the hard work, foundation, and example you set for OCDS. Additionally, I would like to thank my co-presidents, Dr. Tejas Shah and Dr. Emma Pelegri-O'Day. Not only were you great friends, you were great teammates. I am proud of the work we were able to accomplish together. To my successors, Janice Lin, David Gonzalez, and Kevin Cannon, I am so proud of the work you are doing and am excited to see where you take OCDS next. Moreover, I would like to thank Professor Miguel Garcia-Garibay for your continual support and mentorship. Thank you to the whole OCDS family, I am looking forward to seeing OCDS grow and prosper under the next generation.

Lastly, I want to thank Nick Rivero, without your patience, understanding, support, and friendship I would not be where I am today. You have been my rock for 13 years and have supported me unconditionally through the good as well as the difficult times. I am so fortunate to have someone like you in my life and cannot wait to see where life will take us next.

Vita

Alexandra Mendoza was a Minority Biomedical Research Support-Initiative for Maximizing Student Development Research Scholar, funded by the National Institutes of Health, at San Diego State University (SDSU) from 2011 to 2012, where she earned a Bachelor of Science degree in chemistry, *cum laude*, with a Minor in Spanish. While at SDSU, Alexandra researched how to tune the surface chemistry and antimicrobial properties of silver nanoparticles under the mentorship of Professors David P. Pullman and Karen I. Peterson. Her research led to one co-authored publication and she presented her work at five conferences, where she received an award for Outstanding Poster Presentation at the 43rd American Chemical Society Western Regional Meeting in 2011.

Alexandra continued her academic training with Professor Paul S. Weiss at the University of California, Los Angeles (UCLA) in 2012. During her time at UCLA, Alexandra received two prestigious fellowships to support her during her dissertation work: the Eugene V. Cota Robles Fellowship in 2012 and a National Science Foundation Graduate Research Fellowship in 2013. Outside of research, Alexandra was heavily involved with community outreach, academic service, and technology transfer throughout her time at UCLA. She was co-outreach chair (2014-2015) and co-president (2015-2017) of the Organization for Cultural Diversity in Science. She was also a graduate student representative on the UCLA Division of Physical Science's Diversity Committee from 2016-2018. Alexandra was a Technology Fellow at the UCLA Technology Development Group from July 2016 to September 2018 and was promoted to Senior Technology Fellow in March of 2018.

Publications

Alexandra M. Mendoza, Tzu T. Chiou, Isaura I. Frost, Natcha Wattanatorn, Philseok Kim, Joanna Aizenberg, Satiro N. De Oliveira, Paul S. Weiss, Steve J. Jonas, Slippery Liquid-Infused Porous Surfaces for Rapid Cell Deformation Devices and Cargo Delivery, *in preparation* (2018).

Alexandra M. Mendoza, Tzu T. Chiou, Xiaobin Xu, Natcha Wattanatorn, Satiro N. De Oliveira, Steve J. Jonas, Paul S. Weiss, Delivery of a CD19 Expressing Chimeric antigen Receptor *via* Rapid Cell Deformation, *in preparation* (2018).

Jeffrey J. Schwartz, **Alexandra M. Mendoza**, Natcha Wattanatorn, Yuxi Zhao, Vinh T. Nguyen, Alexander M. Spokoyny, Chad A. Mirkin, Tomáš Baše, Paul S. Weiss, Surface Dipole Control of Liquid Crystal Alignment. *J. Am. Chem. Soc.* **2016**, *138*, 5957.

M. Gabriela Espinoza, Mallory L. Hinks, **Alexandra M. Mendoza**, David P. Pullman, Karen I. Peterson, Kinetics of Halide-Induced Decomposition & Aggregation of Silver Nanoparticles. *J. Phys. Chem. C* **2012,** *116*, 8305.

Selected Conference Presentations

Alexandra M. Mendoza, Chuanzhen Zhao, Qing Yang, Philseok Kim, Steve J. Jonas, Paul S. Weiss, Slippery Liquid-Infused Porous Surfaces for Cell Deformation Microfluidic Devices and Cargo Delivery, 255th American Chemical Society Meeting, March 2018, oral presentation.

Alexandra M. Mendoza, Jeffrey J. Schwartz, Yuxi Zhao, Natcha Wattanatorn, Paul S. Weiss, Surface-Dipole-Induced Alignment of Liquid Crystals, 2015 California Alliance Retreat at the California Institute of Technology, Pasadena, CA, April 2015, poster presentation.

Alexandra M. Mendoza, M. Gabriela Espinoza, Pettus, Karen I. Peterson, David P. Pullman, Influence of Amino Acids with Silver Nanoparticles & their Antimicrobial Properties against *Escherichia coli,* 243rd American Chemical Society Meeting, San Diego, CA, March 2012, poster presentation.

Alexandra M. Mendoza, M. Gabriela Espinoza, Greg Pettus, Karen I. Peterson, David P. Pullman, Influence of Amino Acids with Silver Nanoparticles & their Antimicrobial Properties against *Escherichia coli*, SDSU Student Research Symposium, San Diego, CA, March 2012, oral presentation.

CHAPTER I

Probing and Controlling Interactions and Assemblies at the Nanoscale

I.A. Motivation and Background

Surface-interface interactions have the potential to direct assemblies and to control adsorbates at chemically-defined locations, unmasking new and unexpected properties and functions.[1–15] Understanding how to harness these surface-interface interactions at the micro- and nanoscale will drive the development of innovative methods and new capabilities in materials chemistry and science.[16,17] The ability to tune surface features and their physical properties at these resolutions, more precise control of surface-chemical interactions, either by achieving precise control of over the orientation of chemical moieties[4,9] and/or prohibiting the adsorption of species on surfaces.[10–15] By mastering these surface-interface interactions, I have leveraged self-assembled monolayers (SAMs) on gold surfaces to direct the assembly of liquid crystals (LCs) on surfaces (Chapter II)[9] and applied bioinspired anti-fouling chemistries on to commercially available membranes to enable robust and cost-effective delivery of biomolecular cargo to cells for applications in gene therapy and in cancer immunotherapy (Chapter III and Chapter IV).

I.B. Surface Dipoles to Control Assemblies at the Nano- and Mesoscale

I.B.1. Self-Assembled Monolayers and their Properties

Self-assembled monolayers are used as a versatile and facile nanofabrication technique.[18–21] To improve the control of molecular assembly and the properties of these materials at the meso- and nanoscale, it is critical to probe non-covalent interactions, such as dipolar dispersion forces or van de Waals interactions.[9,17,22–27] Previous studies have demonstrated how SAMs with different terminal groups can alter the surface properties of materials; for instance, surfaces can be rendered hydrophobic or hydrophilic by simply

changing the terminal group from a carboxylic acid to a fluorinated moiety.[15,28,29] Additionally, several studies have shown that other physical properties can be tuned based on the chemical composition of SAMs, such as the work function of metals,[17,30] chemical recognition and adsorption,[31,32] and conductivity.[33] In particular, understanding how SAMs interact with molecules that adsorb to the surface can offer important information about molecular interactions at interfaces at the nanoscale.[9,17,30]

I.B.2. Control of Assemblies on Surfaces

Several groups have previously shown how the terminal groups of SAMs can be used to control how adsorbates interact with surfaces.[9,17,30–33] For example, SAMs presenting different chemical functionalities can be used to modulate the adsorption of different chemical species onto substrate materials and applied to crystal growth[3,5] or to alignment of liquid crystals.[9,22,34–37] Aizenberg and coworkers used SAMs with different terminal functional groups to inhibit or to promote nucleation and crystal growth of small molecules on surfaces and further found that the selection of the underlying substrate material (*e.g.,* Au vs. Ag) alters crystallographic orientation.[3] Additionally, the versatility by which SAMs can be modified has enabled the chemical tethering of proteins, aptamers, or different biomolecules to these surfaces for applications in biosensors.[31,32] It is critical to control the orientation and alignment of chemically-tethered molecules at SAM interfaces. Chen *et al.* engineered surfaces comprised of positively and negatively charged SAMs to control the orientation of two types of antibodies.[4] However, in these studies, there is a convolution of different competing effects that govern surface-interface interactions, ranging from changes in dipole moment, molecular packing, steric effects, and wettability. Designing SAMs where

one property is changed, while all other properties remain constant remains a challenge with conventional SAM building blocks.[30,38]

I.B.3. Carboranethiol and –Dithiol Self-Assembled Monolayers

Carboranethiol and -dithiol isomers are of interest as SAM layers for a variety of reasons. They provide several advantages over alkanethiols and other common SAM molecules, where altering any part of the molecule can change the physical properties (*e.g.,* sterics, internal dipole moment, electronics) of the monolayer and alter how the molecules interact with their environment.[9,26,30,38] These carborane isomers have a nearly regular icosahedral boron carbon cluster geometry with two carbon atoms either adjacent (ortho) or separated (meta) by a boron atom.[9,26,30,38–43] The key advantage of these SAM molecules is that their dipole moment's direction and strength can be altered depending where the carbon atom is placed within the cage and when assembled on a Au{111} surface, they possess the same geometry, lattice, and molecular tilt (Figure I.1A).[9,26,30,38] Additionally, these carboranethiol and -dithiol isomers can be easily functionalized at a number of positions within the cage and are both chemically and thermally stable.[26,30,38–43]

Our group previously demonstrated that when the 1,7-dicarba-*closo*-dodecaborane *m*-1-carboranethiol (M1) and *m*-9-carboranethiol (M9) isomers are assembled on Au{111} (Figure I.1A), the two isomers are indistinguishable by scanning tunneling microscopy in ambient conditions and that the SAMs possess identical hexagonally close-packed adlayer structures (Figure I.1B).[30] In follow up studies, it was observed that it is possible to control the surface potential. For example, using ultraviolet photoelectron spectroscopy, Kim *et al.* found that varying the ratio of M1 to M9 modifies the work function (Figure I.1C).[17] Monolayers with more M1 character (*i.e.,* with a surface dipole pointing toward the surface)

increased the metal's work function, whereas monolayers with higher M9 content (*i.e.,* with the dipole pointing away from the thiol group) lowered the work function of gold (Figure I.1C).[17]

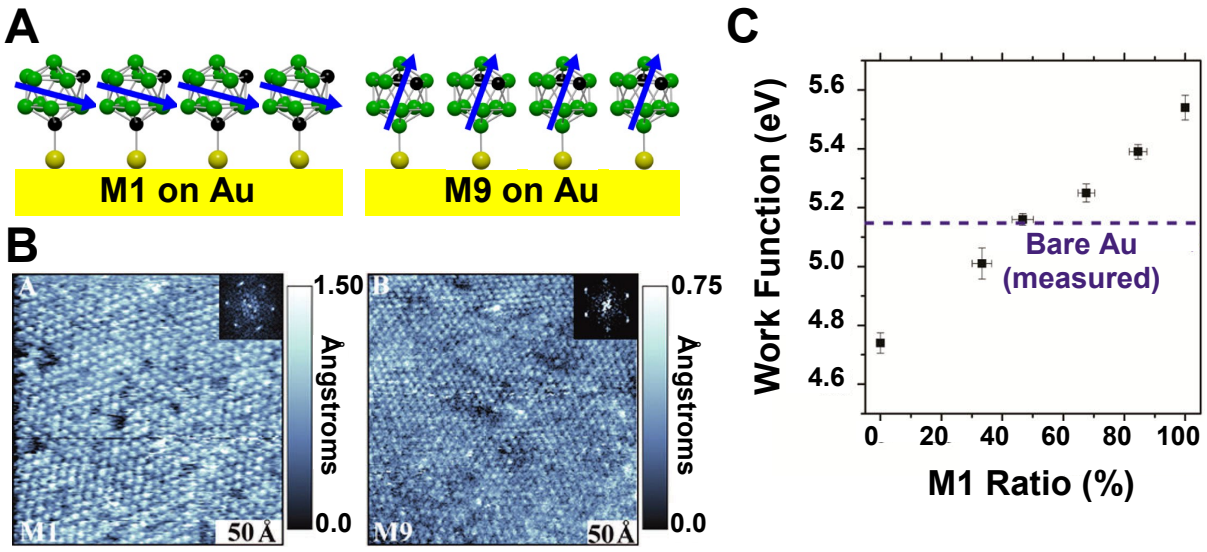

Figure I.1. (A) Schematic of 1,7-dicarba-*closo*-dodecaborane *m*-1-carboranethiol (M1) and *m*-9-carboranethiol (M9) assembled on a Au{111} surface. (B) Scanning tunneling microscope images of M1 (left) and M9 (right) self-assembled monolayers on Au{111} surfaces. Isomers are indistinguishable and have the same hexagonal close-packing. Images were collected at a sample bias of 1.0 V and a tunneling current of 3.0 pA. (C) Ultraviolet photoelectron spectroscopy showing how the work function varies with different ratios of M1 to M9 on gold surfaces. Reproduced with permission from Reference (A, B) 30 and (C) 17. Copyright 2009 and 2014 American Chemical Society.

I.B.4. Control of Liquid Crystal Alignment on Surfaces

Liquid crystals (LCs) are known to be sensitive to surface interactions and have alignment-dependent optical properties.[9,22,34,35,44] Industrially, LC alignment is controlled by unidirectional rubbing that breaks the rotational symmetry of the alignment surfaces.[45,46] Without this mechanical rubbing, random local alignment domains are formed; however, the application of the rubbing method enables uniaxial alignment of the LCs.[45,46] Another approach used to break rotational symmetry utilizes dune-like surface textures of obliquely

deposited, semi-transparent gold films to direct LC alignment (Figure I.2A).[34,44,47] When depositing the metal, the substrate is tilted at an angle to the metal source, creating a textured gold surface and breaking the azimuthal symmetry of the surface (Figure I.2B).[9,34,44,47] The LCs adopt in-plane orientations with their long axes perpendicular to the oblique deposition direction, minimizing elastic strain within the LC assembly.[9,34,44,47]

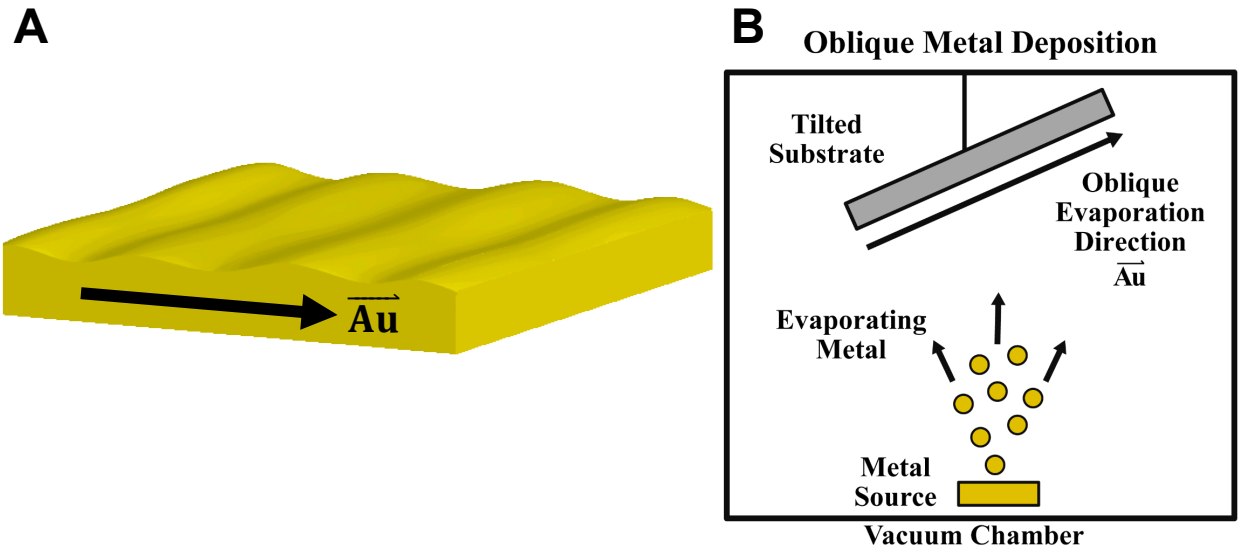

Figure I.2. Schematic of oblique gold deposition. (A) Nano trough, dune-like features generated from oblique gold evaporation. (B) Inside a vacuum chamber, gold is heated by an electron beam (not shown), causing it to evaporate from a source and deposit onto a tiled substrate located above. Reproduced with permission from Reference 9. Copyright 2016 American Chemical Society.

Using these textured Au surfaces, Abbott and others have reported that SAMs also influence the alignment of LCs, with the ability to control both azimuthal and polar orientations.[34,35,48] An "odd–even" effect was shown to occur, where alkanethiols with odd number length chains aligned LCs perpendicular to the oblique gold deposition direction ($\overrightarrow{\text{Au}}$), whereas ones of even lengths aligned the LCs parallel to the $\overrightarrow{\text{Au}}$, and a 1:1 mixture of the two thiols aligned the LCs normal, or homeotropic, to the surface (Figure I.3).[34,35,48] Likewise, the terminal functional groups can also change the alignment of LCs to be either parallel or perpendicular to the $\overrightarrow{\text{Au}}$.[34,35,48] Ultimately, this behavior demonstrates that LC alignment is sensitive to variations in the symmetry and orientation of the exposed terminal moieties of the underlying SAM.[34,35,48] In these studies, many factors influence LC behavior, including steric effects, surface topography, and intermolecular forces, which complicates the mechanisms responsible for alignment. The independent effects of molecular geometry, orientation, and dipole moment on LC alignment are difficult to determine.

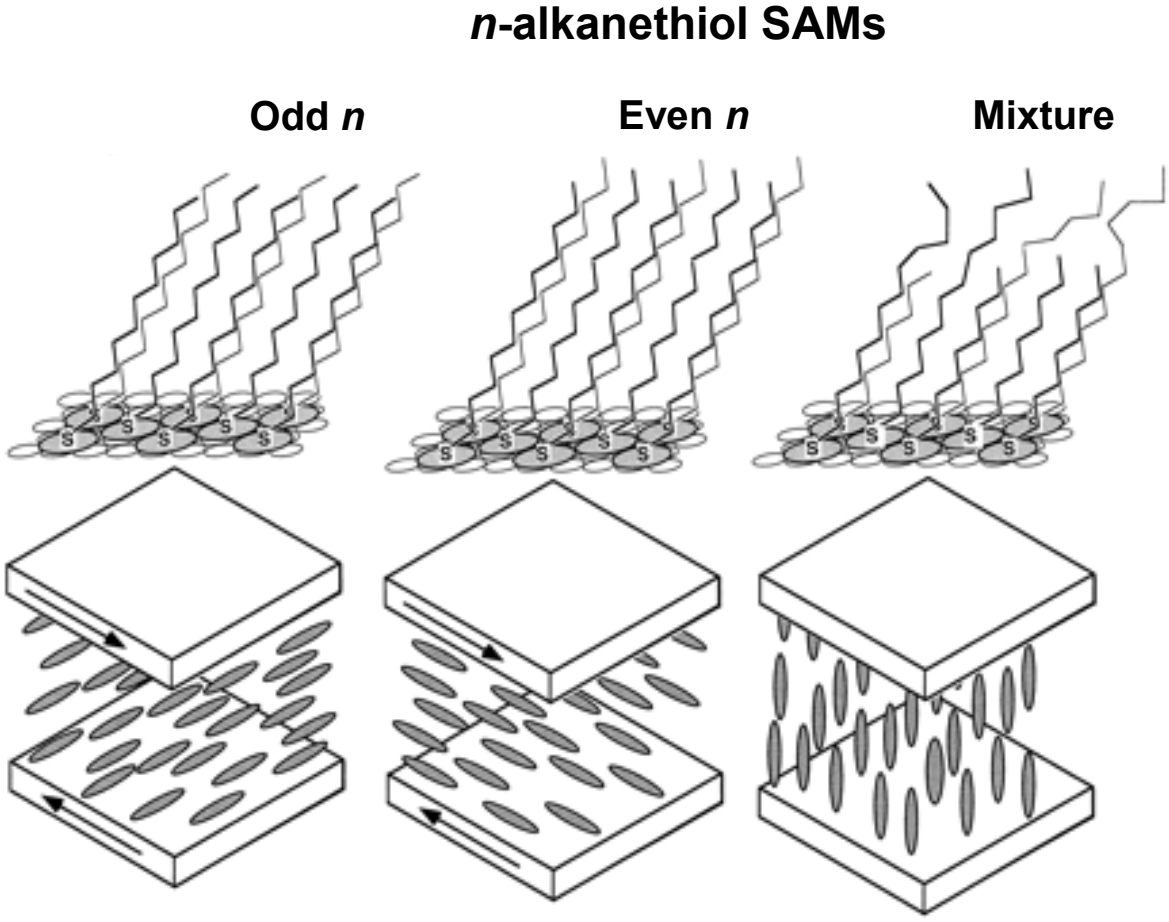

Figure I.3. Azimuthal orientation influenced by SAM odd-even effect. Odd length alkanethiol self-assembled monolayers (SAMs) align liquid crystals perpendicular to the gold evaporation direction (left), whereas even length alkanethiol SAMs align liquid crystals parallel to the gold evaporation direction (center). Alkanethiol mixtures (1:1) of the odd and even length alkanethiols align liquid crystals normal to the surface, or homeotropic (right). Reproduced with permission from Reference 48. Copyright 1997 American Association for the Advancement of Science.

I.B.5. Surface Dipole Moment Control of Liquid Crystals

Following these studies, our group used carboranethiol SAMs to investigate how dipolar forces influence how adsorbates interact with the surface by deconvolving dipole interactions from other factors that affect how molecules adsorb or interact with the surface.[9] To study this phenomenon, we used LCs, which have alignment-dependent optical properties and can transduce and amplify nanoscale forces into a macroscopic optical readout.[9] By using isomers of carboranethiol SAMs that differ only in their dipole moment direction and magnitude (and not lattice, molecular tilt, or geometry), we were able to isolate dipole interactions from other factors that could influence molecular assembly.[9] We tested how changing the surface dipoles on Au surfaces influenced the alignment and anchoring of 4-cyano-4′-pentylbiphenyl (5CB) and *N*-(4-methoxybenzylidene)-4-butylaniline (MBBA) liquid crystals (LCs).[9] We fabricated LC displays using carboranethiol and -dithiol SAMs on thin transparent gold surfaces, prepared by oblique evaporation.[9,22,34,35,44] To characterize these devices, we measured the LC orientation on surfaces treated with each isomer, 1,7-dicarba-*closo*-dodecaborane *m*-9-carboranethiol (M9), *m*-1-carboranethiol (M1), *o*-9-carboranethiol (O9), *o*-1-carboranethiol (O1), *o*-9,12-carboranedithiol (9O12), and *o*-1,2-carboranedithiol (1O2), using a polarizing optical microscope (Figure I.4). Our results demonstrated that the dipole moment direction predominately influences the LC alignment direction and anchoring energy strength (Figure I.4).[9] Our investigation into this field will be fully described in Chapter II, which was first published in the *Journal of the American Chemical Society* in 2016.[9] The use of carboranethiols as an alternative to alkanethiol SAM coatings for electronic devices has only begun, which is leading to interesting device coatings that enable more control over the interface properties.

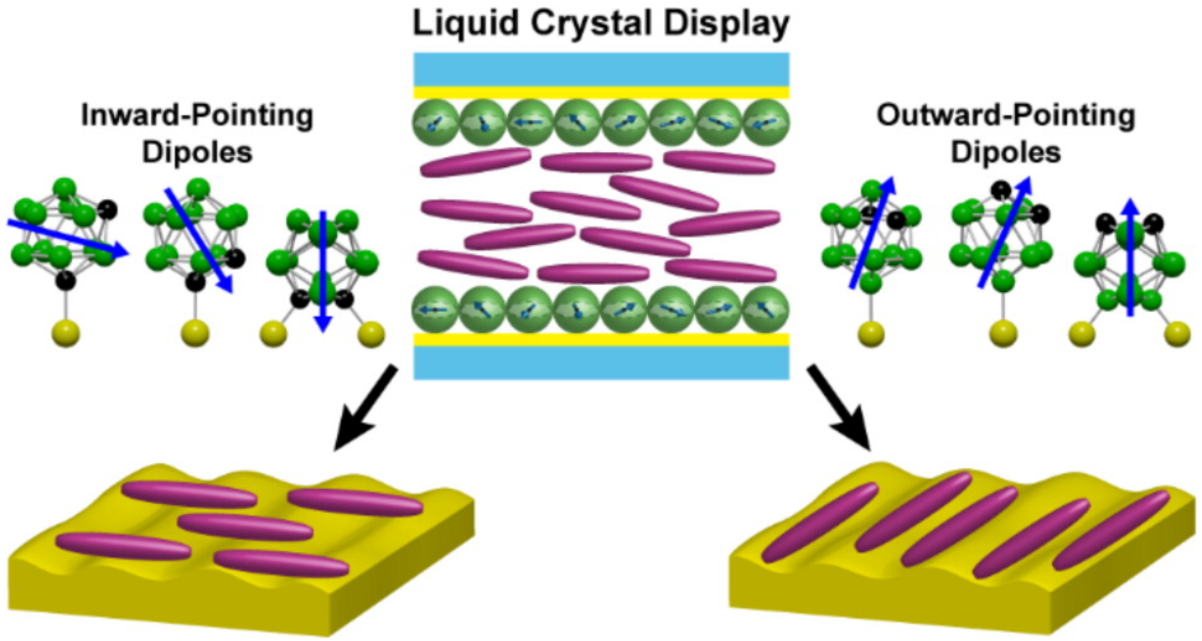

Figure I.4. Molecular structures depicting magnitude and direction of carboranethiol and -dithiol isomers' dipole moment of: 1,7-dicarba-*closo*-dodecaborane *m*-1-carboranethiol (M1), *o*-1-carboranethiol (O1), *o*-1,2-carboranedithiol (1O2), *m*-9-carboranethiol (M9), *o*-9-carboranethiol (O9), and *o*-9,12-carboranedithiol (9O12). Schematic of induced alignment of liquid crystals with inward- or outward-pointing surface dipoles on Au substrates. Reproduced with permission from Reference 9. Copyright 2016 American Chemical Society.

I.C. Rapid Cell Deformation Microfluidic Devices and Intracellular Delivery of Biomolecular Cargo

I.C.1. Gene Therapy Approaches

Emerging cellular therapies are revolutionizing how clinicians approach and treat a wide-range of genetic diseases, including hematological disorders, primary immunodeficiencies, Duchenne muscular dystrophy, and cancers.[49–53] These medical interventions are enabled by genome editing strategies that utilize targeted nuclease-based strategies, such as zinc fingers nucleases (ZFNs),[54–56] transcription activator-like effector nucleases (TALEN),[55,57–59] and clustered regularly interspaced short palindromic repeat (CRISPR) nucleases,[60–66] to achieve site-specific disruption or correction of disease causing mutations. In addition, the application of chimeric antigen receptors (CAR) in adoptive cellular therapies has enabled physicians to harness the immune system to fight cancers directly.[67–72]

The current techniques that enable genetic modification of hematopoietic stem cells (HSCs) and T lymphocytes (T cells), used in bone marrow transplants and cancer immunotherapy, respectively, are inadequate.[49,73] For example, viral vector-based and non-viral-based methods (*i.e.,* electroporation and chemical transfection) suffer from off-target effects and are expensive while suffering from low yields, low processing throughputs, and induce damage to treated cells, which has limited their broader application at clinically relevant scales.[60,74] To address these issues, other approaches, including microinjection,[75–77] rapid cell deformation,[78–84] nanoparticles[85,86] or nanostructures,[87–94] acoustic waves,[95] or sonoporation,[96–99] have been reported for delivery of genetic or other biomolecular cargo into cells. However, the development of methods that are cargo agnostic while achieving

rapid, safe, cost effective, and efficient intracellular delivery remains a challenge.[73] A decade ago, our group showed that when using geometric confinement, membrane vesicles would deform creating transient pores at the membrane.[100] This idea has been further exploited and extended to cell membranes for different type of bimolecular cargo delivery.[73] Unfortunately, these devices suffer from biofouling and cellular buildup rendering them inefficient for clinical applications.[78–84]

I.C.1.a. Gene Editing of Hematopoietic Stem Cells for Monogenetic Disorders

Autologous gene-modified stem cell-based therapies are promising and exciting approaches for treating monogenetic disorders. These gene-therapy strategies rely on correcting disease-causing mutations in a patient's own stem cells prior to reinfusion back to the patient.[49,54,61,67,101–103] In contrast, current allogeneic hematopoietic stem cell transplantation (HSCT) strategies rely on finding a match donor.[49,54,61,67,101–103] However, complications in the form of graft rejection or graft-versus-host disease can occur if a suitable donor cannot be identified.[49,54,61,67,101–104] Hematological monogenetic diseases are promising candidates for these types of cellular therapies based on the well-established history of HSCT for offering curative solutions for pathologies.[49,54,61,67,101–103] The combination of HSCT with gene editing tools (*e.g.,* CRISPR/Cas9 nucleases) paves the way for new types of interventions that target monogenetic diseases, which only have one gene defect to address.[55,60–63,101]

Disease targets for autologous gene-modified stem cell therapies include immunodeficiencies (*e.g.,* SCID),[50,51,105,106] hemoglobinopathies (*e.g.*, thalassemia, sickle cells),[54,107] and coagulopathies (*e.g.*, hemophilia).[49,101,108] Currently, allogeneic hematopoietic stem cell transplant is the definitive management option for these diseases,

but a match is often difficult to find.[49,54,67,101–103] Recent advances in the application of CRISPR-based genome editing tools are opening new possibilities for gene modification in HSCs.[55,60–64,109–112] Although in their infancy, these stem-cell-based gene therapies already show tremendous promise in the treatment of debilitating genetic diseases. For instance, Kohn and coworkers have successfully demonstrated the efficacy of γ-retroviral vector-based insertion of human adenosine deaminase (ADA) cDNA for the treatment of ADA-deficient SCID.[50] Additionally, De Luca and coworkers first reported a possible route to treating epidermolysis bullosa, a rare and painful genetic skin disease that causes skin to be fragile and blister, using genetically modified stem cells.[113] In 2017, De Luca and his team reported the successful treatment of a seven year-old boy suffering from epidermolysis bullosa using a whole body transplant by autologous stem cell engraftment.[114] Sickle cell disease (SCD), one of the most common monogenetic diseases worldwide, represents another promising target for gene therapies. This hemoglobinopathy results from a single point mutation in the seventh codon of the β-globin gene. Recent studies demonstrated that a ZFN could be used to target the β-globin locus containing SCD mutation and be cleaved with minimal off-target effects, suggesting a possible treatment option.[54] Hemophilias have also emerged as tantalizing targets for gene therapies, where ZFNs,[56] TALENs,[115] and CRISPR-Cas9[73] have been used to correct mutations in the genes encoding for factor VIII or IX, which are responsible for different hemophilia subtypes. Moreover, in 2017 George *et al.* demonstrated that a one-time dose of the Factor 9 Padua transgene could be administered to hemophilia B patients to prevent bleeding, without any serious toxicities or adverse effects.[116] In general, for these therapies to be effective, highly efficient and prolonged

expression of genetic constructs and survival of the transfected HSCs are critical to success.[49,111,112,117]

I.C.1.b. Adoptive Cellular Therapies for Engineering T Cells for Cancer Therapy

Adoptive cellular therapies that utilize either engineered T-cell receptors (TCRs) or chimeric antigen receptors (CARs) are enabling powerful immunotherapies in the fight against cancer.[49,68–72,118,119] It has been established for over 50 years that T cells and other immune system cells help promote tumor rejection.[118] Previously, allogeneic T cells have been used to treat patients with leukemias or lymphomas, but the trials resulted in graft-versus-host disease.[104,118,120] These early investigations pointed to the possibility to use the immune system *via* T cells to treat cancer.[118] The ability to collect T cells from patients autologously *via* apheresis and to engineer these cells to target malignancies *via* the insertion of CAR constructs has led to new treatment options for high-risk patients that circumvent manifestations of graft-versus-host disease and other undesirable effects.[49,104,118,120] The successful delivery of the CAR vector to the patient's T cells enables these engineered immune cells to recognize and to specifically target tumor antigens.[49,118,121,122] These cellular immunotherapies approaches effectively harness the immune system to attack malignant cells, reducing reliance on conventional, harsher cancer treatments like surgery, chemotherapy, or radiation, or may be used in conjunction with or when these traditional treatments fail.[118,119,123,124]

Anti-CD19 expressing CARs have emerged as the most common CAR therapy to date. These genetically modified T cells target the CD19 receptor present on the surfaces of B cell-derived lymphomas and leukemias. Recently, two CAR-based approaches have gained Food and Drug Administration (FDA) approval for treating B cell malignancies. Similar CAR T cell

approaches are actively being explored as potential treatments for multiple myeloma, myeloid malignancies, and other solid tumors.[49,119,123–125] Based on their success in treating cancer, other groups are developing similar CAR therapies for application in the treatment of HIV and other autoimmune diseases.[49,118,126] For these therapies to be successful there exists a critical need for stable and long-lasting gene expression of the transferred CAR construct in target T cell populations to maintain immune memory and prohibit relapse, which, to date, has been difficult to achieve safely and at desirable throughputs using current gene delivery methods.[49,119,121,122]

I.C.2. Limitations of Current *ex Vivo* Gene Editing Methods

Despite the promise of emerging cellular therapies, current methods used to process engineered stem or immune cells are limited in their ability to generate appropriate cellular products effectively. New approaches are being developed rapidly, with ZFN- and TALEN-based approaches entering FDA clinical trials, several CRISPR-based packages have already been approved in China,[49] and the first two CAR T cell therapies have recently gained FDA approval.[127,128] Despite these advances, there remains an unmet need for methods that enable the effective delivery of therapeutic packages into cells in a high throughput, efficient, safe, universal, and cost-effective manner.

Both viral vectors and non-viral-based transfection methods are used currently to deliver the genes and genome editing machinery to cells (Figure I.5).[49,111,117,129] However, viral vectors are prone to potential off-target effects and require specialized, good manufacturing practice (GMP)-grade materials and reagents that are expensive at clinical scales.[130] Similarly, non-viral-based transfection approaches (*e.g.*, electroporation, lipofection) tend to be slow, require specialized equipment and/or regents, and yield

variable transfection efficiencies across different cell lines when scaled for therapeutic applications.[49,111,117,129] Moreover, a significant part of the high costs associated with gene editing of therapeutic cell products is the need to process large populations of cells (*i.e.,* $\sim 1x10^6$ cells/kg for T cells and $\sim 2x10^8$ cells/kg for HSCs) to achieve appropriate doses.[131–135] Additionally, the maintenance of cell viability is an important criterion when manipulating HSCs and/or T cells *ex vivo* for therapeutic applications.[112] The broader deployment of these innovative medical interventions will require solutions that address the current unmet needs for improved intracellular delivery tools and methods that enable efficient delivery of biomolecular cargo economically, safely, and quickly. In this section, I review the advantages and setbacks associated with viral and non-viral transfection methods, and later present my research, which targets solutions motivated by advances from the nanoscience community, to streamline the development, manufacture, and access to gene and cellular therapies.

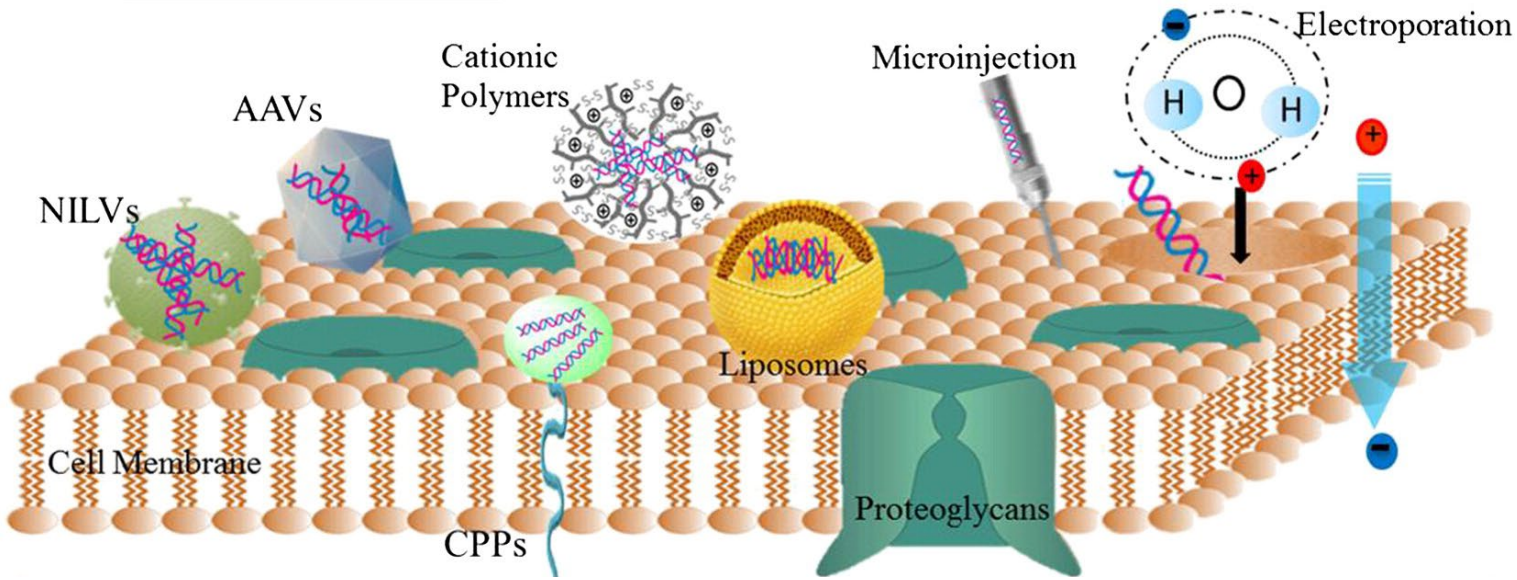

Figure I.5. Schematic of intracellular delivery of plasmids using viral and non-viral delivery methods. Viral vector methods, such as non-integrating lentiviral vectors (NILVs) or adeno-associated viral vectors (AAVVs), utilize evolved viruses to deliver genetic materials to cells, whereas non-viral transfection methods use physical or chemical methods. For example, electroporation uses electric fields, liposome-based methods (lipofection) uses chemicals, cell penetrating peptides (CPPs) use enzymes, and micro-injection relies on directly injecting cells with a needle in order to deliver genetic DNA into cells. Reproduced with permission from Reference 55. Copyright 2015 Elsevier.

I.C.2.a. Viral Vectors for Gene Editing

Viral vectors are inactivated viruses that are engineered to deliver genetic constructs to cells (Figure I.5).[136–138] These genetic delivery vehicles are used routinely in the laboratory setting for investigations in molecular biology and related fields and have more recently achieved limited success when applied in early phase clinical trials.[49] The most commonly used viral vector approaches for *ex vivo* transfection are derived from either γ-retroviruses or lentiviruses.[49,112] As opposed to γ-retroviral vectors, lentiviral-based systems enable gene delivery to non-dividing cells and are able to package larger gene cassettes (~8 kb of DNA).[49,112] However, lentiviral-based delivery remains prone to potentially dangerous off-target effects that can result in undesirable constitutive expression and/or insertional mutagenesis.[112] Despite their relatively high transfection efficiency, safety concerns (off-target effects, immunogenicity, oncogenesis) associated with viral vector-based approaches often out-weigh their potential therapeutic benefits, even when applied to most debilitating diseases.[139–142] In addition, a significant limitation of viral vector carriers is the size of plasmid sequences that can be effectively packaged and delivered to target cells, not to mention the labor intensive and costly methods required to manufacture them.[136,139] Moreover, these methods are limited to gene addition and are not easily reconfigured for targeting other diseases.[49,112] Each new gene therapy would have to go through a separate FDA approval process based on the specific vector system and genetic cargo used, greatly limiting their universal application and effectiveness across a variety of disease targets.[51,136,143]

I.C.2.b. Non-Viral Delivery of Cellular Therapies

Non-viral intracellular delivery approaches often rely on either harsh chemicals or physical and/or energetic manipulation to deliver biomolecular cargo intracellularly (Figure I.5).[74,111,139,144–146] These methods are capable of either gene addition or disruption and, in some cases, are less prone to off-target effects.[49,57,60,62] However, successful gene delivery and/or editing requires genetic cargo to be delivered inside of the nucleus of cells, which often comes at the cost of cell viability and efficiency.[139] In addition, these methods are often highly variable across cell lines and primary cells, where no existing method, to date, has achieved universally robust performance.[139]

Chemical transfection methods (*e.g.*, lipofection) are limited by concerns with toxicity and variable transfection efficiencies.[139,147] For instance, Park *et al.* recently reported a lipofection-based method for delivering CRISPR-Cas9 cargo targeting correction of mutations of the Factor VIII gene in induced pluripotent stem cells.[101] However, the long-term survival of treated mice and the efficacy of Factor VIII gene correction were inadequate in their animal models.[101] Energetic methods (*e.g.*, electroporation) are more efficient than chemical transfection approaches due, in part, to their ability to force cargo directly into the cytoplasmic compartment or nucleus of target cells.[139,148] However, electroporation and related methods tend to result in lower cell viabilities, are highly operator dependent, and require specialized reagents to yield optimal transfection.[139,148] Moreover, the mechanism of delivery is not well understood, leading to difficulties in evaluating the optimal conditions for delivery across different cells lines and types of cargo.[147]

I.C.2.b.i. Rapid Membrane Deformation

Several alternative intracellular delivery technologies have been reported and are in active development.[73] For example, microinjection techniques where genetic cargo is inserted directly into individual cells have enabled breakthroughs in *in vitro* fertilization and somatic cell nuclear transfer for applications in reproductive medicine and stem cell biology.[73] However, microinjection is highly inefficient for processing large numbers of cells (Figure I.5).[75–77] Additional intracellular delivery approaches include sonoporation,[96–99] nanoparticle carriers,[85,86] or membrane piercing nanostructures,[87–94] but have not been optimized for clinically relevant scales or universal use.

One interesting intracellular delivery approach, reported recently by Langer and coworkers, is based on the mechanical deformation of cells as they are passed through microfluidic constrictions.[73,78–81] As target cells are directed to squeeze through narrow microfluidic channels, they are rendered transiently permeable (~5 min), enabling the efficient delivery of biomolecular cargo across mechanically generated pores across the membranes of processed cells *via* diffusion.[73,78–81] Unfortunately, the broader implementation of this technology has been limited by issues with biofouling of cellular debris that leads to device failure due to clogging of the microfluidic network. Effective delivery of biomolecular payloads requires cells to squeezed by approximately 30-80% of their normal diameter (Figure I.6).[73,78–81] Ultimately, the degree of biofouling within the microfluidic channels compromises the long-term reliability of these device and the ability to reach reliable and sustainable cell processing throughputs for clinical applications.

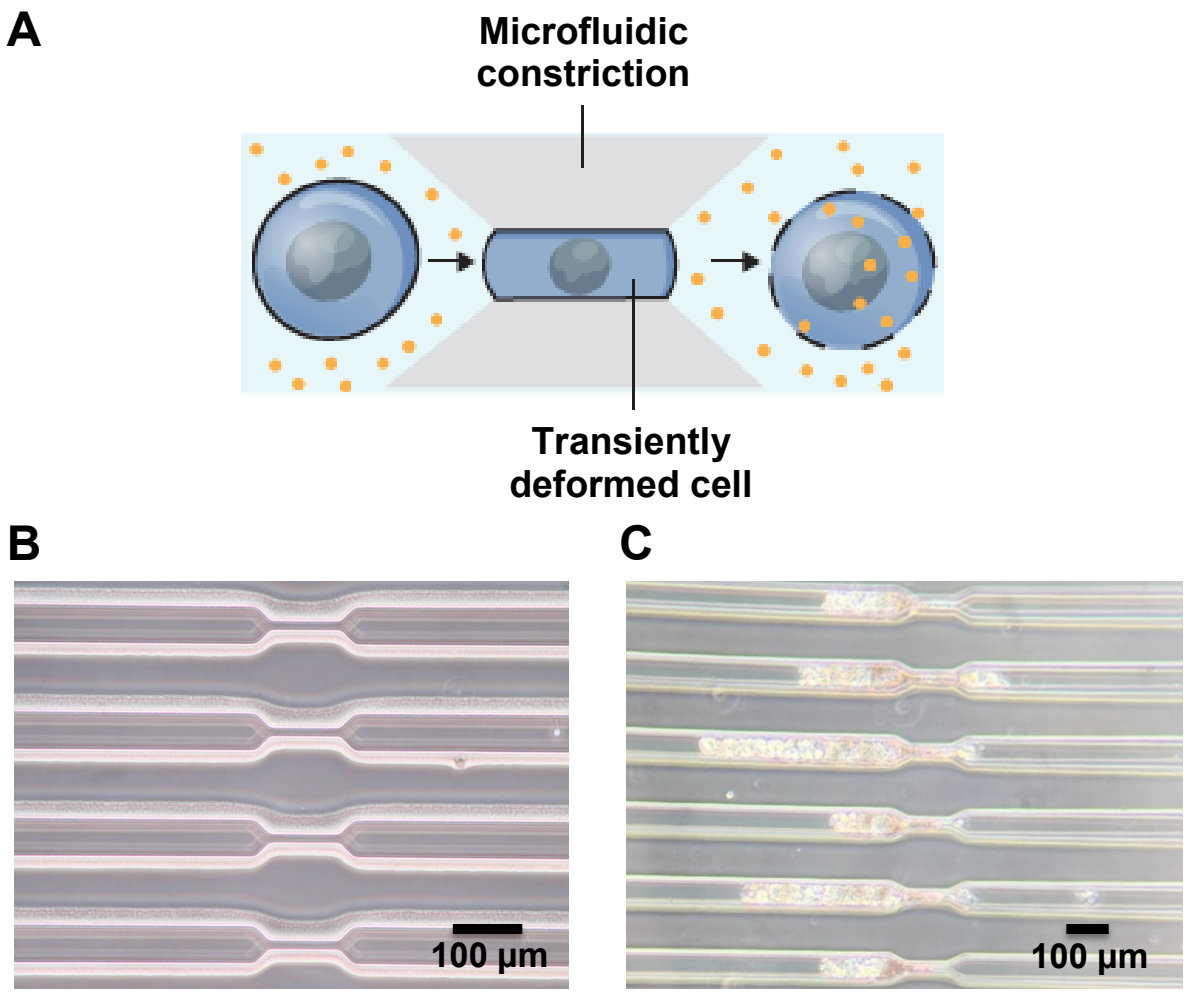

Figure I.6. (A) Rapid cell deformation schematic. Adapted with permission from Reference 81. Copyright 2017 Nature. (B) Poly(dimethylsiloxane) (PDMS) channels before and (C) after flowing with K562 cells. The PDMS microfluidic devices clog within several minutes.

I.C.3. Design of Materials for Rapid Cell Deformation and Cargo Delivery

The current materials used to fabricate microfluidic devices for intracellular cargo delivery *via* rapid membrane deformation clog within minutes and are inadequate for sustainable cell processing. In our group, we have designed and tested a new intracellular delivery where coating commercially-available membranes (pore diameters 3 – 10 μm) are treated with slippery liquid-infused porous surfaces (SLIPS). These bioinspired surface chemistries enable rapid transport of biomolecular payloads (*e.g.,* DNA/RNA, proteins) into target cells *via* transient permeabilization that occurs as cells pass through the narrow constriction and avoid biofouling issues that have precluded existing embodiments of this technique. We have applied these SLIPS-functionalized devices to the delivery of expression plasmid cargo for the generation of gene and cellular therapies.

I.C.3.a. Slippery Liquid-Infused Porous Surface-Coated Cell Deformation Devices

To address the challenges associated with clogging of rapid cell deformation devices, we have developed a cost-effective method where bioinspired omniphobic surface chemistries are incorporated into commercially available membrane materials to enable high-throughput and efficient intracellular delivery nucleic acids to cells. Device performance is characterized using model payloads. Our initial proof-of-concept studies utilize expression plasmid cargo encoding for either green fluorescent protein (GFP) or a CD19 CAR construct. The commercially available syringe filter membranes utilized for our cell-squeezing devices (Fig. I.7) are made from either poly(tetrafluoroethylene) (PTFE) or poly(ethylene terephthalate) (PET). These materials are then treated with a chemically matched oil to establish a SLIPS overlayer that is akin to a layer of "artificial mucous."[11–14] The SLIPS process was first developed by Aizenberg and coworkers for the generation of

materials with unprecedented omniphobic behavior and have applied them broadly to a number of industrial applications.[11–14]

The omniphobic behavior enabled by SLIPS prevents the deposition of biomolecules at treated interfaces, which we leverage to achieve continuous processing of target cells *via* rapid deformation across treated membranes.[11–14] A key advantage of our approach is our use of commercially available membrane materials, which, when combined with SLIPS-coatings, enable scalable, simple to use, biocompatible, non-toxic, and rapid intracellular delivery (Fig. I.7). These devices circumvent several major obstacles that have precluded the generation of genetically modified therapeutic HSCs and T cells *via* conventional intracellular delivery approaches. Materials treated with SLIPS not only prevent clogging but also enable the mechanical properties of the microchannels to be fine tuned. Our investigations into applying these devices made from commercial materials, with and without SLIPS modification, for delivering biomolecular cargo to cells are detailed in Chapter III and Chapter IV.

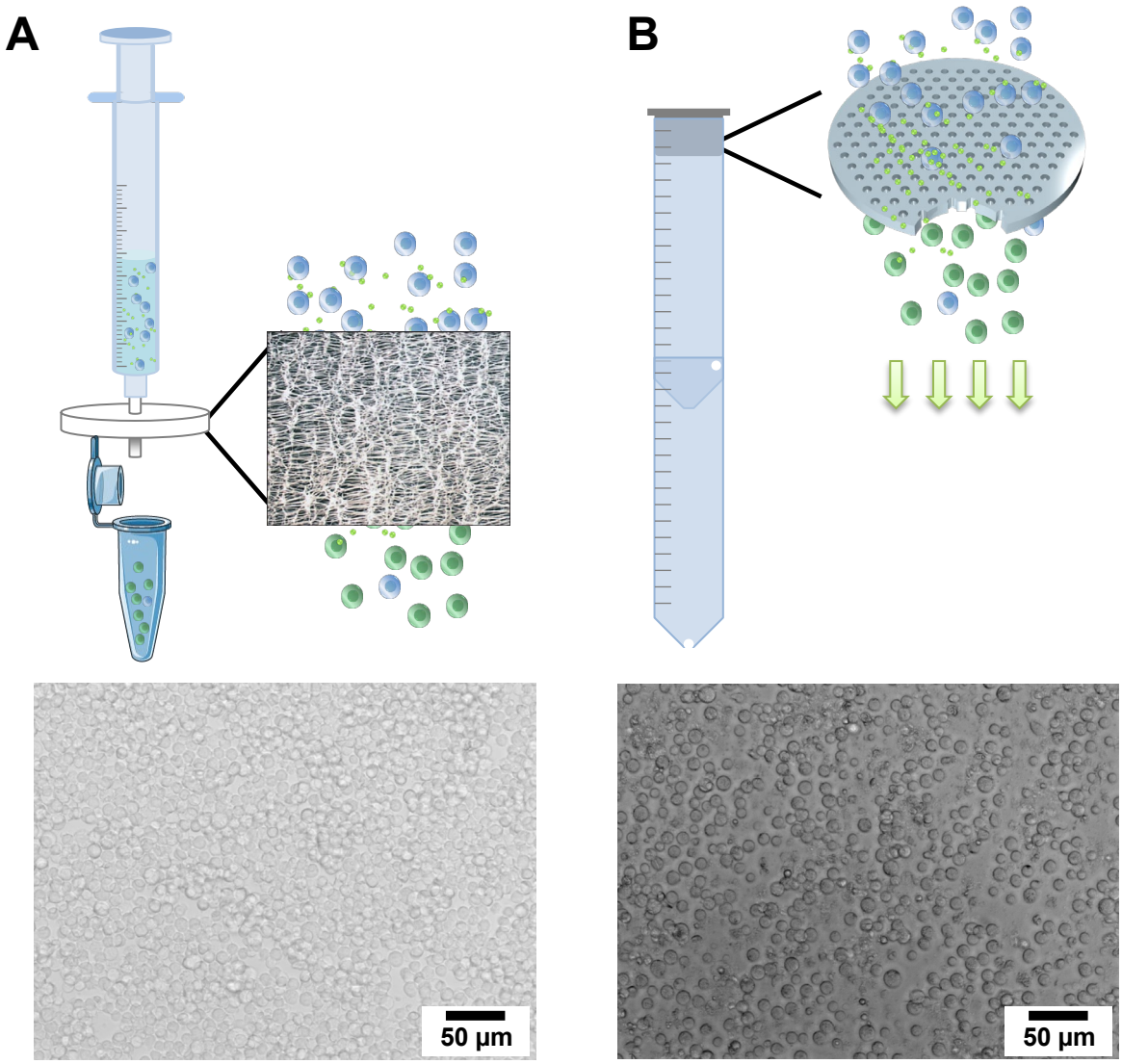

Figure I.7. Schematics of rapid cell deformation devices using commercially available materials. The experimental procedure of a (A) slippery liquid-infused porous surfaces-infused poly(tetrafluoroethylene) syringe filter. Jurkat cells are mixed with either a green fluorescent protein-based plasmid (GFP) or a plasmid encoding for a CD19 chimeric antigen receptor (CAR) and suctioned into a syringe. The syringe is connected to the syringe filter, which is either unmodified or modified with a fluorinated silicone oil. The cells are flowed through the filter using a syringe pump (not shown) with a flow rate of 0.25 mL/min and the cells are cultured for 24 – 72 h and a (B) vacuum filtration system using poly(ethylene terephthalate) cell culture filter inserts, either unmodified or modified with a fluorinated or unfluorinated silicone oil. Jurkat cells and mixed with either a GFP or a CD19 CAR plasmid and vacuum filtered through a porous culture insert membrane with 3-8 µm track-etched pores, using house vacuum. Cells are cultured for 24 to 72 hours after transfection. Corresponding bright field images are shown below of the Jurkat cells 24 hours after cell deformation experiments.

I.D. Dissertation Overview

This dissertation is organized as follows: Chapter I reviews the current methods used for controlling adsorbates and tuning surface properties for applications in electronics and intracellular delivery systems. Chapter II describes research that leverages carboranethiol and -dithiol self-assembled monolayers for precisely controlling the alignment and anchoring energy of liquid crystals to surfaces. Chapter III describes our recent research where SLIPS-modified surfaces are applied to commercial membranes to achieve the reliable and cost-effective generation of engineered cells for gene and cellular therapies *via* precisely controlled membrane disruption. In Chapter IV, a facile SLIPS-modified vacuum filtration system is developed to achieve similarly robust intracellular delivery to target cell populations. Chapter V summarizes the two project areas as well as the future directions and prospects of these fields.

Chapter II has been reformatted from the following manuscript with permission:

Schwartz; J. J.; **Mendoza, A. M.**; Wattanatorn, N.; Zhao, Y.; Nguyen, V.; Spokoyny, A. M.; Mirkin, C. A.; Baše, T.; Weiss, P. S. Surface Dipole Control of Liquid Crystal Alignment. *J. Am. Chem. Soc.* **2016**, *138*, 5957. DOI: 10.1021/jacs.6b02026

Chapter III is based on a manuscript in preparation. Currently, it is as follows:

Mendoza, A.M.; Chiou, T.T.; Frost, I.M.; Wattanatorn, N.; Kim, P.; Aizenberg, J.; De Oliveira, S.N;. Jonas, S.J.; Weiss, P.S. Slippery Liquid-Infused Porous Surfaces for Rapid Cell Deformation Devices and Cargo Delivery. (in preparation).

Chapter IV is based on a manuscript in preparation. Currently, it is as follows:

Mendoza, A.M.; Chiou, T.T.; Xu, X.; Wattanatorn, N.; De Oliveira, S.N.; Jonas, S.J.; Weiss, P.S. Delivery of a CD19 Expressing Chimeric Antigen Receptor *via* Rapid Cell Deformation. (in preparation).

I.E. References

(1) Israelachvili, J. N. *Intermolecular and Surface Forces*, 3rd Edition.; Israelachvili, J. N., Ed.; Academic Press: San Diego, 2011.

(2) Lee, H. J.; Jamison, A. C.; Lee, T. R. Surface Dipoles: A Growing Body of Evidence Supports Their Impact and Importance. *Acc. Chem. Res.* **2015**, *48*, 3007–3015.

(3) Aizenberg, J.; Black, A. J.; Whitesides, G. M. Oriented Growth of Calcite Controlled by Self-Assembled Monolayers of Functionalized Alkanethiols Supported on Gold and Silver. *J. Am. Chem. Soc.* **1999**, *121*, 4500–4509.

(4) Chen, S.; Liu, L.; Zhou, J.; Jiang, S. Controlling Antibody Orientation on Charged Self-Assembled Monolayers. *Langmuir* **2003**, *19*, 2859–2864.

(5) Briseno, A. L.; Aizenberg, J.; Han, Y.-J.; Penkala, R. A.; Moon, H.; Lovinger, A. J.; Kloc, C.; Bao, Z. Patterned Growth of Large Oriented Organic Semiconductor Single Crystals on Self-Assembled Monolayer Templates. *J. Am. Chem. Soc.* **2005**, *127*, 12164–12165.

(6) Hermes, S.; Schröder, F.; Chelmowski, R.; Wöll, C.; Fischer, R. A. Selective Nucleation and Growth of Metal–Organic Open Framework Thin Films on Patterned COOH/CF_3-Terminated Self-Assembled Monolayers on Au(111). *J. Am. Chem. Soc.* **2005**, *127*, 13744–13745.

(7) Lee, C.-Y.; Gong, P.; Harbers, G. M.; Grainger, D. W.; Castner, D. G.; Gamble, L. J. Surface Coverage and Structure of Mixed DNA/Alkylthiol Monolayers on Gold: Characterization by XPS, NEXAFS, and Fluorescence Intensity Measurements. *Anal. Chem.* **2006**, *78*, 3316–3325.

(8) Scherb, C.; Schödel, A.; Bein, T. Directing the Structure of Metal–Organic Frameworks by Oriented Surface Growth on an Organic Monolayer. *Angew. Chem.* **2008**, *120*, 5861–5863.

(9) Schwartz, J. J.; Mendoza, A. M.; Wattanatorn, N.; Zhao, Y.; Nguyen, V. T.; Spokoyny, A. M.; Mirkin, C. A.; Baše, T.; Weiss, P. S. Surface Dipole Control of Liquid Crystal Alignment. *J. Am. Chem. Soc.* **2016**, *138*, 5957–5967.

(10) Howell, C.; Vu, T. L.; Lin, J. J.; Kolle, S.; Juthani, N.; Watson, E.; Weaver, J. C.; Alvarenga, J.; Aizenberg, J. Self-Replenishing Vascularized Fouling-Release Surfaces. *ACS Appl. Mater. Interfaces* **2014**, *6*, 13299–13307.

(11) Howell, C.; Vu, T. L.; Johnson, C. P.; Hou, X.; Ahanotu, O.; Alvarenga, J.; Leslie, D. C.; Uzun, O.; Waterhouse, A.; Kim, P.; Super, M.; Aizenberg, M.; Ingber, D. E.; Aizenberg, J. Stability of Surface-Immobilized Lubricant Interfaces under Flow. *Chem. Mater.* **2015**, *27*, 1792–1800.

(12) MacCallum, N.; Howell, C.; Kim, P.; Sun, D.; Friedlander, R.; Ranisau, J.; Ahanotu, O.; Lin, J. J.; Vena, A.; Hatton, B.; Wong, T.-S.; Aizenberg, J. Liquid-Infused Silicone As a Biofouling-Free Medical Material. *ACS Biomater. Sci. Eng.* **2015**, *1*, 43–51.

(13) Grinthal, A.; Aizenberg, J. Mobile Interfaces: Liquids as a Perfect Structural Material for Multifunctional, Antifouling Surfaces. *Chem. Mater.* **2014**, *26*, 698–708.

(14) Hou, X.; Li, J.; Tesler, A. B.; Yao, Y.; Wang, M.; Min, L.; Sheng, Z.; Aizenberg, J. Dynamic Air/Liquid Pockets for Guiding Microscale Flow. *Nat. Commun.* **2018**, *9*.

(15) Yao, X.; Dunn, S. S.; Kim, P.; Duffy, M.; Alvarenga, J.; Aizenberg, J. Fluorogel Elastomers with Tunable Transparency, Elasticity, Shape-Memory, and Antifouling Properties. *Angew. Chem. Int. Ed.* **2014**, *53*, 4418–4422.

(16) Kudernac, T.; Lei, S.; Elemans, J. A. A. W.; Feyter, S. D. Two-Dimensional Supramolecular Self-Assembly: Nanoporous Networks on Surfaces. *Chem. Soc. Rev.* **2009**, *38*, 402–421.

(17) Kim, J.; Rim, Y. S.; Liu, Y.; Serino, A. C.; Thomas, J. C.; Chen, H.; Yang, Y.; Weiss, P. S. Interface Control in Organic Electronics Using Mixed Monolayers of Carboranethiol Isomers. *Nano Lett.* **2014**, *14*, 2946–2951.

(18) Whitesides, G. M.; Grzybowski, B. Self-Assembly at All Scales. *Science* **2002**, *295*, 2418–2421.

(19) Smith, R. K.; Lewis, P. A.; Weiss, P. S. Patterning Self-Assembled Monolayers. *Prog. Surf. Sci.* **2004**, *75*, 1–68.

(20) Love, J. C.; Estroff, L. A.; Kriebel, J. K.; Nuzzo, R. G.; Whitesides, G. M. Self-Assembled Monolayers of Thiolates on Metals as a Form of Nanotechnology. *Chem. Rev.* **2005**, *105*, 1103–1170.

(21) Claridge, S. A.; Liao, W.-S.; Thomas, J. C.; Zhao, Y.; Cao, H. H.; Cheunkar, S.; Serino, A. C.; Andrews, A. M.; Weiss, P. S. From the Bottom up: Dimensional Control and Characterization in Molecular Monolayers. *Chem. Soc. Rev.* **2013**, *42*, 2725–2745.

(22) Clare, B. H.; Guzmán, O.; de Pablo, J. J.; Abbott, N. L. Measurement of the Azimuthal Anchoring Energy of Liquid Crystals in Contact with Oligo(Ethylene Glycol)-Terminated Self-Assembled Monolayers Supported on Obliquely Deposited Gold Films. *Langmuir* **2006**, *22*, 4654–4659.

(23) Paniagua, S. A.; Hotchkiss, P. J.; Jones, S. C.; Marder, S. R.; Mudalige, A.; Marrikar, F. S.; Pemberton, J. E.; Armstrong, N. R. Phosphonic Acid Modification of Indium−Tin Oxide Electrodes: Combined XPS/UPS/Contact Angle Studies. *J. Phys. Chem. C* **2008**, *112*, 7809–7817.

(24) Bishop, K. J. M.; Wilmer, C. E.; Soh, S.; Grzybowski, B. A. Nanoscale Forces and Their Uses in Self-Assembly. *Small* **2009**, *5*, 1600–1630.

(25) Liang, H.; Sun, W.; Jin, X.; Li, H.; Li, J.; Hu, X.; Teo, B. K.; Wu, K. Two-Dimensional Molecular Porous Networks Formed by Trimesic Acid and 4,4′-Bis(4-Pyridyl)Biphenyl on Au(111) through Hierarchical Hydrogen Bonds: Structural Systematics and Control of Nanopore Size and Shape. *Angew. Chem. Int. Ed.* **2011**, *50*, 7562–7566.

(26) Thomas, J. C.; Schwartz, J. J.; Hohman, J. N.; Claridge, S. A.; Auluck, H. S.; Serino, A. C.; Spokoyny, A. M.; Tran, G.; Kelly, K. F.; Mirkin, C. A.; Gilles, J.; Osher, S. J.; Weiss, P. S. Defect-Tolerant Aligned Dipoles within Two-Dimensional Plastic Lattices. *ACS Nano* **2015**, *9*, 4734–4742.

(27) Kulkarni, C.; Bejagam, K. K.; Senanayak, S. P.; Narayan, K. S.; Balasubramanian, S.; George, S. J. Dipole-Moment-Driven Cooperative Supramolecular Polymerization. *J. Am. Chem. Soc.* **2015**, *137*, 3924–3932.

(28) Dai, X.; Sun, N.; Nielsen, S. O.; Stogin, B. B.; Wang, J.; Yang, S.; Wong, T.-S. Hydrophilic Directional Slippery Rough Surfaces for Water Harvesting. *Sci. Adv.* **2018**, *4*, eaaq0919.

(29) Kondo, R.; Nakajima, D.; Kikuchi, T.; Natsui, S.; Suzuki, R. O. Superhydrophilic and Superhydrophobic Aluminum Alloys Fabricated *via* Pyrophosphoric Acid Anodizing and Fluorinated SAM Modification. *J. Alloys Compd.* **2017**, *725*, 379–387.

(30) Hohman, J. N.; Zhang, P.; Morin, E. I.; Han, P.; Kim, M.; Kurland, A. R.; McClanahan, P. D.; Balema, V. P.; Weiss, P. S. Self-Assembly of Carboranethiol Isomers on Au{111}: Intermolecular Interactions Determined by Molecular Dipole Orientations. *ACS Nano* **2009**, *3*, 527–536.

(31) Nakatsuka, N.; Cao, H. H.; Deshayes, S.; Melkonian, A. L.; Kasko, A. M.; Weiss, P. S.; Andrews, A. M. Aptamer Recognition of Multiplexed Small-Molecule-Functionalized Substrates. *ACS Appl. Mater. Interfaces* **2018**.

(32) Herrwerth, S.; Eck, W.; Reinhardt, S.; Grunze, M. Factors That Determine the Protein Resistance of Oligoether Self-Assembled Monolayers – Internal Hydrophilicity, Terminal Hydrophilicity, and Lateral Packing Density. *J. Am. Chem. Soc.* **2003**, *125*, 9359–9366.

(33) Ishida, T.; Mizutani, W.; Aya, Y.; Ogiso, H.; Sasaki, S.; Tokumoto, H. Electrical Conduction of Conjugated Molecular SAMs Studied by Conductive Atomic Force Microscopy. *J. Phys. Chem. B* **2002**, *106*, 5886–5892.

(34) Gupta, V. K.; Abbott, N. L. Uniform Anchoring of Nematic Liquid Crystals on Self-Assembled Monolayers Formed from Alkanethiols on Obliquely Deposited Films of Gold. *Langmuir* **1996**, *12*, 2587–2593.

(35) Drawhorn, R. A.; Abbott, N. L. Anchoring of Nematic Liquid Crystals on Self-Assembled Monolayers Formed from Alkanethiols on Semitransparent Films of Gold. *J. Phys. Chem.* **1995**, *99*, 16511–16515.

(36) Follonier, S.; Miller, W. J. W.; Abbott, N. L.; Knoesen, A. Characterization of the Molecular Orientation of Self-Assembled Monolayers of Alkanethiols on Obliquely Deposited Gold Films by Using Infrared–Visible Sum-Frequency Spectroscopy. *Langmuir* **2003**, *19*, 10501–10509.

(37) Gupta, V. K.; Abbott, N. L. Azimuthal Anchoring Transition on Nematic Liquid Crystals on Self-Assembled Monolayers Formed from Odd and Even Alkanethiols. *Phys. Rev. E* **1996**, *54*, R4540–R4543.

(38) Hohman, J. N.; Claridge, S. A.; Kim, M.; Weiss, P. S. Cage Molecules for Self-Assembly. *Mater. Sci. Eng. R* **2010**, *70*, 188–208.

(39) Grimes, R. N. *Carboranes*, 2nd Edition.; Academic Press: Oxford, 2011.

(40) Cioran, A. M.; Musteti, A. D.; Teixidor, F.; Krpetić, Ž.; Prior, I. A.; He, Q.; Kiely, C. J.; Brust, M.; Viñas, C. Mercaptocarborane-Capped Gold Nanoparticles: Electron Pools and Ion Traps with Switchable Hydrophilicity. *J. Am. Chem. Soc.* **2012**, *134*, 212–221.

(41) Kabytaev, K. Z.; Everett, T. A.; Safronov, A. V.; Sevryugina, Y. V.; Jalisatgi, S. S.; Hawthorne, M. F. B-Mercaptocarboranes: A New Synthetic Route. *Eur. J. Inorg. Chem.* **2013**, *2013*, 2488–2491.

(42) Kaszynski, P.; G. Douglass, A. Organic Derivatives of Closo-Boranes: A New Class of Liquid Crystal Materials. *J. Organomet. Chem.* **1999**, *581*, 28–38.

(43) Thomas, J. C.; Goronzy, D. P.; Serino, A. C.; Auluck, H. S.; Irving, O. R.; Jimenez-Izal, E.; Deirmenjian, J. M.; Macháček, J.; Sautet, P.; Alexandrova, A. N.; Baše, T.; Weiss, P. S. Acid-Base Control of Valency within Carboranedithiol Self-Assembled Monolayers: Molecules Do the Can-Can. *ACS Nano* **2018**, *12*, 2211–2221.

(44) Skaife, J. J.; Abbott, N. L. Quantitative Characterization of Obliquely Deposited Substrates of Gold by Atomic Force Microscopy: Influence of Substrate Topography on Anchoring of Liquid Crystals. *Chem. Mater.* **1999**, *11*, 612–623.

(45) Stöhr, J.; Samant, M. G. Liquid Crystal Alignment by Rubbed Polymer Surfaces: A Microscopic Bond Orientation Model. *J. Electron Spectrosc. Relat. Phenom.* **1999**, *98–99*, 189–207.

(46) Bryan-Brown, G. P.; Wood, E. L.; Sage, I. C. Weak Surface Anchoring of Liquid Crystals. *Nature* **1999**, *399*, 338–340.

(47) Janning, J. L. Thin Film Surface Orientation for Liquid Crystals. *Appl. Phys. Lett.* **1972**, *21*, 173–174.

(48) Gupta, V. K.; Abbott, N. L. Design of Surfaces for Patterned Alignment of Liquid Crystals on Planar and Curved Substrates. *Science* **1997**, *276*, 1533–1536.

(49) Dunbar, C. E.; High, K. A.; Joung, J. K.; Kohn, D. B.; Ozawa, K.; Sadelain, M. Gene Therapy Comes of Age. *Science* **2018**, *359*, eaan4672.

(50) Shaw, K. L.; Garabedian, E.; Mishra, S.; Barman, P.; Davila, A.; Carbonaro, D.; Shupien, S.; Silvin, C.; Geiger, S.; Nowicki, B.; Smogorzewska, E. M.; Brown, B.; Wang, X.; Oliveira, S. de; Choi, Y.; Ikeda, A.; Terrazas, D.; Fu, P.-Y.; Yu, A.; Fernandez, B. C.; Cooper, A. R.; Engel, B.; Podsakoff, G.; Balamurugan, A.; Anderson, S.; Muul, L.; Jagadeesh, G. J.; Kapoor, N.; Tse, J.; Moore, T. B.; Purdy, K.; Rishi, R.; Mohan, K.; Skoda-Smith, S.; Buchbinder, D.; Abraham, R. S.; Scharenberg, A.; Yang, O. O.; Cornetta, K.; Gjertson, D.; Hershfield, M.; Sokolic, R.; Candotti, F.; Kohn, D. B. Clinical Efficacy of Gene-Modified Stem Cells in Adenosine Deaminase–Deficient Immunodeficiency. *J. Clin. Invest.* **2017**, *127*, 1689–1699.

(51) Milone, M. C.; O'Doherty, U. Clinical Use of Lentiviral Vectors. *Leukemia* **2018**, *32*, 1529–1541.

(52) Tabebordbar, M.; Zhu, K.; Cheng, J. K. W.; Chew, W. L.; Widrick, J. J.; Yan, W. X.; Maesner, C.; Wu, E. Y.; Xiao, R.; Ran, F. A.; Cong, L.; Zhang, F.; Vandenberghe, L. H.; Church, G. M.; Wagers, A. J. *In Vivo* Gene Editing in Dystrophic Mouse Muscle and Muscle Stem Cells. *Science* **2016**, *351*, 407–411.

(53) Long, C.; Amoasii, L.; Mireault, A. A.; McAnally, J. R.; Li, H.; Sanchez-Ortiz, E.; Bhattacharyya, S.; Shelton, J. M.; Bassel-Duby, R.; Olson, E. N. Postnatal Genome Editing Partially Restores Dystrophin Expression in a Mouse Model of Muscular Dystrophy. *Science* **2016**, *351*, 400–403.

(54) Hoban, M. D.; Cost, G. J.; Mendel, M. C.; Romero, Z.; Kaufman, M. L.; Joglekar, A. V.; Ho, M.; Lumaquin, D.; Gray, D.; Lill, G. R.; Cooper, A. R.; Urbinati, F.; Senadheera, S.; Zhu, A.; Liu, P.-Q.; Paschon, D. E.; Zhang, L.; Rebar, E. J.; Wilber, A.; Wang, X.; Gregory, P. D.; Holmes, M. C.; Reik, A.; Hollis, R. P.; Kohn, D. B. Correction of the Sickle Cell Disease Mutation in Human Hematopoietic Stem/Progenitor Cells. *Blood* **2015**, *125*, 2597–2604.

(55) Ain, Q. U.; Chung, J. Y.; Kim, Y.-H. Current and Future Delivery Systems for Engineered Nucleases: ZFN, TALEN and RGEN. *J. Control. Release* **2015**, *205*, 120–127.

(56) Lee, H. J.; Kim, E.; Kim, J.-S. Targeted Chromosomal Deletions in Human Cells Using Zinc Finger Nucleases. *Genome Res.* **2010**, *20*, 81–89.

(57) Joung, J. K.; Sander, J. D. TALENs: A Widely Applicable Technology for Targeted Genome Editing. *Nat. Rev. Mol. Cell Biol.* **2013**, *14*, 49–55.

(58) Osborn, M. J.; Webber, B. R.; Knipping, F.; Lonetree, C.; Tennis, N.; DeFeo, A. P.; McElroy, A. N.; Starker, C. G.; Lee, C.; Merkel, S.; Lund, T. C.; Kelly-Spratt, K. S.; Jensen, M. C.; Voytas, D. F.; von Kalle, C.; Schmidt, M.; Gabriel, R.; Hippen, K. L.; Miller, J. S.; Scharenberg, A. M.; Tolar, J.; Blazar, B. R. Evaluation of TCR Gene Editing Achieved by TALENs, CRISPR/Cas9, and MegaTAL Nucleases. *Mol. Ther.* **2016**, *24*, 570–581.

(59) Berdien, B.; Mock, U.; Atanackovic, D.; Fehse, B. TALEN-Mediated Editing of Endogenous T-Cell Receptors Facilitates Efficient Reprogramming of T Lymphocytes by Lentiviral Gene Transfer. *Gene Ther.* **2014**, *21*, 539–548.

(60) Sander, J. D.; Joung, J. K. CRISPR-Cas Systems for Editing, Regulating and Targeting Genomes. *Nat. Biotechnol.* **2014**, *32*, 347–355.

(61) Zhang, Z.; Zhang, Y.; Gao, F.; Han, S.; Cheah, K. S.; Tse, H.-F.; Lian, Q. CRISPR/Cas9 Genome-Editing System in Human Stem Cells: Current Status and Future Prospects. *Mol. Ther. Nucleic Acids* **2017**, *9*, 230–241.

(62) Komor, A. C.; Badran, A. H.; Liu, D. R. CRISPR-Based Technologies for the Manipulation of Eukaryotic Genomes. *Cell* **2017**, *168*, 20–36.

(63) Waddington, S. N.; Privolizzi, R.; Karda, R.; O'Neill, H. C. A Broad Overview and Review of CRISPR-Cas Technology and Stem Cells. *Curr. Stem Cell Rep.* **2016**, *2*, 9–20.

(64) Hsu, P. D.; Lander, E. S.; Zhang, F. Development and Applications of CRISPR-Cas9 for Genome Engineering. *Cell* **2014**, *157*, 1262–1278.

(65) Doudna, J. A.; Charpentier, E. The New Frontier of Genome Engineering with CRISPR-Cas9. *Science* **2014**, *346*, 1258096.

(66) Cong, L.; Ran, F. A.; Cox, D.; Lin, S.; Barretto, R.; Habib, N.; Hsu, P. D.; Wu, X.; Jiang, W.; Marraffini, L. A.; Zhang, F. Multiplex Genome Engineering Using CRISPR/Cas Systems. *Science* **2013**, *339*, 819–823.

(67) Maude, S. L.; Frey, N.; Shaw, P. A.; Aplenc, R.; Barrett, D. M.; Bunin, N. J.; Chew, A.; Gonzalez, V. E.; Zheng, Z.; Lacey, S. F.; Mahnke, Y. D.; Melenhorst, J. J.; Rheingold, S. R.; Shen, A.; Teachey, D. T.; Levine, B. L.; June, C. H.; Porter, D. L.; Grupp, S. A. Chimeric Antigen Receptor T Cells for Sustained Remissions in Leukemia. *N. Engl. J. Med.* **2014**, *371*, 1507–1517.

(68) Torikai, H.; Reik, A.; Liu, P.-Q.; Zhou, Y.; Zhang, L.; Maiti, S.; Huls, H.; Miller, J. C.; Kebriaei, P.; Rabinovitch, B.; Lee, D. A.; Champlin, R. E.; Bonini, C.; Naldini, L.; Rebar, E. J.; Gregory, P. D.; Holmes, M. C.; Cooper, L. J. N. A Foundation for Universal T-Cell Based Immunotherapy: T Cells Engineered to Express a CD19-Specific Chimeric-Antigen-Receptor and Eliminate Expression of Endogenous TCR. *Blood* **2012**, *119*, 5697–5705.

(69) June, C. H.; Riddell, S. R.; Schumacher, T. N. Adoptive Cellular Therapy: A Race to the Finish Line. *Sci. Transl. Med.* **2015**, *7*, 280ps7-280ps7.

(70) De Oliveira, S. N.; Wang, J.; Ryan, C.; Morrison, S. L.; Kohn, D. B.; Hollis, R. P. A CD19/Fc Fusion Protein for Detection of Anti-CD19 Chimeric Antigen Receptors. *J. Transl. Med.* **2013**, *11*, 23.

(71) Larson, S. M.; Truscott, L. C.; Chiou, T.-T.; Patel, A.; Kao, R.; Tu, A.; Tyagi, T.; Lu, X.; Elashoff, D.; De Oliveira, S. N. Pre-Clinical Development of Gene Modification of Haematopoietic Stem Cells with Chimeric Antigen Receptors for Cancer Immunotherapy. *Hum. Vaccines Immunother.* **2017**, *13*, 1094–1104.

(72) Lee, D. W.; Kochenderfer, J. N.; Stetler-Stevenson, M.; Cui, Y. K.; Delbrook, C.; Feldman, S. A.; Fry, T. J.; Orentas, R.; Sabatino, M.; Shah, N. N.; Steinberg, S. M.; Stroncek, D.; Tschernia, N.; Yuan, C.; Zhang, H.; Zhang, L.; Rosenberg, S. A.; Wayne, A. S.; Mackall, C. L. T Cells Expressing CD19 Chimeric Antigen Receptors for Acute Lymphoblastic Leukaemia in Children and Young Adults: A Phase 1 Dose-Escalation Trial. *The Lancet* **2015**, *385*, 517–528.

(73) Stewart, M. P.; Langer, R.; Jensen, K. F. Intracellular Delivery by Membrane Disruption: Mechanisms, Strategies, and Concepts. *Chem. Rev.* **2018**, *118*, 7409–7531.

(74) Jordan, E. T.; Collins, M.; Terefe, J.; Ugozzoli, L.; Rubio, T. Optimizing Electroporation Conditions in Primary and Other Difficult-to-Transfect Cells. *J. Biomol. Tech.* **2008**, *19*, 328–334.

(75) Tiefenboeck, P.; Kim, J. A.; Trunk, F.; Eicher, T.; Russo, E.; Teijeira, A.; Halin, C.; Leroux, J.-C. Microinjection for the *ex Vivo* Modification of Cells with Artificial Organelles. *ACS Nano* **2017**, *11*, 7758–7769.

(76) Wang, P. M.; Cornwell, M.; Hill, J.; Prausnitz, M. R. Precise Microinjection into Skin Using Hollow Microneedles. *J. Invest. Dermatol.* **2006**, *126*, 1080–1087.

(77) Matsuoka, H.; Komazaki, T.; Mukai, Y.; Shibusawa, M.; Akane, H.; Chaki, A.; Uetake, N.; Saito, M. High Throughput Easy Microinjection with a Single-Cell Manipulation Supporting Robot. *J. Biotechnol.* **2005**, *116*, 185–194.

(78) Sharei, A.; Zoldan, J.; Adamo, A.; Sim, W. Y.; Cho, N.; Jackson, E.; Mao, S.; Schneider, S.; Han, M.-J.; Lytton-Jean, A.; Basto, P. A.; Jhunjhunwala, S.; Lee, J.; Heller, D. A.; Kang, J. W.; Hartoularos, G. C.; Kim, K.-S.; Anderson, D. G.; Langer, R.; Jensen, K. F. A Vector-Free Microfluidic Platform for Intracellular Delivery. *Proc. Natl. Acad. Sci.* **2013**, *110*, 2082–2087.

(79) Sharei, A.; Poceviciute, R.; Jackson, E. L.; Cho, N.; Mao, S.; Hartoularos, G. C.; Jang, D. Y.; Jhunjhunwala, S.; Eyerman, A.; Schoettle, T.; Langer, R.; Jensen, K. F. Plasma Membrane Recovery Kinetics of a Microfluidic Intracellular Delivery Platform. *Integr. Biol.* **2014**, *6*, 470–475.

(80) Saung, M. T.; Sharei, A.; Adalsteinsson, V. A.; Cho, N.; Kamath, T.; Ruiz, C.; Kirkpatrick, J.; Patel, N.; Mino-Kenudson, M.; Thayer, S. P.; Langer, R.; Jensen, K. F.; Liss, A. S.; Love, J. C. A Size-Selective Intracellular Delivery Platform. *Small* **2016**, *12*, 5873–5881.

(81) Ding, X.; Stewart, M. P.; Sharei, A.; Weaver, J. C.; Langer, R. S.; Jensen, K. F. High-Throughput Nuclear Delivery and Rapid Expression of DNA *via* Mechanical and Electrical Cell-Membrane Disruption. *Nat. Biomed. Eng.* **2017**, *1*, 0039.

(82) Szeto, G. L.; Van Egeren, D.; Worku, H.; Sharei, A.; Alejandro, B.; Park, C.; Frew, K.; Brefo, M.; Mao, S.; Heimann, M.; Langer, R.; Jensen, K.; Irvine, D. J. Microfluidic Squeezing for Intracellular Antigen Loading in Polyclonal B-Cells as Cellular Vaccines. *Sci. Rep.* **2015**, *5*.

(83) Kollmannsperger, A.; Sharei, A.; Raulf, A.; Heilemann, M.; Langer, R.; Jensen, K. F.; Wieneke, R.; Tampé, R. Live-Cell Protein Labelling with Nanometre Precision by Cell Squeezing. *Nat. Commun.* **2016**, *7*.

(84) DiTommaso, T.; Cole, J. M.; Cassereau, L.; Buggé, J. A.; Hanson, J. L. S.; Bridgen, D. T.; Stokes, B. D.; Loughhead, S. M.; Beutel, B. A.; Gilbert, J. B.; Nussbaum, K.; Sorrentino, A.; Toggweiler, J.; Schmidt, T.; Gyuelveszi, G.; Bernstein, H.; Sharei, A. Cell Engineering with Microfluidic Squeezing Preserves Functionality of Primary Immune Cells *in Vivo*. *Proc. Natl. Acad. Sci.* **2018**, *115*, E10907–E10914.

(85) Ruiz-Esparza, G. U.; Wu, S.; Segura-Ibarra, V.; Cara, F. E.; Evans, K. W.; Milosevic, M.; Ziemys, A.; Kojic, M.; Meric-Bernstam, F.; Ferrari, M.; Blanco, E. Polymer Nanoparticles Encased in a Cyclodextrin Complex Shell for Potential Site- and Sequence-Specific Drug Release. *Adv. Funct. Mater. 24*, 4753–4761.

(86) Fink, T. L.; Klepcyk, P. J.; Oette, S. M.; Gedeon, C. R.; Hyatt, S. L.; Kowalczyk, T. H.; Moen, R. C.; Cooper, M. J. Plasmid Size up to 20 Kbp Does Not Limit Effective *in Vivo* Lung Gene Transfer Using Compacted DNA Nanoparticles. *Gene Ther.* **2006**, *13*, 1048–1051.

(87) Chiappini, C.; De Rosa, E.; Martinez, J. O.; Liu, X.; Steele, J.; Stevens, M. M.; Tasciotti, E. Biodegradable Silicon Nanoneedles Delivering Nucleic Acids Intracellularly Induce Localized *in Vivo* Neovascularization. *Nat. Mater.* **2015**, *14*, 532–539.

(88) Xu, A. M.; Aalipour, A.; Leal-Ortiz, S.; Mekhdjian, A. H.; Xie, X.; Dunn, A. R.; Garner, C. C.; Melosh, N. A. Quantification of Nanowire Penetration into Living Cells. *Nat. Commun.* **2014**, *5*.

(89) Xie, X.; Xu, A. M.; Angle, M. R.; Tayebi, N.; Verma, P.; Melosh, N. A. Mechanical Model of Vertical Nanowire Cell Penetration. *Nano Lett.* **2013**, *13*, 6002–6008.

(90) Cai, D.; Mataraza, J. M.; Qin, Z.-H.; Huang, Z.; Huang, J.; Chiles, T. C.; Carnahan, D.; Kempa, K.; Ren, Z. Highly Efficient Molecular Delivery into Mammalian Cells Using Carbon Nanotube Spearing. *Nat. Methods* **2005**, *2*, 449–454.

(91) McKnight, T. E.; Melechko, A. V.; Hensley, D. K.; Mann, D. G. J.; Griffin, G. D.; Simpson, M. L. Tracking Gene Expression after DNA Delivery Using Spatially Indexed Nanofiber Arrays. *Nano Lett.* **2004**, *4*, 1213–1219.

(92) McKnight, T. E.; Melechko, A. V.; Griffin, G. D.; Guillorn, M. A.; Merkulov, V. I.; Serna, F.; Hensley, D. K.; Doktycz, M. J.; Lowndes, D. H.; Simpson, M. L. Intracellular Integration of Synthetic Nanostructures with Viable Cells for Controlled Biochemical Manipulation. *Nanotechnology* **2003**, *14*, 551.

(93) McKnight, T. E.; Melechko, A. V.; Hensley, D. K.; Mann, D. G. J.; Griffin, G. D.; Simpson, M. L. Tracking Gene Expression after DNA Delivery Using Spatially Indexed Nanofiber Arrays. *Nano Lett.* **2004**, *4*, 1213–1219.

(94) Mann, D. G. J.; McKnight, T. E.; McPherson, J. T.; Hoyt, P. R.; Melechko, A. V.; Simpson, M. L.; Sayler, G. S. Inducible RNA Interference-Mediated Gene Silencing Using Nanostructured Gene Delivery Arrays. *ACS Nano* **2008**, *2*, 69–76.

(95) Ramesan, S.; Rezk, A. R.; Dekiwadia, C.; Cortez-Jugo, C.; Yeo, L. Y. Acoustically-Mediated Intracellular Delivery. *Nanoscale* **2018**, *10*, 13165–13178.

(96) Tomizawa, M.; Shinozaki, F.; Motoyoshi, Y.; Sugiyama, T.; Yamamoto, S.; Sueishi, M. Sonoporation: Gene Transfer Using Ultrasound. *World J. Methodol.* **2013**, *3*, 39–44.

(97) Lakshmanan, S.; Gupta, G. K.; Avci, P.; Chandran, R.; Sadasivam, M.; Jorge, A. E. S.; Hamblin, M. R. Physical Energy for Drug Delivery; Poration, Concentration and Activation. *Adv. Drug Deliv. Rev.* **2014**, *71*, 98–114.

(98) van Wamel, A.; Kooiman, K.; Harteveld, M.; Emmer, M.; ten Cate, F. J.; Versluis, M.; de Jong, N. Vibrating Microbubbles Poking Individual Cells: Drug Transfer into Cells *via* Sonoporation. *J. Control. Release* **2006**, *112*, 149–155.

(99) Suzuki, R.; Takizawa, T.; Negishi, Y.; Utoguchi, N.; Sawamura, K.; Tanaka, K.; Namai, E.; Oda, Y.; Matsumura, Y.; Maruyama, K. Tumor Specific Ultrasound Enhanced Gene Transfer *in Vivo* with Novel Liposomal Bubbles. *J. Control. Release* **2008**, *125*, 137–144.

(100) Gillmor, S. D.; Weiss, P. S. Dimpled Vesicles: The Interplay between Energetics and Transient Pores. *J. Phys. Chem. B* **2008**, *112*, 13629–13634.

(101) Park, C.-Y.; Kim, D. H.; Son, J. S.; Sung, J. J.; Lee, J.; Bae, S.; Kim, J.-H.; Kim, D.-W.; Kim, J.-S. Functional Correction of Large Factor VIII Gene Chromosomal Inversions in Hemophilia A Patient-Derived IPSCs Using CRISPR-Cas9. *Cell Stem Cell* **2015**, *17*, 213–220.

(102) Hoban, M. D.; Bauer, D. E. A Genome Editing Primer for the Hematologist. *Blood* **2016**, *127*, 2525–2535.

(103) Naldini, L. Gene Therapy Returns to Centre Stage. *Nature* **2015**, *526*, 351–360.

(104) Ferrara, J. L. M.; Levine, J. E.; Reddy, P.; Holler, E. Graft-versus-Host Disease. *Lancet* **2009**, *373*, 1550–1561.

(105) Holstein, M.; Mesa-Nuñez, C.; Miskey, C.; Almarza, E.; Poletti, V.; Schmeer, M.; Grueso, E.; Ordóñez Flores, J. C.; Kobelt, D.; Walther, W.; Aneja, M. K.; Geiger, J.; Bonig, H. B.; Izsvák, Z.; Schleef, M.; Rudolph, C.; Mavilio, F.; Bueren, J. A.; Guenechea, G.; Ivics, Z. Efficient Non-Viral Gene Delivery into Human Hematopoietic Stem Cells by Minicircle Sleeping Beauty Transposon Vectors. *Mol. Ther.* **2018**, *26*, 1137–1153.

(106) Genovese, P.; Schiroli, G.; Escobar, G.; Tomaso, T. D.; Firrito, C.; Calabria, A.; Moi, D.; Mazzieri, R.; Bonini, C.; Holmes, M. C.; Gregory, P. D.; Burg, M. van der; Gentner, B.; Montini, E.; Lombardo, A.; Naldini, L. Targeted Genome Editing in Human Repopulating Haematopoietic Stem Cells. *Nature* **2014**, *510*, 235–240.

(107) Lidonnici, M. R.; Ferrari, G. Gene Therapy and Gene Editing Strategies for Hemoglobinopathies. *Blood Cells. Mol. Dis.* **2018**, *70*, 87–101.

(108) Park, C.-Y.; Kim, J.; Kweon, J.; Son, J. S.; Lee, J. S.; Yoo, J.-E.; Cho, S.-R.; Kim, J.-H.; Kim, J.-S.; Kim, D.-W. Targeted Inversion and Reversion of the Blood Coagulation Factor 8 Gene in Human IPS Cells Using TALENs. *Proc. Natl. Acad. Sci.* **2014**, *111*, 9253–9258.

(109) Yin, H.; Song, C.-Q.; Dorkin, J. R.; Zhu, L. J.; Li, Y.; Wu, Q.; Park, A.; Yang, J.; Suresh, S.; Bizhanova, A.; Gupta, A.; Bolukbasi, M. F.; Walsh, S.; Bogorad, R. L.; Gao, G.; Weng, Z.; Dong, Y.; Koteliansky, V.; Wolfe, S. A.; Langer, R.; Xue, W.; Anderson, D. G. Therapeutic Genome Editing by Combined Viral and Non-Viral Delivery of CRISPR System Components *in Vivo*. *Nat. Biotechnol.* **2016**, *34*, 328–333.

(110) Baltimore, D.; Berg, P.; Botchan, M.; Carroll, D.; Charo, R. A.; Church, G.; Corn, J. E.; Daley, G. Q.; Doudna, J. A.; Fenner, M.; Greely, H. T.; Jinek, M.; Martin, G. S.; Penhoet, E.; Puck, J.; Sternberg, S. H.; Weissman, J. S.; Yamamoto, K. R. A Prudent Path Forward for Genomic Engineering and Germline Gene Modification. *Science* **2015**, *348*, 36–38.

(111) Yin, H.; Kauffman, K. J.; Anderson, D. G. Delivery Technologies for Genome Editing. *Nat. Rev. Drug Discov.* **2017**, *16*, 387–399.

(112) Cox, D. B. T.; Platt, R. J.; Zhang, F. Therapeutic Genome Editing: Prospects and Challenges. *Nat. Med.* **2015**, *21*, 121–131.

(113) Mavilio, F.; Pellegrini, G.; Ferrari, S.; Nunzio, F. D.; Iorio, E. D.; Recchia, A.; Maruggi, G.; Ferrari, G.; Provasi, E.; Bonini, C.; Capurro, S.; Conti, A.; Magnoni, C.; Giannetti, A.; Luca, M. D. Correction of Junctional Epidermolysis Bullosa by Transplantation of Genetically Modified Epidermal Stem Cells. *Nat. Med.* **2006**, *12*, 1397–1402.

(114) Hirsch, T.; Rothoeft, T.; Teig, N.; Bauer, J. W.; Pellegrini, G.; Rosa, L. D.; Scaglione, D.; Reichelt, J.; Klausegger, A.; Kneisz, D.; Romano, O.; Seconetti, A. S.; Contin, R.; Enzo, E.; Jurman, I.; Carulli, S.; Jacobsen, F.; Luecke, T.; Lehnhardt, M.; Fischer, M.; Kueckelhaus, M.; Quaglino, D.; Morgante, M.; Bicciato, S.; Bondanza, S.; Luca, M. D. Regeneration of the Entire Human Epidermis Using Transgenic Stem Cells. *Nature* **2017**, *551*, 327–332.

(115) Park, C.-Y.; Kim, J.; Kweon, J.; Son, J. S.; Lee, J. S.; Yoo, J.-E.; Cho, S.-R.; Kim, J.-H.; Kim, J.-S.; Kim, D.-W. Targeted Inversion and Reversion of the Blood Coagulation Factor 8 Gene in Human IPS Cells Using TALENs. *Proc. Natl. Acad. Sci.* **2014**, *111*, 9253–9258.

(116) George, L. A.; Sullivan, S. K.; Giermasz, A.; Rasko, J. E. J.; Samelson-Jones, B. J.; Ducore, J.; Cuker, A.; Sullivan, L. M.; Majumdar, S.; Teitel, J.; McGuinn, C. E.; Ragni, M. V.; Luk, A. Y.; Hui, D.; Wright, J. F.; Chen, Y.; Liu, Y.; Wachtel, K.; Winters, A.; Tiefenbacher, S.; Arruda, V. R.; van der Loo, J. C. M.; Zelenaia, O.; Takefman, D.; Carr, M. E.; Couto, L. B.; Anguela, X. M.; High, K. A. Hemophilia B Gene Therapy with a High-Specific-Activity Factor IX Variant. *N. Engl. J. Med.* **2017**, *377*, 2215–2227.

(117) Song, M.; Ramakrishna, S. Genome Editing in Stem Cells for Disease Therapeutics. *Mol. Biotechnol.* **2018**, *60*, 329–338.

(118) Sadelain, M.; Rivière, I.; Riddell, S. Therapeutic T Cell Engineering. *Nature* **2017**, *545*, 423–431.

(119) Mochizuki, A. Y.; Frost, I. M.; Mastrodimos, M. B.; Plant, A. S.; Wang, A. C.; Moore, T. B.; Prins, R. M.; Weiss, P. S.; Jonas, S. J. Precision Medicine in Pediatric Neurooncology: A Review. *ACS Chem. Neurosci.* **2018**, *9*, 11–28.

(120) Riddell; Watanabe, K. S.; Goodrich, J. M.; Li, C. R.; Agha, M. E.; Greenberg, P. D. Restoration of Viral Immunity in Immunodeficient Humans by the Adoptive Transfer of T Cell Clones. *Science* **1992**, *257*, 238–241.

(121) Sadelain, M.; Rivière, I.; Brentjens, R. Targeting Tumours with Genetically Enhanced T Lymphocytes. *Nat. Rev. Cancer* **2003**, *3*, 35–45.

(122) Sadelain, M.; Brentjens, R.; Rivière, I. The Basic Principles of Chimeric Antigen Receptor Design. *Cancer Discov.* **2013**, *3*, 388–398.

(123) Klebanoff, C. A.; Rosenberg, S. A.; Restifo, N. P. Prospects for Gene-Engineered T Cell Immunotherapy for Solid Cancers. *Nat. Med.* **2016**, *22*, 26–36.

(124) Ali, S. A.; Shi, V.; Maric, I.; Wang, M.; Stroncek, D. F.; Rose, J. J.; Brudno, J. N.; Stetler-Stevenson, M.; Feldman, S. A.; Hansen, B. G.; Fellowes, V. S.; Hakim, F. T.; Gress, R. E.; Kochenderfer, J. N. T Cells Expressing an Anti–B-Cell Maturation Antigen Chimeric Antigen Receptor Cause Remissions of Multiple Myeloma. *Blood* **2016**, *128*, 1688–1700.

(125) Gill, S. Chimeric Antigen Receptor T Cell Therapy in AML: How Close Are We? *Best Pract. Res. Clin. Haematol.* **2016**, *29*, 329–333.

(126) Ellebrecht, C. T.; Bhoj, V. G.; Nace, A.; Choi, E. J.; Mao, X.; Cho, M. J.; Zenzo, G. D.; Lanzavecchia, A.; Seykora, J. T.; Cotsarelis, G.; Milone, M. C.; Payne, A. S. Reengineering Chimeric Antigen Receptor T Cells for Targeted Therapy of Autoimmune Disease. *Science* **2016**, *353*, 179–184.

(127) FDA Approves CAR T-Cell Therapy for Children with Leukemia https://www.cancer.gov/news-events/cancer-currents-blog/2017/tisagenlecleucel-fda-childhood-leukemia (accessed Jul 13, 2018).

(128) FDA Approves Second CAR T-Cell Therapy https://www.cancer.gov/news-events/cancer-currents-blog/2017/yescarta-fda-lymphoma (accessed Jul 13, 2018).

(129) Bigger, B. W.; Wynn, R. F. Novel Approaches and Mechanisms in Hematopoietic Stem Cell Gene Therapy. *Discov. Med.* **2014**, *17*, 207–215.

(130) Ausubel, L. J.; Hall, C.; Sharma, A.; Shakeley, R.; Lopez, P.; Quezada, V.; Couture, S.; Laderman, K.; McMahon, R.; Huang, P.; Hsu, D.; Couture, L. Production of CGMP-Grade Lentiviral Vectors. *BioProcess Int.* **2012**, *10*, 32–43.

(131) Turtle, C. J.; Hanafi, L.-A.; Berger, C.; Gooley, T. A.; Cherian, S.; Hudecek, M.; Sommermeyer, D.; Melville, K.; Pender, B.; Budiarto, T. M.; Robinson, E.; Steevens, N. N.; Chaney, C.; Soma, L.; Chen, X.; Yeung, C.; Wood, B.; Li, D.; Cao, J.; Heimfeld, S.; Jensen, M. C.; Riddell, S. R.; Maloney, D. G. CD19 CAR–T Cells of Defined CD4+:CD8+ Composition in Adult B Cell ALL Patients. *J. Clin. Invest. 126*, 2123–2138.

(132) Sharpe, M.; Mount, N. Genetically Modified T Cells in Cancer Therapy: Opportunities and Challenges. *Dis. Model. Mech.* **2015**, *8*, 337–350.

(133) Milone, M. C.; Bhoj, V. G. The Pharmacology of T Cell Therapies. *Mol. Ther. Methods Clin. Dev.* **2018**, *8*, 210–221.

(134) Remberger, M.; Törlén, J.; Ringdén, O.; Engström, M.; Watz, E.; Uhlin, M.; Mattsson, J. Effect of Total Nucleated and CD34+ Cell Dose on Outcome after Allogeneic Hematopoietic Stem Cell Transplantation. *Biol. Blood Marrow Transplant.* **2015**, *21*, 889–893.

(135) Wang, X.; Rivière, I. Genetic Engineering and Manufacturing of Hematopoietic Stem Cells. *Mol. Ther. Methods Clin. Dev.* **2017**, *5*, 96–105.

(136) Waehler, R.; Russell, S. J.; Curiel, D. T. Engineering Targeted Viral Vectors for Gene Therapy. *Nat. Rev. Genet.* **2007**, *8*, 573–587.

(137) Kay, M. A.; Glorioso, J. C.; Naldini, L. Viral Vectors for Gene Therapy: The Art of Turning Infectious Agents into Vehicles of Therapeutics. *Nat. Med.* **2001**, *7*, 33–40.

(138) Zhang, X.; Godbey, W. T. Viral Vectors for Gene Delivery in Tissue Engineering. *Adv. Drug Deliv. Rev.* **2006**, *58*, 515–534.

(139) Mellott, A. J.; Forrest, M. L.; Detamore, M. S. Physical Non-Viral Gene Delivery Methods for Tissue Engineering. *Ann. Biomed. Eng.* **2013**, *41*, 446–468.

(140) Check, E. Gene Therapy Put on Hold as Third Child Develops Cancer. *Nature* **2005**, *433*, 561.

(141) Thomas, C. E.; Ehrhardt, A.; Kay, M. A. Progress and Problems with the Use of Viral Vectors for Gene Therapy. *Nat. Rev. Genet.* **2003**, *4*, 346–358.

(142) Sibbald, B. Death but One Unintended Consequence of Gene-Therapy Trial. *Can. Med. Assoc. J.* **2001**, *164*, 1612.

(143) Takefman, D.; Bryan, W. The State of Gene Therapies: The FDA Perspective. *Mol. Ther.* **2012**, *20*, 877–878.

(144) Riley, M. K.; Vermerris, W. Recent Advances in Nanomaterials for Gene Delivery-A Review. *Nanomaterials* **2017**, *7*, 94.

(145) Ramamoorth, M.; Narvekar, A. Non Viral Vectors in Gene Therapy- An Overview. *J. Clin. Diagn. Res.* **2015**, *9*, GE01–GE06.

(146) Kohn, D. B.; Kuo, C. Y. New Frontiers in the Therapy of Primary Immunodeficiency: From Gene Addition to Gene Editing. *J. Allergy Clin. Immunol.* **2017**, *139*, 726–732.

(147) Wiethoff, C. M.; Middaugh, C. R. Barriers to Nonviral Gene Delivery. *J. Pharm. Sci.* **2003**, *92*, 203–217.

(148) Mehier-Humbert, S.; Guy, R. H. Physical Methods for Gene Transfer: Improving the Kinetics of Gene Delivery into Cells. *Adv. Drug Deliv. Rev.* **2005**, *57*, 733–753.

CHAPTER II

Surface Dipole Control of Liquid Crystals

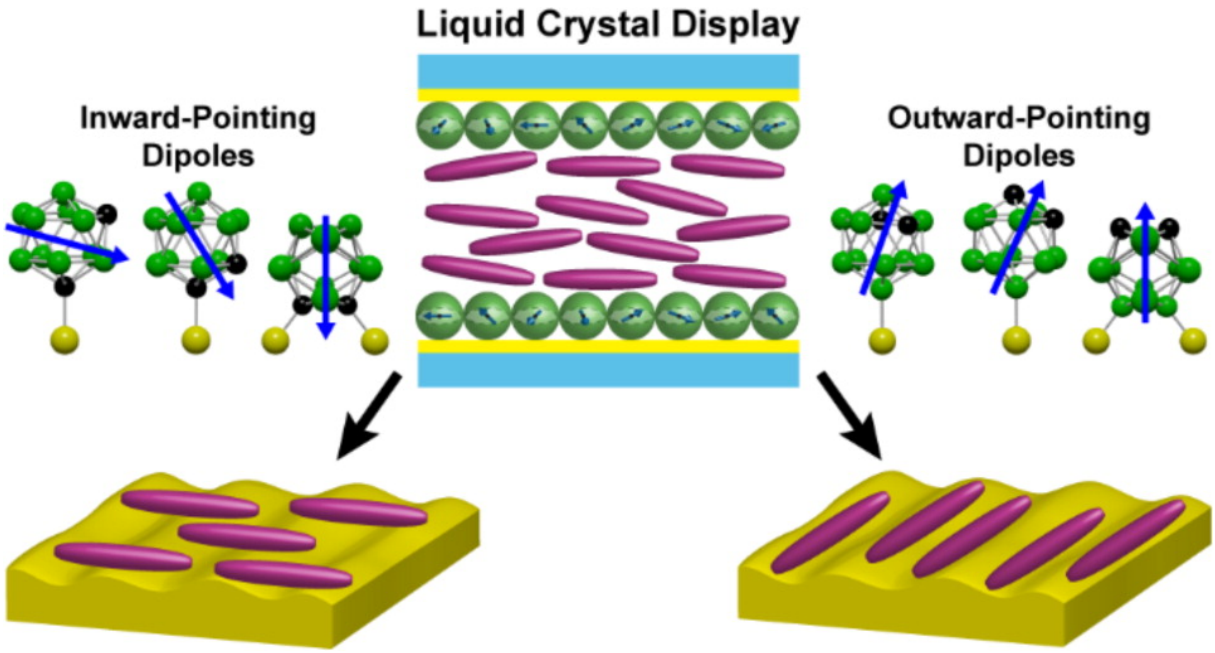

The information in this chapter was published in
***JACS* 2016, 138, 5957-5967**
and has been reproduced here with permission.

Authors: Jeffrey J. Schwarz, Alexandra M. Mendoza, Natcha Wattanatorn, Yuxi Zhao, Vinh T. Nguyen, Alexander M. Spokoyny, Chad A. Mirkin, Tomáš Baše, and Paul S. Weiss

II.A. Introduction

Self-assembly plays critical roles in the development of materials with customized chemical and physical properties from the bottom up, and provides insights into molecular-scale phenomena.[1–4] Non-covalent interactions, including dipolar and dispersion forces, mediate molecular assembly and influence the properties and functions of pure and composite materials.[5–9] Understanding and controlling the types and strengths of these interactions, particularly at interfaces, enables engineering precisely tailored structures at the nanoscale.[10–15] Self-assembled monolayers (SAMs) not only exemplify these structures, but also serve as a powerful and versatile means of tuning the interactions of a surface with its surroundings and other molecular adsorbates.[16–19] A great deal of work has been done using SAMs to control the adsorption, position, orientation, and nucleation of crystalline and molecular assemblies.[20–26] Despite recent progress, however, predictive understanding of complex, extended assemblies across textured surfaces remains challenging.[27,28]

Liquid crystals (LCs) assemble with long-range orientational order due to anisotropic intermolecular interactions with their surroundings and are particularly sensitive to surface textures and coatings.[29–31] Industrially, LC alignment is controlled by unidirectional rubbing[32,33] or other techniques that break the rotational symmetry of the alignment surfaces.[34–36] One such alternative utilizes the dune-like surface texture of obliquely deposited, semi-transparent gold films[37,38] to direct LC alignment.[34,37,39–42] In this case, mesogens adopt in-plane orientations with their long axes perpendicular to the oblique deposition direction, minimizing elastic strain within the LC assembly.

Abbott and others have shown that SAMs also influence the alignment of LCs,[43–48] with the ability to control both azimuthal and polar orientations, which have found use in

sensors.[49] However, a convolution of steric effects, surface topography, and intermolecular forces complicates our understanding of the mechanisms responsible for alignment.[46,47,50–52] Molecular adsorbates, in the form of either well-organized SAMs or adventitious surface contamination, can alter LC arrangement by changing the preferred in-plane alignment axis or inducing homeotropic alignment, normal to the surface.[43,45,53] In the case of alignment layers treated with SAMs, different LC orientations have been observed using polar and nonpolar adsorbate molecules.[38,44,51] Additionally, chiral and "odd–even"[54] effects have been observed, showing that LC alignment is sensitive to variations in the symmetry[55–57] and orientation[46,47] of the exposed moieties of the terminal functionality of the SAM. Self-assembled adsorbates used in previous studies typically varied in two or more of these factors simultaneously (*e.g.*, comparing structural analogues with different exposed moieties: $-CH_3$, −OH, and −COOH). As such, the independent effects of molecular geometry, orientation, and dipole moment on LC alignment are difficult to determine.

We used positional isomers of carboranethiol and -dithiol molecules[58] to deconvolve the effects of SAM dipole magnitude and orientation on the alignment of LCs. The isomers chemisorb onto gold surfaces through the formation of Au–S bonds, thereby assembling into monolayers with exposed carborane moieties. Each isomer possesses an identical molecular geometry and assembles "upright" with negligible tilt and a characteristic lattice spacing (7.2 and 7.6 Å for monothiol and dithiol species, respectively).[14,59–64] The primary attribute that distinguishes SAMs of each isomer is their different constituent dipole moments. Intermolecular forces between carboranethiol monolayers and mesogens resulted in uniaxial planar alignment of LCs along one of two distinct directions relative to the underlying anisotropic substrate: parallel or perpendicular to the oblique gold deposition

direction ($\overrightarrow{Au}$). The effects of these short-range, nanoscale forces[14,65] were transduced and amplified by the LCs to a macroscopic scale, enabling optical readout *via* transmitted light. Azimuthal anchoring energies of LCs on carboranethiol and -dithiol monolayers were measured to quantify SAM-LC coupling. This work targets and elucidates the roles of surface dipoles, in the form of adsorbed molecular dipoles, on the alignment and orientation of subsequent adsorbates (LCs), which has applications in sensing, catalysis, photovoltaics, and templated growth of nanostructures.[66–69] Self-assembled carboranethiols are well suited to this purpose as they enable direct comparison of the effects of different isomers' molecular dipoles, while holding constant other factors influencing LC alignment that have confounded previous studies.

II.B. Results and Discussion

Figure II.1 illustrates the molecules used in these studies. Caboranethiol isomers *m*-9-carboranethiol (M9), *m*-1-carboranethiol (M1), *o*-9-carboranethiol (O9), *o*-1-carboranethiol (O1), and -dithiol isomers *o*-9,12-carboranedithiol (9O12) and *o*-1,2-carboranedithiol (1O2) possess dipole moments with various strengths and orientations.[70] The dipole moments of these six carboranethiols were calculated using density functional theory.[14,60,71,72] Although the molecular dipoles will be altered upon chemisorption to a gold surface,[73] we use these values to make qualitative comparisons of their relative strengths, their orientations, and the degree to which they modify the surface energy of a substrate through their dipolar fields.[60,72] We use two LCs, 4-cyano-4′-pentylbiphenyl (5CB) and N-(4-methoxybenzylidene)-4-butylaniline (MBBA), possessing oppositely signed dielectric anisotropies (Δε), to probe these fields. Mesogens

with positive Δε (5CB) align parallel to an applied electric field, whereas the long axes of mesogens with negative Δε (MBBA) align perpendicular to an applied field. Comparison of the alignment of 5CB and MBBA on carboranethiol monolayers enables us to infer the role of the dipolar field on LC alignment.[43]

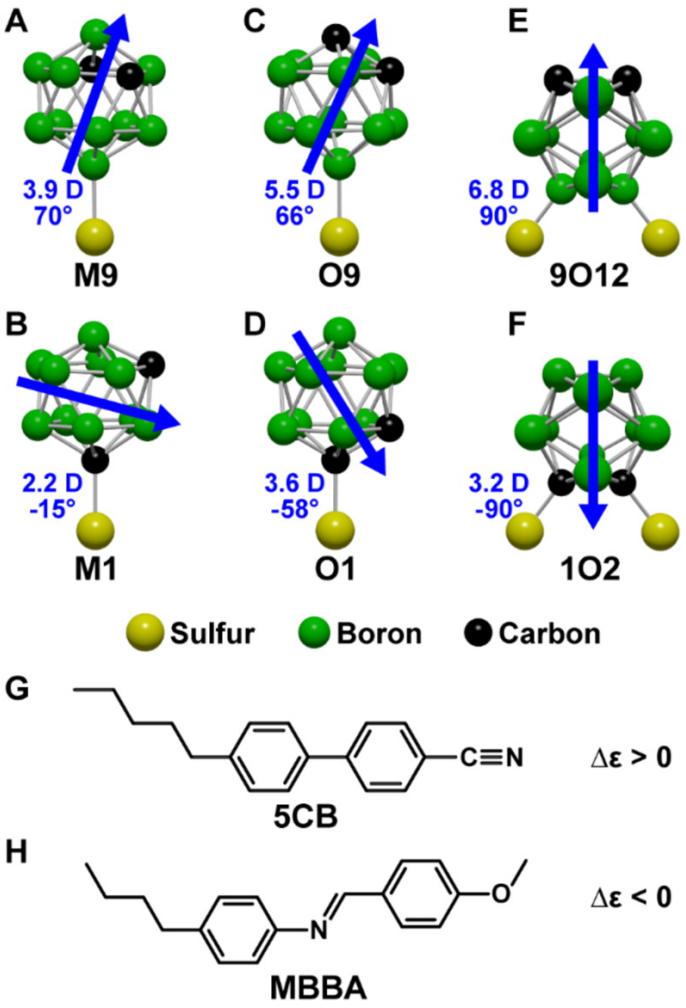

Figure II.1. Molecular structures of carboranethiol and -dithiol isomers: (A) *m*-9-carboranethiol (M9), (B) *m*-1-carboranethiol (M1), (C) *o*-9-carboranethiol (O9), (D) *o*-1-carboranethiol (O1), (E) *o*-9,12-carboranedithiol (9O12), and (F) *o*-1,2-carboranedithiol (1O2). Dipole moment magnitudes and orientations, calculated for isolated molecules, are indicated in blue. Positive (negative) angles estimate dipole orientations above (below) the plane of the substrate when assembled onto gold surfaces. Mesogen molecular structures of (G) 4-cyano-4′-pentylbiphenyl (5CB) and (H) N-(4-methoxybenzylidene)-4-butylaniline (MBBA) with corresponding dielectric anisotropy (Δε) signs noted. Hydrogen atoms are omitted from all structures for clarity.

To monitor SAM-regulated mesogen alignment, LC cells were constructed as shown in Figure II.2A. The outgoing polarization of light transmitted through a cell depends on the angle between the polarization of the incoming light and the orientation of the nematic director, which represents the average alignment direction of mesogens in a LC. If the mesogens align homeotropically, this angle is independent of cell rotations about axes normal to the alignment layers and the cells appear "dark" (0% transmittance) when viewed between crossed polarizers. Variations in the intensity of transmitted light with rotations of the cell, however, indicate planar alignment of the nematic director. Figure II.3 shows the modulation in the intensity of the light transmitted through 5CB cells as they were rotated between crossed polarizers (Figure II.2B); corresponding MBBA data are provided in the Supporting Information. Alignment layers treated with M9, M1, O9, O1, 9O12, and 1O2 SAMs all induced uniaxial planar alignment in both 5CB and MBBA cells, as indicated by the four-fold symmetry of their transmittance spectra. Cells constructed without a twist in their nematic directors vary from nearly extinguishing all transmitted light to transmitting ~50%. By contrast, cells that possess a 90° twist in their directors have transmittances varying from ~50% to nearly 100%, due to the rotation of the transmitted light's polarization as it traverses the cell.[74]

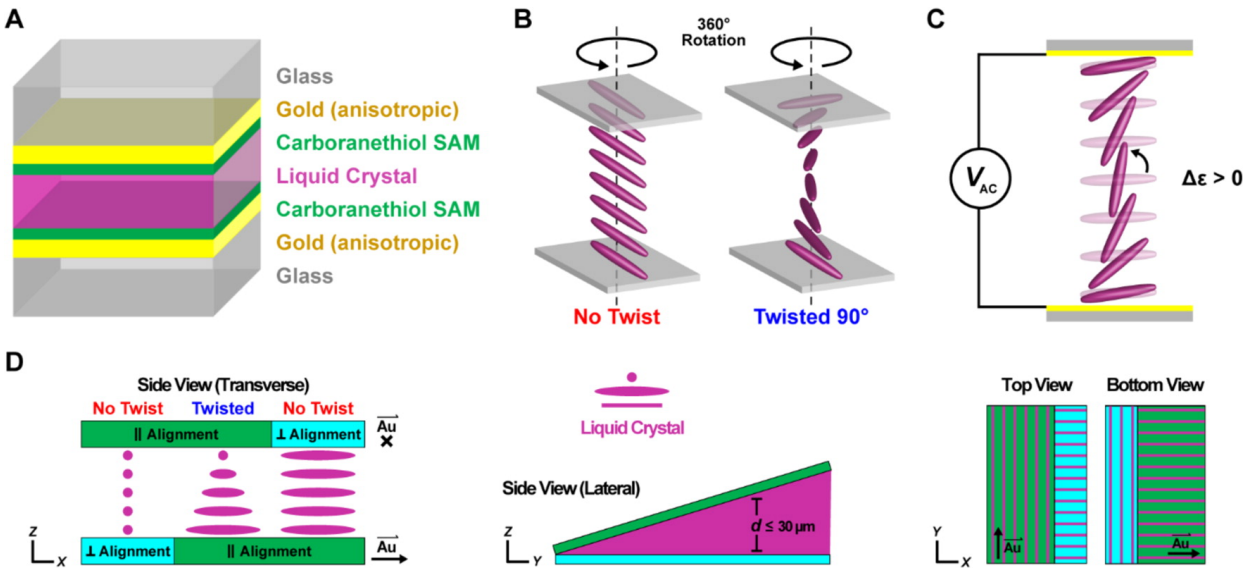

Figure II.2. (A) Schematic of liquid crystal (LC) cells used in rotation and electrically modulated optical transmittance measurements ("transmittance cells"). Carboranethiol and -dithiol self-assembled monolayers (SAMs) adsorbed on semitransparent, anisotropic gold films induced uniaxial planar alignment of a LC at the interface. Schematics illustrating the rotation of LC cells 360° about axes normal to their alignment planes (B) and a Fréedericksz transition (C) in a LC with positive dielectric anisotropy ($\Delta\varepsilon > 0$) upon application of an alternating electric potential (V_{AC}). (D) Wedge cell geometry used to measure azimuthal anchoring energies, as viewed from multiple perspectives ("anchoring energy cells"). Each alignment layer was divided into two distinct sections defined by SAMs composed of complementary molecules. Here, a carboranethiol or -dithiol isomer SAM (green) is shown to induce LC alignment parallel to the gold deposition direction ($\overrightarrow{\text{Au}}$), although other isomers may instead promote planar alignment perpendicular to $\overrightarrow{\text{Au}}$. Alkanethiol SAMs (blue) were used to induce planar LC alignment orthogonal to that induced by the carboranethiol or -dithiol isomer. Once assembled, the cell was comprised of three nematic regions, one possessing a ~90° twist in the azimuthal director orientation, while the other two exhibited untwisted LC alignment (90° apart) through the bulk of the cell. The thickness (d) of the gap between the alignment layers varied due to the presence of a spacer (not shown) at only one end of the cell.

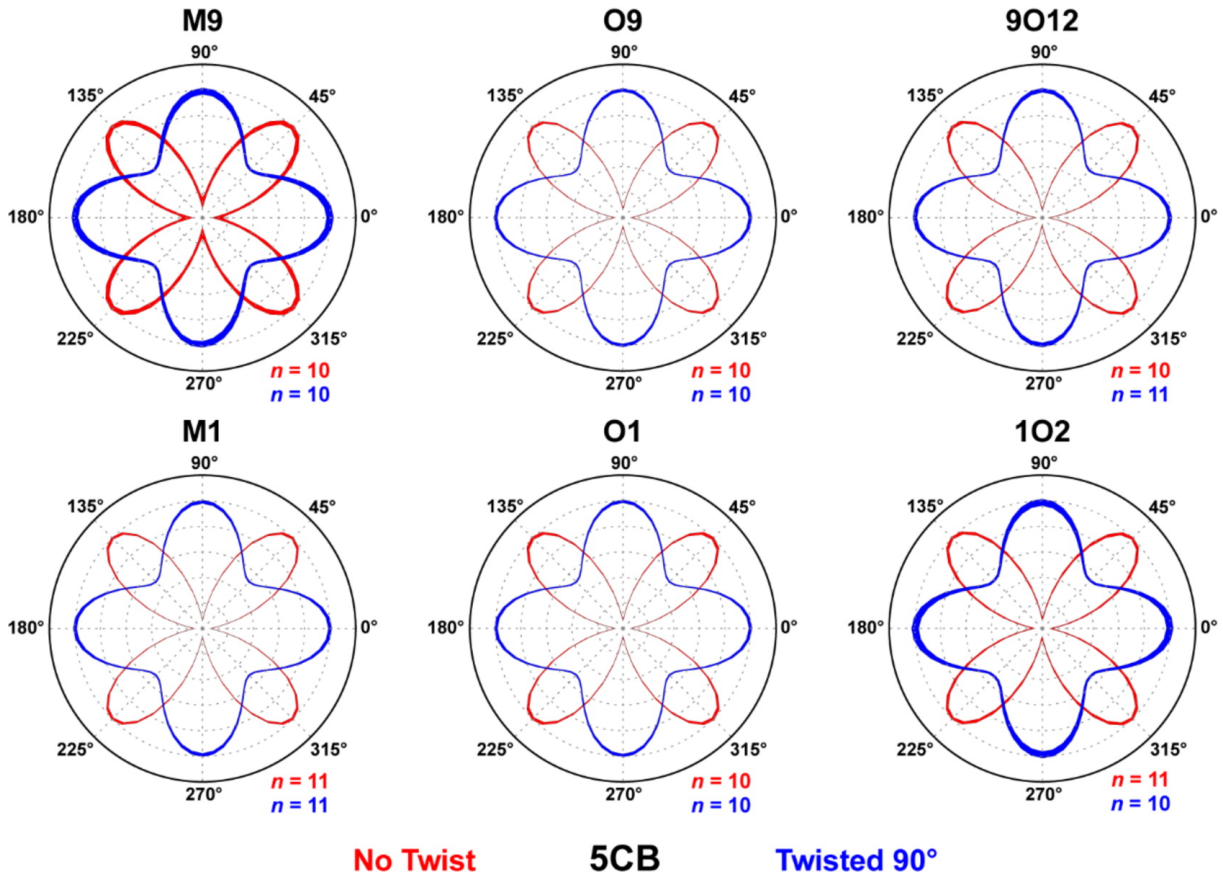

Figure II.3. Optical transmittances (indicated by the radial distance from the origin, in arbitrary units) of liquid crystal (LC) cells rotated between crossed polarizers. Alignment layers were prepared with matching self-assembled monolayers of *m*-9-carboranethiol (M9), *m*-1-carboranethiol (M1), *o*-9-carboranethiol (O9), *o*-1-carboranethiol (O1), *o*-9,12-carboranedithiol (9O12), and *o*-1,2-carboranedithiol (1O2), as indicated. At these surfaces, uniaxial, planar alignment was manifest in 4-cyano-4′-pentylbiphenyl (5BC) LCs, as evidenced by the variations in optical transmittance possessing four-fold rotational symmetry. Cells were constructed with angles of either 0° or 90° between the alignment layers' gold deposition axes, inducing untwisted (red) or twisted (blue) nematic structures, respectively. Initially, one or both of a cell's gold deposition axes were aligned with the polarizer axis, defined to be at 0°. Rotation angles were measured with respect to this reference orientation, incremented in 5° steps. Reported spectra are averages of analyses performed on *n* separate LC cells, each consisting of three measured regions, where the radial line widths indicate the data's standard deviations. Spectra are scaled such that their respective transmittance maxima are equal; in actuality, the maximum transmittance of an untwisted nematic cell nearly equals the minimum transmittance of a cell with a 90° twist in its director.

Applying a potential difference between the alignment layers generates an electric field that can distort the planar alignment of LCs with $\Delta\varepsilon > 0$, inducing them to adopt an orientation parallel to the field (normal to the surface), as illustrated in Figure II.2C.[75] This reorientation of the mesogens alters the transmittances of LC cells viewed between crossed polarizers, as shown in Figure II.4. Transmittances of twisted nematic cells containing **5CB** ($\Delta\varepsilon > 0$) decrease to near 0% with increasing field strengths. By contrast, twisted nematic cells made using MBBA do not exhibit a change in their transmittance due to their $\Delta\varepsilon < 0$, maintaining planar alignments that are reinforced by the applied field (see Supporting Information). The applied potentials produce no lasting changes to the carboranethiol monolayers, as evidenced by the reproducibility of the voltage- modulated transmittance curves through repeated sweeping of the potential's amplitude between 0 and 7 V. The observed optical responses of the cells to applied electric fields is further indication of the planar alignment adopted by both 5CB and MBBA LCs on carboranethiol and -dithiol SAMs.

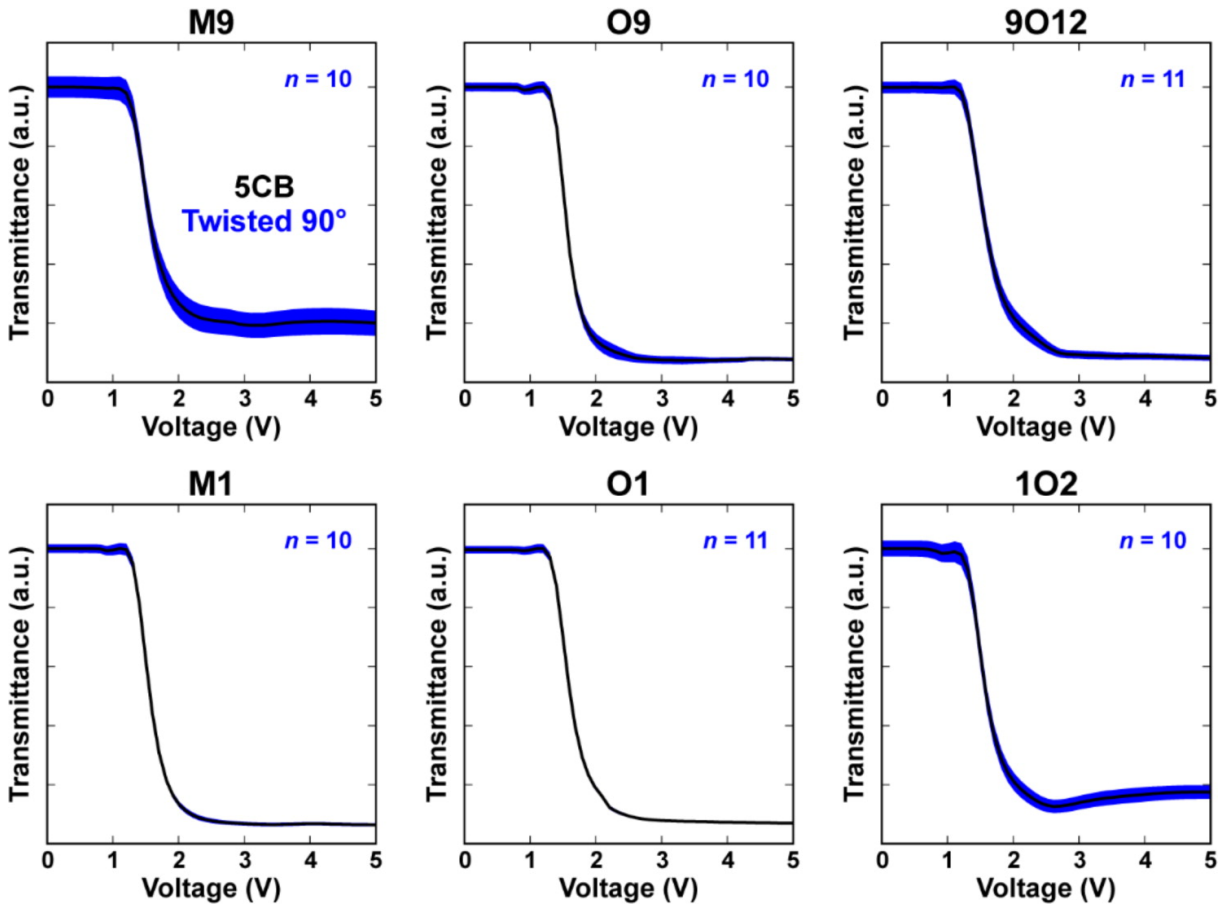

Figure II.4. Normalized optical transmittances of electrically modulated liquid crystal (LC) cells viewed between crossed polarizers. Alignment layers were prepared with matching self-assembled monolayers of *m*-9-carboranethiol (M9), *m*-1-carboranethiol (M1), *o*-9-carboranethiol (O9), *o*-1-carboranethiol (O1), *o*-9,12-carboranedithiol (9O12), and *o*-1,2-carboranedithiol (1O2), as indicated. These surfaces induced uniaxial planar alignment in 4-cyano-4′-pentylbiphenyl (5CB) LCs. Cells were constructed with perpendicular gold deposition axes, producing twisted nematic structures, and were positioned between crossed polarizers such that their zero-voltage optical transmittance was maximized. Subsequently, a sinusoidally varying (1 kHz) voltage was applied between the alignment layers in order to distort the LC director away from the surface. Root-mean-square voltages, varied in 0.1 V steps, are indicated along the horizontal axes. Reported spectra are averages (black lines) of analyses performed on *n* separate LC cells, where the vertical widths of the surrounding blue outlines indicate the data's standard deviations.

The rotation- and field-induced variations in transmittance described above were observed uniformly over the entire area (~1 cm^2) of each cell measured. These results indicate uniaxial planar alignment of 5CB and MBBA on anisotropic gold surfaces treated with each of the six carboranethiols considered here. However, these observations, alone, do not uniquely determine the nematic director orientation on a surface. Transmittance minima of untwisted nematics are expected when the director aligns along either of the crossed polarizers' axes, while maxima are expected at these orientations for cells constructed with 90° twists in their directors. These expectations are realized in Figure II.3; transmittance extrema coincide with cell rotations that align $\overrightarrow{\text{Au}}$ parallel to, and 45° from, the polarizers' axes. Two possible in-plane director orientations can produce this effect: director alignment parallel or perpendicular to $\overrightarrow{\text{Au}}$.

In order to determine, unambiguously, the LC orientation relative to the gold deposition axis (parallel or perpendicular), a wedge cell geometry was used, as illustrated in Figure II.5. Illuminating a LC wedge with monochromatic light, polarized 45° from its optical axis, produced a series of bright and dark fringes visible within the cell when observed between crossed polarizers. These fringes result from changes in the transmitted light's polarization as it traverses the birefringent cell. The optical retardation (Γ) between ordinary and extraordinary waves causes transmitted light to vary continuously between linear and elliptical polarization states, dependent on the wedge thickness (d). In the two extremes, light exits the wedge linearly polarized parallel or perpendicular to its incoming polarization, producing transmittance minima and maxima, respectively. The conditions on the optical retardation (wedge thickness) required for a transmittance extreme are given by

$$\Gamma = \Delta n \cdot d = \begin{cases} (m + ½) \cdot \lambda, \text{maxima} \\ \\ m \cdot \lambda, \text{minima} \end{cases} \quad m = 0, 1, 2, 3, \ldots$$

where λ is the wavelength of light, Δn is the LC's birefringence, and m is an integer enumerating the fringe order. Wave plates, inserted in series with a wedge cell between crossed polarizers, modify the total retardation by fixed amounts and cause the apparent positions of the fringes to shift. When the optical axes of a wave plate and untwisted nematic align, the total retardation of the transmitted light increases, whereas when their optical axes are crossed, the retardation decreases. Increased (decreased) optical retardation results in shifts in the fringe position toward (away from) the vertex of the wedge, toward the thinner (thicker) end of the cell. In this way, one can infer the orientation of the nematic director from the known orientation of a wave plate's slow axis and the direction of the observed shift in fringe positions.

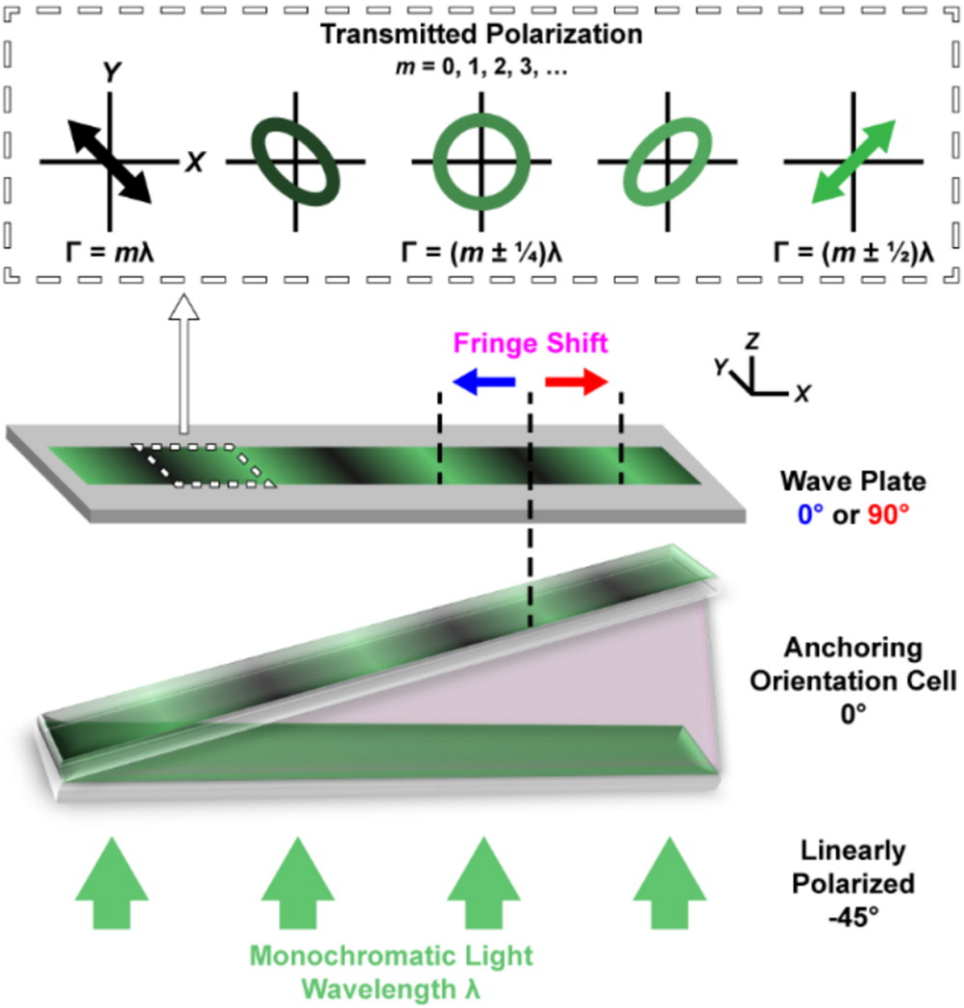

Figure II.5. Wedge cell scheme used to determine the in-plane liquid crystal director orientation with respect to the alignment layers' gold deposition axes ("anchoring orientation cells"). Linearly polarized, monochromatic light (λ = 531 nm) traversing the cell accumulates an optical retardation (Γ) dependent on the wedge thickness. As a result, the transmitted light varies between linear and elliptical polarization states, as indicated along the top of the figure. This retardation is modified by placing wave plates in series with the cell. When the optical axes of the cell and wave plate align, the overall retardation increases, whereas when the optical axis of the wave plate is perpendicular to that of the nematic, the total retardation is reduced. When viewed through an analyzer (not shown), oriented 90° from the incoming light's polarization, a series of bright and dark fringes are visible within the cell due to extinction of light polarized along the initial direction. As shown, the wave plate modifies the optical retardation of the transmitted light by $\lambda/2$, thereby causing the transmittance maxima to become minima, and vice versa. All angles indicate orientations in the *xy*-plane with respect to the *+x*-axis.

As shown in Figure II.6, the fringes observed in cells made using M1, O1, and 1O2 SAMs shift toward the thinner ends of the cells with increased optical retardation along $\overrightarrow{\text{Au}}$. This result indicates that the 5CB director is aligned parallel to $\overrightarrow{\text{Au}}$ in these cells. By contrast, cells prepared with M9, O9, and 9O12 SAMs induced planar alignment of the 5CB director perpendicular to $\overrightarrow{\text{Au}}$, as the fringes were observed to move toward the thicker ends of the cells. We note that self-assembled carboranethiol and -dithiol isomers with dipole moments directed toward the gold surface induced 5CB alignment parallel to $\overrightarrow{\text{Au}}$, whereas isomers with dipoles directed away from the substrate induced planar alignment perpendicular to $\overrightarrow{\text{Au}}$. A similar tendency was also observed in the case of MBBA LCs (see Appendix), with the exceptions of M9 and 1O2 SAMs, *vide infra*. Comparing the in-plane alignment orientations of 5CB and MBBA directors enables us to examine and to constrain the coupling mechanism between the mesogens and carboranethiol SAMs. If a dipolar electric field due to the SAM dominates the interaction, then orthogonal director orientations of the two LCs (with oppositely signed values of $\Delta\varepsilon$) are expected. However, this behavior is not observed, which is understandable due to the inversion symmetry of the nematic director (η and $-\eta$ represent equivalent director orientations).[76] Therefore, the molecular dipole moments in the SAM must influence mesogen alignment by other means.

Anchoring energy measures the work (per unit area) required to reorient a LC director perpendicular to its preferred, "easy axis" orientation on a surface. We compare azimuthal anchoring energies of 5CB aligned by M1, O9, O1, and 9O12 monolayers as a means of quantifying SAM-LC interactions. In doing so, we test for differences in anchoring strengths between isomers that align LCs in the same, and perpendicular, directions on anisotropic gold surfaces. A torque-balance measurement scheme[77,78] was adopted to

estimate anchoring energies on patterned, hybrid, alignment layers assembled in a wedge configuration, as illustrated in Figure II.2D. Twisted and untwisted nematic regions in a cell were created using bifunctional alignment layers, pairing carboranethiol SAMs with alkanethiol monolayers known to induce planar LC alignment in orthogonal directions.[46] The untwisted nematic regions within the cells enable determination of the easy axes of both the top and bottom alignment layers, which coincide with the director orientation. In the twisted nematic regions, however, the director deviates from the surfaces' easy axes due to an elastic restoring torque acting on the mesogens as a result of the twist deformation through the bulk of the cell. The angle (φ) by which the director deviates from the easy axes, and thus partially untwists itself, is related to the azimuthal anchoring energy (W_{az}):

$$W_{az} = \frac{2K_{22}\Psi}{d\sin(2\varphi)},$$

where K_{22} is the twist elastic constant of the mesogen and Ψ is the overall twist of the nematic director through a cell with thickness d (see Figure II.11 in the Appendix). In wedge cells, d varies continuously along their longitudinal axes and, as such, must be determined at each measurement location. Wedge thicknesses may be inferred from their apparent (transmitted) colors. When illuminated with white light and viewed between polarizers crossed at ±45° from the optical axis of an untwisted nematic with known birefringence, the color of transmitted light is related to a cell's thickness using a Michel–Levy interference color chart.[79] However, this chart provides only a qualitative measure since it is based on a subjective judgment of color and is prone to misinterpretation. Monochromatic transmission fringes visible within a cell, like those seen in Figure II.6, provided a quantitative means of estimating the wedge thickness using known values of Δn and λ in eq 1. In this way, we determined the **5CB** azimuthal anchoring energies summarized in Table II.1.

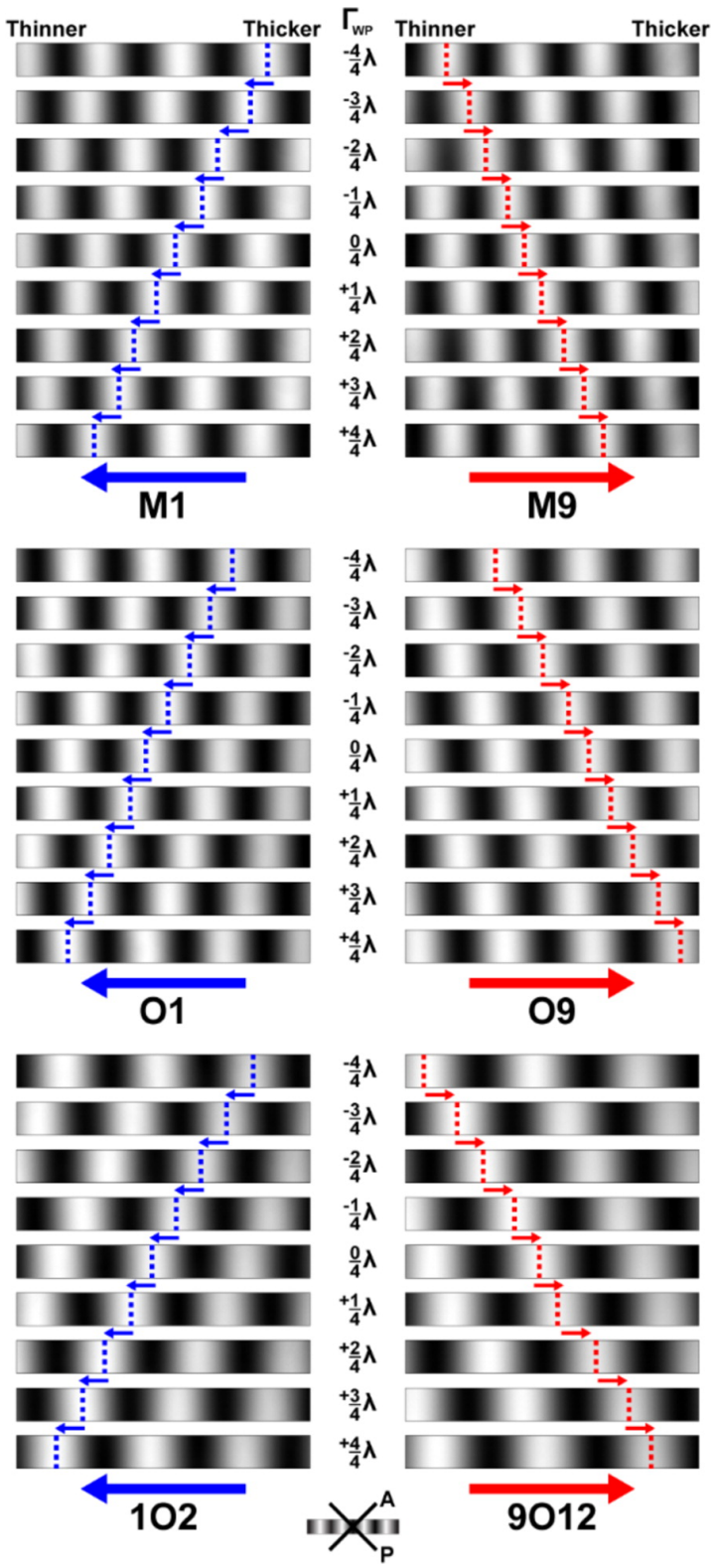

Figure II.6. Transmission fringes observed in liquid crystal (LC) wedge cells viewed between crossed polarizers while illuminated with monochromatic light (wavelength

λ = 531 nm). Alignment layers prepared with matching self-assembled monolayers of *m*-1-carboranethiol (M1), *m*-9-carboranethiol (M9), *o*-1-carboranethiol (O1), *o*-9-carboranethiol (O9), *o*-1,2-carboranedithiol (1O2), and *o*-9,12-carboranedithiol (9O12), as indicated, induced uniaxial planar alignment of 4-cyano-4′-pentylbiphenyl (5CB) LCs. Wave plates inserted between the polarizers modified the optical retardation of light transmitted through the cells by fixed amounts (Γ_{WP}). Here, positive (negative) values of Γ_{WP} signify that a wave plate's optically slow axis was aligned parallel (perpendicular) to a cell's gold deposition direction ($\overrightarrow{Au}$). Arrows and dashed lines track transmittance maxima of constant order within 4.8 mm × 0.5 mm fields of view. Fringes in cells containing M1, O1, and 1O2 monolayers were observed to shift toward the thinner ends of the wedges with increasing Γ_{WP} (blue), indicating that their nematic directors were oriented parallel to $\overrightarrow{Au}$. By contrast, fringes shifted toward the thicker ends of cells containing M9, O9, and 9O12 monolayers (red), indicating director alignment perpendicular to $\overrightarrow{Au}$.

Table II.1. Anchoring energy (W_{az}) of 5CB liquid crystals in cells prepared with various carboranethiol self-assembled monolayers (SAMs).

Anchoring SAM[a]	$p_\perp$[b]	W_{az} (μJ·m^{-2})	Sample Size, *n*
O9[c]	↑	7.5 ± 0.1	28
9O12[d]		6.7 ± 0.1	29
M1[e]	↓	14.3 ± 0.4	36
O1[f]		14.3 ± 0.4	37

[a]Carboranethiol or -dithiol isomer used to align 4-cyano-4′-pentylbiphenyl (5CB). [b]Normal dipole ($p_\perp$) orientation toward (↓) or away from (↑) the gold surface. [c]*o*-9-carboranethiol. [d]*o*-9,12-carboranedithiol. [e]*m*-1-carboranethiol. [f]*o*-1-carboranethiol.

If LC alignment is modulated by the monolayer's constituent dipole moments, we expect to observe differences in the anchoring strengths of alignment layers treated with different carboranethiol and -dithiol isomers. We found a nearly bimodal distribution of anchoring energies from the four carboranethiol SAMs tested here, with the stronger (weaker) anchoring surfaces corresponding to those with normal dipoles oriented toward (away from) the substrate. Anisotropic gold surfaces functionalized with either O9 or 9O12

aligned 5CB with approximately half the strength, perpendicular to $\overrightarrow{Au}$, as monolayers of M1 or O1, which induced alignment parallel to $\overrightarrow{Au}$. Although each of these molecules possesses distinct dipole magnitudes and orientations, the anchoring strengths of M1 and O1 (both monothiol species) SAMs did not differ appreciably. By contrast, the anchoring energy measured on 9O12 (dithiol) SAMs was found to be ~10% less than the value measured on O9 (monothiol) SAMs. However, that decrease in anchoring energy coincides with a matching reduction in the areal density of 9O12 molecules within close-packed SAMs, compared with O9 monolayers, due to the larger nearest-neighbor spacing of carboranedithiol adsorbates.[14,60,64] These findings suggest that the polarity of the normal dipole moment, toward or away from the surface, and the molecular packing density are the dominant factors affecting LC anchoring in these systems. We note that the measured anchoring energies of 5CB LCs on carboranethiol monolayers (~7 $\mu J \cdot m^{-2}$ and ~14 $\mu J \cdot m^{-2}$) exceed the values reported for oligo(ethylene glycol)-containing SAMs (<6 $\mu J \cdot m^{-2}$),[78,80] and are comparable to those on unfunctionalized surfaces.[37,81,82] These values, however, are almost two orders of magnitude weaker than the anchoring strengths of rubbed polyamide films.[83,84]

Uncertainty in the local gold deposition angle is expected to be a major contributor to variations in the measured azimuthal anchoring energies.[38,80,85,86] All of the gold films used in these studies were deposited at the same angle, nominally 50° away from the surface normal. However, due to the finite sizes of the glass substrates and their positions relative to the evaporating metal source, departures of up to 6° from the intended angle are possible (see Appendix). Variations in the average grain size and surface roughness affect the substrate's contribution to LC alignment, resulting in stronger anchoring on gold films

deposited at higher, more oblique angles.[85] Additionally, uncertainty in the anchoring energy typically increases with deposition angle due, in part, to its sensitivity to uncertainties in the nematic director's twist and deviation from the easy axes.[80] This sensitivity becomes more pronounced with increasing anchoring strength (higher deposition angles). The anchoring energies reported here reflect averages of measurements performed on multiple cells, inversely weighted by their estimated variances. Such averaging, however, biases the reported values in favor of lower anchoring energies that possess correspondingly smaller uncertainties. The complete data sets, as well as a discussion of the statistical methods used in our analysis, are provided in the Appendix.

As noted above, we observe a trend in the alignment of LCs by carboranethiol monolayers prepared on anisotropic gold surfaces that follows the polarity of the adsorbate's normal dipole moment. The constituent molecules of a SAM, in general, possess dipoles with components oriented parallel and normal to the functionalized surface. The cumulative effects of the in-plane molecular dipoles are diminished by their varying or disordered azimuthal orientations expected at room temperature.[14] Molecules may adsorb to the surface with random in-plane dipole orientations and, in the cases of M9, M1, O9, and O1, which possess only a single attachment to the substrate, rotate about their Au–S bonds. If long-range orientational order is present, the formation of differently polarized domains (including closure domains) would compensate for a net in-plane dipole over macroscopic scales. Additionally, image dipoles, formed through the redistribution of charge on the underlying gold substrate, would further attenuate the effects of in-plane molecular dipoles. Normal dipole moments, however, are not subject to these mitigating factors. Each carboranethiol in a single-species SAM adsorbs to the surface with the same polar

orientation and, as such, enhances the net dipole moment normal to the surface. Carboranedithiol isomers (9O12 and 1O2) were included in these experiments due to their expected dipole orientations normal to the surface as a result of their bilateral molecular symmetry. Since these isomers bind to the substrate *via* two Au–S bonds, they are not free to rotate azimuthally. In principle, these isomers could tilt about the axis connecting their two adsorbed thiolate moieties, out of the plane normal to the gold substrate, resulting in a portion of their dipole moments orienting parallel to the surface. Nevertheless, we observe the same trend in 5CB alignment induced by carboranedithiol isomers as in the cases of monothiol isomers, dependent upon the polarity of the normal dipole. As such, we conclude that the net in-plane dipole of a SAM is either compensated through one or more of the mechanisms mentioned above, or is a less significant contributor than the normal dipole when determining LC alignment.

In addition to the factors discussed above, other surface anisotropies may contribute to the existence of an easy alignment axis. One such contribution originates from an anisotropic electric susceptibility of the alignment surface. Obliquely deposited films are expected to have an anisotropic response to electric stimuli (*e.g.*, from mesogen dipoles) due to their dune-like or columnar surface textures.[87,88] Molecular monolayers can modify this anisotropy, dependent on the adsorbate polarizabilities and orientations on the surface. To examine this effect, molecular polarizability tensors (α) were calculated using density functional theory for each of the six carboranethiol and -dithiol isomers considered here (see Supporting Information). To facilitate comparison, Cartesian coordinate bases were chosen for each molecule such that the bond(s) connecting the sulfur atom(s) to the carborane cage moiety coincided with (or symmetrically straddled) the z-axis. Additionally, one or both of

the carbon atoms within the isomers were designated to lie along the x-axis, in the cases of M1, O9, O1, 9O12, and 1O2, and symmetrically about the x-axis in the case of M9. These coordinate bases closely coincided with the molecules' principal polarizability axes, such that the off-diagonal polarizability tensor elements ($\alpha_{ij}, i \neq j$) were negligible (<1%) by comparison to the diagonal elements (αii). Considering upright adsorption, we found that the molecular polarizabilities of carboranethiols were nearly symmetric in the plane of the substrate ($\alpha_{xx} \approx \alpha_{yy}$), with variations of <2%. Larger in-plane variations in molecular polarizability were found for 9O12 and 1O2 (~10%), in part due to the lower (two-fold) rotational symmetry of carboranedithiols compared that of with monothiol isomers (five-fold). Symmetric adsorbate polarizabilities reduce the likelihood of anisotropic in-plane polarizations of a SAM inducing LC alignment on flat, isotropic surfaces. On textured surfaces, however, the local (microscopic) surface normal generally deviates from that of the average (macroscopic) plane of the substrate, effectively varying the orientations of molecules within the assembly. As a result, the in-plane electric susceptibility of a SAM depends, in part, on the polarizability of carboranethiols along their z-axes (α_{zz}), which is ~20% greater than their polarizability along orthogonal directions. Therefore, geometric surface anisotropies present in obliquely deposited films, generate additional anisotropies in a monolayer without requiring, a priori, long-range azimuthal alignment of carboranethiols. However, we do not find any consistent correlation between the observed LC alignment and all six of the carboranethiol molecular polarizabilities considered here.

Comparing the alignments of mesogens with oppositely signed dielectric anisotropies provides insight into the role of the dipolar field on LC anchoring by functionalized surfaces. Assuming direct coupling between the mesogens and the field, 5CB and MBBA LCs were

expected to align along orthogonal directions, relative to each other, at the SAM-LC interface. Instead, both mesogens adopted the same planar orientation, dependent on the polarity of the monolayer's constituent molecular dipoles normal to the surface, as detailed previously. However, in the case of MBBA alignment, M9 and 1O2 carboranethiol monolayers were found to be exceptions to this trend. Alignment layers functionalized with M9 induced alignment of MBBA parallel to $\overrightarrow{\text{Au}}$, whereas 1O2 monolayers resulted in more heterogeneous and less reproducible anchoring of MBBA than observed on surfaces treated with other isomers under the same conditions. To understand these anomalies, we reemphasize that the monolayer's constituent dipoles are not the sole factor affecting LC alignment, despite being the focus of these studies. Other influences, including surface topography, molecular geometry, tilt, and order, are still present (albeit consistent) in each cell, while the contribution from carboranethiol dipoles varies between isomers. Out of the three isomers with dipoles directed away from the underlying gold surface tested here, M9 possesses the weakest moment and is the only one to induce LC alignment counter to the prevailing trend (and only with MBBA). Previously, we noted that the anchoring strength of 5CB on carborane-functionalized surfaces did not depend on the magnitude of the molecular dipoles of a SAM. This unexpected alignment of MBBA may indicate a minimum threshold strength of molecular dipoles required to orient LCs along a particular direction on these surfaces. Alternatively, we propose that the properties of MBBA itself may instead be responsible. Relative to 5CB, MBBA has a weaker internal dipole moment and smaller dielectric anisotropy (see Appendix). As a result, the coupling strength of MBBA to external electric fields is weaker than that of 5CB, with which no alignment anomalies were observed. Future experiments using a LC with a more negative dielectric anisotropy could test this hypothesis

and distinguish whether or not the observed alignment is indicative of the carboranethiol monolayer or a property of the mesogen itself. In the case of the heterogeneous alignment of MBBA on 1O2 monolayers, we note the potential for dithiol isomers to chemisorb to the gold surface in either singly or doubly bound states. Here, we used ethanolic solutions of each of the carboranedithiols with added base (sodium hydroxide) to promote dual binding *via* both thiol moieties on each molecule. However, even under these circumstances, not every adsorbed molecule binds to the gold with both thiol moieties. We have observed elsewhere[64] that the 1O2 isomer is more likely to adsorb in mixed states (both singly and doubly bound) compared to the 9O12 isomer under alkaline conditions, resulting in a less uniform SAM. This molecular-scale heterogeneity may, in turn, produce more heterogeneous LC arrangements than those observed on alignment layers treated with other carboranethiol isomers.

II.C. Conclusions and Prospects

Here, LCs serve as advantageous probes of the nanoscale intermolecular forces between SAMs and their environment. These combinations of forces result from several factors, including surface topography, molecular orientation, and chemical functionality, which modulate the properties of the underlying substrate and mediate the assembly of adsorbates. We report on the uniaxial, planar alignment of 5CB and MBBA LCs on obliquely deposited gold films functionalized with carboranethiol and -dithiol SAMs. Carboranethiol monolayers enable direct comparisons of LC alignment modulated by differences in the magnitudes and orientations of assembled molecular dipoles on a surface. Carboranethiol monolayers hold constant other factors that influence LC alignment, such as molecular

geometry, tilt, and order, which have confounded previous studies. Furthermore, comparing LC alignment on monolayers composed of monothiol isomers (M9, M1, O9, and O1) to those composed of carboranedithiols (9O12 and 1O2) enabled inference of the roles of the normal and lateral surface dipoles. We observed that the in-plane, azimuthal orientation of mesogens on anisotropic gold films was modulated predominantly by the carboranethiol dipole component normal to the surface. Monolayers composed of carboranethiols with dipoles oriented toward (away from) the underlying gold surface induced planar alignment of 5CB parallel (perpendicular) to the gold deposition direction. A similar trend was observed in the case of alignment of MBBA, which possesses an oppositely signed dielectric anisotropy. Since LCs with dielectric anisotropies of opposite signs align similarly, dependent on the monolayer's normal dipole polarity, we conclude that it is not a direct result of dipolar field coupling between SAMs and mesogens. We attribute the observed alignment to more complex mechanisms involving intermolecular dispersion forces. To quantify SAM-LC interaction strength, we measured the azimuthal anchoring energies of 5CB on alignment layers treated with M1, O9, O1, and 9O12 monolayers. A nearly bimodal distribution of anchoring energies was measured, dependent on the polarity of the carboranethiol isomer dipole moment component normal to the surface. Monolayers composed of carboranethiol isomers with dipoles oriented away from (O9 and 9O12) and toward (M1 and O1) the substrate were measured to anchor 5CB with strengths of ~7 and ~14 $\mu J \cdot m^{-2}$, respectively. Additionally, comparing the anchoring energies of pairs of isomers with the same polarity normal to the surface, we found no difference in anchoring strengths between monothiol species (M1 and O1). However, we observed that the anchoring energies measured on surfaces treated with 9O12 (dithiol) were about 10% lower than those

measured on surfaces treated of O9 (monothiol), coinciding with the decrease in areal density of carboranethiols within the close-packed monolayers. This result indicates that not only the polarities of the molecular dipoles affect LC anchoring, but also their densities on the surfaces. We also considered other sources of surface anisotropy arising from the molecular polarizabilities of the carboranethiols used in this work that may affect LC anchoring direction and strength. We do not expect that long-range molecular alignment of carboranethiol adsorbates within SAMs at room temperature is likely.[14] However, others have previously observed azimuthal ordering of exposed methyl moieties in alkanethiol monolayers prepared on anisotropic gold films.[41] Complementary techniques, such as sum-frequency generation spectroscopy, may be used in future studies to test this possibility in the case of carboranethiol SAMs.[89] The mechanism involved remain unresolved, but this work isolates elements of the alignment of LCs on functionalized, anisotropic surfaces in order to elucidate the role of molecular dipole moments of the monolayers on the subsequent adsorption and assembly of other molecular species. Extending this knowledge to other molecular systems will enhance the predictive capabilities of nanoscale engineering and enable rational design of structures extended to macroscopic scales on complex surfaces.

II.D. Materials and Methods

II.D.1. Materials

Positional isomers of dicarba-closo-dodecaboranethiol and -dithiol O1, O9, 1O2, and 9O12 were synthesized using previously reported methods;[90–92] M1 and M9 isomers were purchased from Sigma-Aldrich (St. Louis, MO). Mesogens 5CB and MBBA, as well as sodium

hydroxide, and alkanethiols 1-undecanethiol (C11) and 1-octadecanethiol (C18) were also obtained from Sigma- Aldrich. Ethanol (200 proof) was purchased from Goldshield Chemical Company (Hayward, CA), while potassium hydroxide and hydrogen peroxide (30%) were acquired from Fisher Scientific (Pittsburgh, PA). Sulfuric acid (98%) was purchased from EMD Chemicals (Gibbstown, NJ). All commercial chemicals were used as received. Deionized (DI) water (18.2 MΩ·cm) was dispensed from a Milli-Q water purifier (EMD Millipore, Billerica, MA).

II.D.2. Polymeric Stamp Preparation

Polymeric stamps were produced using a Sylgard 184 silicone elastomer kit (Dow Corning, Midland, MI) following a previously reported procedure.[93] Flat, featureless stamps were obtained and cut into strips approximately 8 mm wide, 76 mm long, and 4 mm thick.

II.D.3. Polarizing Microscopy and Image Analysis

An Olympus BX51-P polarizing microscope and CCD camera (Center Valley, PA) were used throughout this work to record the transmittances and optical textures of LC cells as 8-bit grayscale images. The transmittance of a LC cell was computed using the average intensity of all pixels within an image (1600 × 1200 pixels). Variations in the transmittance within the microscope field of view were quantified using the standard deviation of pixel intensities. Reported transmittance values reflect aggregated analyses of multiple cells and multiple locations within each cell. Automated routines facilitated image processing.

II.D.4. Alignment Layer Preparation

Eagle XG glass (Corning Display Technologies, Corning, NY), 1.1 mm thick, was used throughout this work. Glass used in anchoring energy measurements had lateral dimensions of 76 mm × 25 mm, while pieces intended for transmittance measurements were cut to

approximately 19 mm × 25 mm.

II.D.4.a. Substrate Cleaning

Glass substrates were cleaned through sequential rinsing and ultrasonication steps (>20 min) in ethanol, DI water, and concentrated potassium hydroxide solution. Afterward, the glass was rinsed in DI water and then immersed in piranha solution (3:1 H_2SO_4/H_2O_2) for ~1 h before a final rinse in DI water and being blown dry with nitrogen gas.

II.D.4.b. Oblique Metal Deposition

Cleaned glass substrates were loaded into the vacuum chamber of an electron beam metal evaporator (Kurt J. Lesker Company, Jefferson Hills, PA) immediately after drying and held at a base pressure of $\sim 1 \times 10^{-7}$ Torr. The substrates were mounted with fixed positions and orientations within the chamber such that their surface normal was inclined at an angle of 50° away from the metal source. Semitransparent gold films (10 nm) were deposited on top of chromium adhesion layers (2 nm) at rates of ~0.5 Å/s. Nominal film thicknesses were measured using a quartz crystal microbalance orientated toward the metal source, thus overestimating the amount of metal adsorbed on the glass by a factor of sec(50°) ≈ 1.6. Due to the finite sizes of the glass substrates and their positions relative to the metal source, a deviation of <6° from the intended deposition angle is expected for gold films deposited in the same batch.

II.D.4.c. Self-Assembled Monolayer Preparation

Self-assembled monolayers were formed on obliquely deposited Au/glass substrates from 1 mM ethanolic solutions of the desired adsorbate: O1, O9, M1, M9, 1O2, 9O12, C11, or C18. In the cases of 1O2 and 9O12, 1:2 carboranedithiol/NaOH equivalent solutions in ethanol were used to promote divalent adsorption on the gold surface.[64] Immediately prior

to SAM deposition, Au/glass substrates were exposed to an oxygen plasma (Harrick Plasma, Ithaca, NY) for 40 s in order to remove adventitious organic adsorbates. Substrates intended for use in transmittance measurements were immersed in solutions of the desired carboranethiol or -dithiol isomer for 12–18 h. Afterward, the uniformly functionalized surfaces were rinsed in copious amounts of ethanol and then blown dry with nitrogen gas. By contrast, soft lithography was employed to create two adjacent, spatially separated, SAMs on substrates used in anchoring energy measurements. A polymeric stamp was soaked in a solution of either C11 or C18 "ink" for at least 20 min, then rinsed with ethanol and blown dry with nitrogen gas. The inked stamp was placed into conformal contact with a clean Au/glass surface for 10 min. This stamping resulted in the formation of an alkanethiol SAM over about one-third of the alignment surface (conformal contact area). The surface was then immersed into a solution of the carboranethiol or -dithiol under investigation for 60 min in order to functionalize the remaining bare surface. Finally, the surface was rinsed with ethanol and blown dry with nitrogen gas. Observing the distinct wetting behavior of ethanol over the two SAM regions, possessing either nonpolar (aliphatic) or polar (carborane) moieties, confirmed the bifunctional character of the surface.

II.D.5. Liquid Crystal Cell Assembly

All LC cells were assembled (*vide infra*) immediately following alignment layer preparation and their cavities filled with either 5CB or MBBA *via* capillary action. To prevent flow-induced LC alignment, the alignment layers and mesogens were heated to 5–10 °C above the mesogen's clearing temperature during filling. Afterward, the cells were allowed to cool to room temperature (~20 °C) and permanently sealed using cyanoacrylate adhesive (Henkel, Westlake, OH).

II.D.5.a. Transmittance Cells

Transmittance cells were assembled using plastic spacers (30 μm thick) to separate the matching functionalized gold surfaces of two alignment layers. Alignment layers were paired such that their gold deposition axes were either parallel or crossed at angles of ~90°, producing cells with untwisted or twisted nematic structures, respectively. Copper wires were affixed to the outermost edges of both gold surfaces using conductive carbon glue (Ted Pella, Redding, CA), enabling manipulation of LC orientations by applied electric fields (potentials).

II.D.5.b. Anchoring Orientation Cells

The alignment layers of cells used to determine the in-plane LC anchoring orientations were prepared identically to those used in transmittance measurements. However, in contrast to transmittance cells, anchoring orientation cells were constructed as wedges with a spacer separating the alignment layers at only one end. In this configuration, the thickness of the cavity between the alignment layers varied linearly along the cell's longitudinal axis, independent of the transverse position. Only untwisted nematic cells, with parallel anisotropy axes, were used to determine anchoring orientations.

II.D.5.c. Anchoring Energy Cells

Adopting the design described by Abbott and co-workers,[77,78] anchoring energy cells were constructed with the wedge cell geometry described previously and engineered to contain three nematic regions. Alignment layers were arranged with crossed gold deposition axes, oriented along the longitudinal and transverse cell axes, and with matched and mismatched overlapping SAM regions, as illustrated in Figure II.2D. As such, the azimuthal director orientation was induced to twist by ~90° in the central region, whereas the regions

on either side exhibited untwisted, uniaxial LC alignment (90° apart) through the bulk of the cell. To prevent flexing of the alignment layers during assembly, custom-built jigs were used to ensure uniform compression. Flexing was not observed to pose a problem when constructing other, comparatively shorter, types of LC cells.

II.D.6. Transmittance Measurements

Transmittance cells were examined between the crossed polarizers of a polarizing optical microscope while illuminated with white light. The optical axes of the cells were aligned initially with either of the microscope's polarizing axes, thus minimizing (maximizing) the relative intensity of light transmitted through cells constructed with no twist (90° twist) in their nematic directors. The transmittance was measured at 5° intervals over one complete rotation of a cell. This process was repeated three times, in different regions (1.2 mm × 0.9 mm field of view), for each cell measured. Afterward, the orientation of the cell was fixed and its transmittance measured as a sinusoidally varying voltage was applied between the alignment layers (3.0 mm × 2.2 mm field of view).

II.D.7. Anchoring Orientation Determination

Anchoring orientation cells were illuminated with monochromatic light polarized 45° from their optical axes. When viewed through an analyzer crossed 90° from the polarization of the incoming light, a series of bright and dark fringes were observed, as illustrated in Figure II.5. These fringes were a consequence of differences in the optical retardation of light transmitted through the birefringent, LC, wedges. Wave plates (RealD, Beverly Hills, CA, and Edmund Optics, Barrington, NJ) were inserted between the polarizers, in series with the cells, to alter this retardation by fixed amounts. Changes in the fringe positions due to the wave plates were tracked within viewing areas of about 6.0 mm × 4.5 mm.

II.D.8. Anchoring Energy Measurements

Azimuthal anchoring energies were measured using a similar procedure to that reported by Abbott and co-workers.[78] The LC alignment directions and twist angles were determined using automated routines to fit the observed rotation–transmittance spectra in each of the cells' three nematic regions (590 μm × 440 μm field of view) to their expected trigonometric responses. Estimates of local wedge cavity thicknesses were made by comparing the observed color of cells illuminated with white light to a Michel–Levy interference color chart.[79] These estimates were refined using the positions of the transmission fringes made visible by illuminating the cells with monochromatic light. Transmittance minima and maxima bands acted as internal graduations corresponding to known cavity thicknesses. Reported anchoring energies represent an average of all measurements weighted by their respective measurement uncertainties (see Supporting Information).

II.D.9. Density Functional Theory Calculations

The six carboranethiol isomers used in this work were analyzed using density functional theory. Optimized molecular structures, dipole moments, and polarizabilities were computed at the M062X level of theory using the 6-311G** basis set with the Gaussian 09 software package (Gaussian, Wallingford, CT).[94,95]

II.E. Appendix

II.E.1. Physical Properties of Liquid Crystals

Relevant physical properties of the liquid crystals (LCs) used in this work, 5CB and MBBA, are summarized in Table II.2.

Table II.2. Physical properties of 5CB[a] and MBBA[b] liquid crystals.

Property[c]	Liquid Crystals	
	5CB[d]	**MBBA**[e]
Δn[f]	0.1873	0.184
Δε[g]	+11.5	-0.5
K_{22} (pN)[h]	4.22	4.0
T_{NI} (°C)[i]	35	47
μ (D)[j]	5.1	2.2

[a]4-cyano-4′-pentylbiphenyl (**5CB**). [b]N-(4-methoxybenzylidene)-4-butylaniline (MBBA). [c]The values of these properties depend on the specific measurement conditions (*e.g.*, temperature, optical wavelength, and chemical purity). Here, we report values applicable to this work. [d]See Refs. 78,96–98. [e]See Refs. 55,76,99. [f]Birefringence (Δn), calculated as the difference in the indices of refraction of light polarized along the mesogen's extraordinary and ordinary axes. [g]Dielectric anisotropy (Δε), calculated as the difference in the mesogen's dielectric constant parallel and perpendicular to the director. [h]Mesogen twist elastic constant (K_{22}). [i]Transition temperature (T_{NI}) between the nematic and isotropic phases. [j]Permanent molecular dipole moment (μ) of the mesogen. The dipole moment of 5CB lies along its molecular axis, whereas the dipole moment of MBBA is directed primarily perpendicular to its long axis.

II.E.2. MBBA Cell Rotation–Transmittance Spectra

Figure II.7 shows the modulation in the intensity of the light transmitted through MBBA cells as they were rotated between crossed polarizers (Figure II.2B). Alignment layers treated with M9, M1, O9, O1, and 9O12 SAMs induced uniaxial planar alignment in MBBA cells, as indicated by the four-fold symmetry of their transmittance spectra. Cells constructed without a twist in their nematic directors vary from nearly extinguishing all transmitted light to transmitting ~50%. By contrast, cells that possess a 90° twist in their directors have transmittances varying from ~50% to nearly 100%, due to the rotation of the polarization of the transmitted light as it traverses the cell.

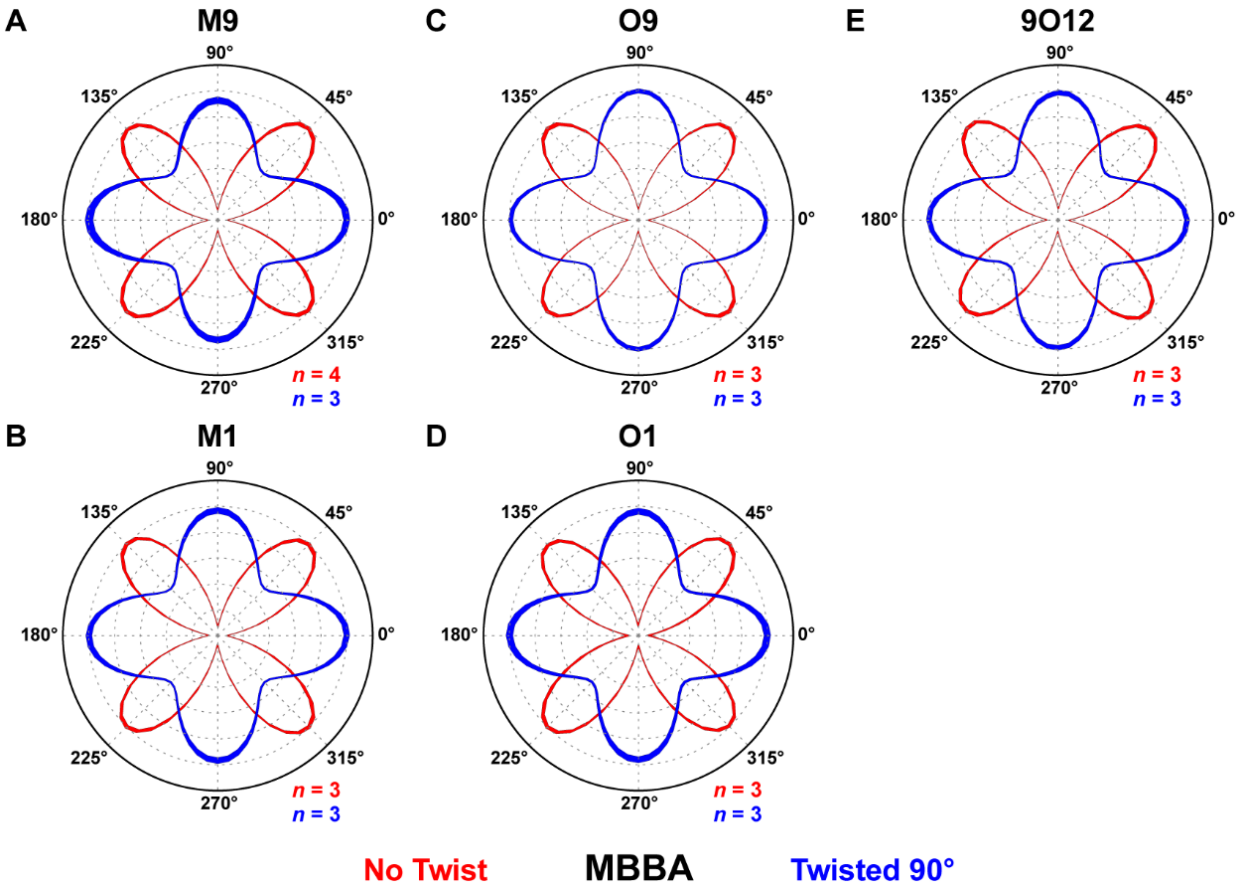

Figure II.7. Optical transmittances (indicated by the radial distance from the origin, in arbitrary units) of liquid crystal (LC) cells rotated between crossed polarizers. Alignment layers were prepared with matching self-assembled monolayers of *m*-9-carboranethiol (M9), *m*-1-carboranethiol (M1), *o*-9-carboranethiol (O9), *o*-1-carboranethiol (O1), and *o*-9,12-carboranedithiol (9O12), as indicated. At these surfaces, uniaxial, planar alignment was manifest in *N*-(4-methoxybenzylidene)-4-butylaniline (MBBA) LCs, as evidenced by the variations in optical transmittance possessing four-fold rotational symmetry. Cells were constructed with 0° or 90° angles between their alignment layers' gold deposition axes, producing untwisted (red) or twisted (blue) nematic structures, respectively. Initially, one or both of a cell's gold deposition axes were aligned with the polarizer axis, defined to be at 0°. Rotation angles were measured with respect to this reference orientation, incremented in 5° steps. Reported spectra are averages of analyses performed on separate LC cells, each consisting of three measured regions, where the radial line widths indicate the data's standard deviation. Spectra are scaled such that their respective transmittance maxima are equal; in actuality, the maximum transmittance of an untwisted nematic cell nearly equals the minimum transmittance of a cell with a 90° twist in its director.

II.E.3. MBBA Cell Voltage–Transmittance Spectra

Applying a potential difference between the alignment layers generates an electric field that can distort the LC alignment. Mesogens with negative Δε adopt an orientation perpendicular to the applied field. In the case of MBBA, such fields would induce (or reinforce) planar alignment, parallel to the surface. Any reorientation of the mesogens upon the application of an electric potential ($V_{AC} \leq 7$ V) would alter the transmittances of LC cells viewed between crossed polarizers. As seen in Figure II.8, transmittance of cells containing MBBA remain constant, indicating prior planar alignment of the mesogens and no subsequent reorientation.

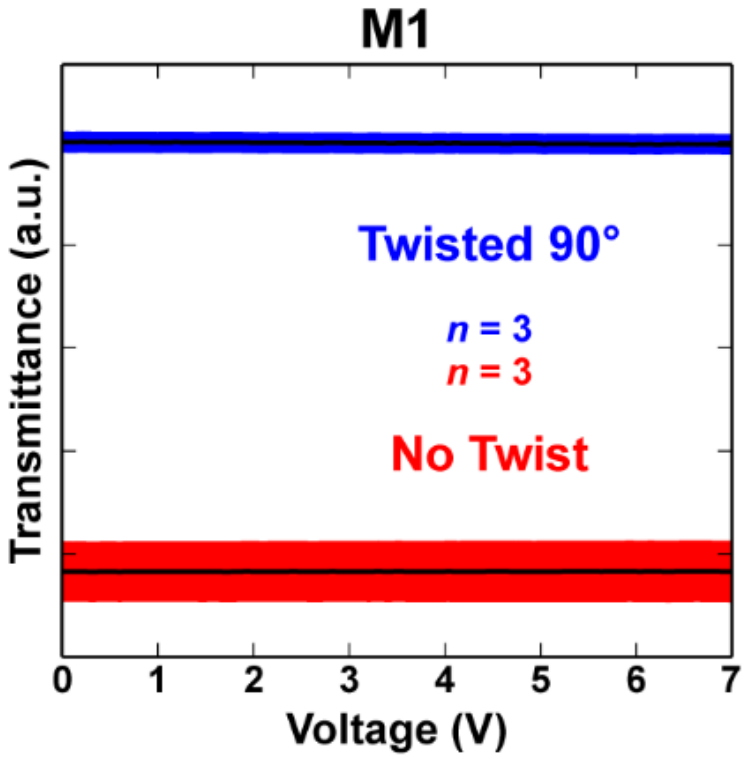

Figure II.8. Normalized optical transmittances of electrically modulated liquid crystal (LC) cells viewed between crossed polarizers. Alignment layers were prepared with matching self- assembled monolayers of *m*-1-carboranethiol (M1), which induced uniaxial planar alignment in *N*-(4-methoxybenzylidene)-4-butylaniline (MBBA) LCs. Cells were constructed with 0° or 90° angles between their alignment layers' gold deposition axes, producing untwisted (red) or twisted (blue) nematic structures, respectively. Cells were positioned between crossed polarizers such that their zero-voltage optical transmittance was maximized (minimized) for twisted (untwisted) nematic structures. Subsequently, a sinusoidally varying (1 kHz) voltage was applied between the alignment layers. Root-mean-square voltages, varied in 0.1 V steps, are indicated along the horizontal axes. Reported spectra are averages (black lines) of analyses performed on = 3 separate LC cells, of each type, where the vertical widths of the surrounding blue outlines indicate the data's standard deviation. No changes in the transmittance spectra were observed with increasing voltage, indicating that the MBBA mesogens did not reorient as a result of the applied electric field.

II.E.4. MBBA Anchoring Orientation Cells

Anchoring orientation wedge cells were used to determine the in-plane orientation of MBBA LCs relative to $\overrightarrow{Au}$: parallel or perpendicular. As shown in Figure II.9, the fringes observed in cells made using M1, M9, and O1 shift toward the thinner ends of the wedges with increased optical retardation along the gold deposition axis, indicating that the MBBA nematic director is aligned parallel to $\overrightarrow{Au}$. By contrast, cells made with O9 and 9O12 exhibited planar alignment of MBBA perpendicular to $\overrightarrow{Au}$, as evident from the observed fringe shifts toward the thicker ends of the wedges. As such, the orientations of the MBBA director match those of 5CB on alignment layers treated with M1, O1, O9, and 9O12 SAMs. However, in the case of M9 SAMs, 5CB and MBBA LCs were observed to align along opposite directions, planar alignment perpendicular and parallel to $\overrightarrow{Au}$, respectively. We attribute this discrepancy to relatively weak interactions of the M9 molecular dipole moment with MBBA mesogens, in comparison to those of other carboranethiol isomers, and other factors contributing to LC alignment that are always present in each cell, though presumed consistent.

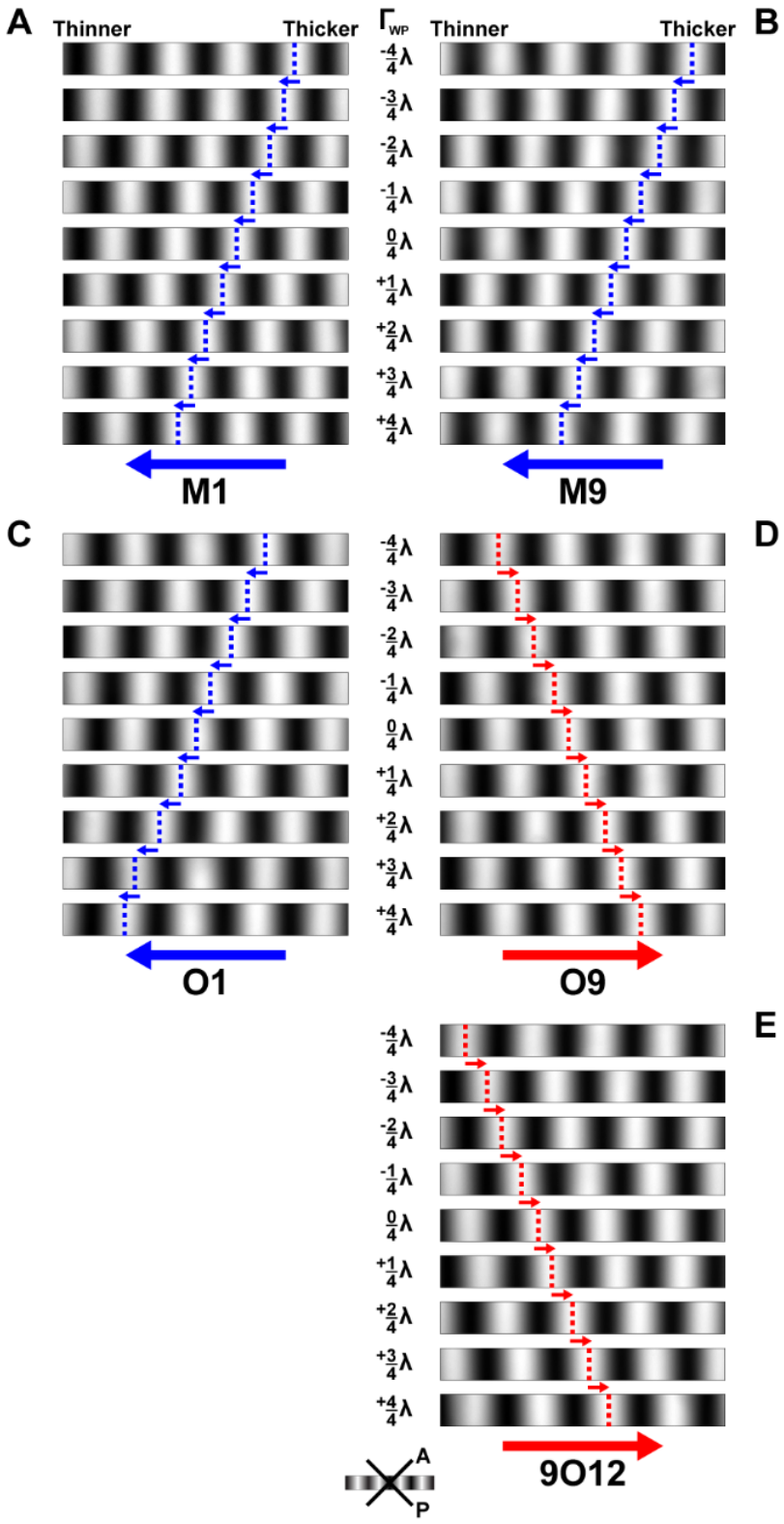

Figure II.9. Transmission fringes observed in liquid crystal (LC) wedge cells viewed between crossed polarizers while illuminated with monochromatic light (wavelength

λ = 531 nm). Alignment layers prepared with matching self-assembled monolayers of *m*-1-carboranethiol (M1), *m*-9-carboranethiol (M9), *o*-1-carboranethiol (O1), *o*-9-carboranethiol (O9), and *o*-9,12-carboranedithiol (9O12), as indicated, induced uniaxial planar alignment of *N*-(4-methoxybenzylidene)-4-butylaniline (MBBA) LCs. Wave plates inserted between the polarizers modified the optical retardation of light transmitted through the cells by fixed amounts (Γ_{WP}). Here, positive (negative) values of Γ_{WP} signify that a wave plate's optically slow axis was aligned parallel (perpendicular) to a cell's gold evaporation direction ($\overrightarrow{Au}$). Arrows and dashed lines track transmittance maxima of constant order within 4.8 mm x 0.5 μm field of view. Fringes in cells containing M1, M9, and O1 monolayers were observed to shift toward the thinner ends of the wedges with increasing Γ_{WP} (blue), indicating that their nematic directors were oriented parallel to $\overrightarrow{Au}$. By contrast, fringes shifted toward the thicker ends of wedges containing O9 and 9O12 monolayers (red), indicating director alignment perpendicular to $\overrightarrow{Au}$.

II.E.5. 5CB Cell Voltage–Transmittance Spectra

Figure II.10 depicts the normalized optical transmittances of untwisted 5CB cells modulated by an electric field. The scaling applied to these spectra exaggerates the apparent variations in the measured transmittances. Comparing absolute transmittances, the change observed in untwisted 5CB cells is only about 10% of that seen in 5CB cells with 90° twists in their directors (Figure II.4). The observed transmittance variations in these cells is similar to those expected from untwisted 5CB cells using other LC alignment techniques (*e.g.*, rubbed polyimide).

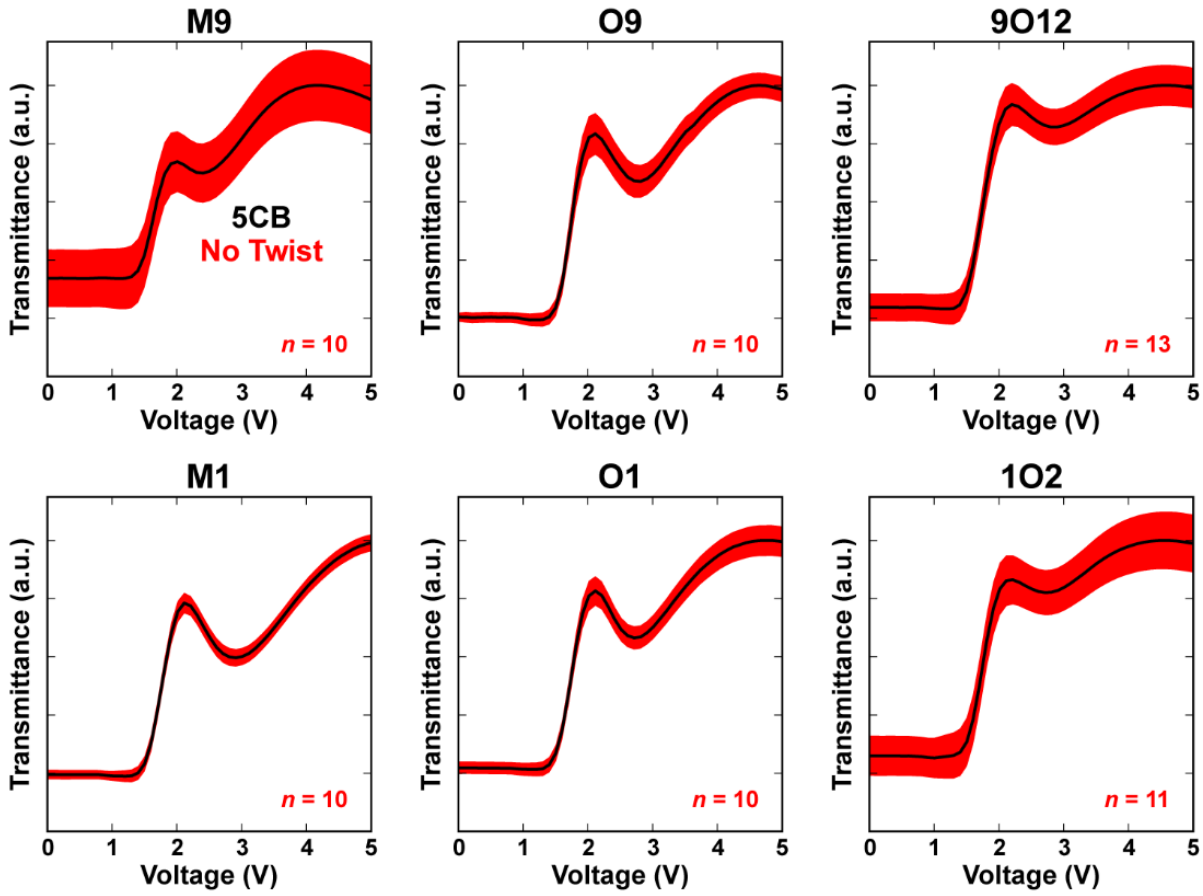

Figure II.10. Normalized optical transmittances of electrically modulated liquid crystal (LC) cells viewed between crossed polarizers. Alignment layers were prepared with matching self- assembled monolayers of *m*-9-carboranethiol (M9), *m*-1-carboranethiol (M1), *o*-9-carboranethiol (O9), *o*-1-carboranethiol (O1), *o*-9,12-carboranedithiol (9O12), and *o*-1,2-carboranedithiol (1O2), as indicated. These surfaces induced uniaxial planar alignment in 4-cyano-4′-pentylbiphenyl (5CB) LCs. Cells were constructed with parallel gold deposition axes, producing untwisted nematic structures, and were positioned between crossed polarizers such that their zero-voltage optical transmittance was minimized. Subsequently, a sinusoidally varying (1 kHz) voltage was applied between the alignment layers in order to distort the LC director away from the surface. Root-mean-square voltages, varied in 0.1 V steps, are indicated along the horizontal axes. Reported spectra are averages (black lines) of analyses performed on *n* separate LC cells, where the vertical widths of the surrounding red outlines indicate the data's standard deviation.

II.E.6. Azimuthal Anchoring Energy

Azimuthal anchoring energies of 5CB aligned by SAMs composed of M1, O9, O1, and 9O12 isomers were measured using the torque balanced method described by Abbott and

coworkers.[78] Here, we summarize the methods used to determine the parameters d, φ, and Ψ in Eq. 2. All measurements were made on anchoring energy wedge cells (Figure II.2D) viewed between crossed polarizers. Wedge thicknesses (d) were estimated by comparing the observed (transmitted) color of the cells, illuminated with white light polarized ±45° from their optical axes, to a Michel-Lévy interference color chart,[79] and then refined using Eq. 1 and the positions of the transmission fringes made visible using monochromatic light (λ = 531 nm).

We calculated φ and Ψ using the values of δ and γ (Figure II.11), which were determined by monitoring the transmission of light through each of the three nematic regions within an anchoring energy cell. The easy alignment axis of the bottom carboranethiol alignment layer (η_0-bottom) was found by rotating the cell with respect to crossed polarizers while examining an untwisted nematic region. There, transmission minima occur when η_0-bottom coincides with either of the polarizer or analyzer axes. After aligning η_0-bottom with the polarizer, the easy axis of the top carboranethiol alignment layer (η_0-top) was identified by rotating the analyzer with respect the fixed cell until the intensity of light transmitted through the second untwisted nematic region was minimized. In doing so, the analyzer was aligned perpendicular to η_0-top. The relative angle formed between the polarizer and analyzer axes equaled δ. Finally, the optical transmittance in the central, twisted nematic, region was minimized by, again, rotating the analyzer while keeping the cell orientation fixed. In this configuration, the analyzer was orthogonal to the equilibrium orientation of the director anchored by the top alignment layer (η_d-top), and the angle formed between the analyzer and polarizer axes equaled γ.

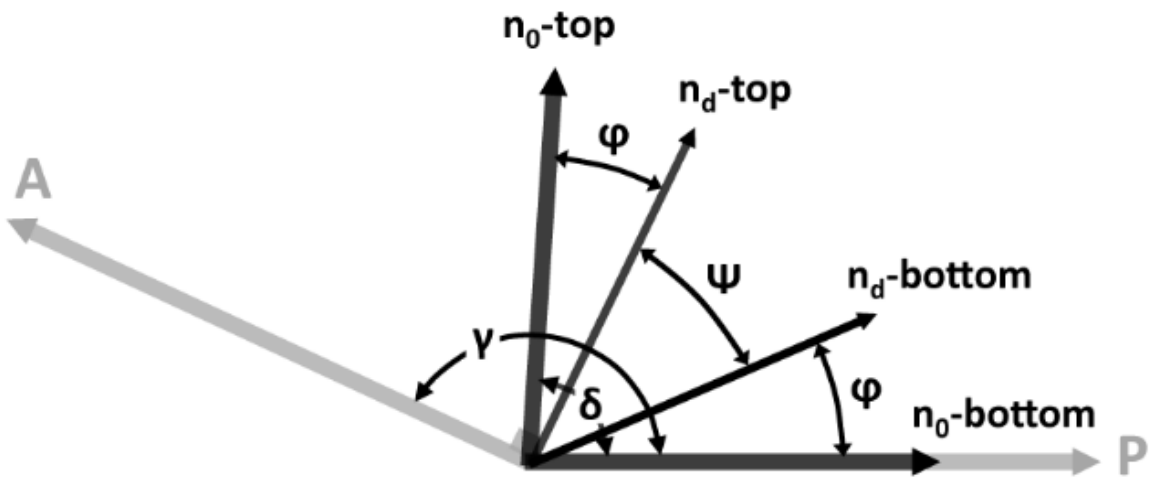

Figure II.11. Schematic illustrating the angles used to compute the azimuthal anchoring energy. Orientations of the polarizer and analyzer are denoted by P and A, respectively. Easy alignment axes are indicated for the top (η_0-top) and bottom (η_0-bottom) alignment layers, while η_d-top and η_d-bottom indicate the equilibrium director orientations at the top and bottom alignment surfaces, respectively, as a result the opposing torques acting on the twisted nematic. The angle by which the azimuthal orientation of the director deviates from the easy axes is denoted by φ, whereas Ψ is the twist in the LC director between the top and bottom alignment surfaces. Figure adapted with permission from Ref. 78. Copyright 2006 American Chemical Society.

Once δ and γ were determined, the angle (φ) by which the azimuthal orientation of the director departs from the easy alignment axes and the angular twist (Ψ) of the director through the cell's thickness were found using the equations:

$$\varphi = \delta - (\gamma - 90°)$$

$$\Psi = 2\gamma - 90° - \delta$$

The anchoring energies reported in Table 1 represent a weighted average of measurements made on multiple cells (at least four of a given isomer) σ and multiple areas within each cell (up to 10). We computed the uncertainties (σ) of *d*, φ, and Ψ using the following equations:

$$\sigma_d = \frac{\sigma_\Gamma}{\Delta n}$$

$$\sigma_{\varphi} = \sqrt{\sigma_{\delta}^2 + \sigma_{\gamma}^2}$$

$$\sigma_{\Psi} = \sqrt{\sigma_{\delta}^2 + (2\sigma_{\gamma})^2}$$

The partial derivatives of W_{az} were found with respect to φ, Ψ, and d, as shown below:

$$\partial W_{az}/_{\partial \Psi} = {}^{2K_{22}}/_{dsin(2\varphi)}$$

$$\partial W_{az}/_{\partial \varphi} = {}^{-4K_{22}\Psi}/_{dtan(2\varphi)sin(2\varphi)}$$

$$\partial W_{az}/_{\partial d} = {}^{-2K_{22}\Psi}\Big/_{d^2 sin(2\varphi)}$$

These quantities evaluated using the parameters of each measurement, were then used to compute the compute the uncertainty in W_{az} ($\sigma_{w_{az}}$):

$$\sigma_{W_{az}} = \sqrt{\left(\partial W_{az}/_{\partial \Psi} \text{ x } \sigma_{\Psi}\right)^2 + \left(\partial W_{az}/_{\partial \varphi} \text{ x } \sigma_{\varphi}\right)^2 + \left(\partial W_{az}/_{\partial d} \text{ x } \sigma_{d}\right)^2}$$

The weighted average of W_{az} and $\sigma_{W_{az}}$ were calculated for i independent measurements using:

$$\text{Weighted Average } W_{az} = {\sum_i \frac{W_{az_i}}{\sigma_{W_{az_i}}^2}}\Big/{\sum_i \frac{1}{\sigma_{W_{az_i}}^2}}$$

$$\text{Weighted Average } \sigma_{W_{az}} = {1}\Big/{\sqrt{\sum_i \frac{1}{\sigma_{W_{az_i}}^2}}}$$

Table II.3. Azimuthal anchoring energy (W_{az}) of 4-cyano-4′-pentylbiphenyl (5CB) liquid crystals in cells prepared with *m*-1-carboranethiol (M1) SAMs.

M1		Γ (nm)[a]	δ (°)[b]	γ (°)[c]	W_{az} (μJ·m^{-2})
Sample 1	Spot 1	1590	86.1	1.6	24 ± 3
	Spot 2	2120	86.2	0.8	21 ± 3
Sample 2	Spot 1	800	89.2	1.7	160 ± 30
	Spot 2	1060	89.0	1.2	90 ± 30
	Spot 3	1330	81.8	5.5	11 ± 1
	Spot 4	1590	88.6	1.3	49 ± 13
	Spot 5	1860	88.4	1.4	37 ± 9
	Spot 6	2120	88.5	0.9	41 ± 12
Sample 3	Spot 1	1860	88.0	1.3	35 ± 8
	Spot 2	2120	87.7	2.8	19 ± 3
Sample 4	Spot 1	800	89.1	1.5	110 ± 30
	Spot 2	1060	89.4	1.3	110 ± 40
	Spot 3	1330	89.6	1.0	120 ± 60
	Spot 4	1590	89.8	1.1	110 ± 60
	Spot 5	1860	89.8	0.6	150 ± 140
	Spot 6	2120	89.7	0.9	85 ± 51
	Spot 7	2390	89.9	0.4	180 ± 270
Sample 5	Spot 1	800	86.3	2.0	46 ± 6
	Spot 2	1060	85.0	3.3	24 ± 2
	Spot 3	1330	86.0	2.7	24 ± 3
	Spot 4	1590	85.6	2.9	18 ± 2
	Spot 5	1860	85.5	2.3	16 ± 2
	Spot 6	2120	85.5	3.0	13 ± 1
	Spot 7	2390	86.2	2.2	15 ± 2
	Spot 8	2660	85.7	2.6	11 ± 1
	Spot 9	2920	85.9	2.3	11 ± 1
	Spot 10	3190	86.3	1.9	12 ± 2
Sample 6	Spot 1	1330	88.9	0.8	85 ± 32
	Spot 2	1590	88.6	0.9	58 ± 18
	Spot 3	1860	88.6	0.4	65 ± 26
	Spot 4	2120	88.0	0.0	49 ± 17
	Spot 5	2390	88.0	0.7	32 ± 9
	Spot 6	2660	88.2	0.1	43 ± 17
	Spot 7	2920	88.5	0.1	45 ± 20
Sample 7	Spot 1	1330	86.7	2.7	26 ± 3
	Spot 2	1590	85.8	3.4	17 ± 2
Weighted Average (*n* = 36)					**14.3 ± 0.4**

[a]Retardation (Γ) between ordinary and extraordinary waves traversing the cell. All retardation values are assumed to have a measurement uncertainty of $\sigma_\Gamma = 50$ nm. [b]The

angle (δ) formed between the alignment layers' easy axes. [c]The relative angle (γ) between the polarizer and analyzer. The measurement uncertainty in the measured angles (δ and γ) are $\sigma_\delta = \sigma_\gamma = 0.5^\circ$.

Table II.4. Azimuthal anchoring energy (W_{az}) of 4-cyano-4′-pentylbiphenyl (5CB) liquid crystals in cells prepared with *o*-1-carboranethiol (O1) SAMs.

O1		Γ (nm)[a]	δ (°)[b]	γ (°)[c]	W_{az} (μJ·m^{-2})
Sample 1	Spot 1	1060	84.7	3.5	22 ± 2
	Spot 2	1330	83.1	4.3	14 ± 1
	Spot 3	1590	84.8	2.9	16 ± 2
	Spot 4	1860	85.3	2.5	16 ± 2
	Spot 5	2120	85.4	2.2	14 ± 2
Sample 2	Spot 1	800	87.0	2.1	51 ± 8
	Spot 2	1060	86.7	3.4	29 ± 3
	Spot 3	1330	86.9	3.2	25 ± 3
	Spot 4	1590	86.9	2.5	24 ± 3
	Spot 5	1860	87.5	1.6	27 ± 5
	Spot 6	2120	87.2	0.1	35 ± 9
Sample 3	Spot 1	1330	88.3	3.5	30 ± 4
	Spot 2	1590	88.1	1.1	45 ± 11
	Spot 3	1860	88.7	2.4	30 ± 6
	Spot 4	2120	88.6	2.7	24 ± 4
	Spot 5	2390	89.4	2.3	30 ± 7
	Spot 6	2660	89.0	2.0	27 ± 6
Sample 4	Spot 1	2920	88.2	1.7	20 ± 4
	Spot 2	3190	88.0	1.4	19 ± 4
	Spot 3	3450	87.4	1.1	17 ± 3
Sample 5	Spot 1	530	81.9	0.5	46 ± 6
	Spot 2	800	85.3	4.8	27 ± 2
	Spot 3	1330	85.4	4.3	17 ± 2
	Spot 4	1590	85.4	2.3	19 ± 2
	Spot 5	1860	86.3	2.5	18 ± 2
	Spot 6	2120	85.7	3.7	12 ± 1
	Spot 7	2390	86.6	3.0	14 ± 2
	Spot 8	2660	86.8	2.6	13 ± 2
Sample 6	Spot 1	1060	85.7	3.7	24 ± 2
	Spot 2	1330	86.0	3.5	21 ± 2
	Spot 3	1590	86.0	2.8	19 ± 2
	Spot 4	1860	86.6	1.9	21 ± 3
	Spot 5	2120	86.4	2.9	15 ± 2
	Spot 6	2390	86.6	2.4	15 ± 2
	Spot 7	2660	86.6	2.4	14 ± 2
	Spot 8	2920	87.0	2.4	13 ± 2
	Spot 9	3190	87.2	1.9	14 ± 2
Weighted Average (*n* = 37)					**14.3 ± 0.4**

[a]Retardation (Γ) between ordinary and extraordinary waves traversing the cell. All retardation values are assumed to have a measurement uncertainty of $\sigma_\Gamma = 50$ nm. [b]The angle (δ) formed between the alignment layers' easy axes. [c]The relative angle (γ) between the polarizer and analyzer. The measurement uncertainty in the measured angles (δ and γ) are $\sigma_\delta = \sigma_\gamma = 0.5^\circ$.

Table II.5. Azimuthal anchoring energy (W_{az}) of 4-cyano-4′-pentylbiphenyl (5CB) liquid crystals in cells prepared with *o*-9-carboranethiol (O9) SAMs.

O9		Γ (nm)[a]	δ (°)[b]	γ (°)[c]	W_{az} (μJ·m^{-2})
Sample 1	Spot 1	1060	87.4	2.4	40 ± 6
	Spot 2	1590	87.5	2.3	27 ± 4
	Spot 3	3190	88.6	0.7	32 ± 11
Sample 2	Spot 1	1060	90.3	2.0	110 ± 50
	Spot 2	1330	90.0	1.6	96 ± 41
	Spot 3	1590	89.9	2.4	54 ± 16
	Spot 4	1860	89.4	0.8	83 ± 43
Sample 3	Spot 1	800	85.4	5.5	26 ± 2
	Spot 2	1060	83.4	7.6	14 ± 1
	Spot 3	1330	84.8	5.6	14 ± 1
	Spot 4	1590	84.9	7.0	11 ± 1
	Spot 5	1860	85.3	5.1	11 ± 1
	Spot 6	2120	84.3	6.5	7.9 ± 0.5
Sample 4	Spot 1	1060	84.4	4.3	20 ± 2
	Spot 2	1330	84.6	3.8	17 ± 1
	Spot 3	1590	84.7	4.0	14 ± 1
	Spot 4	1860	85.2	3.0	14 ± 1
	Spot 5	2120	85.7	3.3	13 ± 1
	Spot 6	2390	85.2	3.4	11 ± 1
Sample 5	Spot 1	1060	81.5	9.9	11 ± 1
	Spot 2	1330	83.4	7.4	11 ± 1
	Spot 3	1590	83.1	7.7	8.9 ± 0.5
	Spot 4	1860	83.5	6.7	8.4 ± 0.5
	Spot 5	2120	83.2	7.4	6.8 ± 0.4
	Spot 6	2390	83.7	6.4	6.8 ± 0.4
	Spot 7	2660	83.3	7.0	5.6 ± 0.3
	Spot 8	2920	83.7	6.5	5.5 ± 0.3
	Spot 9	3190	83.7	6.1	5.2 ± 0.3
Weighted Average (*n* = 28)					**7.5 ± 0.1**

[a]Retardation (Γ) between ordinary and extraordinary waves traversing the cell. All retardation values are assumed to have a measurement uncertainty of $\sigma_\Gamma = 50$ nm. [b]The angle (δ) formed between the alignment layers' easy axes. [c]The relative angle (γ) between the polarizer and analyzer. The measurement uncertainty in the measured angles (δ and γ) are $\sigma_\delta = \sigma_\gamma = 0.5^\circ$.

Table II.6. Azimuthal anchoring energy (W_{az}) of 4-cyano-4′-pentylbiphenyl (5CB) liquid crystals in cells prepared with *o*-9,12-carboranedithiol (9O12) SAMs.

9O12		Γ (nm)[a]	δ (°)[b]	γ (°)[c]	W_{az} (μJ·m^{-2})
Sample 1	Spot 1	800	86.2	4.6	31 ± 3
	Spot 2	1060	83.5	3.1	20 ± 2
	Spot 3	1330	84.7	0.3	28 ± 4
	Spot 4	1590	84.2	0.7	20 ± 2
	Spot 5	1860	85.5	2.0	17 ± 2
	Spot 6	2120	84.2	0.6	15 ± 2
	Spot 7	2390	85.9	0.8	18 ± 3
Sample 2	Spot 1	1590	89.9	3.4	38 ± 8
	Spot 2	1860	89.9	2.4	46 ± 13
	Spot 3	2120	88.7	2.2	29 ± 6
	Spot 4	2390	89.1	1.7	34 ± 9
	Spot 5	2660	89.9	2.4	32 ± 9
	Spot 6	2920	88.8	3.3	16 ± 3
Sample 3	Spot 1	1330	81.6	7.0	10 ± 1
	Spot 2	1590	80.9	7.5	7.8 ± 0.4
	Spot 3	1860	82.6	5.7	8.5 ± 0.5
	Spot 4	2120	81.9	6.5	6.6 ± 0.3
	Spot 5	2390	82.8	5.4	6.8 ± 0.4
	Spot 6	2660	81.8	5.8	5.6 ± 0.3
	Spot 7	2920	83.5	5.2	6.0 ± 0.4
	Spot 8	3190	81.5	6.4	4.3 ± 0.2
Sample 4	Spot 1	1330	85.8	5.8	16 ± 1
	Spot 2	1590	86.0	5.7	13 ± 1
	Spot 3	1860	85.8	3.8	14 ± 1
	Spot 4	2120	85.7	4.4	11 ± 1
	Spot 5	2390	86.0	2.9	13 ± 1
	Spot 6	2660	86.1	2.7	12 ± 1
	Spot 7	2920	85.9	2.4	11 ± 1
	Spot 8	3190	84.9	3.0	8.0 ± 0.7
Weighted Average (n = 29)					**6.7 ± 0.1**

[a]Retardation (Γ) between ordinary and extraordinary waves traversing the cell. All retardation values are assumed to have a measurement uncertainty of $\sigma_\Gamma = 50$ nm. [b]The angle (δ) formed between the alignment layers' easy axes. [c]The relative angle (γ) between the polarizer and analyzer. The measurement uncertainty in the measured angles (δ and γ) are $\sigma_\delta = \sigma_\gamma = 0.5^\circ$.

II.E.7. Oblique Gold Deposition

Gold was deposited at an oblique angle (50° away from the normal) onto glass substrates, as shown in Figure II.12. This angle describes the incidence angle of metal deposited in the center of the tilted substrate, located directly above the metal source. However, for extended substrates, this angle depends on the surface's distance away from the central deposition axis. Here, this deviation is no more than 6° from the intended deposition angle.

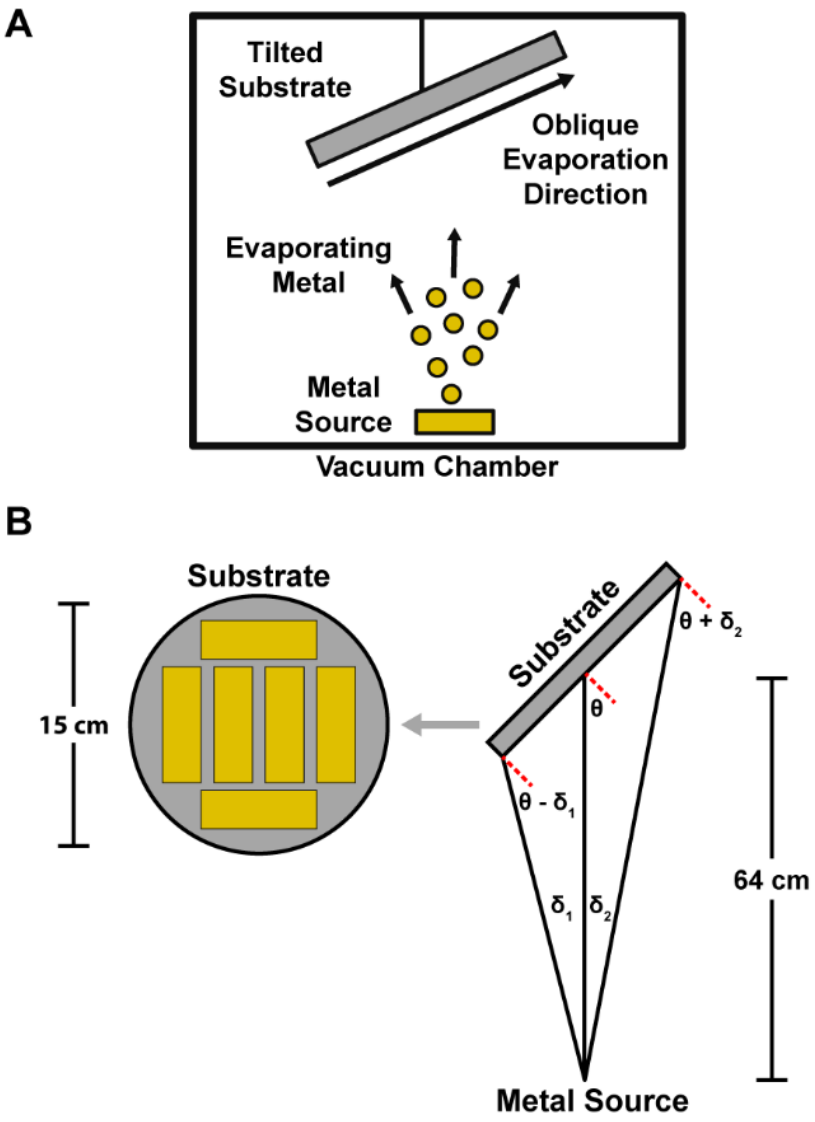

Figure II.12. Schematic of oblique gold deposition. (A) Inside a vacuum chamber, gold is heated by an electron beam (not shown), causing it to evaporate from a source and deposit onto a tiled substrate located above. (B) Due to the non-zero widths and arrangement of glass, the deposition angle varies across the surface and between slides. Deviations from the intended angle ($\theta = 50°$) are expected to be, at most, $ß_1 = ß_2 = 6°$ for the dimensions and configuration used in this work.

II.E.8. Gaussian Calculations

II.E.8.a. Molecular Dipole Moments

Table II.8 summarizes the molecular dipole moments of M9, M1, O9, O1, 9O12, and 1O2 calculated using density functional theory and the Gaussian 09 software package at the M062X level with the 6-311G** basis set. Dipole component vectors ($p_{\parallel}$ and $p_{\perp}$) assume upright adsorption of the carboranethiol species on a gold surface.

Table II.7. Molecular dipole moments (p) of carboranethiol and -dithiol isomers.

Isomer	Molecular Dipole Moment (D)		
	Magnitude	$p_{\parallel}$ [a]	$p_{\perp}$ [b]
M9 [c]	3.94	1.38	3.70
M1 [d]	2.20	2.13	-0.558
O9 [e]	5.46	2.18	5.01
O1 [f]	3.59	1.90	-3.05
9O12 [g]	6.78	0.00	6.78
1O2 [h]	3.20	0.00	-3.20

[a]In-plane dipole moment, parallel to the surface. [b]Out-of-plane dipole moment, normal to the surface. [c]*m*-9-carboranethiol (M9). [d]*m*-1-carboranethiol (M1). [e]*o*-9-carboranethiol (O9). [f]*o*-1-carboranethiol (O1). [g]*o*-9,12-carboranedithiol (9O12). [h]*o*-1,2-carboranedithiol (1O2).

II.E.8.b. Molecular Polarizability Tensor

The molecular polarizability tensor (α) of all six carboranethiols studied here were computed with the Gaussian 09 software package:

$$\alpha = \begin{bmatrix} \alpha_{xx} & \alpha_{xy} & \alpha_{xz} \\ \alpha_{xy} & \alpha_{yy} & \alpha_{yz} \\ \alpha_{xz} & \alpha_{yz} & \alpha_{zz} \end{bmatrix}$$

As described in the main text, Cartesian coordinate bases were chosen for each isomer based on its molecular symmetry and assumed upright adsorption onto underlying gold substrates. We found the polarizability tensors of each isomer to be *nearly* diagonalized in the chosen

coordinate basis. As such, we consider only the carboranethiol polarizabilities along each of the coordinate axes (α_{xx}, α_{yy}, and α_{zz}), as summarized in Table II.8.

Table II.8. Molecular polarizabilities (α) of carboranethiol and -dithiol isomers.

Isomer	Principal Polarizabilities		
	α_{xx}	α_{yy}	α_{zz}
M9[a]	19.4	19.2	24.3
M1[b]	19.4	19.6	23.6
O9[c]	19.5	19.8	24.0
O1[d]	19.4	19.7	23.7
9O12[e]	24.0	21.3	26.3
1O2[f]	23.4	21.3	26.4

[a]*m*-9-carboranethiol (M9). [b]*m*-1-carboranethiol (M1). [c]*o*-9-carboranethiol (O9). [d]*o*-1-carboranethiol (O1). [e]*o*-9,12-carboranedithiol (9O12). [f]*o*-1,2-carboranedithiol (1O2).

II.E.8.c. Optimized Molecular Geometries and Dipoles

Computed values of the molecular dipole vectors and polarizability tensors depend on the optimized orientation of the thiol moiety (S–H bond) in each carboranethiol isomer. However, the hydrogen on the molecule's thiol functionality is lost during chemisoption onto the gold surface (becoming -thiol*ate*). As such, the dipoles and polarizabilities computed for these structures do not accurately reflect those of the actual *adsorbed* molecule. To account for this change in molecular structure upon chemisorption, we computed the molecular dipoles and polarizabilities of each isomer as the average of those values from multiple (nearly degenerate) conformations of each isomer. Each molecular conformation was distinguished by the initial value of the carborane–sulfur–hydrogen dihedral angle in the unoptimized structure, reflecting the rotational symmetry of the thiol moieties in each isomer (five-fold and two-fold symmetries in the cases of mono- and dithiol species,

respectively). Averaging effectively eliminates the thiol contributions to the in-plane molecular dipole and polarizability. Table II.9 present the atomic coordinates of each structure after optimization, labeled with the initial thiol dihedral angles. During optimization, atoms in each structure were allowed to relax into their lowest energy positions with the exceptions of dihedral angles denoted by "F." In these "frozen" structures, the value of the thiol dihedral angle was not optimized in order to maintain the desired molecular symmetry. These molecular conformations do not represent energetically optimized structures. If optimized without restrictions, an unfavorable interaction between the electron deficient carbon atoms in the carborane cage and the polar S–H bond would cause the thiol dihedral angle to deviate significantly from its initial value and disrupt the symmetry of the model. As such, these structures were used with only partial structural optimization. We reiterate, however, that the adsorbed molecule does not possess the carborane–sulfur–hydrogen dihedral angle left unoptimized here. In the cases of carboranedithiol isomers, the two conformations are distinguished by an "M" (or its absence) in the table heading. These conformations are mirror-symmetric versions of the fully optimized structures, reflecting the bilateral symmetry of the dithiol species.

Table II.9. Optimized molecular geometries and dipoles of each carboranethiol and –dithiol isomer.

M9 (0°) Energy: -730.121306 E_h

Atom	Position Coordinates (Å)		
	X	Y	Z
B	0.112328	-0.4994	-1.422584
B	-1.393971	-1.240065	-0.862785
B	0.131359	1.192437	-0.906861
B	1.065263	-0.016128	-0.000362
B	0.115184	-1.520253	0.025303
B	-1.360695	1.500783	-0.024783
B	0.132472	1.22187	0.865364
B	0.113277	-0.451841	1.437922
B	-1.393854	-1.210304	0.904755
C	-1.319917	0.443261	1.287942
H	0.545346	-0.778257	-2.48149
H	0.633748	-2.580157	0.042517
H	0.562947	2.034117	-1.609023
H	-1.965234	2.508414	-0.040872
H	0.54684	-0.695522	2.505253
H	0.564102	2.086491	1.539219
H	-1.978863	-1.950561	1.609212
H	-1.979496	-2.003201	-1.541961
B	-2.308671	-0.005531	0.000636
C	-1.321212	0.400457	-1.301621
H	-1.816124	0.69738	-2.21541
H	-3.478525	0.103897	-0.00055
H	-1.813884	0.770472	2.191888
S	2.927707	-0.084822	-0.000618
H	3.119158	1.243927	0.010164

M9 (72°, F) Energy: -730.121033 E_h

Atom	Position Coordinates (Å)		
	X	Y	Z
B	-0.107117	1.489342	-0.232513
B	1.407478	1.341038	0.681516
B	-0.124049	0.23107	-1.485054
B	-1.064653	0.023934	0.015641
B	-0.099851	0.71243	1.358978
B	1.361379	-0.70142	-1.331054
B	-0.144687	-1.331282	-0.667711
B	-0.12732	-1.032239	1.085953
B	1.396634	-0.222552	1.496113
C	1.298797	-1.351164	0.224497
H	-0.52408	2.559672	-0.494616
H	-0.619224	1.205486	2.295336
H	-0.556541	0.456686	-2.556171
H	1.961981	-1.17588	-2.222646
H	-0.567869	-1.855249	1.805434
H	-0.587619	-2.333491	-1.100653
H	1.982563	-0.502995	2.478173
H	2.004867	2.297188	1.021268
B	2.308309	-0.015211	0.004933
C	1.326391	0.944199	-0.974342
H	1.825069	1.607339	-1.666786
H	3.477842	-0.077383	-0.089676
H	1.778651	-2.3084	0.37096
S	-2.928377	0.083104	-0.008285
H	-3.103354	-1.236404	0.156996

M9 (144°) Energy: -730.121494 E_h

Atom	Position Coordinates (Å)		
	X	Y	Z
B	0.115038	-0.247782	1.486599
B	-1.389949	0.678357	1.355552
B	0.123054	-1.48438	0.211914
B	1.064465	0.002157	0.005351
B	0.124923	1.340214	0.714753
B	-1.376141	-1.318956	-0.701775
B	0.11839	-0.660627	-1.352864
B	0.124748	1.079833	-1.040262
B	-1.378709	1.50418	-0.204677
C	-1.321241	0.238252	-1.340791
H	0.547625	-0.521716	2.54693
H	0.654528	2.273163	1.206619
H	0.543676	-2.564026	0.422844
H	-1.989435	-2.205945	-1.168597
H	0.560845	1.805697	-1.859864
H	0.546522	-1.092243	-2.360608
H	-1.95537	2.496756	-0.466906
H	-1.972793	1.023154	2.318847
B	-2.308361	0.019761	0.005842
C	-1.322341	-0.970733	0.950342
H	-1.818246	-1.668702	1.609747
H	-3.479332	-0.064677	-0.041078
H	-1.815604	0.39646	-2.288699
S	2.927231	-0.080245	0.011026
H	3.116097	1.237102	-0.155119

M9 (216°) Energy: -730.121477 E_h

Atom	Position Coordinates (Å)		
	X	Y	Z
B	-0.124597	1.086609	-1.033387
B	1.379	1.505224	-0.195074
B	-0.118495	-0.651983	-1.35705
B	-1.06448	0.002546	0.005272
B	-0.124588	1.335919	0.723338
B	1.37587	-1.314633	-0.71017
B	-0.123365	-1.485513	0.202565
B	-0.115139	-0.256927	1.48488
B	1.390147	0.669584	1.359842
C	1.322024	-0.976836	0.944141
H	-0.560253	1.817911	-1.848367
H	-0.653903	2.265837	1.221148
H	-0.546574	-1.077265	-2.367499
H	1.988938	-2.198763	-1.182581
H	-0.548029	-0.537573	2.543311
H	-0.544392	-2.566275	0.40671
H	1.973231	1.007945	2.325235
H	1.955856	2.499308	-0.451081
B	2.308375	0.019311	0.005949
C	1.321141	0.246531	-1.339235
H	1.815492	0.410709	-2.286122
H	3.479296	-0.064984	-0.041786
H	1.817685	-1.679032	1.599219
S	-2.927112	-0.080227	0.011179
H	-3.116187	1.236947	-0.157323

M9 (288°, F) Energy: -730.121018 E_h

Atom	Position Coordinates (Å)		
	X	Y	Z
B	0.127109	-1.028763	1.089338
B	-1.396597	-0.217475	1.496728
B	0.144485	-1.33351	-0.663294
B	1.064659	0.023668	0.015675
B	0.099985	0.716784	1.356662
B	-1.361459	-0.705701	-1.328731
B	0.124055	0.226207	-1.485686
B	0.10728	1.488266	-0.237305
B	-1.407242	1.34333	0.677033
C	-1.326282	0.941081	-0.977404
H	0.567346	-1.849514	1.81159
H	0.619366	1.212841	2.291423
H	0.587356	-2.337148	-1.092998
H	-1.961899	-1.18308	-2.21888
H	0.524468	2.557678	-0.502845
H	0.556726	0.44801	-2.557526
H	-2.004556	2.300618	1.013718
H	-1.982526	-0.494497	2.479764
B	-2.308381	-0.014963	0.00492
C	-1.298953	-1.350281	0.228872
H	-1.778958	-2.306977	0.378352
H	-3.477942	-0.077368	-0.089287
H	-1.824922	1.602042	-1.671963
S	2.928368	0.083084	-0.008571
H	3.103583	-1.235965	0.160289

M1 (0°) Energy: -730.087128 E_h

Atom	Position Coordinates (Å)		
	X	Y	Z
B	-0.006375	-2.29319	0
B	-0.459726	-1.363726	1.437534
B	-0.459726	-1.363726	-1.437534
B	1.223728	-1.384639	-0.891013
B	1.223728	-1.384639	0.891013
B	-1.182181	0.149111	-0.892629
B	0.48693	0.123759	-1.444556
B	1.518888	0.119307	0
B	0.48693	0.123759	1.444556
B	0.024159	0.931496	0
S	0.083814	2.73539	0
H	-0.167801	-3.459906	0
H	2.067258	-1.914586	1.522554
H	2.067258	-1.914586	-1.522554
H	-0.921438	-1.89197	-2.383428
H	-2.065369	0.721566	-1.41736
H	-1.248119	2.907203	0
H	2.505108	0.764927	0
H	0.772391	0.773359	-2.38313
H	0.772391	0.773359	2.38313
H	-0.921438	-1.89197	2.383428
B	-1.182181	0.149111	0.892629
C	-1.363978	-1.267222	0
H	-2.347043	-1.716478	0
H	-2.065369	0.721566	1.41736

M1 (72°) Energy: -730.086719 E_h

Atom	Position Coordinates (Å)		
	X	Y	Z
B	-2.292922	0.008104	0.001202
B	-1.351529	1.477475	-0.319174
B	-1.366046	-1.382705	-0.59101
B	-1.384156	-0.997583	1.139364
B	-1.379755	0.774135	1.307899
B	0.135976	-0.774191	-1.272138
B	0.130363	-1.474634	0.347126
B	0.113794	-0.145286	1.521828
B	0.140591	1.378588	0.620809
C	0.931724	-0.00727	0.019786
S	2.734587	-0.082457	0.004335
H	-3.460917	0.028378	-0.149555
H	-1.904398	1.332514	2.204708
H	-1.913163	-1.710976	1.915695
H	-1.899745	-2.282461	-1.131451
H	0.704107	-1.213897	-2.20145
H	2.914123	1.246972	-0.047249
H	0.765394	-0.243144	2.497542
H	0.774677	-2.442482	0.538475
H	0.790995	2.289757	0.99037
H	-1.872732	2.469755	-0.681038
B	0.147192	0.989834	-1.103327
C	-1.281687	0.132558	-1.354182
H	-1.738415	0.228793	-2.329122
H	0.71892	1.595678	-1.932806

M1 (144°) Energy: -730.087017 E_h

Atom	Position Coordinates (Å)		
	X	Y	Z
B	-2.293109	0.017216	0.001486
B	-1.360217	0.669061	-1.354707
B	-1.373176	-1.313809	0.72623
B	-1.380499	0.282112	1.492663
B	-1.361946	1.51154	0.203894
B	0.134621	-1.474987	-0.174985
B	0.12058	-0.64859	1.381965
B	0.132345	1.09069	1.051876
B	0.143705	1.333847	-0.710188
C	0.932064	0.001243	0.013466
S	2.734744	-0.080646	-0.013276
H	-3.462148	-0.082814	-0.103683
H	-1.873994	2.567262	0.326204
H	-1.906431	0.46288	2.532934
H	-1.911767	-2.294378	1.094128
H	0.69376	-2.483458	-0.404766
H	2.912093	1.23049	0.212904
H	0.787364	1.799228	1.729461
H	0.766035	-1.098792	2.256971
H	0.799147	2.184055	-1.196109
H	-1.887121	0.999917	-2.354646
B	0.135456	-0.251719	-1.468886
C	-1.285171	-0.976151	-0.939641
H	-1.745808	-1.684442	-1.613714
H	0.7028	-0.536976	-2.456955

M1 (288°) Energy: -730.086719 E_h

Atom	Position Coordinates (Å)		
	X	Y	Z
B	2.292922	0.008104	0.001202
B	1.366046	-1.382705	-0.59101
B	1.351529	1.477475	-0.319174
B	1.379755	0.774135	1.307899
B	1.384156	-0.997583	1.139364
B	-0.147192	0.989834	-1.103327
B	-0.140591	1.378588	0.620809
B	-0.113794	-0.145286	1.521828
B	-0.130363	-1.474634	0.347126
C	-0.931724	-0.00727	0.019786
S	-2.734587	-0.082457	0.004335
H	3.460917	0.028378	-0.149555
H	1.913163	-1.710976	1.915695
H	1.904398	1.332514	2.204708
H	1.872732	2.469755	-0.681038
H	-0.71892	1.595678	-1.932806
H	-2.914123	1.246972	-0.047249
H	-0.765394	-0.243144	2.497542
H	-0.790995	2.289757	0.99037
H	-0.774677	-2.442482	0.538475
H	1.899745	-2.282461	-1.131451
B	-0.135976	-0.774191	-1.272138
C	1.281687	0.132558	-1.354182
H	1.738415	0.228793	-2.329123
H	-0.704107	-1.213897	-2.20145

M1 (216°) Energy: -730.087017 E_h

Atom	Position Coordinates (Å)		
	X	Y	Z
B	2.293109	0.017216	0.001486
B	1.373176	-1.313809	0.72623
B	1.360217	0.669061	-1.354707
B	1.361946	1.51154	0.203894
B	1.380499	0.282112	1.492663
B	-0.135456	-0.251719	-1.468886
B	-0.143705	1.333847	-0.710188
B	-0.132345	1.09069	1.051876
B	-0.12058	-0.64859	1.381965
C	-0.932064	0.001243	0.013466
S	-2.734744	-0.080646	-0.013276
H	3.462148	-0.082814	-0.103683
H	1.906431	0.46288	2.532934
H	1.873994	2.567262	0.326204
H	1.887121	0.999917	-2.354646
H	-0.7028	-0.536976	-2.456955
H	-2.912093	1.23049	0.212904
H	-0.787364	1.799228	1.729461
H	-0.799147	2.184055	-1.196109
H	-0.766035	-1.098792	2.256971
H	1.911767	-2.294378	1.094128
B	-0.134621	-1.474987	-0.174985
C	1.285171	-0.976151	-0.939641
H	1.745808	-1.684442	-1.613714
H	-0.69376	-2.483458	-0.404766

O9 (0°) Energy: -730.094599 E_h

Atom	Position Coordinates (Å)		
	X	Y	Z
B	0.542841	0.916284	0
B	1.083677	-0.516861	0.891108
B	1.083677	-0.516861	-0.891108
B	-0.350068	0.357946	-1.448694
B	-1.227917	0.912141	0
B	-0.350068	0.357946	1.448694
B	-0.350068	-1.400445	-1.44712
B	-1.778961	-0.51853	-0.88931
B	-1.778961	-0.51853	0.88931
B	-0.350068	-1.400445	1.44712
C	0.464261	-1.805781	0
C	-1.152496	-1.811643	0
H	-0.338989	0.957717	2.463669
H	-1.861642	1.90792	0
H	-0.338989	0.957717	-2.463669
H	2.096703	-0.672771	-1.472741
H	-0.344929	-2.189553	-2.319443
H	-2.788995	-0.685343	1.471825
H	-2.788995	-0.685343	-1.471825
H	-0.344929	-2.189553	2.319443
H	2.096703	-0.672771	1.472741
H	0.945015	-2.77296	0
H	-1.627003	-2.78164	0
S	1.505326	2.513933	0
H	2.719823	1.944986	0

O9 (72°) Energy: -730.0948 E_h

Atom	Position Coordinates (Å)		
	X	Y	Z
B	1.064565	-0.007598	0.027938
B	0.134338	-0.810727	-1.258873
B	0.143316	0.956589	-1.144262
B	0.12899	1.404468	0.576582
B	0.107352	-0.099379	1.526885
B	0.118428	-1.470079	0.38939
B	-1.357907	1.47662	-0.363681
B	-1.387357	0.81101	1.280286
B	-1.393438	-0.959102	1.166661
B	-1.371079	-1.41017	-0.549248
C	-1.287983	0.089642	-1.355432
C	-2.1468	0.007	0.006049
H	0.620355	-2.509586	0.634328
H	0.616099	-0.1701	2.588755
H	0.640394	2.4016	0.948246
H	0.552876	1.598589	-2.043203
H	-2.01611	2.381335	-0.726398
H	-2.075255	-1.594078	1.887139
H	-2.064889	1.354372	2.07603
H	-2.038895	-2.255197	-1.021612
H	0.540415	-1.333767	-2.232292
H	-1.853578	0.151736	-2.27357
H	-3.220411	0.019033	-0.108353
S	2.928301	-0.082815	0.011069
H	3.11884	1.243098	-0.068264

O9 (144°) Energy: -730.094923 E_h

Atom	Position Coordinates (Å)		
	X	Y	Z
B	1.065074	0.002122	0.023183
B	0.131243	-1.41369	-0.487481
B	0.136771	0.050894	-1.495056
B	0.133297	1.456604	-0.419792
B	0.121093	0.852553	1.261458
B	0.109025	-0.925264	1.219941
B	-1.363324	0.942262	-1.193502
B	-1.374003	1.431907	0.509057
B	-1.393051	-0.034717	1.511838
B	-1.37787	-1.444914	0.443129
C	-1.288402	-0.758845	-1.122134
C	-2.145982	0.016273	0.004706
H	0.614246	-1.594332	2.048968
H	0.631342	1.453155	2.140577
H	0.649726	2.46875	-0.739337
H	0.546208	-0.002402	-2.597481
H	-2.024455	1.432524	-2.033672
H	-2.075201	-0.078673	2.471003
H	-2.04357	2.353589	0.807858
H	-2.050969	-2.399175	0.583474
H	0.529885	-2.428919	-0.932385
H	-1.855808	-1.278364	-1.880146
H	-3.220111	-0.040784	-0.090707
S	2.927638	-0.075125	-0.021175
H	3.121548	1.183284	0.401344

O9 (216°) Energy: -730.094923 E_h

Atom	Position Coordinates (Å)		
	X	Y	Z
B	-1.065074	0.002122	0.023183
B	-0.136771	0.050906	-1.495056
B	-0.131243	-1.413686	-0.487492
B	-0.109025	-0.925274	1.219934
B	-0.121093	0.852544	1.261465
B	-0.133297	1.456607	-0.41978
B	1.37787	-1.444918	0.443117
B	1.393051	-0.034729	1.511837
B	1.374003	1.431903	0.509069
B	1.363324	0.942272	-1.193494
C	1.288402	-0.758837	-1.12214
C	2.145982	0.016273	0.004706
H	-0.649726	2.468756	-0.739317
H	-0.631342	1.453138	2.140589
H	-0.614246	-1.594348	2.048955
H	-0.529884	-2.428912	-0.932404
H	2.050969	-2.39918	0.583455
H	2.04357	2.353583	0.807876
H	2.075201	-0.078692	2.471003
H	2.024455	1.43254	-2.033661
H	-0.546207	-0.002381	-2.597482
H	1.855808	-1.278349	-1.880156
H	3.220111	-0.040784	-0.090707
S	-2.927638	-0.075125	-0.021175
H	-3.121547	1.183287	0.401335

O9 (288°) Energy: -730.094802 E_h

Atom	Position Coordinates (Å)		
	X	Y	Z
B	-1.064536	-0.007643	0.027622
B	-0.143157	0.954654	-1.145996
B	-0.134092	-0.812797	-1.257729
B	-0.11843	-1.469495	0.391623
B	-0.107604	-0.096901	1.526948
B	-0.129094	1.405411	0.574124
B	1.3712	-1.410938	-0.546798
B	1.393238	-0.957141	1.168435
B	1.387126	0.813125	1.279144
B	1.357892	1.475956	-0.36596
C	1.288246	0.087446	-1.355482
C	2.146739	0.007061	0.006297
H	-0.640899	2.402939	0.944164
H	-0.616934	-0.165838	2.588657
H	-0.620565	-2.508485	0.63831
H	-0.539891	-1.337663	-2.230285
H	2.039156	-2.25677	-1.017509
H	2.064568	1.358071	2.07388
H	2.075001	-1.591204	1.889772
H	2.016151	2.380114	-0.729966
H	-0.552612	1.595351	-2.045913
H	1.85402	0.148077	-2.273603
H	3.220378	0.018915	-0.107836
S	-2.928263	-0.082801	0.01103
H	-3.118797	1.243109	-0.068106

O1 (36°, F) Energy: -730.060377 E_h

Atom	Position Coordinates (Å)		
	X	Y	Z
B	-2.30685	0.033849	-0.027383
B	-1.328504	1.451868	-0.443923
B	-1.348304	0.036824	-1.512923
B	-1.395652	-1.419808	-0.50585
B	-1.421482	-0.895385	1.195554
B	-1.385301	0.882307	1.234811
B	0.121861	-0.902669	-1.218768
B	0.092666	-1.464022	0.464238
B	0.088928	-0.049452	1.542483
B	0.14777	1.401038	0.53479
C	0.094886	0.79469	-1.064737
C	0.919258	-0.049581	0.053283
S	2.718972	-0.073822	0.019126
H	-3.485049	0.078135	-0.074749
H	-1.884132	1.531127	2.084568
H	-1.955341	-1.531757	2.03398
H	-1.904568	-2.414726	-0.884153
H	-1.701203	0.148253	-2.631379
H	0.80432	-1.367142	-2.054957
H	2.852449	1.198599	-0.389503
H	0.749676	-0.06051	2.516726
H	0.743071	-2.408403	0.737016
H	0.836606	2.332059	0.745296
H	-1.669078	2.503683	-0.850972
H	0.699184	1.32844	-1.784302

O1 (108°) Energy: -730.064318 E_h

Atom	Position Coordinates (Å)		
	X	Y	Z
B	-2.306267	0.00202	-0.040636
B	-1.339281	0.75951	-1.314289
B	-1.341434	-1.003303	-1.132273
B	-1.38994	-1.384791	0.599931
B	-1.423673	0.156642	1.487431
B	-1.3781	1.484951	0.304025
B	0.139879	-1.475167	-0.273575
B	0.084712	-0.75728	1.347705
B	0.097254	1.006965	1.163099
B	0.143612	1.386444	-0.572655
C	0.086061	-0.135484	-1.328059
C	0.921732	0.001967	0.076731
S	2.710186	-0.082665	-0.015151
H	-3.48456	0.000161	-0.102136
H	-1.873222	2.53962	0.490543
H	-1.958579	0.268377	2.533586
H	-1.896601	-2.376141	0.990377
H	-1.693514	-1.691212	-2.021323
H	0.821799	-2.385723	-0.575103
H	2.902823	1.240347	0.102007
H	0.752809	1.668739	1.885281
H	0.738169	-1.2607	2.187737
H	0.829823	2.215287	-1.049843
H	-1.687246	1.253901	-2.325501
H	0.704755	-0.228859	-2.20906

O1 (180°) Energy: -730.060695 E_h

Atom	Position Coordinates (Å)		
	X	Y	Z
B	-0.027166	-2.3076	0
B	-1.220813	-1.348573	0.888096
B	-1.220813	-1.348573	-0.888096
B	0.460222	-1.389453	-1.442525
B	1.500646	-1.406745	0
B	0.460222	-1.389453	1.442525
B	-0.427438	0.12721	-1.45233
B	1.249234	0.101204	-0.890081
B	1.249234	0.101204	0.890081
B	-0.427438	0.12721	1.45233
C	-1.329101	0.090015	0
C	0.059761	0.918474	0
S	-0.089639	2.717101	0
H	-0.081066	-3.486251	0
H	0.759699	-1.890494	2.467891
H	2.560175	-1.927466	0
H	0.759699	-1.890494	-2.467891
H	-2.178727	-1.703393	-1.474799
H	-0.821022	0.810995	-2.323021
H	1.238015	2.913728	0
H	2.03239	0.761416	1.473893
H	2.03239	0.761416	-1.473893
H	-0.821022	0.810995	2.323021
H	-2.178727	-1.703393	1.474799
H	-2.230976	0.686226	0

O1 (252°) Energy: -730.064318 E_h

Atom	Position Coordinates (Å)		
	X	Y	Z
B	2.306267	0.00202	-0.040636
B	1.341434	-1.003303	-1.132273
B	1.339281	0.75951	-1.314289
B	1.3781	1.484951	0.304025
B	1.423673	0.156642	1.487431
B	1.38994	-1.384791	0.599931
B	-0.143612	1.386444	-0.572655
B	-0.097254	1.006965	1.163099
B	-0.084712	-0.75728	1.347705
B	-0.139879	-1.475167	-0.273575
C	-0.086061	-0.135484	-1.328059
C	-0.921732	0.001967	0.076731
S	-2.710186	-0.082665	-0.015151
H	3.48456	0.000161	-0.102136
H	1.896601	-2.376141	0.990377
H	1.958579	0.268377	2.533586
H	1.873222	2.53962	0.490543
H	1.687246	1.253901	-2.325501
H	-0.829823	2.215287	-1.049843
H	-2.902823	1.240347	0.102007
H	-0.738169	-1.2607	2.187737
H	-0.752809	1.668739	1.885281
H	-0.821799	-2.385723	-0.575103
H	1.693514	-1.691212	-2.021323
H	-0.704755	-0.228859	-2.20906

O1 (324°, F) Energy: -730.060377 E_h

Atom	Position Coordinates (Å)		
	X	Y	Z
B	2.30685	0.033849	-0.027383
B	1.348304	0.036824	-1.512923
B	1.328504	1.451868	-0.443923
B	1.385301	0.882307	1.234811
B	1.421482	-0.895385	1.195553
B	1.395652	-1.419808	-0.505851
B	-0.14777	1.401038	0.53479
B	-0.088928	-0.049452	1.542483
B	-0.092666	-1.464022	0.464238
B	-0.121862	-0.902669	-1.218768
C	-0.094886	0.79469	-1.064737
C	-0.919258	-0.049581	0.053283
S	-2.718972	-0.073822	0.019126
H	3.485049	0.078135	-0.074749
H	1.904568	-2.414726	-0.884153
H	1.955341	-1.531757	2.03398
H	1.884132	1.531127	2.084568
H	1.669078	2.503683	-0.850972
H	-0.836606	2.332059	0.745296
H	-2.852449	1.198599	-0.389503
H	-0.743071	-2.408403	0.737016
H	-0.749675	-0.060511	2.516726
H	-0.80432	-1.367142	-2.054957
H	1.701203	0.148253	-2.631379
H	-0.699184	1.32844	-1.784302

9O12 (±45°) Energy: -1128.303216 E_h

Atom	Position Coordinates (Å)		
	X	Y	Z
B	0.535882	0.897152	0.003172
B	-0.902604	1.433649	-0.889713
B	-0.902743	1.435681	0.882307
B	-0.015434	0.000035	1.441041
B	0.535975	-0.897034	0.003185
B	-0.014025	0.000031	-1.437214
B	-1.77226	-0.000068	1.446071
B	-0.902593	-1.435704	0.882248
B	-0.90249	-1.433668	-0.889672
B	-1.779833	-0.000048	-1.445936
C	-2.193546	0.806423	-0.003676
C	-2.193468	-0.806438	-0.003681
H	0.590193	0.000054	-2.450789
H	0.586889	0.000075	2.456094
H	-1.059389	2.445061	1.469722
H	-2.555257	-0.000124	2.323534
H	-1.054603	-2.441755	-1.477865
H	-1.059401	-2.444977	1.469814
H	-2.558908	-0.000119	-2.326608
H	-1.054576	2.441888	-1.477674
H	-3.16217	1.284042	0.000373
H	-3.161933	-1.284378	0.000376
S	2.111133	-1.884974	-0.066359
S	2.111078	1.885012	-0.066373
H	1.928085	-2.521092	1.101578
H	1.928399	2.520681	1.101867

1O2 (±45°) Energy: -1128.239475 E_h

Atom	Position Coordinates (Å)		
	X	Y	Z
B	2.335055	0.883042	0.006139
B	0.913764	1.438384	-0.885606
B	0.904109	1.440401	0.884974
B	1.765084	-0.000011	1.443479
B	2.335052	-0.883037	0.006125
B	1.77926	0.000017	-1.434374
B	0.000667	0.000003	1.415744
B	0.904088	-1.440395	0.884941
B	0.91377	-1.438375	-0.885644
B	0.006779	0.00001	-1.418041
C	-0.409429	0.860743	-0.002616
C	-0.409434	-0.860747	-0.00264
H	2.354583	0.000047	-2.464216
H	2.330562	-0.000056	2.479187
H	0.734061	2.43911	1.487298
H	-0.78023	-0.000066	2.298465
H	0.746364	-2.436059	-1.487646
H	0.7341	-2.439103	1.487277
H	-0.771712	0.000081	-2.302012
H	0.746422	2.436074	-1.487613
H	3.322752	1.528521	0.012549
H	3.322727	-1.528551	0.012538
S	-1.969506	1.717671	-0.080274
S	-1.969479	-1.717719	-0.080256
H	-2.045457	-1.962396	1.23783
H	-2.045378	1.962987	1.237691

9O12 (±45°, M) Energy: -1128.303216 E_h

Atom	Position Coordinates (Å)		
	X	Y	Z
B	-0.535882	0.897152	0.003172
B	0.902743	1.435681	0.882307
B	0.902604	1.433649	-0.889713
B	0.014025	0.000031	-1.437214
B	-0.535975	-0.897034	0.003185
B	0.015434	0.000035	1.441041
B	1.779833	-0.000048	-1.445936
B	0.90249	-1.433668	-0.889672
B	0.902593	-1.435704	0.882248
B	1.77226	-0.000068	1.446071
C	2.193546	0.806423	-0.003676
C	2.193468	-0.806438	-0.003682
H	-0.586889	0.000075	2.456094
H	-0.590193	0.000054	-2.450789
H	1.054576	2.441888	-1.477674
H	2.558908	-0.000119	-2.326608
H	1.059401	-2.444977	1.469814
H	1.054603	-2.441755	-1.477865
H	2.555257	-0.000124	2.323534
H	1.059389	2.445061	1.469722
H	3.16217	1.284042	0.000373
H	3.161933	-1.284378	0.000376
S	-2.111133	-1.884974	-0.066359
S	-2.111078	1.885012	-0.066373
H	-1.928085	-2.521092	1.101578
H	-1.928399	2.520681	1.101867

1O2 (±45°, M) Energy: -1128.239475 E_h

Atom	Position Coordinates (Å)		
	X	Y	Z
B	-2.335055	0.883042	0.006139
B	-0.904109	1.440401	0.884974
B	-0.913764	1.438384	-0.885606
B	-1.77926	0.000017	-1.434374
B	-2.335052	-0.883037	0.006125
B	-1.765084	-0.000011	1.443479
B	-0.006779	0.00001	-1.418041
B	-0.91377	-1.438375	-0.885644
B	-0.904088	-1.440395	0.884941
B	-0.000667	0.000003	1.415744
C	0.409429	0.860743	-0.002616
C	0.409434	-0.860747	-0.00264
H	-2.330562	-0.000056	2.479187
H	-2.354583	0.000047	-2.464216
H	-0.746422	2.436074	-1.487613
H	0.771712	0.000081	-2.302012
H	-0.7341	-2.439103	1.487277
H	-0.746364	-2.436059	-1.487646
H	0.78023	-0.000066	2.298465
H	-0.734061	2.43911	1.487298
H	-3.322752	1.528521	0.012549
H	-3.322727	-1.528551	0.012538
S	1.969506	1.717672	-0.080274
S	1.969479	-1.717719	-0.080256
H	2.045457	-1.962396	1.23783
H	2.045377	1.962988	1.237691

II.F. References

(1) Whitesides, G. M.; Grzybowski, B. Self-Assembly at All Scales. *Science* **2002**, *295*, 2418–2421.

(2) Smith, R. K.; Lewis, P. A.; Weiss, P. S. Patterning Self-Assembled Monolayers. *Prog. Surf. Sci.* **2004**, *75*, 1–68.

(3) Love, J. C.; Estroff, L. A.; Kriebel, J. K.; Nuzzo, R. G.; Whitesides, G. M. Self-Assembled Monolayers of Thiolates on Metals as a Form of Nanotechnology. *Chem. Rev.* **2005**, *105*, 1103–1170.

(4) Claridge, S. A.; Liao, W.-S.; Thomas, J. C.; Zhao, Y.; Cao, H. H.; Cheunkar, S.; Serino, A. C.; Andrews, A. M.; Weiss, P. S. From the Bottom up: Dimensional Control and Characterization in Molecular Monolayers. *Chem. Soc. Rev.* **2013**, *42*, 2725–2745.

(5) Fersht, A. R.; Matouschek, A.; Serrano, L. The Folding of an Enzyme: I. Theory of Protein Engineering Analysis of Stability and Pathway of Protein Folding. *J. Mol. Biol.* **1992**, *224*, 771–782.

(6) Kudernac, T.; Lei, S.; Elemans, J. A. A. W.; Feyter, S. D. Two-Dimensional Supramolecular Self-Assembly: Nanoporous Networks on Surfaces. *Chem. Soc. Rev.* **2009**, *38*, 402–421.

(7) Grzelczak, M.; Vermant, J.; Furst, E. M.; Liz-Marzán, L. M. Directed Self-Assembly of Nanoparticles. *ACS Nano* **2010**, *4*, 3591–3605.

(8) Israelachvili, J. N. *Intermolecular and Surface Forces*, 3rd Edition.; Israelachvili, J. N., Ed.; Academic Press: San Diego, 2011.

(9) Lee, H. J.; Jamison, A. C.; Lee, T. R. Surface Dipoles: A Growing Body of Evidence Supports Their Impact and Importance. *Acc. Chem. Res.* **2015**, *48*, 3007–3015.

(10) Paniagua, S. A.; Hotchkiss, P. J.; Jones, S. C.; Marder, S. R.; Mudalige, A.; Marrikar, F. S.; Pemberton, J. E.; Armstrong, N. R. Phosphonic Acid Modification of Indium−Tin Oxide Electrodes: Combined XPS/UPS/Contact Angle Studies. *J. Phys. Chem. C* **2008**, *112*, 7809–7817.

(11) Bishop, K. J. M.; Wilmer, C. E.; Soh, S.; Grzybowski, B. A. Nanoscale Forces and Their Uses in Self-Assembly. *Small* **2009**, *5*, 1600–1630.

(12) Liang, H.; Sun, W.; Jin, X.; Li, H.; Li, J.; Hu, X.; Teo, B. K.; Wu, K. Two-Dimensional Molecular Porous Networks Formed by Trimesic Acid and 4,4′-Bis(4-Pyridyl)Biphenyl on Au(111) through Hierarchical Hydrogen Bonds: Structural Systematics and Control of Nanopore Size and Shape. *Angew. Chem. Int. Ed.* **2011**, *50*, 7562–7566.

(13) Kim, J.; Rim, Y. S.; Liu, Y.; Serino, A. C.; Thomas, J. C.; Chen, H.; Yang, Y.; Weiss, P. S. Interface Control in Organic Electronics Using Mixed Monolayers of Carboranethiol Isomers. *Nano Lett.* **2014**, *14*, 2946–2951.

(14) Thomas, J. C.; Schwartz, J. J.; Hohman, J. N.; Claridge, S. A.; Auluck, H. S.; Serino, A. C.; Spokoyny, A. M.; Tran, G.; Kelly, K. F.; Mirkin, C. A.; Gilles, J.; Osher, S. J.; Weiss, P. S. Defect-Tolerant Aligned Dipoles within Two-Dimensional Plastic Lattices. *ACS Nano* **2015**, *9*, 4734–4742.

(15) Kulkarni, C.; Bejagam, K. K.; Senanayak, S. P.; Narayan, K. S.; Balasubramanian, S.; George, S. J. Dipole-Moment-Driven Cooperative Supramolecular Polymerization. *J. Am. Chem. Soc.* **2015**, *137*, 3924–3932.

(16) Lewis, P. A.; Smith, R. K.; Kelly, K. F.; Bumm, L. A.; Reed, S. M.; Clegg, R. S.; Gunderson, J. D.; Hutchison, J. E.; Weiss, P. S. The Role of Buried Hydrogen Bonds in Self-Assembled Mixed Composition Thiols on Au{111}. *J. Phys. Chem. B* **2001**, *105*, 10630–10636.

(17) Zhang, S. Fabrication of Novel Biomaterials through Molecular Self-Assembly. *Nat. Biotechnol.* **2003**, *21*, 1171–1178.

(18) Dameron, A. A.; Charles, L. F.; Weiss, P. S. Structures and Displacement of 1-Adamantanethiol Self-Assembled Monolayers on Au{111}. *J. Am. Chem. Soc.* **2005**, *127*, 8697–8704.

(19) Barth, J. V.; Costantini, G.; Kern, K. Engineering Atomic and Molecular Nanostructures at Surfaces. *Nature* **2005**, *437*, 671–679.

(20) Aizenberg, J.; Black, A. J.; Whitesides, G. M. Oriented Growth of Calcite Controlled by Self-Assembled Monolayers of Functionalized Alkanethiols Supported on Gold and Silver. *J. Am. Chem. Soc.* **1999**, *121*, 4500–4509.

(21) Chen, S.; Liu, L.; Zhou, J.; Jiang, S. Controlling Antibody Orientation on Charged Self-Assembled Monolayers. *Langmuir* **2003**, *19*, 2859–2864.

(22) Briseno, A. L.; Aizenberg, J.; Han, Y.-J.; Penkala, R. A.; Moon, H.; Lovinger, A. J.; Kloc, C.; Bao, Z. Patterned Growth of Large Oriented Organic Semiconductor Single Crystals on Self-Assembled Monolayer Templates. *J. Am. Chem. Soc.* **2005**, *127*, 12164–12165.

(23) Hermes, S.; Schröder, F.; Chelmowski, R.; Wöll, C.; Fischer, R. A. Selective Nucleation and Growth of Metal−Organic Open Framework Thin Films on Patterned COOH/CF_3-Terminated Self-Assembled Monolayers on Au(111). *J. Am. Chem. Soc.* **2005**, *127*, 13744–13745.

(24) Lee, C.-Y.; Gong, P.; Harbers, G. M.; Grainger, D. W.; Castner, D. G.; Gamble, L. J. Surface Coverage and Structure of Mixed DNA/Alkylthiol Monolayers on Gold: Characterization by XPS, NEXAFS, and Fluorescence Intensity Measurements. *Anal. Chem.* **2006**, *78*, 3316–3325.

(25) Scherb, C.; Schödel, A.; Bein, T. Directing the Structure of Metal–Organic Frameworks by Oriented Surface Growth on an Organic Monolayer. *Angew. Chem.* **2008**, *120*, 5861–5863.

(26) Yao, Y.; Dong, H.; Hu, W. Ordering of Conjugated Polymer Molecules: Recent Advances and Perspectives. *Polym. Chem.* **2013**, *4*, 5197–5205.

(27) Palma, C.-A.; Cecchini, M.; Samorì, P. Predicting Self-Assembly: From Empirism to Determinism. *Chem. Soc. Rev.* **2012**, *41*, 3713–3730.

(28) Roussel, T. J.; Barrena, E.; Ocal, C.; Faraudo, J. Predicting Supramolecular Self-Assembly on Reconstructed Metal Surfaces. *Nanoscale* **2014**, *6*, 7991–8001.

(29) Meier, G.; Sackmann, E.; Grabmaier, J. G. *Applications of Liquid Crystals*; Springer-Verlag: Berlin, 1975.

(30) Gelbart, W. M. Molecular Theory of Nematic Liquid Crystals. *J. Phys. Chem.* **1982**, *86*, 4298–4307.

(31) Jerome, B. Surface Effects and Anchoring in Liquid Crystals. *Rep. Prog. Phys.* **1991**, *54*, 391.

(32) Lee, K.-W.; Paek, S.-H.; Lien, A.; Durning, C.; Fukuro, H. Microscopic Molecular Reorientation of Alignment Layer Polymer Surfaces Induced by Rubbing and Its Effects on LC Pretilt Angles. *Macromolecules* **1996**, *29*, 8894–8899.

(33) Stöhr, J.; Samant, M. G. Liquid Crystal Alignment by Rubbed Polymer Surfaces: A Microscopic Bond Orientation Model. *J. Electron Spectrosc. Relat. Phenom.* **1999**, *98–99*, 189–207.

(34) Janning, J. L. Thin Film Surface Orientation for Liquid Crystals. *Appl. Phys. Lett.* **1972**, *21*, 173–174.

(35) Ichimura, K. Photoalignment of Liquid-Crystal Systems. *Chem. Rev.* **2000**, *100*, 1847–1874.

(36) O'Neill, M.; Kelly, S. M. Photoinduced Surface Alignment for Liquid Crystal Displays. *J. Phys. D: Appl. Phys.* **2000**, *33*, R67.

(37) Skaife, J. J.; Abbott, N. L. Quantitative Characterization of Obliquely Deposited Substrates of Gold by Atomic Force Microscopy: Influence of Substrate Topography on Anchoring of Liquid Crystals. *Chem. Mater.* **1999**, *11*, 612–623.

(38) Wilderbeek, H. T. A.; van der Meer, F. J. A.; Feldman, K.; Broer, D. J.; Bastiaansen, C. W. M. Alignment of Liquid Crystals on Self-Assembled Monolayers Using Ultra-Thin Gold Films. *Adv. Mater.* **2002**, *14*, 655–658.

(39) Berreman, D. W. Solid Surface Shape and the Alignment of an Adjacent Nematic Liquid Crystal. *Phys. Rev. Lett.* **1972**, *28*, 1683–1686.

(40) Abelmann, L.; Lodder, C. Oblique Evaporation and Surface Diffusion. *Thin Solid Films* **1997**, *305*, 1–21.

(41) Follonier, S.; Miller, W. J. W.; Abbott, N. L.; Knoesen, A. Characterization of the Molecular Orientation of Self-Assembled Monolayers of Alkanethiols on Obliquely Deposited Gold Films by Using Infrared–Visible Sum-Frequency Spectroscopy. *Langmuir* **2003**, *19*, 10501–10509.

(42) Hoogboom, J.; Rasing, T.; Rowan, A. E.; Nolte, R. J. M. LCD Alignment Layers. Controlling Nematic Domain Properties. *J. Mater. Chem.* **2006**, *16*, 1305–1314.

(43) Drawhorn, R. A.; Abbott, N. L. Anchoring of Nematic Liquid Crystals on Self-Assembled Monolayers Formed from Alkanethiols on Semitransparent Films of Gold. *J. Phys. Chem.* **1995**, *99*, 16511–16515.

(44) Evans, S. D.; Allinson, H.; Boden, N.; Henderson, J. R. Surface-Field Induced Organisation at Solid/Fluid Interfaces. *Faraday Discuss.* **1996**, *104*, 37–48.

(45) Gupta, V. K.; Abbott, N. L. Uniform Anchoring of Nematic Liquid Crystals on Self-Assembled Monolayers Formed from Alkanethiols on Obliquely Deposited Films of Gold. *Langmuir* **1996**, *12*, 2587–2593.

(46) Gupta, V. K.; Abbott, N. L. Azimuthal Anchoring Transition on Nematic Liquid Crystals on Self-Assembled Monolayers Formed from Odd and Even Alkanethiols. *Phys. Rev. E* **1996**, *54*, R4540–R4543.

(47) Gupta, V. K.; Abbott, N. L. Design of Surfaces for Patterned Alignment of Liquid Crystals on Planar and Curved Substrates. *Science* **1997**, *276*, 1533–1536.

(48) Alkhairalla, B.; Allinson, H.; Boden, N.; Evans, S. D.; Henderson, J. R. Anchoring and Orientational Wetting of Nematic Liquid Crystals on Self-Assembled Monolayer Substrates: An Evanescent Wave Ellipsometric Study. *Phys. Rev. E* **1999**, *59*, 3033–3039.

(49) Carlton, R. J.; Hunter, J. T.; Miller, D. S.; Abbasi, R.; Mushenheim, P. C.; Tan, L. N.; Abbott, N. L. Chemical and Biological Sensing Using Liquid Crystals. *Liq. Cryst. Rev.* **2013**, *1*, 29–51.

(50) Bramble, J. P.; Evans, S. D.; Henderson, J. R.; Anquetil, C.; Cleaver, D. J.; Smith, N. J. Nematic Liquid Crystal Alignment on Chemical Patterns. *Liq. Cryst.* **2007**, *34*, 1059–1069.

(51) Critchley, K.; Cheadle, E. M.; Zhang, H.-L.; Baldwin, K. J.; Liu, Q.; Cheng, Y.; Fukushima, H.; Tamaki, T.; Batchelder, D. N.; Bushby, R. J.; Evans, S. D. Surface Plasmon Raman Scattering Studies of Liquid Crystal Anchoring on Liquid-Crystal-Based Self-Assembled Monolayers. *J. Phys. Chem. B* **2009**, *113*, 15550–15557.

(52) Yoon, H.; Kang, S.-W.; Lehmann, M.; Park, J. O.; Srinivasarao, M.; Kumar, S. Homogeneous and Homeotropic Alignment of Bent-Core Uniaxial and Biaxial Nematic Liquid Crystals. *Soft Matter* **2011**, *7*, 8770–8775.

(53) Crawford, G. P.; Ondris-Crawford, R. J.; Doane, J. W.; Zumer, S. Systematic Study of Orientational Wetting and Anchoring at a Liquid-Crystal-Surfactant Interface. *Phys. Rev. E* **1996**, *53*, 3647–3661.

(54) Tao, F.; Bernasek, S. L. Understanding Odd−Even Effects in Organic Self-Assembled Monolayers. *Chem. Rev.* **2007**, *107*, 1408–1453.

(55) Nakata, M.; Zanchetta, G.; Buscaglia, M.; Bellini, T.; Clark, N. A. Liquid Crystal Alignment on a Chiral Surface: Interfacial Interaction with Sheared DNA Films. *Langmuir* **2008**, *24*, 10390–10394.

(56) Bai, Y.; Abbott, N. L. Enantiomeric Interactions between Liquid Crystals and Organized Monolayers of Tyrosine-Containing Dipeptides. *J. Am. Chem. Soc.* **2012**, *134*, 548–558.

(57) Bai, Y.; Abbasi, R.; Wang, C.; Abbott, N. L. Liquid Crystals Anchored on Mixed Monolayers of Chiral versus Achiral Molecules: Continuous Change in Orientation as a Function of Enantiomeric Excess. *Angew. Chem. Int. Ed.* **2014**, *53*, 8079–8083.

(58) Grimes, R. N. *Carboranes*, 2nd Edition.; Academic Press: Oxford, 2011.

(59) Kaszynski, P.; G. Douglass, A. Organic Derivatives of Closo-Boranes: A New Class of Liquid Crystal Materials. *J. Organomet. Chem.* **1999**, *581*, 28–38.

(60) Hohman, J. N.; Zhang, P.; Morin, E. I.; Han, P.; Kim, M.; Kurland, A. R.; McClanahan, P. D.; Balema, V. P.; Weiss, P. S. Self-Assembly of Carboranethiol Isomers on Au{111}: Intermolecular Interactions Determined by Molecular Dipole Orientations. *ACS Nano* **2009**, *3*, 527–536.

(61) Hohman, J. N.; Claridge, S. A.; Kim, M.; Weiss, P. S. Cage Molecules for Self-Assembly. *Mater. Sci. Eng., R* **2010**, *70*, 188–208.

(62) Cioran, A. M.; Musteti, A. D.; Teixidor, F.; Krpetić, Ž.; Prior, I. A.; He, Q.; Kiely, C. J.; Brust, M.; Viñas, C. Mercaptocarborane-Capped Gold Nanoparticles: Electron Pools and Ion Traps with Switchable Hydrophilicity. *J. Am. Chem. Soc.* **2012**, *134*, 212–221.

(63) Kabytaev, K. Z.; Everett, T. A.; Safronov, A. V.; Sevryugina, Y. V.; Jalisatgi, S. S.; Hawthorne, M. F. B-Mercaptocarboranes: A New Synthetic Route. *Eur. J. Inorg. Chem.* **2013**, *2013*, 2488–2491.

(64) Thomas, J. C.; Goronzy, D. P.; Serino, A. C.; Auluck, H. S.; Irving, O. R.; Jimenez-Izal, E.; Deirmenjian, J. M.; Macháček, J.; Sautet, P.; Alexandrova, A. N.; Baše, T.; Weiss, P. S. Acid-Base Control of Valency within Carboranedithiol Self-Assembled Monolayers: Molecules Do the Can-Can. *ACS Nano* **2018**, *12*, 2211–2221.

(65) Kristiansen, K.; Stock, P.; Baimpos, T.; Raman, S.; Harada, J. K.; Israelachvili, J. N.; Valtiner, M. Influence of Molecular Dipole Orientations on Long-Range Exponential Interaction Forces at Hydrophobic Contacts in Aqueous Solutions. *ACS Nano* **2014**, *8*, 10870–10877.

(66) Dey, S.; Pal, A. J. Layer-by-Layer Electrostatic Assembly with a Control over Orientation of Molecules: Anisotropy of Electrical Conductivity and Dielectric Properties. *Langmuir* **2011**, *27*, 8687–8693.

(67) Brennan, T. P.; Tanskanen, J. T.; Bakke, J. R.; Nguyen, W. H.; Nordlund, D.; Toney, M. F.; McGehee, M. D.; Sellinger, A.; Bent, S. F. Dynamical Orientation of Large Molecules on Oxide Surfaces and Its Implications for Dye-Sensitized Solar Cells. *Chem. Mater.* **2013**, *25*, 4354–4363.

(68) Breuer, T.; Witte, G. Controlling Nanostructures by Templated Templates: Inheriting Molecular Orientation in Binary Heterostructures. *ACS Appl. Mater. Interfaces* **2015**, *7*, 20485–20492.

(69) Pang, S. H.; Medlin, J. W. Controlling Catalytic Selectivity *via* Adsorbate Orientation on the Surface: From Furfural Deoxygenation to Reactions of Epoxides. *J. Phys. Chem. Lett.* **2015**, *6*, 1348–1356.

(70) Arrows Illustrating Dipole Moments Point from Regions of Relative Negative to Positive Charge within the Molecule.

(71) Baše, T.; Bastl, Z.; Šlouf, M.; Klementová, M.; Šubrt, J.; Vetushka, A.; Ledinský, M.; Fejfar, A.; Macháček, J.; Carr, M. J.; Londesborough, M. G. S. Gold Micrometer Crystals Modified with Carboranethiol Derivatives. *J. Phys. Chem. C* **2008**, *112*, 14446–14455.

(72) Lübben, J. F.; Baše, T.; Rupper, P.; Künniger, T.; Macháček, J.; Guimond, S. Tuning the Surface Potential of Ag Surfaces by Chemisorption of Oppositely-Oriented Thiolated Carborane Dipoles. *J. Colloid Interface Sci.* **2011**, *354*, 168–174.

(73) Kunkel, D. A.; Hooper, J.; Simpson, S.; Miller, D. P.; Routaboul, L.; Braunstein, P.; Doudin, B.; Beniwal, S.; Dowben, P.; Skomski, R.; Zurek, E.; Enders, A. Self-Assembly of Strongly Dipolar Molecules on Metal Surfaces. *J. Chem. Phys.* **2015**, *142*, 101921.

(74) Mauguin, C. Sur Les Cristaux Liquides de Lehman. *Bull. Soc. Fr. Miner.* **1911**, *34*, 71–117.

(75) Fréedericksz, V.; Zolina, V. Forces Causing the Orientation of an Anisotropic Liquid. *Trans. Faraday Soc.* **1933**, *29*, 919–930.

(76) de Jeu, W. H. *Physical Properties of Liquid Crystalline Materials*; Gordon and Breach: New York, 1980.

(77) Fonseca, J. G.; Galerne, Y. Simple Method for Measuring the Azimuthal Anchoring Strength of Nematic Liquid Crystals. *Appl. Phys. Lett.* **2001**, *79*, 2910–2912.

(78) Clare, B. H.; Guzmán, O.; de Pablo, J. J.; Abbott, N. L. Measurement of the Azimuthal Anchoring Energy of Liquid Crystals in Contact with Oligo(Ethylene Glycol)-Terminated Self-Assembled Monolayers Supported on Obliquely Deposited Gold Films. *Langmuir* **2006**, *22*, 4654–4659.

(79) Sørensen, B. E. A Revised Michel-Lévy Interference Colour Chart Based on First-Principles Calculations. *Eur. J. Mineral.* **2013**, *25*, 5–10.

(80) Lowe, A. M.; Ozer, B. H.; Bai, Y.; Bertics, P. J.; Abbott, N. L. Design of Surfaces for Liquid Crystal-Based Bioanalytical Assays. *ACS Appl. Mater. Interfaces* **2010**, *2*, 722–731.

(81) Fukuda, J.; Yoneya, M.; Yokoyama, H. Consistent Numerical Evaluation of the Anchoring Energy of a Grooved Surface. *Phys. Rev. E* **2009**, *79*, 011705.

(82) Choi, Y.; Yokoyama, H.; Gwag, J. S. Determination of Surface Nematic Liquid Crystal Anchoring Strength Using Nano-Scale Surface Grooves. *Opt. Express* **2013**, *21*, 12135–12144.

(83) Faetti, S.; Marianelli, P. Strong Azimuthal Anchoring Energy at a Nematic-Polyimide Interface. *Phys. Rev. E* **2005**, *72*, 051708.

(84) Anchoring Energies Depend on a Variety of Factors. When Comparing Values from Such Dissimilar Surfaces, One Should Acknowledge the Significant Influence of Textural and Chemical Differences in Determining Anchoring Strengths.

(85) Skaife, J. J.; Brake, J. M.; Abbott, N. L. Influence of Nanometer-Scale Topography of Surfaces on the Orientational Response of Liquid Crystals to Proteins Specifically Bound to Surface-Immobilized Receptors. *Langmuir* **2001**, *17*, 5448–5457.

(86) Clare, B. H.; Guzmán, O.; de Pablo, J.; Abbott, N. L. Anchoring Energies of Liquid Crystals Measured on Surfaces Presenting Oligopeptides. *Langmuir* **2006**, *22*, 7776–7782.

(87) Otiti, T.; Niklasson, G. A.; Svedlindh, P.; Granqvist, C. G. Anisotropic Optical, Magnetic, and Electrical Properties of Obliquely Evaporated Ni Films. *Thin Solid Films* **1997**, *307*, 245–249.

(88) Everitt, D. L.; Miller, W. J. W.; Abbott, N. L.; Zhu, X. D. Evolution of a Preferred Orientation of Polycrystalline Grains in Obliquely Deposited Gold Films on an Amorphous Substrate. *Phys. Rev. B* **2000**, *62*, R4833–R4836.

(89) Jang, J. H.; Jacob, J.; Santos, G.; Lee, T. R.; Baldelli, S. Image Contrast in Sum Frequency Generation Microscopy Based on Monolayer Order and Coverage. *J. Phys. Chem. C* **2013**, *117*, 15192–15202.

(90) Smith, H. D.; Obenland, C. O.; Papetti, S. A New Series of Organoboranes. IX. The Preparation and Some Reactions of Sulfur-Carborane Derivatives. *Inorg. Chem.* **1966**, *5*, 1013–1015.

(91) Plešek, J.; Janoušek, Z.; Heřmánek, S. Synthesis and Properties of Some Icosahedral Carborane B,B'-Dithiols. *Collect. Czechoslov. Chem. Commun.* **1980**, *45*, 1775–1779.

(92) Spokoyny, A. M.; Machan, C. W.; Clingerman, D. J.; Rosen, M. S.; Wiester, M. J.; Kennedy, R. D.; Stern, C. L.; Sarjeant, A. A.; Mirkin, C. A. A Coordination Chemistry Dichotomy for Icosahedral Carborane-Based Ligands. *Nat. Chem.* **2011**, *3*, 590–596.

(93) Schwartz, J. J.; Hohman, J. N.; Morin, E. I.; Weiss, P. S. Molecular Flux Dependence of Chemical Patterning by Microcontact Printing. *ACS Appl. Mater. Interfaces* **2013**, *5*, 10310–10316.

(94) Goerigk, L.; Grimme, S. A Thorough Benchmark of Density Functional Methods for General Main Group Thermochemistry, Kinetics, and Noncovalent Interactions. *Phys. Chem. Chem. Phys.* **2011**, *13*, 6670–6688.

(95) Hickey, A. L.; Rowley, C. N. Benchmarking Quantum Chemical Methods for the Calculation of Molecular Dipole Moments and Polarizabilities. *J. Phys. Chem. A* **2014**, *118*, 3678–3687.

(96) Toyooka, T.; Chen, G.; Takezoe, H.; Fukuda, A. Determination of Twist Elastic Constant K22 in 5CB by Four Independent Light-Scattering Techniques. *Jpn. J. Appl. Phys.* **1987**, *26*, 1959.

(97) Belyaev, B. A.; Drokin, N. A.; Shabanov, V. F.; Shepov, V. N. Dielectric Anisotropy of 5CB Liquid Crystal in a Decimeter Wavelength Range. *Phys. Solid State* **2000**, *42*, 577–579.

(98) Li, J.; Wen, C.-H.; Gauza, S.; Lu, R.; Wu, S.-T. Refractive Indices of Liquid Crystals for Display Applications. *J. Disp. Technol.* **2005**, *1*, 51–61.

(99) Maurel, P.; Price, A. H. Dipole Moment of N-(p-Methoxybenzylidene)-p-Butylaniline. *J. Chem. Soc., Faraday Trans. 2* **1973**, *69*, 1486–1490.

CHAPTER III

Slippery Liquid-Infused Porous Surfaces for Rapid Cell Deformation Devices and Cargo Delivery

The information in this chapter is in preparation for publication

Authors: Alexandra M. Mendoza, Tzu T. Chiou, Isaura M. Frost, Natcha Wattanatorn, Thomas D. Young, Philseok Kim, Joanna Aizenberg, Satiro N. De Oliveira, Paul S. Weiss, and Steve J. Jonas

III.A. Introduction

Efficient, rapid, and inexpensive techniques that can deliver biomolecular cargo into cells is important for enabling gene therapies to treat a wide range of diseases from cancer[1–9] to monogenetic disorders, such as severe combined immunodeficiency,[10–14] sickle cell,[15,16] hemophilias,[3,17,18] retinal diseases,[19,20] and Duchenne muscular dystropy.[21,22] The promise of applying newly developed gene editing methods, such as clustered regularly interspaced short palindromic repeats (CRISPR),[19,21,23–28] chimeric antigen receptors (CARs),[2,3,23,29–34] transcription activator-like effector nucleases (TALEN),[18,23,28,35–37] and zinc fingers nucleases (ZFNs),[15,28,35,38–40] to treat these debilitating diseases is offering new hope to the field. Current methods to treat cancer rely on chemotherapy, radiation, or surgery, which is invasive and not always successful.[1,32,33,41–43] Engineered T cells have emerged as a potential alternative that can be used in conjunction with or when these cancer treatments fail, where the genetically modified CAR T cells recruit the immune system to recognize tumor antigens to clear the malignant cells from the body.[2,3,23,29–34] As well, gene editing of hematopoietic stem cells (HSCs) has shown promise, where a single point mutations or larger defects can be corrected with a patient's own cells *via* a bone marrow transplant, instead of relying on a matched donor.[11,13–16,44,45] Presently, the only treatment for these rare, monogenetic diseases is a bone marrow transplant, which, if a suitable donor can be found, is often met with graft-versus-host-disease or graft rejection.[3,15,41,46] The option to perform autologous gene-modified stem cell therapies circumvents these issues and broadens the scope of pathologies that can be treated *via* gene therapy.[3,15,41]

Existing methods used to deliver gene editing materials into cells rely primarily on viral vectors[47–52] or non-viral methods, such as electroporation.[24,35,45,53–56] Although there

has been some success with viral vectors,[14,57,58] their general use for a variety of disease treatments is laborious and would need to go through separate Food and Drug Administration approvals, limiting their universal application.[3,12,51,54] Additionally, viral vectors are exceptionally expensive and suffer from off-target effects, concerns of immunogenicity, and cell toxicities.[12,51,54,59,60] Similarly, electroporation is expensive at clinically relevant scales, is toxic to cells, and has a low throughput and transfection efficiency. Lipofection, another common non-viral technique, has variable transfection efficiency, low cell viability, and is expensive.[36,56,61–65] Other non-viral transfection methods, such as nanoparticles,[66–68] sonoporation,[56,69–71] and microinjection,[64,72–74] have been reported but generally suffer from low throughput, high cost, low viability, low transfection efficiency, or some combination of the above.[3,65,75,76] For emerging cellular therapies to have the most impact, a suitable delivery system needs to be developed that can address these present limitations.[3,65]

An interesting alternative to these viral and non-viral delivery methods is to mechanically deform cells *via* a rapid cell deformation platform, first developed by Langer and coworkers (Figure III.1A).[65,77–83] This system circumvents several of the disadvantages of the current state of the art techniques.[65,77–83] Using microfluidics enables a potentially high throughput system, while maintain high viability and transfection efficiency.[65,77–83] Additionally, the channel constriction size can be easily tuned to fit the need for a variety of cell diameters, generating a versatile system.[65,77–83] However, the materials used in the fabrication of these microfluidic devices are prone to cellular buildup (Figure III.1B and III.1C),[77] rendering them inefficient for sustainable cell processing. Moreover, these devices require expertise photolithography and microfluidic design skills.[65,77–83]

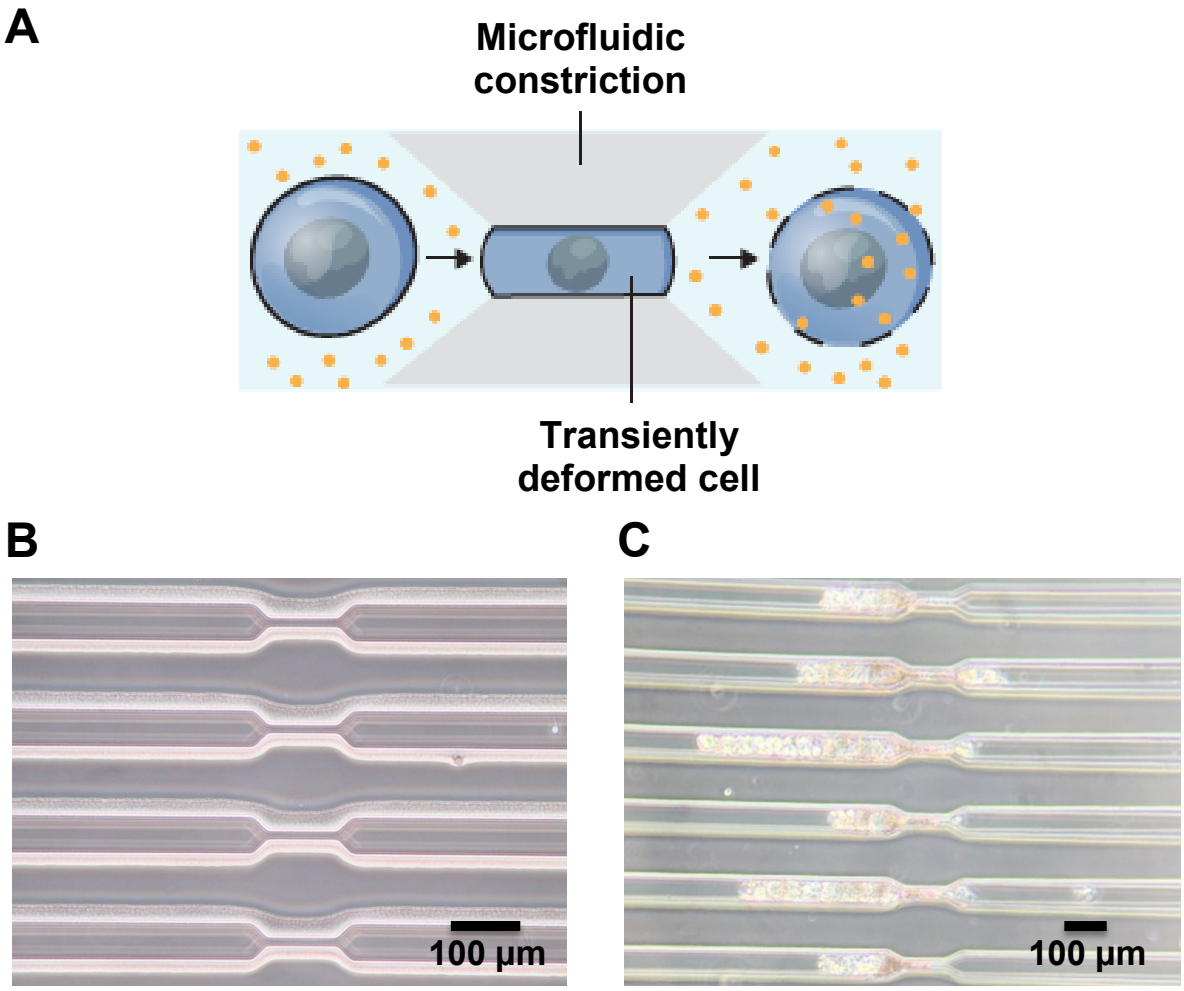

Figure III.1. (A) Rapid cell deformation schematic. As cells are flowed through a narrow constriction, transient pores form for ~5 min, enabling biomolecular cargo to be delivered *via* diffusion across the cell membrane. Adapted with permission from Reference 80. Copyright 2017 Nature. (B) Poly(dimethylsiloxane) (PDMS) channels before and (C) after flowing with K562 cells. The PDMS microfluidic devices clog within several minutes.

Herein, we have developed a method for coating pores, 5 – 8 μm in diameter, of commercial syringe filters and cell culture inserts with slippery liquid-infused porous surfaces (SLIPS), first developed by Aizenberg and coworkers (Figure III.2).[84–90] These bioinspired surface chemistries enable rapid transport of biomolecular payloads (*e.g.,* DNA/RNA, proteins) into target cells *via* transient permeabilization that occurs as cells pass through the narrow channels and avoid biofouling issues that have precluded existing examples of this technology. Commercial poly(tetrafluoroethylene) (PTFE) syringe filters and poly(ethylene terephthalate) (PET) cell culture inserts were infused with fluorinated or non-fluorinated oils, respectively, to establish a SLIPS interface (Figure III.2).[84–90] These porous filters infused with oil are a straightforward and easy to use alternative strategy to rapidly deform cells in a scalable, facile, and economical manner.

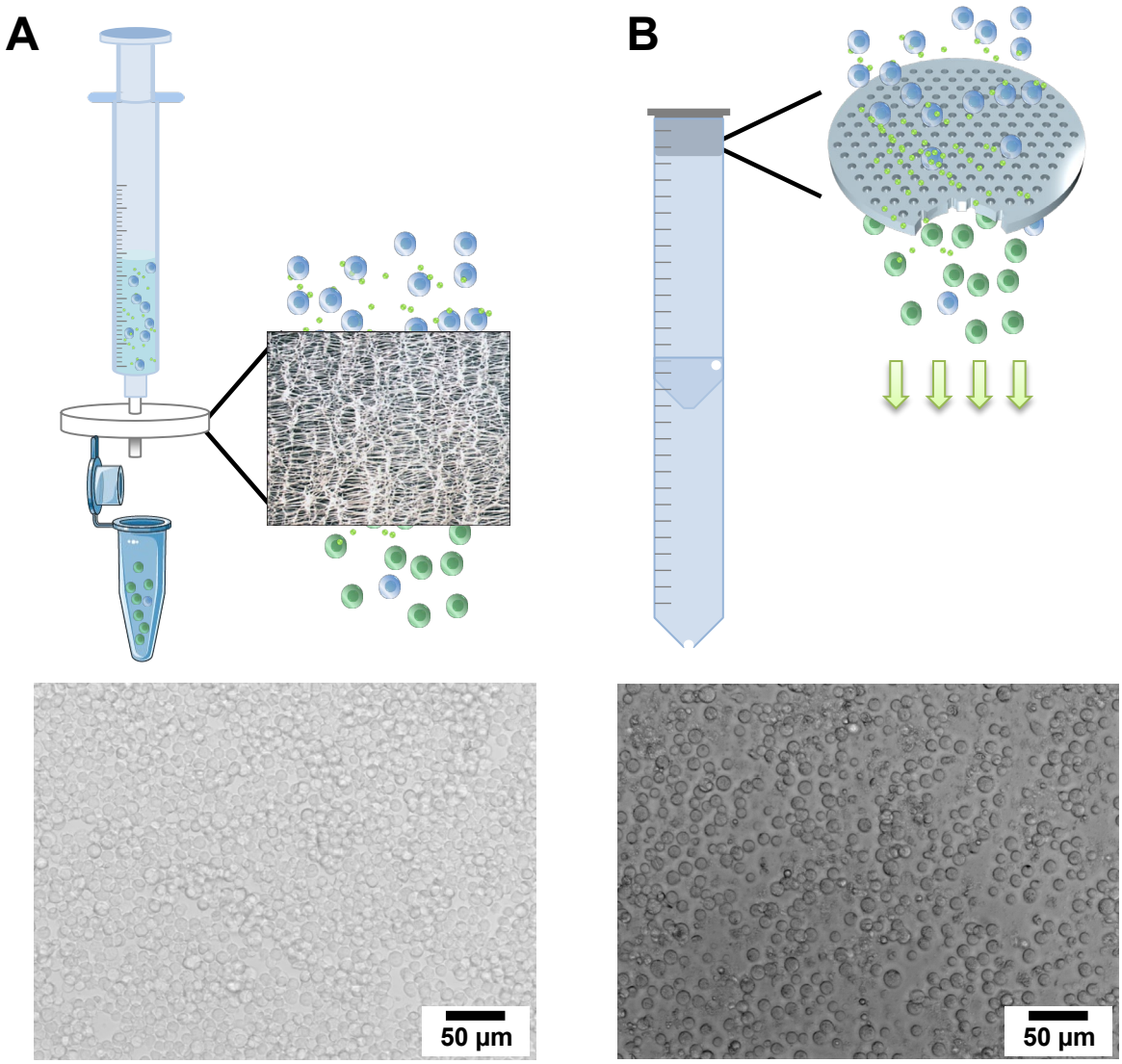

Figure III.2. Schematic showing the experimental procedures of a (A) slippery liquid-infused porous surfaces (SLIPS) -infused poly(tetrafluoroethylene) syringe filter. Jurkat cells are suctioned into a syringe. The syringe is connected to the syringe filter, which is either unmodified or modified with a fluorinated oil. The cells are flowed through the filter using a syringe pump (not shown) with a 0.25 mL/min flow rate and the cells are cultured for 24 – 72 h. (B) SLIPS-infused cell culture insets. Jurkat cells are vacuum filtered through a poly(ethylene terephthalate) porous culture insert membrane with 8 µm track-etched pores, using house vacuum. After permeabilized, the cells are directly incubated with a green fluorescent protein (GFP) plasmid and cultured for 24 to 72 h after transfection.

III.B. Results and Discussion

A simplistic approach to squeeze cells rapidly using commercial materials that are economical has been developed. This approach does not require expensive and time-consuming lithographic techniques or specialized materials and methods, as do current techniques, and could be performed by any user. Here, we use commercial syringe and cell culture insert filters with pores ranging from 5 to 8 μm in diameter. Both PTFE and PET filter materials were used, which were subsequently infused for at least 24 h with oil. The PTFE syringe filters were infused with a fluorinated oil, whereas the PET cell culture inserts were infused with a silicone oil in order to match the material's surface energy.[84–90] After infusing the filters with oil, air, and/or media were flowed through the filters, *via* positive or negative pressure, respectively, to establish the SLIPS interface at the pores and to remove any excess oil from the devices.

For the syringe filters, a 5 μm micromesh membrane was used (Figure III.1A). Jurkat cells were used as a model T lymphocyte line, which have an average diameter of 10 microns, making the pore sizes ~50% of the cell diameter. The cells were run through the filters at a density of two million cells per 100 μL in cell culture media (Roswell Park Memorial Institute, RPMI, media) without fetal bovine serum (FBS) at a flow rate of 0.25 mL/min using a syringe pump (Figure III.1A). A vacuum filtration system was used to rapidly deform Jurkat cells with track-etched filters with 8 μm pores (Figure III.1B). Here, two 15 mL centrifuge tubes were placed in parallel, with a hole punctured at the bottom of the lower tube and a hole on the top tube, right below where the lower tube came in contact with the upper tube (Figure III.1B). The cells were resuspended in RPMI media without FBS at a density of 4 million cells per 150 μL. Upon application of the vacuum, the cells were added to the cell

culture insert and placed on top of the upper centrifuge tube with the house vacuum already turned on. Once the culture was vacuum filtered through the device, the filter was washed with 100 μL of extra media to improve the cell recovery. The cells recovered were cultured in 10% FBS RPMI media for 24 to 72 h to monitor their growth and viability post-cell deformation. Figure III.1 (bottom images) show bright field images of the Jurkat cells at 24 h post-cell deformation after either using the syringe filter (left) or vacuum filtration system (right) with positive and negative differential pressure, respectively.

The microporous syringe filter modified with the fluorinated silicone oil was able to recover ~25% of cells inputted into the device, whereas the unmodified PTFE filter recover almost no cells (Figure III.3A). The syringe filter devices maintained relatively high viability 24 – 72 h post-deformation (Figure III.3B). Using the vacuum filtration system, with straight-through pores, we were able to recover roughly ~50% of the cells put into the SLIPS-modified device, whereas the unmodified device returned ~25% of the cells directly after the cell deformation experiment (Figure III.3C). Moreover, for the SLIPS modified vacuum filter device, the cells continued to expand and proliferate over the subsequent 72 h (Figure III.3C). The viability of the recovered cells was maintained around 80-90% for both the unmodified and SLIPS-modified filters when rapidly deformed with the vacuum-filtration system (Figure III.3D). However, for the syringe filter devices, the number of cells recovered and their proliferation was not as favorable as the vacuum filtration system (Figure III.3B), which may be due to the micromesh nature of the filter material that can trap cells inside the device (Figure III.2A).

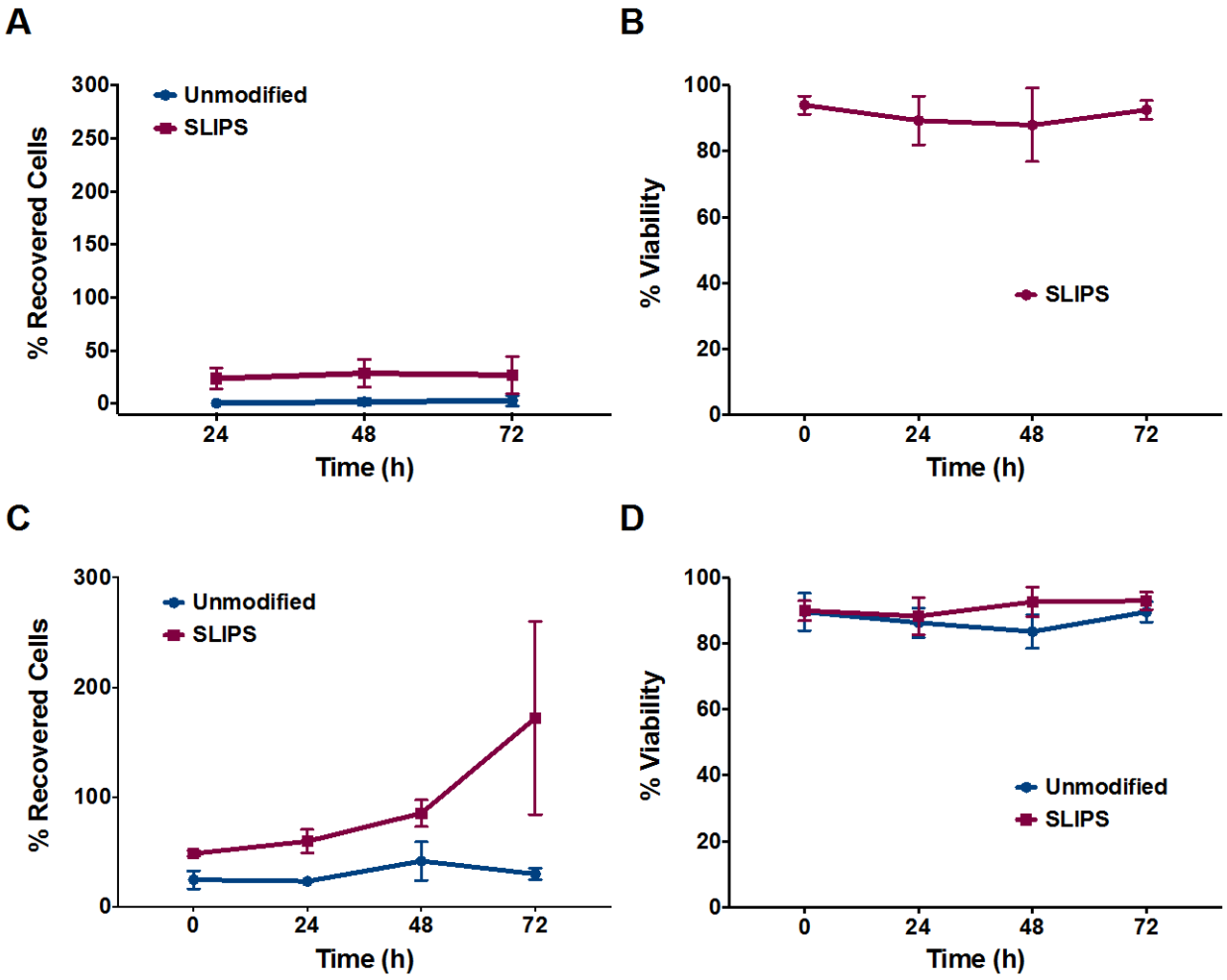

Figure III.3. (A) Cell recovery and (B) percent viability of Jurkat cells after rapid-cell deformation experiments for 5 µm poly(tetrafluoroethylene) syringe filters that were either unmodified (blue) or slippery liquid-infused porous surfaces (SLIPS) -modified (purple) with a fluorinated oil from 24 - 72 h (not enough cells were recovered to obtain accurate cell viability values for the unmodified syringe filters). (C) Cell recovery and (D) percent viability after rapid cell deformation experiments with the vacuum filtration system for 8 µm poly(ethylene terephthalate) cell culture filters, which were either unmodified (blue) or SLIPS-modified with silicone oil (purple) from 24 - 72 h. The "% Recovered Cells" is relative to the initial number of cells put into the device.

To evaluate the cargo delivery efficiency of the unmodified and SLIPS-modified vacuum filtration devices, a green fluorescent protein (GFP) plasmid was directly administered to the cells post-cell deformation at a concentration of 0.1 mg/mL. Using a fluorescence microscope, the GFP-transformed Jurkat cells were imaged 24 to 72 h post-cell deformation with the vacuum filter system using both the unmodified filter and the SLIPS-modified porous membrane (Appendix, Figure III.7 and Figure III.8). Figure III.4 shows fluorescence images of the Jurkat wild-type (Figure III.4A), the Jurkat EGFP-EGFR (enhanced GFP-epidermal growth factor receptor) cell line (Figure III.4B), and the Jurkat cells that were transfected with CMV (cytomegalovirus) -EGFP plasmid using the unmodified (Figure III.4C) and SLIPS-modified (Figure III.4D) devices at 24 h. We observed similar transfection with both devices when delivering a CMV-EGFP plasmid (~4500 bp) to the Jurkat cells (Figure III.4C and III.4D).

Subsequently, we analyzed the transfected cells *via* flow cytometry for both the unmodified and SLIPS-modified rapidly deformed cells with negative differential pressure (Figure III.5). We delivered either a CMV- (~4500 bp) (Figure III.5) or a MNDU3-EGFP (~7400 bp) (Appendix, Figure III.9) plasmid, which showed similar expression when analyzed by flow cytometry for both the unmodified and SLIPS-modified filter membranes. Figure III.5 shows flow cytometry plots for the CMV-EGFP expression for the unmodified (Figure III.5C) and SLIPS-modified (Figure III.5E) vacuum filters and their corresponding histograms at 72 h post-transfection compared to the Jurkat wild-type and Jurkat EGFP-EGFR cell line (Figures III.5D and Figure III.5F, respectively). We observed a maximum transfection efficiency of ~40% using this system (Figure III.5 and Appendix, Figure III.9). The average transfection efficiency was ~25% for both the unmodified and SLIPS-modified

devices when delivering the CMV- and MNDU3-EGFP (Figure III.6). Using a commercial electroporation kit, we observed ~80% transfection of the Jurkat cells using the CMV-EGFP plasmid (Appendix, Figure III.10), showing that in comparison, our transfection efficiency is moderate.

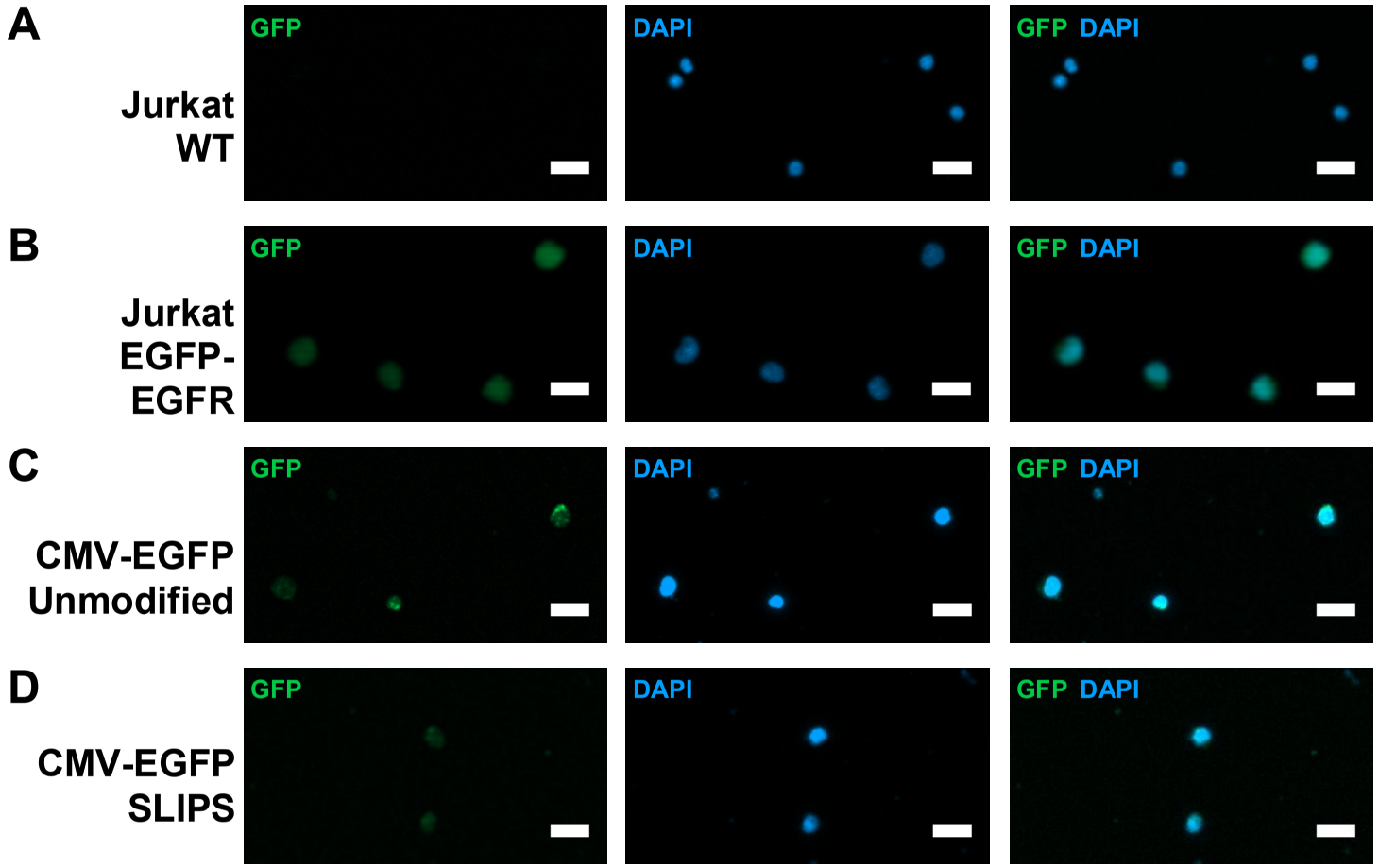

Figure III.4. Fluorescence microscope images of green fluorescent protein (GFP) (left) and DAPI (a nuclear counterstain) (middle) channels as well as their merge (right). (A) Jurkat wild-type (WT) cells, (B) Jurkat enhanced GFP (EGFP) -epidermal growth factor receptor (EGFR) cell line, and CMV (cytomegalovirus) -EGFP transfected Jurkat cells 24 h post-cell deformation using the (C) unmodified or (D) slippery liquid-infused porous surfaces (SLIPS) -modified vacuum filtration system using commercial porous culture insert membrane with 8 μm pores. Jurkat cells were incubated with 0.1 mg/mL of the CMV-EGFP plasmid. Scale bars = 20 μm.

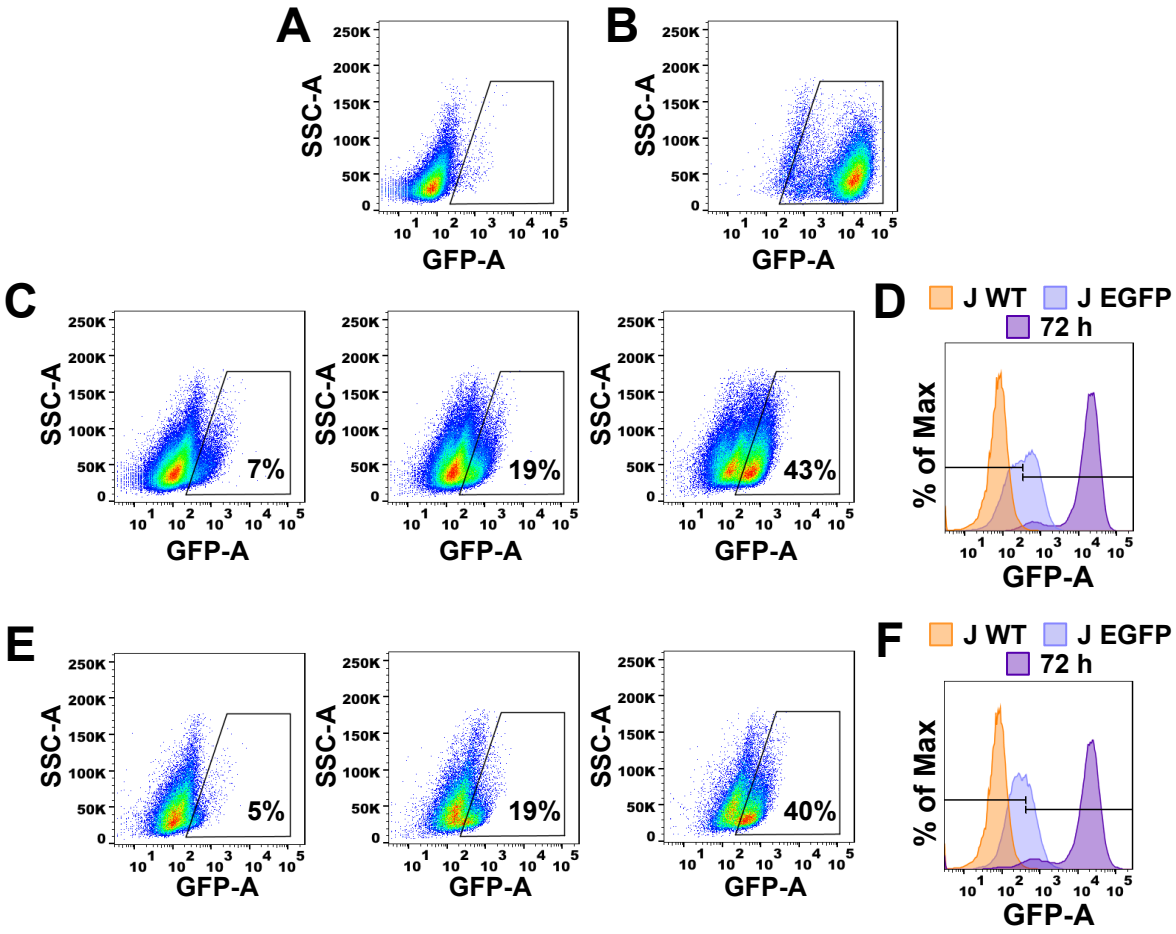

Figure III.5. Maximum green fluorescent protein (GFP) expression from Jurkat cells 24 - 72 h after transfection *via* the vacuum filtration delivery system using commercial poly(ethylene terephthalate) cell culture filters inserts with 8 µm pores. Jurkat cells were immediately exposed to a CMV (cytomegalovirus) -EGFP plasmid and analyzed *via* flow cytometry for 24-, 48-, and 72-h time points. Flow cytometry plots of (A) Jurkat wild-type, (B) Jurkat EGFP-EGFR (enhanced GFP-epidermal growth factor receptor) cell line, and CMV-EGFP transfected Jurkat cells from 24 – 72 h for (C) unmodified and (E) slippery liquid-infused porous surfaces (SLIPS) -modified filters. A histogram overlay of Jurkat wild-type, Jurkat EGFP-EGFR cell line, and CMV-EGFP transfected Jurkat cells after 72 h for (D) unmodified and (F) SLIPS-modified filters.

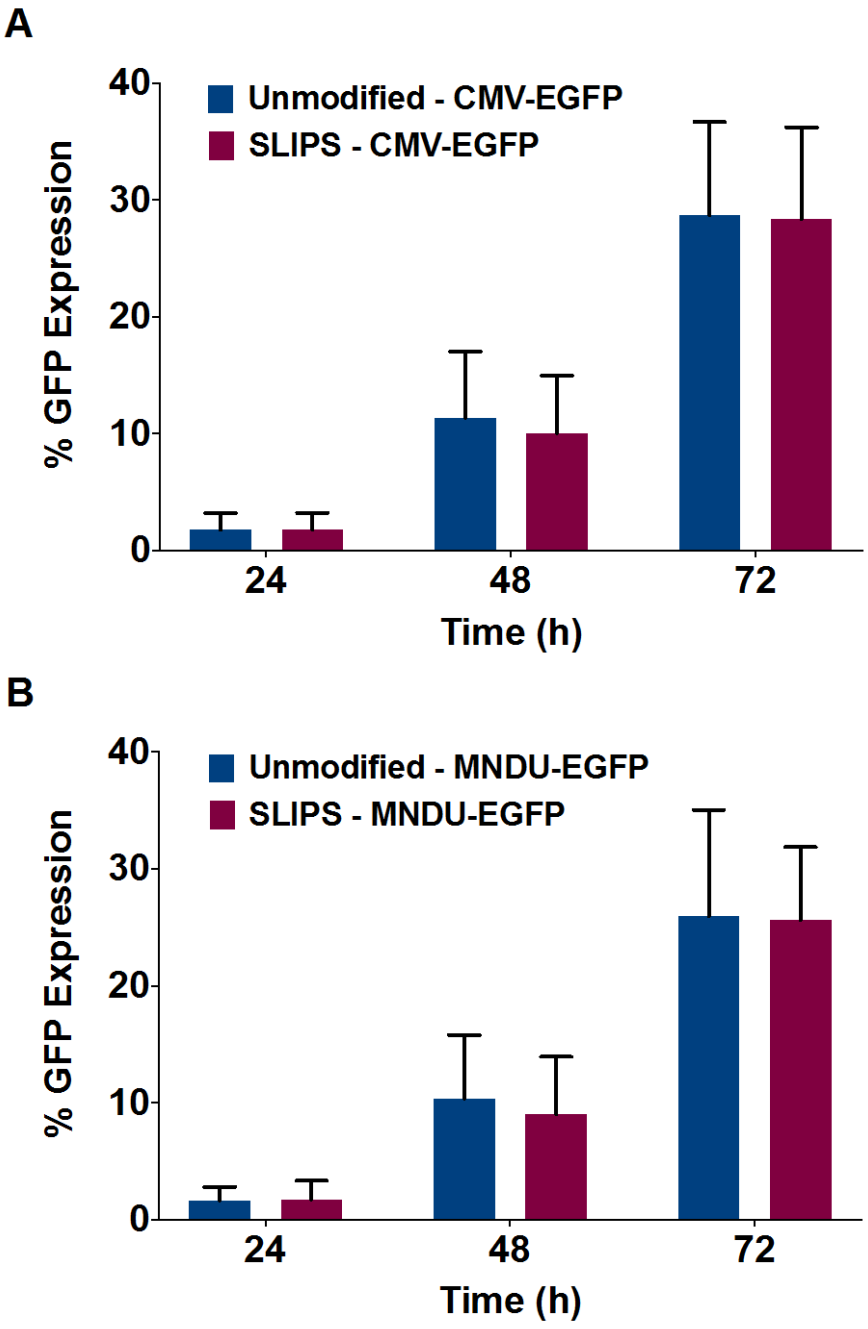

Figure III.6. Average green fluorescent protein (GFP) expression from Jurkat cells 24-72 h after transfection *via* the vacuum filtration gene delivery system using commercial poly(ethylene terephthalate) cell culture filters inserts (8 μm pore size). Jurkat cells were immediately exposed to (A) CMV- (cytomegalovirus) or (B) MNDU3-EGFP plasmids for both unmodified and slippery liquid-infused porous surfaces (SLIPS) -modified devices and analyzed *via* flow cytometry for 24-, 48-, and 72-h time points.

III.C. Conclusions and Prospects

A rapid, facile, and inexpensive platform for cargo delivery to cells has been developed and demonstrated. Here, we report a facile and economical way to deform cells rapidly in a high-throughput manner, while maintaining cell viability and proliferative capacity. Using SLIPS-modified filters, we were able to recover from 25% to 50% more cells than with unmodified filters. In particular, the vacuum filtration system offers an exciting approach, where potentially billions of cells can be deformed within a few minutes. For emerging delivery techniques to be effective, this processing scale would need to be achieved to address clinical needs for gene modification of HSCs and T cells for transplants.[91] As proof of concept, we delivered a GFP plasmid to Jurkat cells and achieved up to 40% transfection efficiency with ~80% cell viability in model T cells. In comparison to electroporation, commercial kits are able to transfect model cell lines, such as Jurkat cells, with high transfection efficiency (~80%) (Appendix, Figure III.10). The key advantage of our system is that, at a fraction of the cost, we can safely achieve moderate transfect and high cell viability. Improvements to the recovery of cells can be further optimized as well as the delivery efficiency. Likewise, more materials and pore sizes can be used with other cell lines. In particular, translating this to primary cell lines and stem cells will be an important next step to evaluating the potential of this systems.

These SLIPS-modified filter membranes offer a route to circumvent biofouling issues that have prohibited their usage for clinical applications. Additionally, the key advantage of these systems is that they are inexpensive, fast, user-friendly, and are customizable based on cell diameter. Moreover, these systems may enable a way to size select healthier and younger cells, increasing the fitness of the cells and the overall success of the transplant.[92] These

SLIPS-functionalized filters will enable new opportunities in the development of gene and cellular therapies for a wide variety of disease treatments, which are currently limited when applied at clinically relevant scales in part by toxicities and off-target effects arising from technical limitations associated with viral and non-viral transduction methods (*e.g.,* electroporation). In additions to the cost and ease of this biophysical technique, another key advantage is that this method does not suffer from immunogenicity issues that are associated with viral vectors methods, which has limited their use as a clinical treatment option.[60]

III.D. Materials and Methods

III.D.1. Jurkat Cell Culture

Jurkat cells (ATCC, Manassas, VA, USA) were cultured in Roswell Park Memorial Institute (RPMI) 1640 medium (Invitrogen, Darmstadt, Germany) containing 10% fetal bovine serum (FBS) (R10 medium) (Invitrogen, Darmstadt, Germany) and 100 IU/mL penicillin/streptomycin (Thermo Fisher Scientific, Waltham, MA, USA) in 5% CO_2 at 37 °C.

III.D.2. Vectors

Construction of the pCCL-MNDU3-EGFP (7411 bp) has been described previously.[93] The pCMV-EGFP (4479 bp) was purchased from Addgene (Plasmid #11153, Cambridge, MA, USA). The DNA plasmids were isolated from *E. coli* using PureLink™ HiPure Plasmid MaxiPrep kits (Invitrogen, Darmstadt, Germany) according to the manufacture's guidelines.

III.D.3. Slippery Liquid-Infused Porous Surfaces-Modified Filters

Syringe filters made from PVDF (Tisch Scientific, North Bend, OH, USA) with 5-micron pores were infused with Krytox GP 103 (ChemPoint, Bellevue, WA, USA) for 24 h, followed

by flowing air for 10-15 h and RPMI media directly before the rapid cell deformation studies. Falcon™ cell culture inserts with 8-micron pores (Corning, Corning, NY, USA) were infused with silicone oil, viscosity 10 cSt, (Sigma-Aldrich, Saint Louis, MO, USA) for at least 24 h. Before processing the cells through the device, the vacuum was turned on while connected to the apparatus to remove the excess oil, followed by a media rinse.

III.D.4. Transfection Methods

III.D.4.a. Syringe Filter for Rapid Cell Deformation

After the PTFE syringe filter was SLIPS-modified, Jurkat cells were flowed through the device using a syringe pump (positive pressure) (Figure III.2A). The cells were flowed through the devices at a density of two million cells per 100 µL in RPMI media without FBS at a flow rate of 0.25 mL/min. After the cells were flowed through, both media and then air were flowed through the devices to enhance the number of cells recovered. The cells were cultured in a well plate (Corning, Corning, NY, USA) at 37 ˚C for 24-72 h post-deformation, where their cell count and viability were assessed post-deformation.

III.D.4.b. Vacuum Filtration Apparatus for Rapid Cell Deformation

The vacuum filtration system was made by placing two 15 mL conical centrifuge tubes (Thermo Fisher Scientific, Waltham, MA, USA) together, where the top one was punctured right below where the bottom tube seals and the bottom tube was punctured at the bottom, which was subsequently connected to the house vacuum line (Figure III.2B). The cell culture insert was placed in the first tube with cells, at a density of four million cells per 150 µL, in RPMI media without FBS with the vacuum on (Figure III.2B). Once the Jurkat cells were rapidly deformed through the inserts, the permeabilized cells were incubated with either a CMV- or MNDU3-expressing EGFP plasmid for 10-15 min with a plasmid

concentration of 0.1 mg/mL and a 1% Pluronic F-68 (Thermo Fisher Scientific, Waltham, MA, USA) solution (Figure III.2B). After incubating the cells in plasmid, they were transferred to a well plate to maintain a density for 500-800K cells per mL for 24-72 h at 37 ˚C and subsequently characterized.

III.D.4.c. Electroporation

The Jurkat cells were resuspended in 4D-Nucleofector™ Solution (Lonza, Basel, Switzerland) at a concentration of 3.5×10^5 cells per 200 µL and combined with CMV-EGFP at a concentration of 50 µg/mL. The DNA/cell mixture was then transferred to the reaction strip. Electroporation was carried out using the Lonza 4D-Nucleofector X-unit system (Basel, Switzerland), and the cells were allowed to sit at room temperature for 10 min following the reaction. The cells were resuspended with pre-warmed medium by gently pipetting up and down two to three times. The cells were cultured in a well plate for 24 h and characterized with flow cytometry.

III.D.5. Characterization

III.D.5.a. Cell Fixing for Post-Analysis

After cells were counted, they were fixed for post-analysis with fluorescence microscopy and flow cytometry at 24-, 48-, and 72-h time points. Using a 1:1 dilution with trypan blue (Invitrogen, Darmstadt, Germany), cells were counted and their viability was accessed using the Countess™ Automated Cell Counter (Invitrogen, Darmstadt, Germany). Cells were fixed after the viability and cell counts were taken, where cells were pelleted and resuspended in phosphate-buffered saline (PBS) (Thermo Fisher Scientific, Waltham, MA, USA) with 2.5% FBS and fixation using BD stabilizing fixative (BD Biosciences, NJ, USA).

III.D.5.b. Fluorescence Microscopy Imaging

Cells were pelleted and resuspended in PBS with 2.5% FBS and fixation using BD stabilizing fixative (BD Biosciences, NJ, USA). The fixed cells were either directly mounted or mixed in a 3:1 ratio with ProLong™ Diamond Antifade Mountant with DAPI (4',6-diamidino-2-phenylindole, a nuclear counterstain) (Invitrogen, Darmstadt, Germany) onto clean microscope glass slides (VWR International, Radnor, PA, USA) and sealed with a coverslip (Fisher Scientific, Hampton, NH, USA). Images were taken with the Zeiss M2 Imager with Apotome 2 and Zen Blue software (Zeiss, Oberkochen, Germany) with the DAPI fluorescent channel (exposure time = 100 ms) and the GFP fluorescent channel (exposure time = 350 ms). Brightfield images were taken with the Zeiss AxioImager fluorescence microscope with AxioVision (Zeiss, Oberkochen, Germany). All post-analysis and image processing were done with Fiji (ImageJ).

III.D.5.c. Flow Cytometry

All flow cytometry measurement were processed by a Fortessa cytometer (BD Biosciences, NJ, USA) and data analyses performed using BD FACS Diva Software 6.1 (BD Biosciences, NJ, USA). The presence of GFP was detected through flow cytometry, where the GFP expression was assessed by washing in PBS with 2.5% FBS and fixation using BD stabilizing fixative (BD Biosciences, NJ, USA) as described previously.[94] All experiments with determinations of geometric MFI were performed using the same protocol, fluorochrome voltages, and cytometer.

III.D.6. Statistical Analysis

Statistical analysis was performed using Graph Pad Prism 6.01 (GraphPad Software, Irvine, CA, USA). All data were expressed as mean ± standard deviation (s.d.). Analysis of

variance (ANOVA) was used for multiple comparison. $P < 0.05$ was considered statistically significant.

III.E. Appendix

III.E.1. Fluorescence Microscope Images

Fluorescence microscope images for 24 – 72 h time points for delivery of CMV-EGFP plasmids to Jurkat cells with the unmodified (Figure III.7) and SLIPS-modified (Figure III.8) vacuum filtration system.

III.E.2. Flow Cytometry Plots

Figure III.9 shows flow cytometry plots for 24 – 72 h time points for delivery of MNDU-EGPF plasmids to Jurkat cells with the unmodified and SLIPS-modified (Figure III.9) vacuum filtration system.

III.E.3. Electroporation

Figure III.10 shows flow cytometry plots of electroporated Jurkat cells that were transfected with the CMV-EGFP plasmid using the Lonza 4D-Nucleofector X-unit system. After 24 h, flow cytometry plots show ~80% transfection of the Jurkat cells.

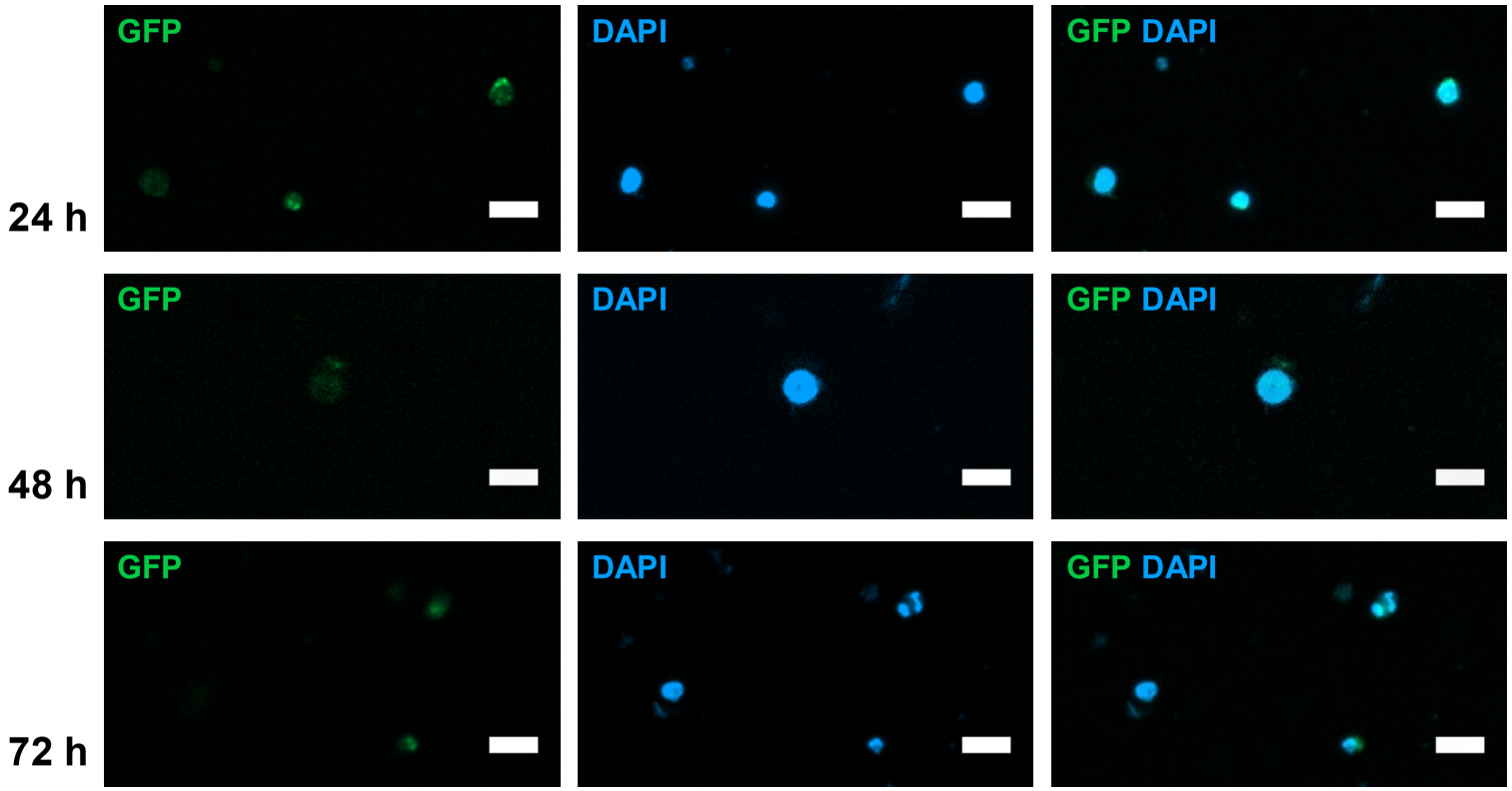

Figure III.7. Fluorescence microscope images of green fluorescent protein (GFP) (left) and DAPI (a nuclear counterstain) (middle) channels as well as their merge (right). Images of CMV (cytomegalovirus) -EGFP transfected Jurkat cells at (A) 24 h, (B) 48 h, and (C) 72 h post-cell deformation using an unmodified vacuum filtration system using commercial porous culture insert membrane with 8 μm pores. Jurkat cells were incubated with 0.1 mg/mL of the CMV-EGFP plasmid. Scale bars = 20 μm.

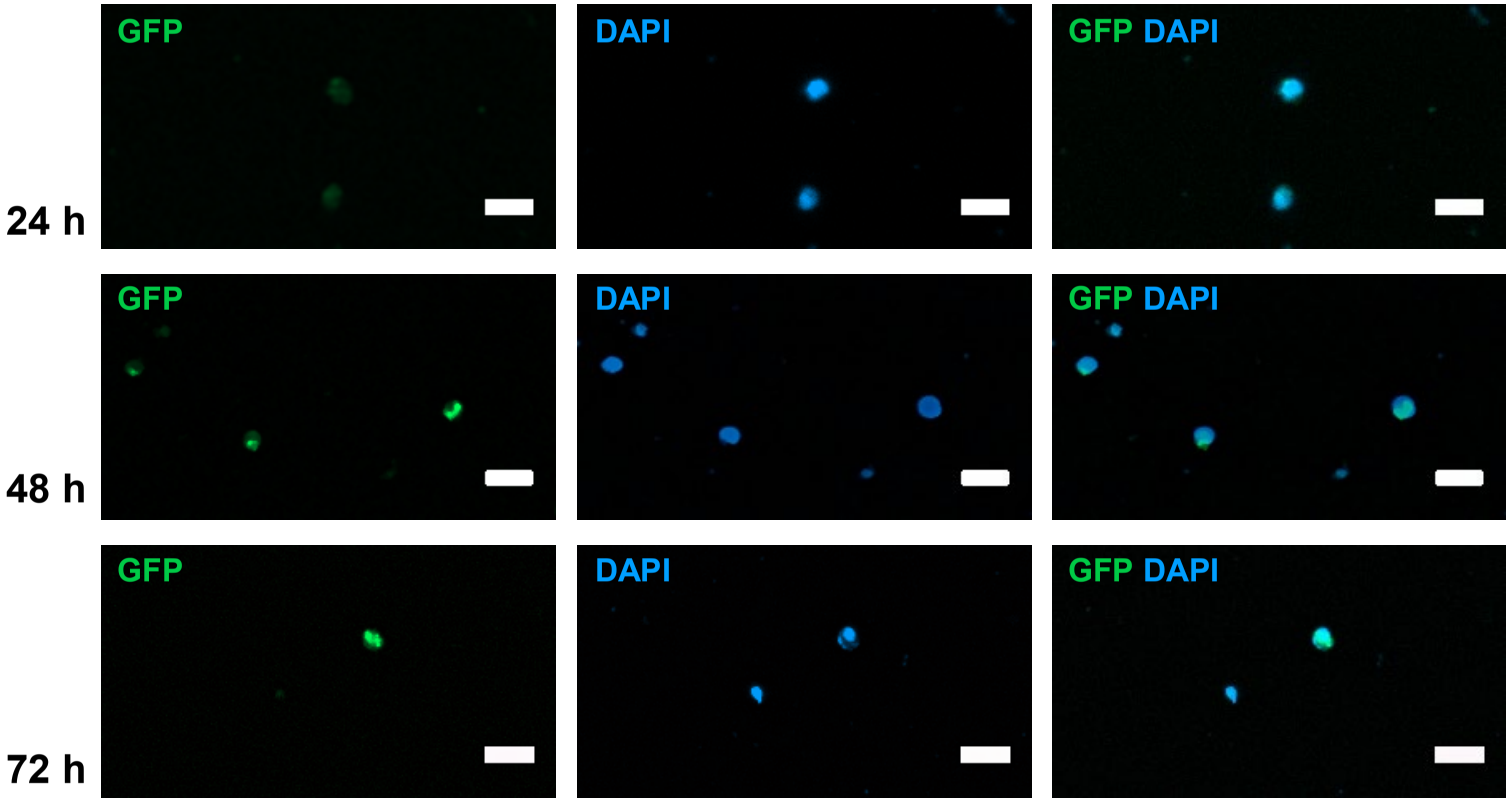

Figure III.8. Fluorescence microscope images of green fluorescent protein (GFP) (left) and DAPI (a nuclear counterstain) (middle) channels as well as their merge (right). Images of CMV (cytomegalovirus) -EGFP transfected Jurkat cells at (A) 24 h, (B) 48 h, and (C) 72 h post-cell deformation using a slippery liquid-infused porous surfaces (SLIPS) -modified vacuum filtration system using commercial porous culture insert membrane with 8 μm pores. Jurkat cells were incubated with 0.1 mg/mL of the CMV-EGFP plasmid. Scale bars = 20 μm.

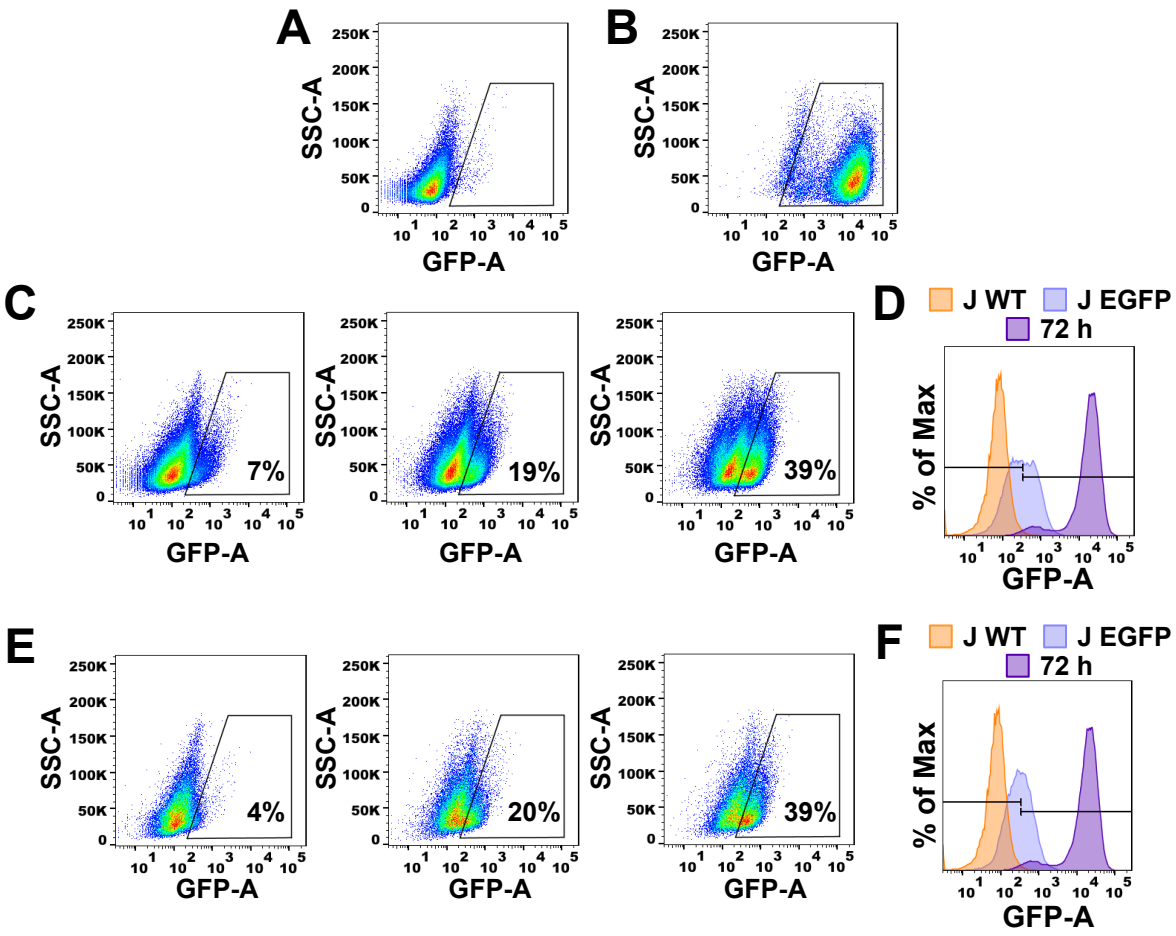

Figure III.9. Maximum green fluorescent protein (GFP) expression from Jurkat cells 24 - 72 h after transfection *via* the vacuum filtration gene delivery system using commercial poly(ethylene terephthalate) cell culture filters inserts with 8 μm pores. Jurkat cells were immediately exposed to a MNDU3-EGFP plasmid and analyzed *via* flow cytometry for 24-, 48-, and 72-h time points. Flow cytometry plots of (A) Jurkat wild-type, (B) Jurkat EGFP-EGFR (enhanced GFP-epidermal growth factor receptor) cell line, and MNDU3-EGFP transfected Jurkat cells from 24 – 72 h for (C) unmodified and (E) slippery liquid-infused porous surfaces (SLIPS) -modified filters. A histogram overlay of Jurkat wild-type, Jurkat EGFP-EGFR cell line, and MNDU3-EGFP transfected Jurkat cells after 72 h for (D) unmodified and (F) SLIPS-modified filters.

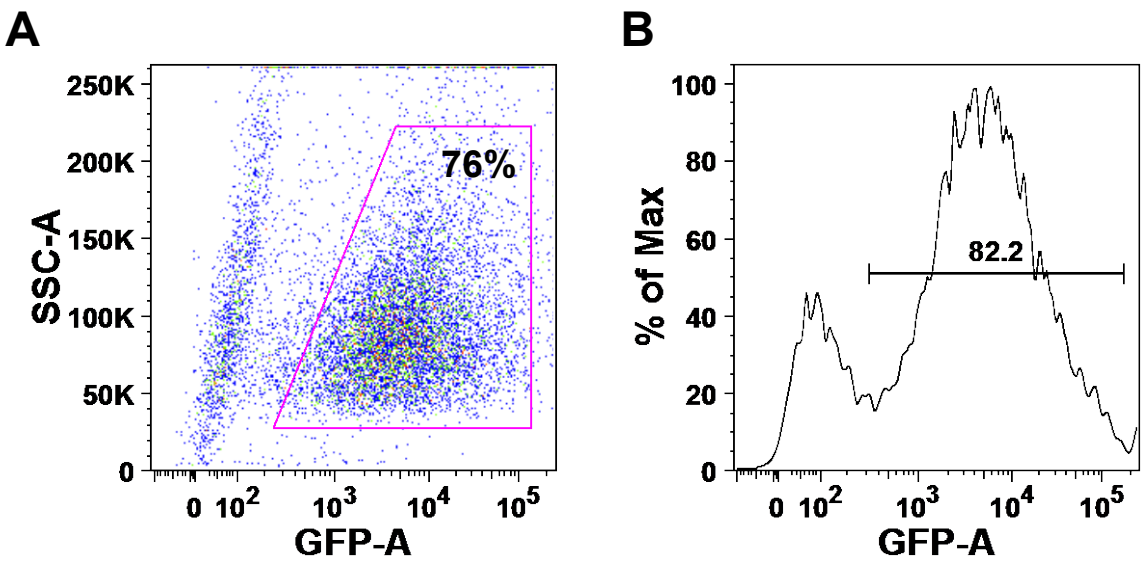

Figure III.10. Electroporation of Jurkat cells. (A) Flow cytometry plots showing the transfection of Jurkat cells 24 h after transfection with CMV-EGFP plasmid (50 µg/mL) using a commercial electroporation kit and (B) corresponding histogram plot.

III.F. References

(1) Mochizuki, A. Y.; Frost, I. M.; Mastrodimos, M. B.; Plant, A. S.; Wang, A. C.; Moore, T. B.; Prins, R. M.; Weiss, P. S.; Jonas, S. J. Precision Medicine in Pediatric Neurooncology: A Review. *ACS Chem. Neurosci.* **2018**, *9*, 11–28.

(2) De Oliveira, S. N.; Wang, J.; Ryan, C.; Morrison, S. L.; Kohn, D. B.; Hollis, R. P. A CD19/Fc Fusion Protein for Detection of Anti-CD19 Chimeric Antigen Receptors. *J. Transl. Med.* **2013**, *11*, 23.

(3) Dunbar, C. E.; High, K. A.; Joung, J. K.; Kohn, D. B.; Ozawa, K.; Sadelain, M. Gene Therapy Comes of Age. *Science* **2018**, *359*, eaan4672.

(4) Rosenberg, S. A.; Restifo, N. P. Adoptive Cell Transfer as Personalized Immunotherapy for Human Cancer. *Science* **2015**, *348*, 62–68.

(5) Sadelain, M.; Rivière, I.; Riddell, S. Therapeutic T Cell Engineering. *Nature* **2017**, *545*, 423–431.

(6) Sadelain, M.; Rivière, I.; Brentjens, R. Targeting Tumours with Genetically Enhanced T Lymphocytes. *Nat. Rev. Cancer* **2003**, *3*, 35–45.

(7) Klebanoff, C. A.; Rosenberg, S. A.; Restifo, N. P. Prospects for Gene-Engineered T Cell Immunotherapy for Solid Cancers. *Nat. Med.* **2016**, *22*, 26–36.

(8) Ellebrecht, C. T.; Bhoj, V. G.; Nace, A.; Choi, E. J.; Mao, X.; Cho, M. J.; Zenzo, G. D.; Lanzavecchia, A.; Seykora, J. T.; Cotsarelis, G.; Milone, M. C.; Payne, A. S. Reengineering Chimeric Antigen Receptor T Cells for Targeted Therapy of Autoimmune Disease. *Science* **2016**, *353*, 179–184.

(9) Naldini, L. Gene Therapy Returns to Centre Stage. *Nature* **2015**, *526*, 351–360.

(10) Kohn, D. B.; Kuo, C. Y. New Frontiers in the Therapy of Primary Immunodeficiency: From Gene Addition to Gene Editing. *J. Allergy Clin. Immunol.* **2017**, *139*, 726–732.

(11) Genovese, P.; Schiroli, G.; Escobar, G.; Tomaso, T. D.; Firrito, C.; Calabria, A.; Moi, D.; Mazzieri, R.; Bonini, C.; Holmes, M. C.; Gregory, P. D.; Burg, M. van der; Gentner, B.; Montini, E.; Lombardo, A.; Naldini, L. Targeted Genome Editing in Human Repopulating Haematopoietic Stem Cells. *Nature* **2014**, *510*, 235–240.

(12) Anson, D. S. The Use of Retroviral Vectors for Gene Therapy-What Are the Risks? A Review of Retroviral Pathogenesis and Its Relevance to Retroviral Vector-Mediated Gene Delivery. *Genet. Vaccines Ther.* **2004**, *2*, 9.

(13) Masiuk, K. E.; Brown, D.; Laborada, J.; Hollis, R. P.; Urbinati, F.; Kohn, D. B. Improving Gene Therapy Efficiency through the Enrichment of Human Hematopoietic Stem Cells. *Mol. Ther.* **2017**, *25*, 2163–2175.

(14) Shaw, K. L.; Garabedian, E.; Mishra, S.; Barman, P.; Davila, A.; Carbonaro, D.; Shupien, S.; Silvin, C.; Geiger, S.; Nowicki, B.; Smogorzewska, E. M.; Brown, B.; Wang, X.; Oliveira, S. de; Choi, Y.; Ikeda, A.; Terrazas, D.; Fu, P.-Y.; Yu, A.; Fernandez, B. C.; Cooper, A. R.; Engel, B.; Podsakoff, G.; Balamurugan, A.; Anderson, S.; Muul, L.; Jagadeesh, G. J.; Kapoor, N.; Tse, J.; Moore, T. B.; Purdy, K.; Rishi, R.; Mohan, K.; Skoda-Smith, S.; Buchbinder, D.; Abraham, R. S.; Scharenberg, A.; Yang, O. O.; Cornetta, K.; Gjertson, D.; Hershfield, M.; Sokolic, R.; Candotti, F.; Kohn, D. B. Clinical Efficacy of Gene-Modified Stem Cells in Adenosine Deaminase–Deficient Immunodeficiency. *J. Clin. Invest.* **2017**, *127*, 1689–1699.

(15) Hoban, M. D.; Cost, G. J.; Mendel, M. C.; Romero, Z.; Kaufman, M. L.; Joglekar, A. V.; Ho, M.; Lumaquin, D.; Gray, D.; Lill, G. R.; Cooper, A. R.; Urbinati, F.; Senadheera, S.; Zhu, A.; Liu, P.-Q.; Paschon, D. E.; Zhang, L.; Rebar, E. J.; Wilber, A.; Wang, X.; Gregory, P. D.; Holmes, M. C.; Reik, A.; Hollis, R. P.; Kohn, D. B. Correction of the Sickle Cell Disease Mutation in Human Hematopoietic Stem/Progenitor Cells. *Blood* **2015**, *125*, 2597–2604.

(16) Lidonnici, M. R.; Ferrari, G. Gene Therapy and Gene Editing Strategies for Hemoglobinopathies. *Blood Cells. Mol. Dis.* **2018**, *70*, 87–101.

(17) Park, C.-Y.; Kim, D. H.; Son, J. S.; Sung, J. J.; Lee, J.; Bae, S.; Kim, J.-H.; Kim, D.-W.; Kim, J.-S. Functional Correction of Large Factor VIII Gene Chromosomal Inversions in Hemophilia A Patient-Derived IPSCs Using CRISPR-Cas9. *Cell Stem Cell* **2015**, *17*, 213–220.

(18) Park, C.-Y.; Kim, J.; Kweon, J.; Son, J. S.; Lee, J. S.; Yoo, J.-E.; Cho, S.-R.; Kim, J.-H.; Kim, J.-S.; Kim, D.-W. Targeted Inversion and Reversion of the Blood Coagulation Factor 8 Gene in Human IPS Cells Using TALENs. *Proc. Natl. Acad. Sci.* **2014**, *111*, 9253–9258.

(19) Waddington, S. N.; Privolizzi, R.; Karda, R.; O'Neill, H. C. A Broad Overview and Review of CRISPR-Cas Technology and Stem Cells. *Curr. Stem Cell Rep.* **2016**, *2*, 9–20.

(20) Balaggan, K. S.; Binley, K.; Esapa, M.; Iqball, S.; Askham, Z.; Kan, O.; Tschernutter, M.; Bainbridge, J. W. B.; Naylor, S.; Ali, R. R. Stable and Efficient Intraocular Gene Transfer Using Pseudotyped EIAV Lentiviral Vectors. *J. Gene Med. Chichester* **2006**, *8*, 275–285.

(21) Tabebordbar, M.; Zhu, K.; Cheng, J. K. W.; Chew, W. L.; Widrick, J. J.; Yan, W. X.; Maesner, C.; Wu, E. Y.; Xiao, R.; Ran, F. A.; Cong, L.; Zhang, F.; Vandenberghe, L. H.; Church, G. M.; Wagers, A. J. *In Vivo* Gene Editing in Dystrophic Mouse Muscle and Muscle Stem Cells. *Science* **2016**, *351*, 407–411.

(22) Long, C.; Amoasii, L.; Mireault, A. A.; McAnally, J. R.; Li, H.; Sanchez-Ortiz, E.; Bhattacharyya, S.; Shelton, J. M.; Bassel-Duby, R.; Olson, E. N. Postnatal Genome Editing Partially Restores Dystrophin Expression in a Mouse Model of Muscular Dystrophy. *Science* **2016**, *351*, 400–403.

(23) Osborn, M. J.; Webber, B. R.; Knipping, F.; Lonetree, C.; Tennis, N.; DeFeo, A. P.; McElroy, A. N.; Starker, C. G.; Lee, C.; Merkel, S.; Lund, T. C.; Kelly-Spratt, K. S.; Jensen, M. C.; Voytas, D. F.; von Kalle, C.; Schmidt, M.; Gabriel, R.; Hippen, K. L.; Miller, J. S.; Scharenberg, A. M.; Tolar, J.; Blazar, B. R. Evaluation of TCR Gene Editing Achieved by TALENs, CRISPR/Cas9, and MegaTAL Nucleases. *Mol. Ther.* **2016**, *24*, 570–581.

(24) Yin, H.; Song, C.-Q.; Dorkin, J. R.; Zhu, L. J.; Li, Y.; Wu, Q.; Park, A.; Yang, J.; Suresh, S.; Bizhanova, A.; Gupta, A.; Bolukbasi, M. F.; Walsh, S.; Bogorad, R. L.; Gao, G.; Weng, Z.; Dong, Y.; Koteliansky, V.; Wolfe, S. A.; Langer, R.; Xue, W.; Anderson, D. G. Therapeutic Genome Editing by Combined Viral and Non-Viral Delivery of CRISPR System Components *in Vivo*. *Nat. Biotechnol.* **2016**, *34*, 328–333.

(25) Zhang, Z.; Zhang, Y.; Gao, F.; Han, S.; Cheah, K. S.; Tse, H.-F.; Lian, Q. CRISPR/Cas9 Genome-Editing System in Human Stem Cells: Current Status and Future Prospects. *Mol. Ther. Nucleic Acids* **2017**, *9*, 230–241.

(26) Sander, J. D.; Joung, J. K. CRISPR-Cas Systems for Editing, Regulating and Targeting Genomes. *Nat. Biotechnol.* **2014**, *32*, 347–355.

(27) Komor, A. C.; Badran, A. H.; Liu, D. R. CRISPR-Based Technologies for the Manipulation of Eukaryotic Genomes. *Cell* **2017**, *168*, 20–36.

(28) Ain, Q. U.; Chung, J. Y.; Kim, Y.-H. Current and Future Delivery Systems for Engineered Nucleases: ZFN, TALEN and RGEN. *J. Control. Release* **2015**, *205*, 120–127.

(29) Eyquem, J.; Mansilla-Soto, J.; Giavridis, T.; van der Stegen, S. J. C.; Hamieh, M.; Cunanan, K. M.; Odak, A.; Gönen, M.; Sadelain, M. Targeting a CAR to the TRAC Locus with CRISPR/Cas9 Enhances Tumour Rejection. *Nature* **2017**, *543*, 113–117.

(30) Maude, S. L.; Frey, N.; Shaw, P. A.; Aplenc, R.; Barrett, D. M.; Bunin, N. J.; Chew, A.; Gonzalez, V. E.; Zheng, Z.; Lacey, S. F.; Mahnke, Y. D.; Melenhorst, J. J.; Rheingold, S. R.; Shen, A.; Teachey, D. T.; Levine, B. L.; June, C. H.; Porter, D. L.; Grupp, S. A. Chimeric Antigen Receptor T Cells for Sustained Remissions in Leukemia. *N. Engl. J. Med.* **2014**, *371*, 1507–1517.

(31) June, C. H.; Riddell, S. R.; Schumacher, T. N. Adoptive Cellular Therapy: A Race to the Finish Line. *Sci. Transl. Med.* **2015**, *7*, 280ps7-280ps7.

(32) Ali, S. A.; Shi, V.; Maric, I.; Wang, M.; Stroncek, D. F.; Rose, J. J.; Brudno, J. N.; Stetler-Stevenson, M.; Feldman, S. A.; Hansen, B. G.; Fellowes, V. S.; Hakim, F. T.; Gress, R. E.; Kochenderfer, J. N. T Cells Expressing an Anti–B-Cell Maturation Antigen Chimeric Antigen Receptor Cause Remissions of Multiple Myeloma. *Blood* **2016**, *128*, 1688–1700.

(33) Lee, D. W.; Kochenderfer, J. N.; Stetler-Stevenson, M.; Cui, Y. K.; Delbrook, C.; Feldman, S. A.; Fry, T. J.; Orentas, R.; Sabatino, M.; Shah, N. N.; Steinberg, S. M.; Stroncek, D.; Tschernia, N.; Yuan, C.; Zhang, H.; Zhang, L.; Rosenberg, S. A.; Wayne, A. S.; Mackall, C. L. T Cells Expressing CD19 Chimeric Antigen Receptors for Acute Lymphoblastic Leukaemia in Children and Young Adults: A Phase 1 Dose-Escalation Trial. *The Lancet* **2015**, *385*, 517–528.

(34) Sharpe, M.; Mount, N. Genetically Modified T Cells in Cancer Therapy: Opportunities and Challenges. *Dis. Model. Mech.* **2015**, *8*, 337–350.

(35) Yin, H.; Kauffman, K. J.; Anderson, D. G. Delivery Technologies for Genome Editing. *Nat. Rev. Drug Discov.* **2017**, *16*, 387–399.

(36) Berdien, B.; Mock, U.; Atanackovic, D.; Fehse, B. TALEN-Mediated Editing of Endogenous T-Cell Receptors Facilitates Efficient Reprogramming of T Lymphocytes by Lentiviral Gene Transfer. *Gene Ther.* **2014**, *21*, 539–548.

(37) Joung, J. K.; Sander, J. D. TALENs: A Widely Applicable Technology for Targeted Genome Editing. *Nat. Rev. Mol. Cell Biol.* **2013**, *14*, 49–55.

(38) Torikai, H.; Reik, A.; Liu, P.-Q.; Zhou, Y.; Zhang, L.; Maiti, S.; Huls, H.; Miller, J. C.; Kebriaei, P.; Rabinovitch, B.; Lee, D. A.; Champlin, R. E.; Bonini, C.; Naldini, L.; Rebar, E. J.; Gregory, P. D.; Holmes, M. C.; Cooper, L. J. N. A Foundation for Universal T-Cell Based Immunotherapy: T Cells Engineered to Express a CD19-Specific Chimeric-Antigen-Receptor and Eliminate Expression of Endogenous TCR. *Blood* **2012**, *119*, 5697–5705.

(39) Lee, H. J.; Kim, E.; Kim, J.-S. Targeted Chromosomal Deletions in Human Cells Using Zinc Finger Nucleases. *Genome Res.* **2010**, *20*, 81–89.

(40) Song, M.; Ramakrishna, S. Genome Editing in Stem Cells for Disease Therapeutics. *Mol. Biotechnol.* **2018**, *60*, 329–338.

(41) Hoban, M. D.; Bauer, D. E. A Genome Editing Primer for the Hematologist. *Blood* **2016**, *127*, 2525–2535.

(42) Smith, M.; Zakrzewski, J.; James, S.; Sadelain, M. Posttransplant Chimeric Antigen Receptor Therapy. *Blood* **2018**, *131*, 1045–1052.

(43) Gill, S. Chimeric Antigen Receptor T Cell Therapy in AML: How Close Are We? *Best Pract. Res. Clin. Haematol.* **2016**, *29*, 329–333.

(44) Morgan, R. A.; Gray, D.; Lomova, A.; Kohn, D. B. Hematopoietic Stem Cell Gene Therapy: Progress and Lessons Learned. *Cell Stem Cell* **2017**, *21*, 574–590.

(45) Holstein, M.; Mesa-Nuñez, C.; Miskey, C.; Almarza, E.; Poletti, V.; Schmeer, M.; Grueso, E.; Ordóñez Flores, J. C.; Kobelt, D.; Walther, W.; Aneja, M. K.; Geiger, J.; Bonig, H. B.; Izsvák, Z.; Schleef, M.; Rudolph, C.; Mavilio, F.; Bueren, J. A.; Guenechea, G.; Ivics, Z. Efficient Non-Viral Gene Delivery into Human Hematopoietic Stem Cells by Minicircle Sleeping Beauty Transposon Vectors. *Mol. Ther.* **2018**, *26*, 1137–1153.

(46) Ferrara, J. L. M.; Levine, J. E.; Reddy, P.; Holler, E. Graft-versus-Host Disease. *Lancet* **2009**, *373*, 1550–1561.

(47) Thomas, C. E.; Ehrhardt, A.; Kay, M. A. Progress and Problems with the Use of Viral Vectors for Gene Therapy. *Nat. Rev. Genet.* **2003**, *4*, 346–358.

(48) Waehler, R.; Russell, S. J.; Curiel, D. T. Engineering Targeted Viral Vectors for Gene Therapy. *Nat. Rev. Genet.* **2007**, *8*, 573–587.

(49) Kay, M. A.; Glorioso, J. C.; Naldini, L. Viral Vectors for Gene Therapy: The Art of Turning Infectious Agents into Vehicles of Therapeutics. *Nat. Med.* **2001**, *7*, 33–40.

(50) Zhang, X.; Godbey, W. T. Viral Vectors for Gene Delivery in Tissue Engineering. *Adv. Drug Deliv. Rev.* **2006**, *58*, 515–534.

(51) Milone, M. C.; O'Doherty, U. Clinical Use of Lentiviral Vectors. *Leukemia* **2018**, *32*, 1529–1541.

(52) Manfredsson, F. P. Introduction to Viral Vectors and Other Delivery Methods for Gene Therapy of the Nervous System. In *Gene Therapy for Neurological Disorders*; Methods in Molecular Biology; Humana Press, New York, NY, 2016; pp 3–18.

(53) Jordan, E. T.; Collins, M.; Terefe, J.; Ugozzoli, L.; Rubio, T. Optimizing Electroporation Conditions in Primary and Other Difficult-to-Transfect Cells. *J. Biomol. Tech.* **2008**, *19*, 328–334.

(54) Kataoka, K.; Harashima, H. Gene Delivery Systems: Viral vs. Non-Viral Vectors. *Adv. Drug Deliv. Rev.* **2001**, *52*, 151.

(55) Ramamoorth, M.; Narvekar, A. Non Viral Vectors in Gene Therapy- An Overview. *J. Clin. Diagn. Res.* **2015**, *9*, GE01–GE06.

(56) Lakshmanan, S.; Gupta, G. K.; Avci, P.; Chandran, R.; Sadasivam, M.; Jorge, A. E. S.; Hamblin, M. R. Physical Energy for Drug Delivery; Poration, Concentration and Activation. *Adv. Drug Deliv. Rev.* **2014**, *71*, 98–114.

(57) Hirsch, T.; Rothoeft, T.; Teig, N.; Bauer, J. W.; Pellegrini, G.; Rosa, L. D.; Scaglione, D.; Reichelt, J.; Klausegger, A.; Kneisz, D.; Romano, O.; Seconetti, A. S.; Contin, R.; Enzo, E.; Jurman, I.; Carulli, S.; Jacobsen, F.; Luecke, T.; Lehnhardt, M.; Fischer, M.; Kueckelhaus, M.; Quaglino, D.; Morgante, M.; Bicciato, S.; Bondanza, S.; Luca, M. D. Regeneration of the Entire Human Epidermis Using Transgenic Stem Cells. *Nature* **2017**, *551*, 327–332.

(58) George, L. A.; Sullivan, S. K.; Giermasz, A.; Rasko, J. E. J.; Samelson-Jones, B. J.; Ducore, J.; Cuker, A.; Sullivan, L. M.; Majumdar, S.; Teitel, J.; McGuinn, C. E.; Ragni, M. V.; Luk, A. Y.; Hui, D.; Wright, J. F.; Chen, Y.; Liu, Y.; Wachtel, K.; Winters, A.; Tiefenbacher, S.; Arruda, V. R.; van der Loo, J. C. M.; Zelenaia, O.; Takefman, D.; Carr, M. E.; Couto, L. B.; Anguela, X. M.; High, K. A. Hemophilia B Gene Therapy with a High-Specific-Activity Factor IX Variant. *N. Engl. J. Med.* **2017**, *377*, 2215–2227.

(59) Takefman, D.; Bryan, W. The State of Gene Therapies: The FDA Perspective. *Mol. Ther.* **2012**, *20*, 877–878.

(60) Sibbald, B. Death but One Unintended Consequence of Gene-Therapy Trial. *Can. Med. Assoc. J.* **2001**, *164*, 1612.

(61) Jordan, E. T.; Collins, M.; Terefe, J.; Ugozzoli, L.; Rubio, T. Optimizing Electroporation Conditions in Primary and Other Difficult-to-Transfect Cells. *J. Biomol. Tech.* **2008**, *19*, 328–334.

(62) Mellott, A. J.; Forrest, M. L.; Detamore, M. S. Physical Non-Viral Gene Delivery Methods for Tissue Engineering. *Ann. Biomed. Eng.* **2013**, *41*, 446–468.

(63) Mehier-Humbert, S.; Guy, R. H. Physical Methods for Gene Transfer: Improving the Kinetics of Gene Delivery into Cells. *Adv. Drug Deliv. Rev.* **2005**, *57*, 733–753.

(64) Nayerossadat, N.; Maedeh, T.; Ali, P. A. Viral and Nonviral Delivery Systems for Gene Delivery. *Adv. Biomed. Res.* **2012**, *1*.

(65) Stewart, M. P.; Langer, R.; Jensen, K. F. Intracellular Delivery by Membrane Disruption: Mechanisms, Strategies, and Concepts. *Chem. Rev.* **2018**, *118*, 7409–7531.

(66) Ruiz-Esparza, G. U.; Wu, S.; Segura-Ibarra, V.; Cara, F. E.; Evans, K. W.; Milosevic, M.; Ziemys, A.; Kojic, M.; Meric-Bernstam, F.; Ferrari, M.; Blanco, E. Polymer Nanoparticles Encased in a Cyclodextrin Complex Shell for Potential Site- and Sequence-Specific Drug Release. *Adv. Funct. Mater. 24*, 4753–4761.

(67) Fink, T. L.; Klepcyk, P. J.; Oette, S. M.; Gedeon, C. R.; Hyatt, S. L.; Kowalczyk, T. H.; Moen, R. C.; Cooper, M. J. Plasmid Size up to 20 Kbp Does Not Limit Effective *in Vivo* Lung Gene Transfer Using Compacted DNA Nanoparticles. *Gene Ther.* **2006**, *13*, 1048–1051.

(68) Lyu, Z.; Zhou, F.; Liu, Q.; Xue, H.; Yu, Q.; Chen, H. A Universal Platform for Macromolecular Delivery into Cells Using Gold Nanoparticle Layers *via* the Photoporation Effect. *Adv. Funct. Mater.* **2016**, *26*, 5787–5795.

(69) Tomizawa, M.; Shinozaki, F.; Motoyoshi, Y.; Sugiyama, T.; Yamamoto, S.; Sueishi, M. Sonoporation: Gene Transfer Using Ultrasound. *World J. Methodol.* **2013**, *3*, 39–44.

(70) van Wamel, A.; Kooiman, K.; Harteveld, M.; Emmer, M.; ten Cate, F. J.; Versluis, M.; de Jong, N. Vibrating Microbubbles Poking Individual Cells: Drug Transfer into Cells *via* Sonoporation. *J. Control. Release* **2006**, *112*, 149–155.

(71) Suzuki, R.; Takizawa, T.; Negishi, Y.; Utoguchi, N.; Sawamura, K.; Tanaka, K.; Namai, E.; Oda, Y.; Matsumura, Y.; Maruyama, K. Tumor Specific Ultrasound Enhanced Gene Transfer *in Vivo* with Novel Liposomal Bubbles. *J. Control. Release* **2008**, *125*, 137–144.

(72) Tiefenboeck, P.; Kim, J. A.; Trunk, F.; Eicher, T.; Russo, E.; Teijeira, A.; Halin, C.; Leroux, J.-C. Microinjection for the *ex Vivo* Modification of Cells with Artificial Organelles. *ACS Nano* **2017**, *11*, 7758–7769.

(73) Wang, P. M.; Cornwell, M.; Hill, J.; Prausnitz, M. R. Precise Microinjection into Skin Using Hollow Microneedles. *J. Invest. Dermatol.* **2006**, *126*, 1080–1087.

(74) Matsuoka, H.; Komazaki, T.; Mukai, Y.; Shibusawa, M.; Akane, H.; Chaki, A.; Uetake, N.; Saito, M. High Throughput Easy Microinjection with a Single-Cell Manipulation Supporting Robot. *J. Biotechnol.* **2005**, *116*, 185–194.

(75) Wiethoff, C. M.; Middaugh, C. R. Barriers to Nonviral Gene Delivery. *J. Pharm. Sci.* **2003**, *92*, 203–217.

(76) Jin, L.; Zeng, X.; Liu, M.; Deng, Y.; He, N. Current Progress in Gene Delivery Technology Based on Chemical Methods and Nano-Carriers. *Theranostics* **2014**, *4*, 240–255.

(77) Sharei, A.; Zoldan, J.; Adamo, A.; Sim, W. Y.; Cho, N.; Jackson, E.; Mao, S.; Schneider, S.; Han, M.-J.; Lytton-Jean, A.; Basto, P. A.; Jhunjhunwala, S.; Lee, J.; Heller, D. A.; Kang, J. W.; Hartoularos, G. C.; Kim, K.-S.; Anderson, D. G.; Langer, R.; Jensen, K. F. A Vector-Free Microfluidic Platform for Intracellular Delivery. *Proc. Natl. Acad. Sci.* **2013**, *110*, 2082–2087.

(78) Sharei, A.; Poceviciute, R.; Jackson, E. L.; Cho, N.; Mao, S.; Hartoularos, G. C.; Jang, D. Y.; Jhunjhunwala, S.; Eyerman, A.; Schoettle, T.; Langer, R.; Jensen, K. F. Plasma Membrane Recovery Kinetics of a Microfluidic Intracellular Delivery Platform. *Integr. Biol.* **2014**, *6*, 470–475.

(79) Saung, M. T.; Sharei, A.; Adalsteinsson, V. A.; Cho, N.; Kamath, T.; Ruiz, C.; Kirkpatrick, J.; Patel, N.; Mino-Kenudson, M.; Thayer, S. P.; Langer, R.; Jensen, K. F.; Liss, A. S.; Love, J. C. A Size-Selective Intracellular Delivery Platform. *Small* **2016**, *12*, 5873–5881.

(80) Ding, X.; Stewart, M. P.; Sharei, A.; Weaver, J. C.; Langer, R. S.; Jensen, K. F. High-Throughput Nuclear Delivery and Rapid Expression of DNA *via* Mechanical and Electrical Cell-Membrane Disruption. *Nat. Biomed. Eng.* **2017**, *1*, 0039.

(81) Kollmannsperger, A.; Sharei, A.; Raulf, A.; Heilemann, M.; Langer, R.; Jensen, K. F.; Wieneke, R.; Tampé, R. Live-Cell Protein Labelling with Nanometre Precision by Cell Squeezing. *Nat. Commun.* **2016**, *7*.

(82) Szeto, G. L.; Van Egeren, D.; Worku, H.; Sharei, A.; Alejandro, B.; Park, C.; Frew, K.; Brefo, M.; Mao, S.; Heimann, M.; Langer, R.; Jensen, K.; Irvine, D. J. Microfluidic Squeezing for Intracellular Antigen Loading in Polyclonal B-Cells as Cellular Vaccines. *Sci. Rep.* **2015**, *5*.

(83) DiTommaso, T.; Cole, J. M.; Cassereau, L.; Buggé, J. A.; Hanson, J. L. S.; Bridgen, D. T.; Stokes, B. D.; Loughhead, S. M.; Beutel, B. A.; Gilbert, J. B.; Nussbaum, K.; Sorrentino, A.; Toggweiler, J.; Schmidt, T.; Gyuelveszi, G.; Bernstein, H.; Sharei, A. Cell Engineering with Microfluidic Squeezing Preserves Functionality of Primary Immune Cells *in Vivo*. *Proc. Natl. Acad. Sci.* **2018**, *115*, E10907–E10914.

(84) MacCallum, N.; Howell, C.; Kim, P.; Sun, D.; Friedlander, R.; Ranisau, J.; Ahanotu, O.; Lin, J. J.; Vena, A.; Hatton, B.; Wong, T.-S.; Aizenberg, J. Liquid-Infused Silicone As a Biofouling-Free Medical Material. *ACS Biomater. Sci. Eng.* **2015**, *1*, 43–51.

(85) Hou, X.; Hu, Y.; Grinthal, A.; Khan, M.; Aizenberg, J. Liquid-Based Gating Mechanism with Tunable Multiphase Selectivity and Antifouling Behaviour. *Nature* **2015**, *519*, 70–73.

(86) Cui, J.; Daniel, D.; Grinthal, A.; Lin, K.; Aizenberg, J. Dynamic Polymer Systems with Self-Regulated Secretion for the Control of Surface Properties and Material Healing. *Nat. Mater.* **2015**, *14*, 790–795.

(87) Amini, S.; Kolle, S.; Petrone, L.; Ahanotu, O.; Sunny, S.; Sutanto, C. N.; Hoon, S.; Cohen, L.; Weaver, J. C.; Aizenberg, J.; Vogel, N.; Miserez, A. Preventing Mussel Adhesion Using Lubricant-Infused Materials. *Science* **2017**, *357*, 668–673.

(88) Hou, X.; Zhang, Y. S.; Santiago, G. T.; Alvarez, M. M.; Ribas, J.; Jonas, S. J.; Weiss, P. S.; Andrews, A. M.; Aizenberg, J.; Khademhosseini, A. Interplay between Materials and Microfluidics. *Nat. Rev. Mater.* **2017**, *2*, 17016.

(89) Leslie, D. C.; Waterhouse, A.; Berthet, J. B.; Valentin, T. M.; Watters, A. L.; Jain, A.; Kim, P.; Hatton, B. D.; Nedder, A.; Donovan, K.; Super, E. H.; Howell, C.; Johnson, C. P.; Vu, T. L.; Bolgen, D. E.; Rifai, S.; Hansen, A. R.; Aizenberg, M.; Super, M.; Aizenberg, J.; Ingber, D. E. A Bioinspired Omniphobic Surface Coating on Medical Devices Prevents Thrombosis and Biofouling. *Nat. Biotechnol.* **2014**, *32*, 1134–1140.

(90) Hou, X.; Li, J.; Tesler, A. B.; Yao, Y.; Wang, M.; Min, L.; Sheng, Z.; Aizenberg, J. Dynamic Air/Liquid Pockets for Guiding Microscale Flow. *Nat. Commun.* **2018**, *9*.

(91) Wolfraim, L. A.; Takahara, M.; Viley, A. M.; Shivakumar, R.; Nieda, M.; Maekawa, R.; Liu, L. N.; Peshwa, M. V. Clinical Scale Electroloading of Mature Dendritic Cells with Melanoma Whole Tumor Cell Lysate Is Superior to Conventional Lysate Co-Incubation in Triggering Robust *in Vitro* Expansion of Functional Antigen-Specific CTL. *Int. Immunopharmacol.* **2013**, *15*, 488–497.

(92) Cox, D. B. T.; Platt, R. J.; Zhang, F. Therapeutic Genome Editing: Prospects and Challenges. *Nat. Med.* **2015**, *21*, 121–131.

(93) Romero, Z.; Urbinati, F.; Geiger, S.; Cooper, A. R.; Wherley, J.; Kaufman, M. L.; Hollis, R. P.; Assin, R. R. de; Senadheera, S.; Sahagian, A.; Jin, X.; Gellis, A.; Wang, X.; Gjertson, D.; DeOliveira, S.; Kempert, P.; Shupien, S.; Abdel-Azim, H.; Walters, M. C.; Meiselman, H. J.; Wenby, R. B.; Gruber, T.; Marder, V.; Coates, T. D.; Kohn, D. B. β-Globin Gene Transfer to Human Bone Marrow for Sickle Cell Disease. *J. Clin. Invest.* **2013**, *123*, 3317–3330.

(94) De Oliveira, S. N.; Ryan, C.; Giannoni, F.; Hardee, C. L.; Tremcinska, I.; Katebian, B.; Wherley, J.; Sahaghian, A.; Tu, A.; Grogan, T.; Elashoff, D.; Cooper, L. J. N.; Hollis, R. P.; Kohn, D. B. Modification of Hematopoietic Stem/Progenitor Cells with CD19-Specific Chimeric Antigen Receptors as a Novel Approach for Cancer Immunotherapy. *Hum. Gene Ther.* **2013**, *24*, 824–839.

CHAPTER IV

Delivery of a CD19 Expressing Chimeric Antigen Receptor *via* Rapid Cell Deformation

The information in this chapter is in preparation for publication.

Authors: Alexandra M. Mendoza, Tzu T. Chiou, Natcha Wattanatorn, Xiaobin Xu, Satiro N. De Oliveira, Steve J. Jonas, and Paul S. Weiss

IV.A. Introduction

Rapid, efficient, safe, and cost effective delivery of genetic materials, such as expression plasmids and/or gene editing nucleases (*e.g.,* CRISPR-Cas9, zinc finger nuclease, etc.), to large populations of cells is essential for the manufacturing of gene-modified stem cell therapies and adoptive cellular therapies[1–7] that are now being deployed clinically for the treatment of diseases, such as immunodeficiencies,[8,9] hemoglobinopathies,[10,11] hemophilia, Duchenne muscular dystrophy,[12,13] retinal diseases,[14] or cancer.[15–18] In particular, the development of adoptive cellular therapies that utilize either engineered T-cell receptors or chimeric antigen receptors (CARs) are facilitating powerful immunotherapies for cancer, and if successful, can potentially be applied to HIV and other autoimmune diseases.[1,2,19] These CAR T-cell approaches harness the immune system to fight cancers directly.[1,2,15,16,20–24] To date, anti-CD19 expressing chimeric receptors are used in the current two current FDA approved CAR T-cell therapies for the treatment of refractory B cell-derived lymphomas and leukemias.[1,2,19] However, for these treatments to be successful, the delivery of CAR transgene constructs needs to be stable and maintain long-lasting gene expression in T cell populations to endure immune memory and to prohibit relapse, which has been difficult to achieve safely and at desirable throughputs using current gene delivery methods.[1,2,15,18,25] State-of-the-art strategies employ electroporation[26–32] or viral vectors;[33–37] however, these methods are expensive at cell processing scales required for clinical translation, suffer from toxicity and potential immunogenicity and/or off-target effects, and are unable to be universally deployed across different cell lines.[34,38–44]

Alternative intracellular delivery methods that are being studied to deform the cell membrane to permeate and to deliver biomolecular payloads to cells include the use of

microinjection,[45–51] acoustic waves,[52] sonoporation,[53,54] nanoparticles,[55–57] and nanostructures.[58–63] However, these approaches have not yet been demonstrated at clinically relevant scales or universal use.[64] In particular, rapid cell deformation techniques enable an elegant solution to permeabilize cells temporarily as they pass through mechanical barriers or electric fields to enable cargo delivery.[64–71] However, existing membrane deformation techniques use expensive, specialized fabrication processes and equipment where devices are often plagued with fouling and fail due to clogging of the channels.[64–71] In particular, recently reported cell squeezing microfluidic devices, can only treat ~1-5 million cells before devices fail.[65] Ultimately a fast, efficient, scalable, cost-effective, and user-friendly system is needed for sustainable processing of homogeneous cell products using emerging cellular therapies for monogenetic diseases and cancer immunotherapy.[1,2]

We have developed a vacuum filtration system for rapid cell deformation using commercial and cost-effective materials. Herein, we describe a vacuum filtration system that uses commercial cell culture inserts comprised of membranes fabricated using track-etched on-wire lithography and uses negative pressure to deform cells mechanically as they pass through pores with 8 μm features. This system is capable of transporting biomolecular payloads (*e.g.*, nucleic acids, proteins) into target cells *via* transient permeabilization shortly after cells pass through the narrow pores of the filter. Using this method, we have successfully delivered a green fluorescent protein (GFP) plasmid and a CD19 expressing CAR to Jurkat cells, a model T lymphocyte (T cell) line. This vacuum filtration system, made from commercial filter inserts and materials, enables new opportunities in the development of gene and cellular therapies for a wide variety of disease treatments.

IV.B. Results and Discussion

We have developed and tested a facile approach to deform cells rapidly using commercial and inexpensive materials. This "tabletop" strategy does not require expensive and time-consuming lithographic techniques or specialized materials and methods to assemble devices, as do current techniques, and could be performed by any user. We use a commercial filter insert with 8 μm pores made from poly(ethylene terephthalate) (PET), shown in Figure IV.1. Two centrifuge tubes are placed in series, where the bottom tube has a punctured hole in the bottom that connects to the vacuum line, and the top centrifuge tube has a punctured hole on the side, just below where the bottom tube comes into contact with the top tube (Figure IV.1). The vacuum is then turned on and the cell culture insert, which contains the cells in media, is placed on top of centrifuge tube. The cells are suctioned through the filter and collected at the bottom of the top tube (Figure IV.1). The cells are then added to the plasmid of interest, CMV (cytomegalovirus) -EGFP (~4500 bp), MNDU3-EGFP (~7400 bp), or MNDU3-CD19 CAR (~8700 bp), immediately and allowed to incubate for 15 min before culturing in a well plate for post analysis at 24-, 48-, and 72-h time points.

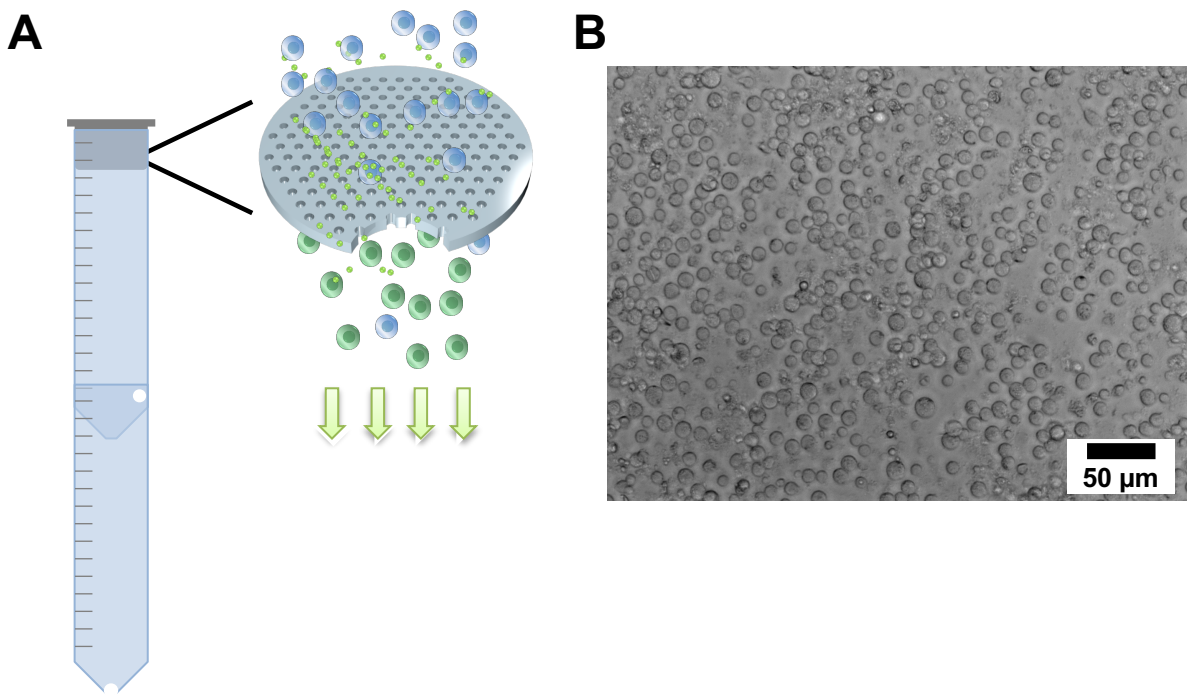

Figure IV.1. Schematic illustrating (A) the gene delivery vacuum filtration system using poly(ethylene terephthalate) (PET) cell culture filter inserts. Jurkat cells are passed through the filters using negative differential pressure using house vacuum. Two centrifuge tubes are place in series, where the bottom tube has a punctured hole at the bottom, which is connected to a vacuum line (not shown), and the upper tube on the side. The cells are added to the filter and place on top of the upper tube with the vacuum already turned on. The cells are rapidly deformed as they pass through the porous membrane and collect in the top tube, and then directly treated with either a green fluorescent protein or a CD19 expressing chimeric antigen receptor plasmid. The cells are cultured for 24 – 72 h after transfection for post analysis. (B) Bright field image of the Jurkat cells 24 h after the cell deformation experiment.

An average of ~25% of the cells were recovered from these devices with an average viability of ~80%. In order for the Jurkat cells to express GFP, the plasmid must reach the nucleus or cytoplasm of the cell for expression to occur,[47] which was evaluated by three different methods: fluorescence microscopy (Figure IV.2 and Appendix, Figure IV.6), flow cytometry (Figure IV.3, Figure IV.4A, and Appendix, Figure IV.7), and digital droplet polymerase chain reaction (ddPCR) (Figure IV.4B and Figure IV.5). First, the transfection of the Jurkat cells with a CMV-plasmid was characterized with fluorescence microscopy (Figure IV.2 and Figure IV.6). Figure IV.2 shows fluorescent images of DAPI (a nuclear counterstain) -stained Jurkat wild-type (WT), Jurkat EGFP-EGFR (enhanced GFP-epidermal growth factor receptor), and the transfected cells using the system described here at 72 h post-transfection. No fluorescence was observed for the Jurkat WT in the GFP channel, whereas GFP fluorescence was detected for the Jurkat EGFP-EGFR cell line as well as the Jurkat cells 72-h post-transfection with a CMV-EGFP plasmid (Figure IV.2).

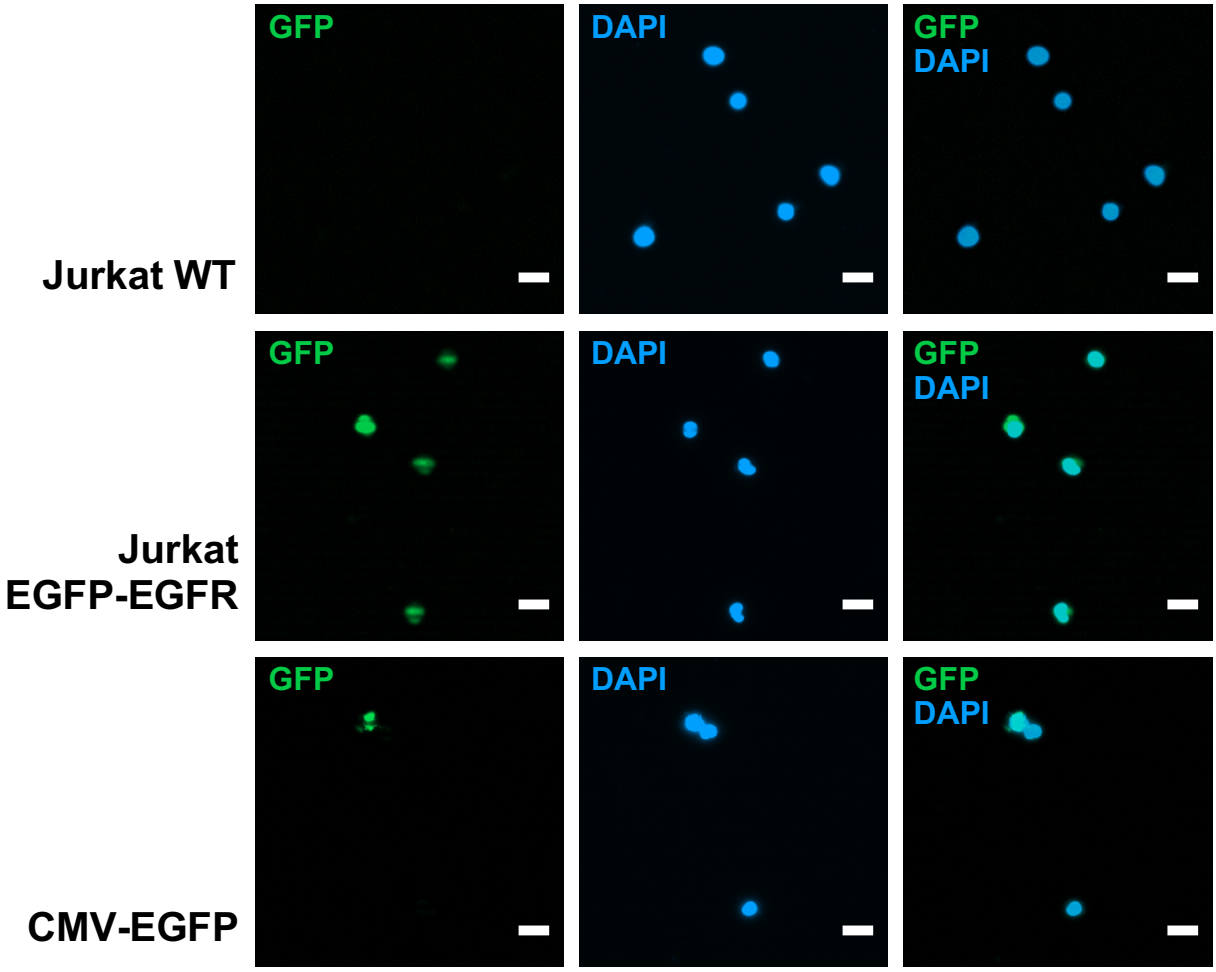

Figure IV.2. Fluorescence microscope images of Jurkat cells with green fluorescent protein (GFP), DAPI (a nuclear counterstain), and their merged channels. (Top) Jurkat wild-type (WT) cells, (middle) Jurkat enhanced GFP (EGFP) -epidermal growth factor receptor (EGFR) cell line, and (bottom) GFP transfected Jurkat cells 72 h after vacuum filtration using commercial porous culture insert membrane with 8 μm pores. Jurkat cells were incubated with 0.1 mg/mL of GFP plasmid. Scale bars = 20 μm.

To quantitate GFP expression using this rapid-cell deformation technique, flow cytometry was used to monitor the transfection from 24 - 72 h. Flow cytometry plots are shown in Figure IV.3, where we achieved a maximum transfection of ~40% GFP expression with two different GFP plasmids, driven by either the CMV- (Figure IV.3C) or MNDU3-EGFP promotor (Appendix, Figure IV.7C). The 24 – 72 h time course for CMV-EGFP (MNDU3-EGFP) transfected Jurkat cells are shown in Figure IV.3C (Appendix, Figure IV.7C) and its corresponding histogram overlay in Figure IV.3E (Appendix, Figure IV.7E). An overlay histogram of GFP fluorescence of Jurkat wild-type, Jurkat EGFP-EGFR, and the transfected Jurkat cells with CMV-EGFP (MNDU3-EGFP) at 72 h are shown in Figure IV.3D (Appendix, Figure IV.7D). The average transfection efficiency was ~15-20% for both the CMV- and MNDU3-GFP plasmids (Figure IV.4A). In comparison to electroporation of these model cell lines, where up to ~80% transfection is observed (Chapter III, Appendix, Figure III.10), we can achieve moderate transfection using this simple and cheap system.

Additionally, ddPCR was used to verify the messenger RNA (mRNA) level of the transformed cells. Detection of mRNA was used as a tertiary assay to assess if the DNA was delivered to the nucleus of the cells. Using ddPCR, we confirmed the successful delivery of the two GFP plasmids to Jurkat cells (Figure IV.4B). Additionally, we were also able to achieve delivery of a MNDU3-CD19 expressing CAR to Jurkat cells detected *via* ddPCR (Figure IV.5). In each of these cases, we were able to observe a significant difference in the copy/μL values compared to the negative control, which ran the cells through the vacuum filter membrane without any added DNA (Figure IV.4B and Figure IV.5).

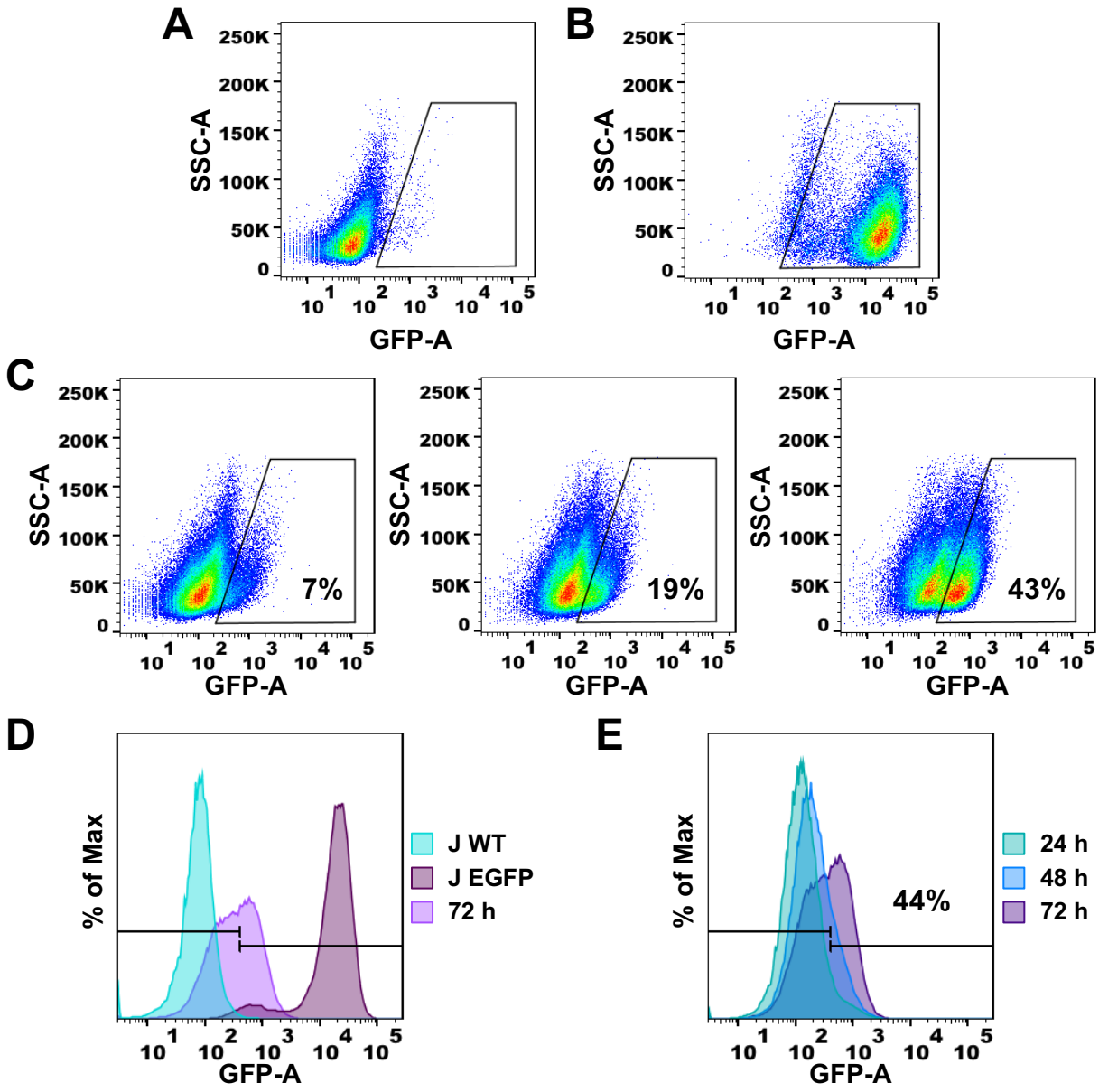

Figure IV.3. Maximum green fluorescent protein (GFP) expression from Jurkat cells 24 – 72 h after transfection *via* the vacuum filtration gene delivery system using commercial poly(ethylene terephthalate) cell culture filters inserts (8 μm pore size). Flow cytometry plots showing GFP expression of (A) Jurkat wild-type (negative control), (B) Jurkat enhanced GFP (EGFP) -epidermal growth factor receptor (EGFR) cell line (positive control), and (C) Jurkat cells that were immediately exposed to a CMV (cytomegalovirus) -EGFP plasmid at 24- (left), 48- (middle), and 72-h (right) time points. (D) Histogram overlay of Jurkat wild-type, Jurkat EGFP-EGFR, and transfected Jurkat cells at 72 h. (E) Histogram overlay of transfected Jurkat cells at 24 h, 48 h, and 72 h.

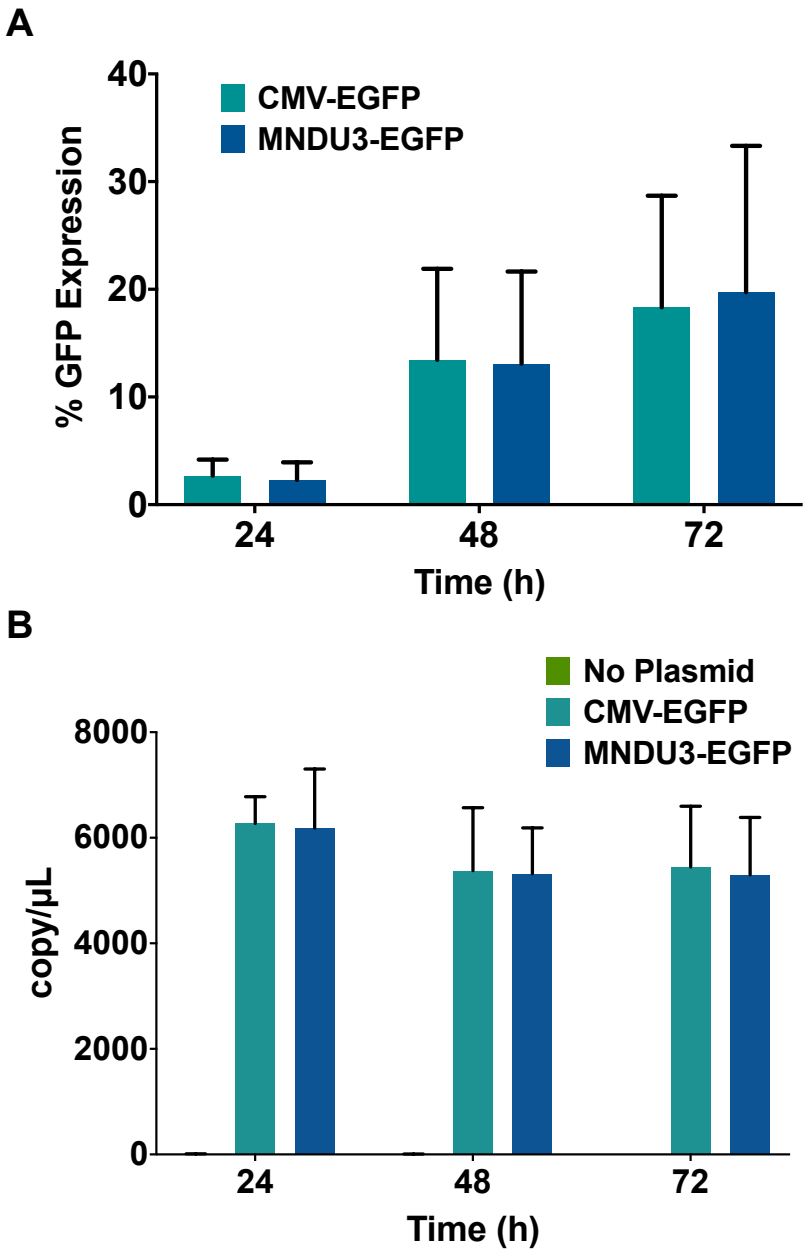

Figure IV.4. Average green fluorescent protein (GFP) expression using the vacuum filtration system. Either a CMV- (cytomegalovirus) or MNDU3-EGFP plasmid was delivered to Jurkat cells *via* the vacuum filtration platform using a commercial porous culture insert membrane with 8 µm pores. Jurkat cells passed through the filter membrane with 0.1 mg/mL of a plasmid encoding for a CMV- or MNDU3-GFP and analyzed *via* flow cytometry and digital droplet polymerase chain reaction (ddPCR). Average GFP expression *via* (A) flow cytometry and (B) corresponding ddPCR results.

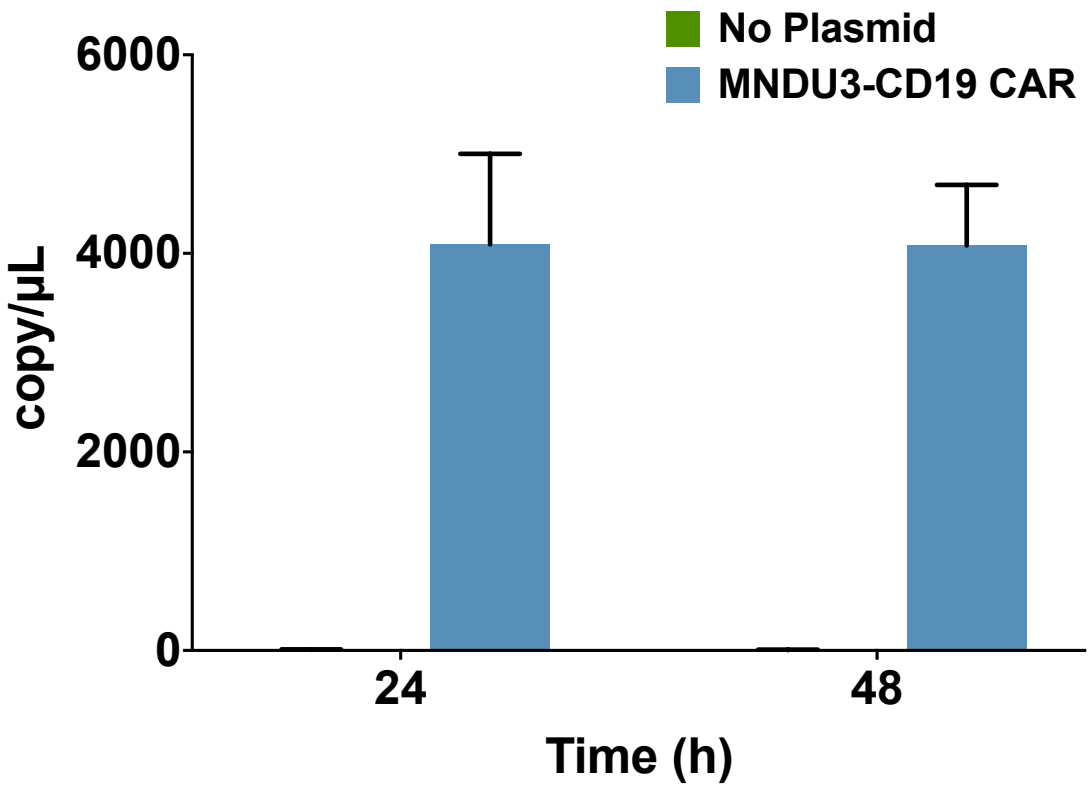

Figure IV.5. Digital droplet polymerase chain reaction (ddPCR) results. A MNDU3-CD19 expressing chimeric antigen receptor (CAR) plasmid was delivered to Jurkat cells *via* the gene delivery platform using a commercial porous culture insert membrane with 8 µm pores. Jurkat cells passed through the filter membrane with 0.2 mg/mL of a plasmid encoding for a MNDU3-CD19 CAR and analyzed with digital droplet polymerase chain reaction. The "No Plasmid" bars are on the order of the lines of the x-axis.

IV.C. Conclusions and Prospects

We developed a system to deform cells rapidly to enable the intracellular delivery of biomolecular cargo using scalable, economical, and easy-to-use materials. Using this simple, tabletop system, we were able to deliver GFP and a CD19 expressing CAR plasmid to model T cell lines with an average viability of ~80% and average transfection efficiency of ~15-20%. The key benefit of this facile vacuum filtration system is that we can attain moderate transfection and favorable cell viability, compared to electroporation (Chapter III, Appendix, Figure III.10), with a method that does not require expensive materials or specialized fabrication tools. Moreover, we have the potential to process billions of cells within a few minutes efficiently, easily, and safely. Additionally, this technique could also be used to select smaller and/or younger populations of cells, which may yield a more durable therapeutic response when deployed clinically.[72] These systems, made from commercial filters and materials, will enable new opportunities in the development of gene and cellular therapies for a wide variety of disease treatments.

IV.D. Materials and Methods

IV.D.1. Jurkat Cell Culture

Jurkat cells (ATCC, Manassas, VA, USA) were cultured in the Roswell Park Memorial Institute (RPMI) 1640 medium (Invitrogen, Darmstadt, Germany) containing 10% fetal bovine serum (FBS) (R10 medium) (Invitrogen, Darmstadt, Germany) and 100 IU/mL penicillin/streptomycin (Thermo Fisher Scientific, Waltham, MA, USA) in 5% CO_2 at 37 °C.

IV.D.2. Vectors

Construction of the pCCL-MNDU3-EGFP (7411 bp) has been described previously.[73] The pCMV-EGFP (4479 bp) was purchased from Addgene (Plasmid #11153, Cambridge, MA, USA). The vector construct for huEGFRt combined with an anti-CD19 second-generation chimeric antigen receptor with the CD28 costimulatory molecule and CD3ζchain (8657 bp) were developed as previously described[74,75] and generously provided by Stephen Forman (City of Hope, Duarte, CA). The DNA plasmids were isolated from *E. coli* using PureLink™ HiPure Plasmid MaxiPrep kits (Invitrogen, Darmstadt, Germany) according to the manufacture's guidelines.

IV.D.3. Transfection Methods

IV.D.3.a. Vacuum Filtration Apparatus for Rapid Cell Deformation

The vacuum filtration system was made by placing two 15 mL conical centrifuge tubes (Thermo Fisher Scientific, Waltham, MA, USA) together, where the top one was punctured right below where the bottom tube seals and the bottom tube was punctured at the bottom, which was subsequently connected to the house vacuum line (Figure IV.1A). Falcon™ cell culture inserts with 8-micron pores (Corning, Corning, NY, USA) were placed in the first tube with cells, at a density of 4 – 8 million cells per 150 µL, in RPMI media without FBS with the vacuum on (Figure IV.1A). Once the Jurkat cells were rapidly deformed through the inserts, the permeabilized cells were incubated with either a GFP or a CD19 CAR expressing plasmid for 10-15 min with a plasmid concentration of 0.1–0.2 mg/mL (Figure IV.1A). For the EGFP delivery, a 1% Pluronic F-68 (Thermo Fisher Scientific, Waltham, MA, USA) solution was added to the plasmid before incubating the cells post-cell deformation. After incubating the cells in plasmid, they were transferred to a well plate

(Corning, Corning, NY, USA) to maintain a density of 500-800K cells per mL for 24 - 72 h and subsequently characterized.

IV.D.4. Characterization

IV.D.4.a. Cell Fixing for Post-Analysis

After cells were counted, they were fixed for post-analysis with fluorescence microscopy and flow cytometry at 24-, 48-, and 72-h time points. Using a 1:1 dilution with trypan blue (Invitrogen, Darmstadt, Germany), cells were counted and their viability was accessed using the Countess™ Automated Cell Counter (Invitrogen, Darmstadt, Germany). Cells were fixed after the viability and cell counts were taken, where cells were pelleted and resuspended in phosphate-buffered saline (PBS) (Thermo Fisher Scientific, Waltham, MA, USA) with 2.5% FBS and fixation using BD stabilizing fixative (BD Biosciences, NJ, USA).

IV.D.4.b. Fluorescence Microscopy

Cells were pelleted and resuspended in PBS with 2.5% FBS and fixation using BD stabilizing fixative (BD Biosciences, NJ, USA). The fixed cells were either directly mounted or mixed in a 3:1 ratio with ProLong™ Diamond Antifade Mountant with DAPI (4',6-diamidino-2-phenylindole) (Invitrogen, Darmstadt, Germany) onto clean microscope glass slides (VWR International, Radnor, PA, USA) and sealed with a coverslip (Fisher Scientific, Hampton, NH, USA). Images were taken with the Zeiss M2 Imager with Apotome 2 and Zen Blue software (Zeiss, Oberkochen, Germany) with the DAPI fluorescent channel (exposure time = 100 ms) and the GFP fluorescent channel (exposure time = 350 ms). Brightfield images were taken with the Zeiss AxioImager fluorescence microscope with AxioVision (Zeiss, Oberkochen, Germany). All post-analysis and image processing were done with Fiji (ImageJ).

IV.D.4.c. Flow Cytometry

All flow cytometry measurements were processed by a Fortessa cytometer (BD Biosciences, NJ, USA) and data analyses performed using BD FACS Diva Software 6.1 (BD Biosciences, NJ, USA). The presence of GFP was detected through flow cytometry, where the GFP expression was assessed by washing in PBS with 2.5% FBS and fixation using BD stabilizing fixative (BD Biosciences, NJ, USA) as described previously.[76] All experiments with determinations of geometric MFI were performed using the same protocol, fluorochrome voltages, and cytometer.

IV.D.4.d. Digital Droplet Polymerase Chain Reaction

Extraction of RNA and reverse transcription was first performed before ddPCR after collecting cells. First, ~5 x 10^5 cells were pelleted and resuspended in 100 µL of lyses buffer from RNeasy Plus Mini Kit (Qiagen, Hilden, Germany). Total RNA was extracted from collecting cells with spin-columns (RNeasy Plus Mini Kit; Qiagen, Hilden, Germany) and follow the manufacturer's protocol. RNA quality was determined using nanodrop spectrophotometer (Thermo Fisher Scientific, Waltham, MA, USA). All of the RNA samples used for the study were pure (A260/A280 ≥ 1.9; A260/A230 ≥ 2). Then, 200 ng of RNA was subjected for reverse transcription in 50 µL of reaction using M-MLV reverse transcriptase (Thermo Fisher Scientific, Waltham, MA, USA) and random hexamers (Thermo Fisher Scientific, Waltham, MA, USA). The reactions were carried on at 37 °C for 50 min and stopped by incubation at 70 °C for 15 min.

Digital droplet PCR was performed with QX200 Droplet Digital PCR System (Bio-Rad, Hercules, CA, USA), according to the manufacturer's protocol and the work of McDermott *et al*.[77] Briefly, each of the 20 µL reactions contained 1× EvaGreen ddPCR Supermix (Bio-Rad,

Hercules, CA, USA), 250 nM gene-specific primers and 2 μL of the cDNA sample. The following primers for CD19RCD28MZ were designed with Vector NTI software: forward: 5'- CCTGGTGAAGGGCTTCTACC -3' and reverse: 5'- CGGAGCAGCTAAAGACGTTG -3' (179 bp amplicon). Primers targeting GFP were designed based on work previously reported.[78] Human beta actin (SKU# 10031258) primers as the internal control (Bio-Rad, Hercules, CA, USA). Each reaction was mixed with 70 μL of Droplet Generation Oil (Bio-Rad, Hercules, CA, USA), partitioned into 14,000-17,000 droplets in QX200 Droplet Generator (Bio-Rad, Hercules, CA, USA), transferred to 96-well plates (Bio-Rad, Hercules, CA, USA) and heat sealed with foil by PXTM PCR Plate Sealer (Bio-Rad, Hercules, CA, USA). The PCR reactions were performed in a T100TM Thermal Cycler (Bio-Rad, Hercules, CA, USA) with the following cycling conditions: 1× (95 °C for 5 min), 40× (95 °C for 30 s, 60 °C for 1 min), 1× (4°C for 5 min, 90 °C for 5 min) with 2 °C/s ramp rate, hold at 4 °C. Immediately following end-point amplification, the fluorescence intensity of individual droplets was measured with the QX200 Droplet Reader (Bio-Rad, Hercules, CA, USA). After data acquisition, the data analysis was performed with QuantaSoft droplet reader software (Bio-Rad, Hercules, CA, USA). Examine the manually thresholding applied to the 1-D amplitude data. The absolute transcript levels reported were copies/μL of the final 1x ddPCR reaction.

IV.D.5. Statistical Analysis

Statistical analysis was performed using Graph Pad Prism 6.01 (GraphPad Software, Irvine, CA, USA). All data were expressed as mean ± standard deviation (s.d.). Analysis of variance (ANOVA) was used for multiple comparison. $P < 0.05$ was considered statistically significant.

IV.E. Appendix

IV.E.1. Fluorescence Microscope Images

Fluorescence microscope images for 24 – 72 h time points for delivery of CMV-EGFP plasmids to Jurkat cells with the vacuum filtration system (Figure IV.6).

IV.E.2. Flow Cytometry

The maximum transfection of the Jurkat cells with the MNDU3-EGFP plasmid is ~40%. A representative flow cytometry plot is shown in Figure IV.7C for MNDU3-EGFP with corresponding histogram plots for each time point (Figure IV.7E). Jurkat wild-type (Figure IV.7A) serves as a negative control, showing no significant fluorescence, and the Jurkat EGFP-EGFR (Figure IV.7B) cell line, the positive control showing GFP expression, is shown as well as an overlay of their histograms in comparison to the 72-h time point of the MNDU3-EGFP transfected cells (Figure IV.7D).

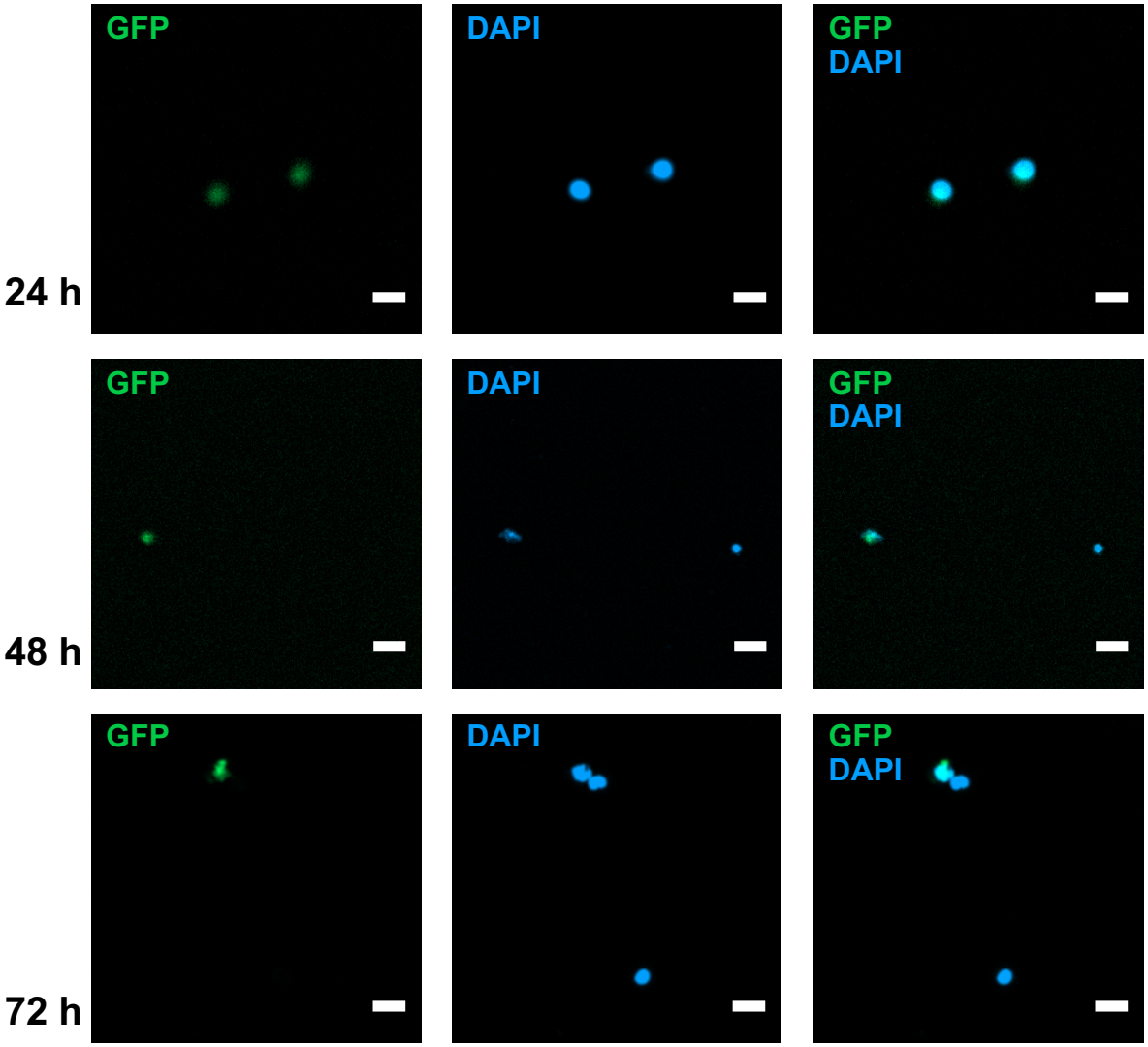

Figure IV.6. Fluorescence microscope images of green fluorescent protein (GFP) (left) and DAPI (a nuclear counterstain) (middle) channels as well as their merged channels (right). Images of CMV (cytomegalovirus) -EGFP transfected Jurkat cells at (A) 24 h, (B) 48 h, and (C) 72 h after vacuum filtration using commercial porous culture insert membrane with 8 μm pores. Jurkat cells were incubated with 0.1 mg/mL of the CMV-EGFP plasmid. Scale bars = 20 μm.

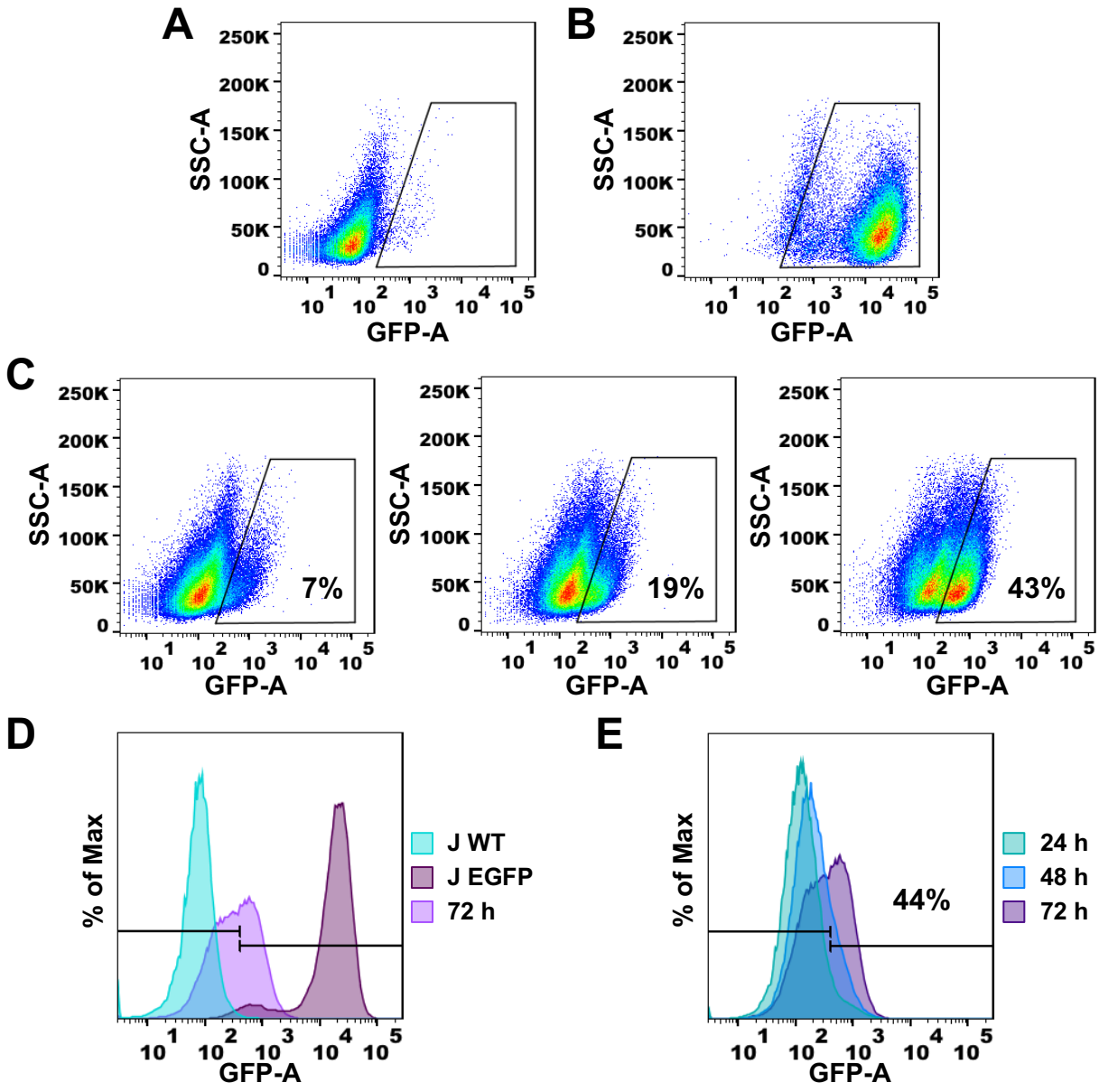

Figure IV.7. Maximum green fluorescent protein (GFP) expression from Jurkat cells 24 – 72 h after transfection via the vacuum filtration gene delivery system using commercial poly(ethylene terephthalate) cell culture filters inserts (8 μm pore size). Flow cytometry plots showing GFP expression of (A) Jurkat wild-type (negative control), (B) Jurkat enhanced GFP (EGFP) -epidermal growth factor receptor (EGFR) cell line (positive control), and (C) Jurkat cells that were immediately exposed to a MNDU3-EGFP plasmid at 24- (left), 48- (middle), and 72-h (right) time points. (D) Histogram overlay of Jurkat wild-type, Jurkat EGFP-EGFR, and transfected Jurkat cells at 72 h. (E) Histogram overlay of transfected Jurkat cells at 24 h, 48 h, and 72 h.

IV.F. References

(1) Dunbar, C. E.; High, K. A.; Joung, J. K.; Kohn, D. B.; Ozawa, K.; Sadelain, M. Gene Therapy Comes of Age. *Science* **2018**, *359*, eaan4672.

(2) Sadelain, M.; Rivière, I.; Riddell, S. Therapeutic T Cell Engineering. *Nature* **2017**, *545*, 423–431.

(3) Hoban, M. D.; Bauer, D. E. A Genome Editing Primer for the Hematologist. *Blood* **2016**, *127*, 2525–2535.

(4) Komor, A. C.; Badran, A. H.; Liu, D. R. CRISPR-Based Technologies for the Manipulation of Eukaryotic Genomes. *Cell* **2017**, *168*, 20–36.

(5) Waddington, S. N.; Privolizzi, R.; Karda, R.; O'Neill, H. C. A Broad Overview and Review of CRISPR-Cas Technology and Stem Cells. *Curr. Stem Cell Rep.* **2016**, *2*, 9–20.

(6) Osborn, M. J.; Webber, B. R.; Knipping, F.; Lonetree, C.; Tennis, N.; DeFeo, A. P.; McElroy, A. N.; Starker, C. G.; Lee, C.; Merkel, S.; Lund, T. C.; Kelly-Spratt, K. S.; Jensen, M. C.; Voytas, D. F.; von Kalle, C.; Schmidt, M.; Gabriel, R.; Hippen, K. L.; Miller, J. S.; Scharenberg, A. M.; Tolar, J.; Blazar, B. R. Evaluation of TCR Gene Editing Achieved by TALENs, CRISPR/Cas9, and MegaTAL Nucleases. *Mol. Ther.* **2016**, *24*, 570–581.

(7) Eyquem, J.; Mansilla-Soto, J.; Giavridis, T.; van der Stegen, S. J. C.; Hamieh, M.; Cunanan, K. M.; Odak, A.; Gönen, M.; Sadelain, M. Targeting a CAR to the TRAC Locus with CRISPR/Cas9 Enhances Tumour Rejection. *Nature* **2017**, *543*, 113–117.

(8) Shaw, K. L.; Garabedian, E.; Mishra, S.; Barman, P.; Davila, A.; Carbonaro, D.; Shupien, S.; Silvin, C.; Geiger, S.; Nowicki, B.; Smogorzewska, E. M.; Brown, B.; Wang, X.; Oliveira, S. de; Choi, Y.; Ikeda, A.; Terrazas, D.; Fu, P.-Y.; Yu, A.; Fernandez, B. C.; Cooper, A. R.; Engel, B.; Podsakoff, G.; Balamurugan, A.; Anderson, S.; Muul, L.; Jagadeesh, G. J.; Kapoor, N.; Tse, J.; Moore, T. B.; Purdy, K.; Rishi, R.; Mohan, K.; Skoda-Smith, S.; Buchbinder, D.; Abraham, R. S.; Scharenberg, A.; Yang, O. O.; Cornetta, K.; Gjertson, D.; Hershfield, M.; Sokolic, R.; Candotti, F.; Kohn, D. B. Clinical Efficacy of Gene-Modified Stem Cells in Adenosine Deaminase–Deficient Immunodeficiency. *J. Clin. Invest.* **2017**, *127*, 1689–1699.

(9) Kohn, D. B.; Kuo, C. Y. New Frontiers in the Therapy of Primary Immunodeficiency: From Gene Addition to Gene Editing. *J. Allergy Clin. Immunol.* **2017**, *139*, 726–732.

(10) Hoban, M. D.; Cost, G. J.; Mendel, M. C.; Romero, Z.; Kaufman, M. L.; Joglekar, A. V.; Ho, M.; Lumaquin, D.; Gray, D.; Lill, G. R.; Cooper, A. R.; Urbinati, F.; Senadheera, S.; Zhu, A.; Liu, P.-Q.; Paschon, D. E.; Zhang, L.; Rebar, E. J.; Wilber, A.; Wang, X.; Gregory, P. D.; Holmes, M. C.; Reik, A.; Hollis, R. P.; Kohn, D. B. Correction of the Sickle Cell Disease Mutation in Human Hematopoietic Stem/Progenitor Cells. *Blood* **2015**, *125*, 2597–2604.

(11) Lidonnici, M. R.; Ferrari, G. Gene Therapy and Gene Editing Strategies for Hemoglobinopathies. *Blood Cells. Mol. Dis.* **2018**, *70*, 87–101.

(12) Tabebordbar, M.; Zhu, K.; Cheng, J. K. W.; Chew, W. L.; Widrick, J. J.; Yan, W. X.; Maesner, C.; Wu, E. Y.; Xiao, R.; Ran, F. A.; Cong, L.; Zhang, F.; Vandenberghe, L. H.; Church, G. M.; Wagers, A. J. *In Vivo* Gene Editing in Dystrophic Mouse Muscle and Muscle Stem Cells. *Science* **2016**, *351*, 407–411.

(13) Long, C.; Amoasii, L.; Mireault, A. A.; McAnally, J. R.; Li, H.; Sanchez-Ortiz, E.; Bhattacharyya, S.; Shelton, J. M.; Bassel-Duby, R.; Olson, E. N. Postnatal Genome Editing Partially Restores Dystrophin Expression in a Mouse Model of Muscular Dystrophy. *Science* **2016**, *351*, 400–403.

(14) Balaggan, K. S.; Binley, K.; Esapa, M.; Iqball, S.; Askham, Z.; Kan, O.; Tschernutter, M.; Bainbridge, J. W. B.; Naylor, S.; Ali, R. R. Stable and Efficient Intraocular Gene Transfer Using Pseudotyped EIAV Lentiviral Vectors. *J. Gene Med. Chichester* **2006**, *8*, 275–285.

(15) Mochizuki, A. Y.; Frost, I. M.; Mastrodimos, M. B.; Plant, A. S.; Wang, A. C.; Moore, T. B.; Prins, R. M.; Weiss, P. S.; Jonas, S. J. Precision Medicine in Pediatric Neurooncology: A Review. *ACS Chem. Neurosci.* **2018**, *9*, 11–28.

(16) Maude, S. L.; Frey, N.; Shaw, P. A.; Aplenc, R.; Barrett, D. M.; Bunin, N. J.; Chew, A.; Gonzalez, V. E.; Zheng, Z.; Lacey, S. F.; Mahnke, Y. D.; Melenhorst, J. J.; Rheingold, S. R.; Shen, A.; Teachey, D. T.; Levine, B. L.; June, C. H.; Porter, D. L.; Grupp, S. A. Chimeric Antigen Receptor T Cells for Sustained Remissions in Leukemia. *N. Engl. J. Med.* **2014**, *371*, 1507–1517.

(17) Rosenberg, S. A.; Restifo, N. P. Adoptive Cell Transfer as Personalized Immunotherapy for Human Cancer. *Science* **2015**, *348*, 62–68.

(18) Sadelain, M.; Rivière, I.; Brentjens, R. Targeting Tumours with Genetically Enhanced T Lymphocytes. *Nat. Rev. Cancer* **2003**, *3*, 35–45.

(19) Ellebrecht, C. T.; Bhoj, V. G.; Nace, A.; Choi, E. J.; Mao, X.; Cho, M. J.; Zenzo, G. D.; Lanzavecchia, A.; Seykora, J. T.; Cotsarelis, G.; Milone, M. C.; Payne, A. S. Reengineering Chimeric Antigen Receptor T Cells for Targeted Therapy of Autoimmune Disease. *Science* **2016**, *353*, 179–184.

(20) De Oliveira, S. N.; Wang, J.; Ryan, C.; Morrison, S. L.; Kohn, D. B.; Hollis, R. P. A CD19/Fc Fusion Protein for Detection of Anti-CD19 Chimeric Antigen Receptors. *J. Transl. Med.* **2013**, *11*, 23.

(21) Larson, S. M.; Truscott, L. C.; Chiou, T.-T.; Patel, A.; Kao, R.; Tu, A.; Tyagi, T.; Lu, X.; Elashoff, D.; De Oliveira, S. N. Pre-Clinical Development of Gene Modification of Haematopoietic Stem Cells with Chimeric Antigen Receptors for Cancer Immunotherapy. *Hum. Vaccines Immunother.* **2017**, *13*, 1094–1104.

(22) Torikai, H.; Reik, A.; Liu, P.-Q.; Zhou, Y.; Zhang, L.; Maiti, S.; Huls, H.; Miller, J. C.; Kebriaei, P.; Rabinovitch, B.; Lee, D. A.; Champlin, R. E.; Bonini, C.; Naldini, L.; Rebar, E. J.; Gregory, P. D.; Holmes, M. C.; Cooper, L. J. N. A Foundation for Universal T-Cell Based Immunotherapy: T Cells Engineered to Express a CD19-Specific Chimeric-Antigen-Receptor and Eliminate Expression of Endogenous TCR. *Blood* **2012**, *119*, 5697–5705.

(23) June, C. H.; Riddell, S. R.; Schumacher, T. N. Adoptive Cellular Therapy: A Race to the Finish Line. *Sci. Transl. Med.* **2015**, *7*, 280ps7-280ps7.

(24) Lee, D. W.; Kochenderfer, J. N.; Stetler-Stevenson, M.; Cui, Y. K.; Delbrook, C.; Feldman, S. A.; Fry, T. J.; Orentas, R.; Sabatino, M.; Shah, N. N.; Steinberg, S. M.; Stroncek, D.; Tschernia, N.; Yuan, C.; Zhang, H.; Zhang, L.; Rosenberg, S. A.; Wayne, A. S.; Mackall, C. L. T Cells Expressing CD19 Chimeric Antigen Receptors for Acute Lymphoblastic Leukaemia in Children and Young Adults: A Phase 1 Dose-Escalation Trial. *The Lancet* **2015**, *385*, 517–528.

(25) Sadelain, M.; Brentjens, R.; Rivière, I. The Basic Principles of Chimeric Antigen Receptor Design. *Cancer Discov.* **2013**, *3*, 388–398.

(26) Jordan, E. T.; Collins, M.; Terefe, J.; Ugozzoli, L.; Rubio, T. Optimizing Electroporation Conditions in Primary and Other Difficult-to-Transfect Cells. *J. Biomol. Tech.* **2008**, *19*, 328–334.

(27) Lakshmanan, S.; Gupta, G. K.; Avci, P.; Chandran, R.; Sadasivam, M.; Jorge, A. E. S.; Hamblin, M. R. Physical Energy for Drug Delivery; Poration, Concentration and Activation. *Adv. Drug Deliv. Rev.* **2014**, *71*, 98–114.

(28) Mehier-Humbert, S.; Guy, R. H. Physical Methods for Gene Transfer: Improving the Kinetics of Gene Delivery into Cells. *Adv. Drug Deliv. Rev.* **2005**, *57*, 733–753.

(29) Holstein, M.; Mesa-Nuñez, C.; Miskey, C.; Almarza, E.; Poletti, V.; Schmeer, M.; Grueso, E.; Ordóñez Flores, J. C.; Kobelt, D.; Walther, W.; Aneja, M. K.; Geiger, J.; Bonig, H. B.; Izsvák, Z.; Schleef, M.; Rudolph, C.; Mavilio, F.; Bueren, J. A.; Guenechea, G.; Ivics, Z. Efficient Non-Viral Gene Delivery into Human Hematopoietic Stem Cells by Minicircle Sleeping Beauty Transposon Vectors. *Mol. Ther.* **2018**, *26*, 1137–1153.

(30) Ramamoorth, M.; Narvekar, A. Non Viral Vectors in Gene Therapy- An Overview. *J. Clin. Diagn. Res.* **2015**, *9*, GE01–GE06.

(31) Rosazza, C.; Meglic, S. H.; Zumbusch, A.; Rols, M.-P.; Miklavcic, D. Gene Electrotransfer: A Mechanistic Perspective. *Curr. Gene Ther.* **2016**, *16*, 98–129.

(32) Rosazza, C.; Buntz, A.; Rieß, T.; Wöll, D.; Zumbusch, A.; Rols, M.-P. Intracellular Tracking of Single-Plasmid DNA Particles After Delivery by Electroporation. *Mol. Ther.* **2013**, *21*, 2217–2226.

(33) Milone, M. C.; O'Doherty, U. Clinical Use of Lentiviral Vectors. *Leukemia* **2018**, *32*, 1529–1541.

(34) Anson, D. S. The Use of Retroviral Vectors for Gene Therapy-What Are the Risks? A Review of Retroviral Pathogenesis and Its Relevance to Retroviral Vector-Mediated Gene Delivery. *Genet. Vaccines Ther.* **2004**, *2*, 9.

(35) Kay, M. A.; Glorioso, J. C.; Naldini, L. Viral Vectors for Gene Therapy: The Art of Turning Infectious Agents into Vehicles of Therapeutics. *Nat. Med.* **2001**, *7*, 33–40.

(36) Zhang, X.; Godbey, W. T. Viral Vectors for Gene Delivery in Tissue Engineering. *Adv. Drug Deliv. Rev.* **2006**, *58*, 515–534.

(37) Waehler, R.; Russell, S. J.; Curiel, D. T. Engineering Targeted Viral Vectors for Gene Therapy. *Nat. Rev. Genet.* **2007**, *8*, 573–587.

(38) Nayerossadat, N.; Maedeh, T.; Ali, P. A. Viral and Nonviral Delivery Systems for Gene Delivery. *Adv. Biomed. Res.* **2012**, *1*.

(39) Kataoka, K.; Harashima, H. Gene Delivery Systems: Viral vs. Non-Viral Vectors. *Adv Drug Deliv. Rev.* **2001**, *52*, 151.

(40) Wiethoff, C. M.; Middaugh, C. R. Barriers to Nonviral Gene Delivery. *J. Pharm. Sci.* **2003**, *92*, 203–217.

(41) Hill, A. B.; Chen, M.; Chen, C.-K.; Pfeifer, B. A.; Jones, C. H. Overcoming Gene-Delivery Hurdles: Physiological Considerations for Nonviral Vectors. *Trends Biotechnol.* **2016**, *34*, 91–105.

(42) Thomas, C. E.; Ehrhardt, A.; Kay, M. A. Progress and Problems with the Use of Viral Vectors for Gene Therapy. *Nat. Rev. Genet.* **2003**, *4*, 346–358.

(43) Lenz, P.; Bacot, S. M.; Frazier-Jessen, M. R.; Feldman, G. M. Nucleoporation of Dendritic Cells: Efficient Gene Transfer by Electroporation into Human Monocyte-Derived Dendritic Cells 1. *FEBS Lett.* **2003**, *538*, 149–154.

(44) Sibbald, B. Death but One Unintended Consequence of Gene-Therapy Trial. *Can. Med. Assoc. J.* **2001**, *164*, 1612.

(45) Graessmann, M.; Graessmann, A.; Hoffmann, E.; Niebel, J.; Pilaski, K. The Biological Activity of Different Forms of Polyoma Virus DNA and Viral DNA Fragments. *Mol. Biol. Rep.* **1973**, *1*, 233–241.

(46) Mertz, J. E.; Gurdon, J. B. Purified DNAs Are Transcribed after Microinjection into Xenopus Oocytes. *Proc. Natl. Acad. Sci.* **1977**, *74*, 1502–1506.

(47) Capecchi, M. R. High Efficiency Transformation by Direct Microinjection of DNA into Cultured Mammalian Cells. *Cell* **1980**, *22*, 479–488.

(48) Tiefenboeck, P.; Kim, J. A.; Trunk, F.; Eicher, T.; Russo, E.; Teijeira, A.; Halin, C.; Leroux, J.-C. Microinjection for the *Ex Vivo* Modification of Cells with Artificial Organelles. *ACS Nano* **2017**, *11*, 7758–7769.

(49) Wang, P. M.; Cornwell, M.; Hill, J.; Prausnitz, M. R. Precise Microinjection into Skin Using Hollow Microneedles. *J. Invest. Dermatol.* **2006**, *126*, 1080–1087.

(50) Matsuoka, H.; Komazaki, T.; Mukai, Y.; Shibusawa, M.; Akane, H.; Chaki, A.; Uetake, N.; Saito, M. High Throughput Easy Microinjection with a Single-Cell Manipulation Supporting Robot. *J. Biotechnol.* **2005**, *116*, 185–194.

(51) Tesson, L.; Usal, C.; Ménoret, S.; Leung, E.; Niles, B. J.; Remy, S.; Santiago, Y.; Vincent, A. I.; Meng, X.; Zhang, L.; Gregory, P. D.; Anegon, I.; Cost, G. J. Knockout Rats Generated by Embryo Microinjection of TALENs. *Nat. Biotechnol.* **2011**, *29*, 695–696.

(52) Ramesan, S.; Rezk, A. R.; Dekiwadia, C.; Cortez-Jugo, C.; Yeo, L. Y. Acoustically-Mediated Intracellular Delivery. *Nanoscale* **2018**, *10*, 13165–13178.

(53) van Wamel, A.; Kooiman, K.; Harteveld, M.; Emmer, M.; ten Cate, F. J.; Versluis, M.; de Jong, N. Vibrating Microbubbles Poking Individual Cells: Drug Transfer into Cells *via* Sonoporation. *J. Control. Release* **2006**, *112*, 149–155.

(54) Tomizawa, M.; Shinozaki, F.; Motoyoshi, Y.; Sugiyama, T.; Yamamoto, S.; Sueishi, M. Sonoporation: Gene Transfer Using Ultrasound. *World J. Methodol.* **2013**, *3*, 39–44.

(55) Ruiz-Esparza, G. U.; Wu, S.; Segura-Ibarra, V.; Cara, F. E.; Evans, K. W.; Milosevic, M.; Ziemys, A.; Kojic, M.; Meric-Bernstam, F.; Ferrari, M.; Blanco, E. Polymer Nanoparticles Encased in a Cyclodextrin Complex Shell for Potential Site- and Sequence-Specific Drug Release. *Adv. Funct. Mater. 24*, 4753–4761.

(56) Fink, T. L.; Klepcyk, P. J.; Oette, S. M.; Gedeon, C. R.; Hyatt, S. L.; Kowalczyk, T. H.; Moen, R. C.; Cooper, M. J. Plasmid Size up to 20 Kbp Does Not Limit Effective *in Vivo* Lung Gene Transfer Using Compacted DNA Nanoparticles. *Gene Ther.* **2006**, *13*, 1048–1051.

(57) Lyu, Z.; Zhou, F.; Liu, Q.; Xue, H.; Yu, Q.; Chen, H. A Universal Platform for Macromolecular Delivery into Cells Using Gold Nanoparticle Layers *via* the Photoporation Effect. *Adv. Funct. Mater.* **2016**, *26*, 5787–5795.

(58) Chiappini, C.; De Rosa, E.; Martinez, J. O.; Liu, X.; Steele, J.; Stevens, M. M.; Tasciotti, E. Biodegradable Silicon Nanoneedles Delivering Nucleic Acids Intracellularly Induce Localized *in Vivo* Neovascularization. *Nat. Mater.* **2015**, *14*, 532–539.

(59) Cai, D.; Mataraza, J. M.; Qin, Z.-H.; Huang, Z.; Huang, J.; Chiles, T. C.; Carnahan, D.; Kempa, K.; Ren, Z. Highly Efficient Molecular Delivery into Mammalian Cells Using Carbon Nanotube Spearing. *Nat. Methods* **2005**, *2*, 449–454.

(60) Shalek, A. K.; Robinson, J. T.; Karp, E. S.; Lee, J. S.; Ahn, D.-R.; Yoon, M.-H.; Sutton, A.; Jorgolli, M.; Gertner, R. S.; Gujral, T. S.; MacBeath, G.; Yang, E. G.; Park, H. Vertical Silicon Nanowires as a Universal Platform for Delivering Biomolecules into Living Cells. *Proc. Natl. Acad. Sci.* **2010**, *107*, 1870–1875.

(61) McKnight, T. E.; Melechko, A. V.; Griffin, G. D.; Guillorn, M. A.; Merkulov, V. I.; Serna, F.; Hensley, D. K.; Doktycz, M. J.; Lowndes, D. H.; Simpson, M. L. Intracellular Integration of Synthetic Nanostructures with Viable Cells for Controlled Biochemical Manipulation. *Nanotechnology* **2003**, *14*, 551.

(62) McKnight, T. E.; Melechko, A. V.; Hensley, D. K.; Mann, D. G. J.; Griffin, G. D.; Simpson, M. L. Tracking Gene Expression after DNA Delivery Using Spatially Indexed Nanofiber Arrays. *Nano Lett.* **2004**, *4*, 1213–1219.

(63) Mann, D. G. J.; McKnight, T. E.; McPherson, J. T.; Hoyt, P. R.; Melechko, A. V.; Simpson, M. L.; Sayler, G. S. Inducible RNA Interference-Mediated Gene Silencing Using Nanostructured Gene Delivery Arrays. *ACS Nano* **2008**, *2*, 69–76.

(64) Stewart, M. P.; Langer, R.; Jensen, K. F. Intracellular Delivery by Membrane Disruption: Mechanisms, Strategies, and Concepts. *Chem. Rev.* **2018**, *118*, 7409–7531.

(65) Sharei, A.; Zoldan, J.; Adamo, A.; Sim, W. Y.; Cho, N.; Jackson, E.; Mao, S.; Schneider, S.; Han, M.-J.; Lytton-Jean, A.; Basto, P. A.; Jhunjhunwala, S.; Lee, J.; Heller, D. A.; Kang, J. W.; Hartoularos, G. C.; Kim, K.-S.; Anderson, D. G.; Langer, R.; Jensen, K. F. A Vector-Free Microfluidic Platform for Intracellular Delivery. *Proc. Natl. Acad. Sci.* **2013**, *110*, 2082–2087.

(66) Sharei, A.; Poceviciute, R.; Jackson, E. L.; Cho, N.; Mao, S.; Hartoularos, G. C.; Jang, D. Y.; Jhunjhunwala, S.; Eyerman, A.; Schoettle, T.; Langer, R.; Jensen, K. F. Plasma Membrane Recovery Kinetics of a Microfluidic Intracellular Delivery Platform. *Integr. Biol.* **2014**, *6*, 470–475.

(67) Szeto, G. L.; Van Egeren, D.; Worku, H.; Sharei, A.; Alejandro, B.; Park, C.; Frew, K.; Brefo, M.; Mao, S.; Heimann, M.; Langer, R.; Jensen, K.; Irvine, D. J. Microfluidic Squeezing for Intracellular Antigen Loading in Polyclonal B-Cells as Cellular Vaccines. *Sci. Rep.* **2015**, *5*.

(68) Kollmannsperger, A.; Sharei, A.; Raulf, A.; Heilemann, M.; Langer, R.; Jensen, K. F.; Wieneke, R.; Tampé, R. Live-Cell Protein Labelling with Nanometre Precision by Cell Squeezing. *Nat. Commun.* **2016**, *7*.

(69) Saung, M. T.; Sharei, A.; Adalsteinsson, V. A.; Cho, N.; Kamath, T.; Ruiz, C.; Kirkpatrick, J.; Patel, N.; Mino-Kenudson, M.; Thayer, S. P.; Langer, R.; Jensen, K. F.; Liss, A. S.; Love, J. C. A Size-Selective Intracellular Delivery Platform. *Small* **2016**, *12*, 5873–5881.

(70) Ding, X.; Stewart, M. P.; Sharei, A.; Weaver, J. C.; Langer, R. S.; Jensen, K. F. High-Throughput Nuclear Delivery and Rapid Expression of DNA *via* Mechanical and Electrical Cell-Membrane Disruption. *Nat. Biomed. Eng.* **2017**, *1*, 0039.

(71) DiTommaso, T.; Cole, J. M.; Cassereau, L.; Buggé, J. A.; Hanson, J. L. S.; Bridgen, D. T.; Stokes, B. D.; Loughhead, S. M.; Beutel, B. A.; Gilbert, J. B.; Nussbaum, K.; Sorrentino, A.; Toggweiler, J.; Schmidt, T.; Gyuelveszi, G.; Bernstein, H.; Sharei, A. Cell Engineering with Microfluidic Squeezing Preserves Functionality of Primary Immune Cells *in Vivo*. *Proc. Natl. Acad. Sci.* **2018**, *115*, E10907–E10914.

(72) Cox, D. B. T.; Platt, R. J.; Zhang, F. Therapeutic Genome Editing: Prospects and Challenges. *Nat. Med.* **2015**, *21*, 121–131.

(73) Romero, Z.; Urbinati, F.; Geiger, S.; Cooper, A. R.; Wherley, J.; Kaufman, M. L.; Hollis, R. P.; Assin, R. R. de; Senadheera, S.; Sahagian, A.; Jin, X.; Gellis, A.; Wang, X.; Gjertson, D.; DeOliveira, S.; Kempert, P.; Shupien, S.; Abdel-Azim, H.; Walters, M. C.; Meiselman, H. J.; Wenby, R. B.; Gruber, T.; Marder, V.; Coates, T. D.; Kohn, D. B. β-Globin Gene Transfer to Human Bone Marrow for Sickle Cell Disease. *J. Clin. Invest.* **2013**, *123*, 3317–3330.

(74) Wang, X.; Chang, W.-C.; Wong, C. W.; Colcher, D.; Sherman, M.; Ostberg, J. R.; Forman, S. J.; Riddell, S. R.; Jensen, M. C. A Transgene-Encoded Cell Surface Polypeptide for Selection, *in Vivo* Tracking, and Ablation of Engineered Cells. *Blood* **2011**, *118*, 1255–1263.

(75) Jonnalagadda, M.; Mardiros, A.; Urak, R.; Wang, X.; Hoffman, L. J.; Bernanke, A.; Chang, W.-C.; Bretzlaff, W.; Starr, R.; Priceman, S.; Ostberg, J. R.; Forman, S. J.; Brown, C. E. Chimeric Antigen Receptors With Mutated IgG4 Fc Spacer Avoid Fc Receptor Binding and Improve T Cell Persistence and Antitumor Efficacy. *Mol. Ther.* **2015**, *23*, 757–768.

(76) De Oliveira, S. N.; Ryan, C.; Giannoni, F.; Hardee, C. L.; Tremcinska, I.; Katebian, B.; Wherley, J.; Sahaghian, A.; Tu, A.; Grogan, T.; Elashoff, D.; Cooper, L. J. N.; Hollis, R. P.; Kohn, D. B. Modification of Hematopoietic Stem/Progenitor Cells with CD19-Specific Chimeric Antigen Receptors as a Novel Approach for Cancer Immunotherapy. *Hum. Gene Ther.* **2013**, *24*, 824–839.

(77) McDermott, G. P.; Do, D.; Litterst, C. M.; Maar, D.; Hindson, C. M.; Steenblock, E. R.; Legler, T. C.; Jouvenot, Y.; Marrs, S. H.; Bemis, A.; Shah, P.; Wong, J.; Wang, S.; Sally, D.; Javier, L.; Dinio, T.; Han, C.; Brackbill, T. P.; Hodges, S. P.; Ling, Y.; Klitgord, N.; Carman, G. J.; Berman, J. R.; Koehler, R. T.; Hiddessen, A. L.; Walse, P.; Bousse, L.; Tzonev, S.; Hefner, E.; Hindson, B. J.; Cauly, T. H.; Hamby, K.; Patel, V. P.; Regan, J. F.; Wyatt, P. W.; Karlin-Neumann, G. A.; Stumbo, D. P.; Lowe, A. J. Multiplexed Target Detection Using DNA-Binding Dye Chemistry in Droplet Digital PCR. *Anal. Chem.* **2013**, *85*, 11619–11627.

(78) Qiu, C.; Cheng, B.; Zhang, Y.; Huang, R.; Liao, L.; Li, Y.; Luo, D.; Hu, W.; Wang, Y. Efficient Knockout of Transplanted Green Fluorescent Protein Gene in Medaka Using TALENs. *Mar. Biotechnol.* **2014**, *16*, 674–683.

CHAPTER V

Conclusions and Future Prospects

V.A. Summary

In the preceding chapters, I detailed how our group can leverage surface-interface interactions to direct and to control assemblies for a variety of applications, from controlling liquid crystal alignment on gold surfaces (Chapter II)[1] to coating pores of devices with bioinspired chemistries to minimize biofouling (Chapter III). Moreover, in Chapters III and IV, used economical materials to develop a cost-effective delivery method that can be used for bimolecular cargo to model T lymphocyte cells in a safe and efficient manner for emerging gene-therapy and cancer immunotherapy methods.

V.A.1. Surface Dipole Control of Liquid Crystals

Using carboranethiol and -dithiol monolayers on gold surfaces, we were able to demonstrate that surface dipoles have a profound effect on how adsorbates, namely liquid crystals, interact and align on the surface. These self-assembled monolayer surfaces offer several advantages over traditional alkanethiol SAMs in that they assemble with the same tilt, geometry, and lattice on Au{111} surfaces. We observed that the 5CB LCs, possessing a positive dielectric anisotropy (Δε), aligned parallel to the oblique gold deposition direction ($\overrightarrow{\text{Au}}$) by M1, O1, and 1O2 SAMs, which have dipole moments orientated towards the surface (Figure I.4).[1] However, SAMs composed of M9, O9, and 9O12 isomers, which have dipole moments orientated away from the surface, aligned 5CB perpendicular to the $\overrightarrow{\text{Au}}$.[1] The MBBA LCs, which have a negative Δε, aligned similarly to the 5CB LCs, suggesting that LC alignment on these surfaces is not merely a result of dipolar field coupling, but is a result of a more complex mechanism involving intermolecular dispersion forces.[1] To quantify SAM-LC interaction strengths, the surface anchoring energies of 5CB on SAMs composed of isomers with dipoles oriented away from (O9 and 9O12) and toward (M1 and O1) the substrate were

measured to be ~7 μJ·m^{-2} and ~14 μJ·m^{-2}, respectively,[1] which exceed values reported for other SAM surfaces (<6 μJ·m^{-2}).[2] These data suggest a dependence on the polarity of the carboranethiol dipole component normal to the surface provide insight into how intermolecular interactions at surfaces and their influence on the physical properties of surfaces can be tuned to engineer assemblies.[1,3–7] These results were described in detail in Chapter II and published in the *Journal of the American Chemical Society*.[1]

V.A.1.a. Future Directions of Nanoscale Control of Assemblies on Surfaces

The capabilities of these carboranethiol SAMs as electronic surface coatings has only begun to be explored.[1,3,4,8,9] Another area of interest for these carboranethiol and -dithiol isomers is in the growth of ferroelectric crystals, where tuning the surface dipole is advantageous. Ferroelectric materials are applied routinely in data storage and sensing technologies, but further research is required to understand how to control crystallization of these materials.[10–12] Our group has previously investigated how ferroelectric materials can be probed and switched at the nanoscale and their strong dependence on polarity and surface charge.[13–15] To test how these surface dipoles influence and can be used to control other molecular assemblies on surfaces, the crystal growth, polarization, and switching properties of ferroelectric polymers can be studied using carboranethiol and –dithiol SAMs on Au surfaces to extend this work.

V.A.2. Rapid Cell Deformation Devices and Intracellular Cargo Delivery

Our group has taken first steps to applying our surface science capabilities to a new field, where we are developing innovative approaches and devices to deliver gene and cellular therapies to cells. With my project, we have been able to demonstrate the use of commercial materials to rapidly deform cells and the application of promising slippery

liquid-infused porous surfaces (SLIPS) -modified materials that enable increased throughput and a cost-effective method for the generation of gene and cellular immunotherapies. In proof-of-concept experiments, expression plasmids encoding for green fluorescent protein (Chapter III and Chapter IV) and/or CD19 chimeric antigen receptor (Chapter IV) constructs were delivered to Jurkat cells, which serve as a model T lymphocyte line. Cells were processed by applying either positive or negative differential pressure to direct cells to pass through membrane materials that have been SLIPS-modified or untreated. The SLIPS-modified membranes are able to recover 25–50% more cells compared to unmodified filters. Additionally, with the vacuum filtration systems, we can achieve up to 40% transfection efficiency without compromising the viability or proliferative capacity of the Jurkat cells. Our investigations into applying these device made from commercial materials for delivering biomolecular cargo to cells was described in detail in Chapters III and IV.

V.A.2.a. Future Directions of Rapid Cell Deformation for Gene Editing *ex Vivo*

An interesting feature of the vacuum filtration system is that it can potentially be used to select for younger and smaller cells during processing, potentially biasing the population to express plasmid cargo longer and more efficiently. Current HSCT-based therapeutic strategies are more effective when more homogenous cell products are utilized.[16] Ultimately, an unintended advantage enabled by these materials is the capability to select for populations of cells that are more potent and more readily transfected, which perhaps could lead to more effective transplanted products.[16] Our next steps will focus on validating these methods in primary cell lines (hematopoietic stem cells and T cells) and to evaluate the cell populations we recover from these devices.

Our overarching goal is to develop and to validate microfluidic devices with constrictions that are coated with SLIPS to enable scalable, sustainable, and high-throughput transfection of cell products, targeting the modification of a billion cells within an hour (Figure I.8). These nanosystems represent our group's first steps toward the development of tools and methods that target the robust generation of homogenous therapeutic cell products. We ultimately wish to apply these methods for mimicking the hematopoietic stem cell niche where current culturing technologies fail to achieve long term maintenance and expansion of HSCs *in vitro*.[17] The capability to control the physical and chemical properties at the surfaces of engineered materials would pave the way to establishing these artificial stem cell niches.[18]

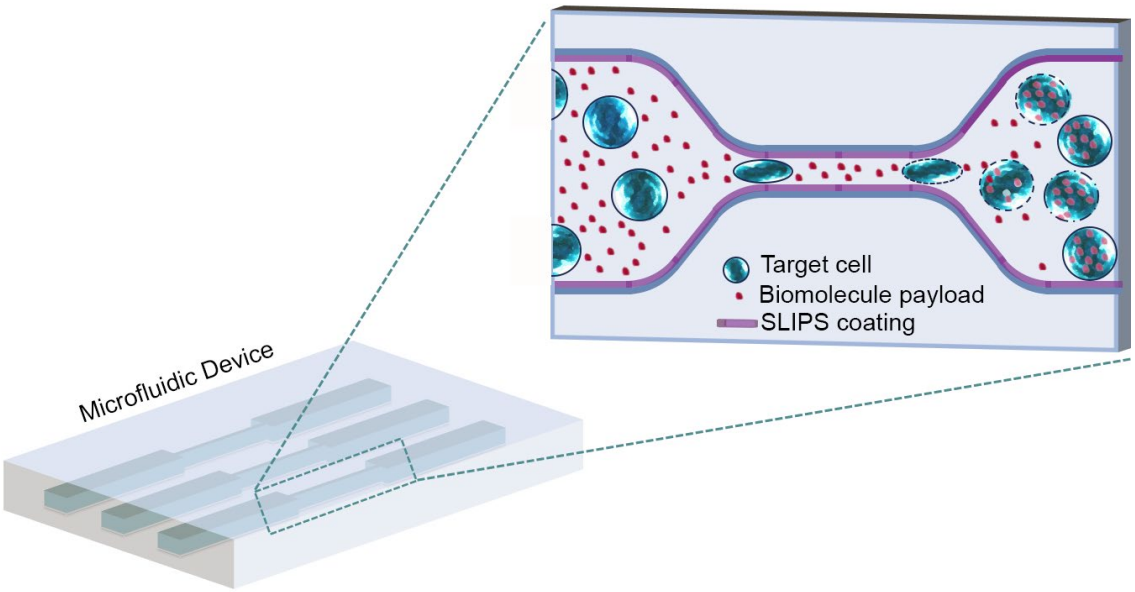

Figure V.1. Schematic illustrating the delivery of biomolecules for gene-editing applications to target cells temporarily permeabilized after passing through slippery liquid-infused porous surfaces (SLIPS)-coated constrictions in channels of a microfluidic device.

V.B. References

(1) Schwartz, J. J.; Mendoza, A. M.; Wattanatorn, N.; Zhao, Y.; Nguyen, V. T.; Spokoyny, A. M.; Mirkin, C. A.; Baše, T.; Weiss, P. S. Surface Dipole Control of Liquid Crystal Alignment. *J. Am. Chem. Soc.* **2016**, *138*, 5957–5967.

(2) Clare, B. H.; Guzmán, O.; de Pablo, J. J.; Abbott, N. L. Measurement of the Azimuthal Anchoring Energy of Liquid Crystals in Contact with Oligo(Ethylene Glycol)-Terminated Self-Assembled Monolayers Supported on Obliquely Deposited Gold Films. *Langmuir* **2006**, *22*, 4654–4659.

(3) Kim, J.; Rim, Y. S.; Liu, Y.; Serino, A. C.; Thomas, J. C.; Chen, H.; Yang, Y.; Weiss, P. S. Interface Control in Organic Electronics Using Mixed Monolayers of Carboranethiol Isomers. *Nano Lett.* **2014**, *14*, 2946–2951.

(4) Hohman, J. N.; Zhang, P.; Morin, E. I.; Han, P.; Kim, M.; Kurland, A. R.; McClanahan, P. D.; Balema, V. P.; Weiss, P. S. Self-Assembly of Carboranethiol Isomers on Au{111}: Intermolecular Interactions Determined by Molecular Dipole Orientations. *ACS Nano* **2009**, *3*, 527–536.

(5) Nakatsuka, N.; Cao, H. H.; Deshayes, S.; Melkonian, A. L.; Kasko, A. M.; Weiss, P. S.; Andrews, A. M. Aptamer Recognition of Multiplexed Small-Molecule-Functionalized Substrates. *ACS Appl. Mater. Interfaces* **2018**.

(6) Herrwerth, S.; Eck, W.; Reinhardt, S.; Grunze, M. Factors That Determine the Protein Resistance of Oligoether Self-Assembled Monolayers – Internal Hydrophilicity, Terminal Hydrophilicity, and Lateral Packing Density. *J. Am. Chem. Soc.* **2003**, *125*, 9359–9366.

(7) Ishida, T.; Mizutani, W.; Aya, Y.; Ogiso, H.; Sasaki, S.; Tokumoto, H. Electrical Conduction of Conjugated Molecular SAMs Studied by Conductive Atomic Force Microscopy. *J. Phys. Chem. B* **2002**, *106*, 5886–5892.

(8) Thomas, J. C.; Schwartz, J. J.; Hohman, J. N.; Claridge, S. A.; Auluck, H. S.; Serino, A. C.; Spokoyny, A. M.; Tran, G.; Kelly, K. F.; Mirkin, C. A.; Gilles, J.; Osher, S. J.; Weiss, P. S. Defect-Tolerant Aligned Dipoles within Two-Dimensional Plastic Lattices. *ACS Nano* **2015**, *9*, 4734–4742.

(9) Thomas, J. C.; Goronzy, D. P.; Serino, A. C.; Auluck, H. S.; Irving, O. R.; Jimenez-Izal, E.; Deirmenjian, J. M.; Macháček, J.; Sautet, P.; Alexandrova, A. N.; Baše, T.; Weiss, P. S. Acid-Base Control of Valency within Carboranedithiol Self-Assembled Monolayers: Molecules Do the Can-Can. *ACS Nano* **2018**, *12*, 2211–2221.

(10) Chen, S.; Yao, K.; Tay, F. E. H.; Liow, C. L. Ferroelectric Poly(Vinylidene Fluoride) Thin Films on Si Substrate with the β Phase Promoted by Hydrated Magnesium Nitrate. *J. Appl. Phys.* **2007**, *102*, 104108.

(11) Chen, S.; Li, X.; Yao, K.; Tay, F. E. H.; Kumar, A.; Zeng, K. Self-Polarized Ferroelectric PVDF Homopolymer Ultra-Thin Films Derived from Langmuir–Blodgett Deposition. *Polymer* **2012**, *53*, 1404–1408.

(12) Sharma, P.; Poddar, S.; Korlacki, R.; Ducharme, S.; Gruverman, A. Investigation of Ferroelectric Domains in Thin Films of Vinylidene Fluoride Oligomers. *Appl. Phys. Lett.* **2014**, *105*, 022906.

(13) Chen, X.; Yamada, H.; Horiuchi, T.; Matsushige, K.; Weiss, P. S. Formation of Nanoscale Polarized Domains in Organic Ferroelectric Thin Films by Scanning Force Microscopy. *Mol. Cryst. Liq. Cryst. A* **1999**, *337*, 285–288.

(14) Chen, X. Q.; Yamada, H.; Horiuchi, T.; Matsushige, K.; Watanabe, S.; Kawai, M.; Weiss, P. S. Surface Potential of Ferroelectric Thin Films Investigated by Scanning Probe Microscopy. *J. Vac. Sci. Technol. B* **1999**, *17*, 1930–1934.

(15) Chen, X. Q.; Yamada, H.; Terai, Y.; Horiuchi, T.; Matsushige, K.; Weiss, P. S. Strong Substrate Effect in Local Poling of Ultrathin Ferroelectric Polymer Films. *Thin Solid Films* **1999**, *353*, 259–263.

(16) Cox, D. B. T.; Platt, R. J.; Zhang, F. Therapeutic Genome Editing: Prospects and Challenges. *Nat. Med.* **2015**, *21*, 121–131.

(17) Mendelson, A.; Frenette, P. S. Hematopoietic Stem Cell Niche Maintenance during Homeostasis and Regeneration. *Nat. Med.* **2014**, *20*, 833–846.

(18) Stevens, M. M.; George, J. H. Exploring and Engineering the Cell Surface Interface. *Science* **2005**, *310*, 1135–1138.